Molecular Dynamics Simulations of Lubricants and Additives

by

James Patrick Ewen

A thesis submitted to Imperial College London for the degree of

Doctor of Philosophy

and for the Diploma of Imperial College (D.I.C.)

2017

Tribology Group

Department of Mechanical Engineering

Imperial College London

Declaration of Originality

This thesis describes work carried out in the Department of Mechanical Engineering at Imperial College London. I declare, to the best of my knowledge, that the work presented in this thesis is my own, except where acknowledged.

James Ewen 12/09/2017

Copyright Declaration

Abstract

In many areas of science and technology, behaviour at the smallest scales has been shown to drive the performance of macroscopic systems. Such relationships are particularly pertinent in tribology, where key phenomena (e.g. friction and flow of lubricants) ultimately depend on atomic-scale interactions. Nonequilibrium molecular dynamics simulations can probe these scales and give unique insights into the tribological behaviour of complex molecular systems.

In this thesis, several industrially important tribological systems are studied through nonequilibrium molecular dynamics simulations. Firstly, in order to ensure reliable results, potential models are compared in terms of their ability to reproduce realistic viscous behaviour of a model lubricant. These accurate models are then used to study the atomic-scale behaviour of various organic friction modifier additives under boundary lubrication conditions. The effect of molecular structure and surface coverage along with sliding velocity, pressure and surface roughness are investigated. The friction and wear reduction mechanisms of promising carbon nanoparticle additives are also examined. Finally, the effect of base oil molecular structure on friction and flow behaviour in the elastohydrodynamic lubrication regime is studied. The work has contributed to a more complete understanding of the atomic-scale behaviour of lubricants and additives and, in combination with experiments, has helped to explain several important macroscopic phenomena.

Acknowledgements

I would like to thank the following people without whom this work would not have been possible. Firstly, my academic supervisors Prof. Daniele Dini and Prof. Hugh Spikes whose invaluable guidance, motivation, insights, time and support have made this work possible.

My thanks are also expressed to all of the members of the Tribology Group at Imperial College. I have greatly enjoyed my time in the group and this is chiefly because I have been surrounded by such a diverse and fun group of people. I would also like to thank Chrissy Stevens for her assistance throughout the course of this project.

I would also like to thank my collaborators, particularly Chiara Gattinoni from ETH Zurich who taught me the basics of molecular dynamics and was always happy to help with any more advanced problems. Also Prof. David Heyes whose unrivalled knowledge of the fundamentals of molecular dynamics simulation made my introduction to the subject far easier. Sebastian Echeverri of SKF and Sridhar Kumar Kannam and Prof. Billy Todd of Swinburne University of Technology whom I hope to continue to work with well into the future.

Thanks are also expressed to my sponsors the Engineering and Physical Science Research Council (EPSRC) and Shell, who have provided the funding that made this research possible. I am greatful to Neal Morgan of Shell UK for his supervision throughout my PhD and Foram Thakkar, Indranil Rudra, Abhinav Verma, and Abhiroop Guha of Shell India, who kindly hosted me for three months which was invaluable both academically and for my personal development.

Finally, and most importantly, I would like to thank my friends and family, and my partner India Martin for supporting me throughout the course of my postgraduate studies.

Contents

List of Tables

List of Figures

Abbreviations, Acronyms and Terminology

μ	Friction coefficient
AFM	Atomic force microscopy
DFT	Density functional theory
EHL	Elastohydrodynamic lubrication
GMO	Glycerol monooleate
GMS	Glycerol monostearate
HFRR	High frequency reciprocating rig
HTHP	High temperature, high pressure
LAMMPS	Large-scale atomic/molecular massively parallel simulator
LB	Langmuir-Blodgett
MAPS	Materials and process simulation
MD	Molecular dynamics
MTM	Mini-traction machine
NEMD	Nonequilibrium molecular dynamics
OA	Oleic acid
OAm	Oleamide
OEM	Original Equipment Manufacturer
OFM	Organic Friction Modifier
OPLS	Optimized potentials for liquid simulations

PPPM	Particle-particle, particle-mesh
SA	Stearic acid
SAm	Stearamide
SAM	Self-assembled monolayer
SFA	Surface force apparatus
SHAKE	Non-linear constraint equations
SRR	Slide-to-roll ratio
VMD	Visual molecular dynamics

Chapter 1. Introduction

The project entitled 'Molecular Dynamics Simulations of Lubricants and Additives' is formally introduced. This project was funded by the Engineering and Physical Sciences Research Council (EPSRC) and Shell Global Solutions through a CASE conversion scholarship. In this chapter, the chief targets of the project are stated and the layout of the thesis is set out.

1.1. Motivation

In order to reduce energy consumption and thus CO_2 emissions, it is necessary to increase the energy efficiency of engineering systems and an important way to achieve this is to design lubricants that give low friction [1]. Automotive lubricants have become progressively more complex and sophisticated due to increasingly demanding original equipment manufacturer (OEM) and environmental regulatory requirements. Modern automotive lubricants are comprised of a blend of two or more base oils, in which ten or more different additives are dissolved [2]. The main role of the base oil is to provide an appropriate viscosity over the operating conditions to ensure adequate lubrication, whilst each additive is included to improve a different aspect of lubricant performance, from reducing friction reduction to ensuring engine cleanliness. Therefore, lubricant formulation has become a considerable challenge, not least because most additives, and some base oils are polar, surface active and chemically reactive molecules. This means that the molecules in lubricants can interact unpredictably, both in base oil solution and at surfaces, often to the detriment of lubricant performance. With so many molecular species present, it is not possible to physically test the performance of all possible combinations of additives and base oils. Consequently, lubricant development still tends to be rather evolutionary, with new components being added to existing formulations based on heritage knowledge and research. This style of lubricant development is struggling to keep pace with the increasingly stringent demands posed by OEMs and regulators, and hence new methods are needed in order to accelerate the process.

As in many areas of science and engineering, a powerful tool which could help to accelerate future lubricant design is computer simulation. The aim of this project is to utilise computational modelling in order to give atomic-scale insights into the behaviour of various important lubricant and additive molecules. Through building understanding of this important behaviour, hopefully the computational methods described herein can be applied in order to accelerate future lubricant development. More specifically, molecular dynamics (MD) simulations have been utilised, to model the motions and interactions of large systems of lubricant and additive molecules, to shed light on various aspects of their behaviour at the atomic-scale.

1.2. Chief Targets of the Project

This project aims to achieve a more complete understanding of how lubricants and additives behave at the atomic scale to rationalise experimental observations. For MD simulations to give useful results which can be directly compared to experiments, it should be applied to study systems which are well-characterised, and the molecular composition of the system is well known. Systems of interest which meet these constraints include:

- Friction modifier additives

These additives are added to reduce friction and wear in the boundary lubrication regime. There are many different types of friction modifier, but most form thin films which preventing the sliding surfaces from coming into contact. In order to design more effective additives, a fundamental understanding of their behaviour at the atomic scale is required, to allow optimisation of molecular structures.

- Base oils and traction fluids

The main constituent of lubricants are base oils. They are composed mainly of mixtures of hydrocarbons in the C_{20}-C_{40} range, with various molecular structures depending on their origin or production process. Their main function is to separate contact surfaces with a fluid film. However, to

reduce hydrodynamic friction losses, these films are becoming thinner, through reductions in base oil viscosity. At the same time, lubricant operating conditions are becoming more sever in modern engines. There is evidence from experiments to suggest that under severe confinement, pressure and shear conditions, lubricants may not behave as conventional lubrication models would suggest. This has far-reaching consequences for the accuracy of these models as well as for lubricant design.

1.3. Layout of the Thesis

The thesis is organised into early chapters where the literature is reviewed and simulation techniques are selected, results chapters where the outcome of simulations are analysed and closing chapters where the main findings of the project are discussed and conclusions are drawn.

In Chapter 2 the literature on classical molecular dynamics simulations of liquid lubricants and additives will be critically reviewed. This will include an overview of automotive lubricants, simulation techniques, a history of nonequilibrium molecular dynamics, methodological developments, examples of bulk and confined nonequilibrium molecular dynamics simulations of lubricants and additives, and finally conclusions.

In Chapter 3, several classical force-fields will be compared through the equilibrium molecular dynamics (EMD) simulations of the density and viscosity of lubricant molecules under ambient as well as high temperature and high pressure conditions. This is important since many molecular dynamics force-fields give erroneous results for lubricant-sized molecules.

In Chapter 4, the structure and friction of boundary films formed by several different organic friction modifier additives at various surface coverages are analysed using nonequilibrium molecular dynamics (NEMD) simulations. The effect of sliding velocity is also investigated.

In Chapter 5, all-atom and united-atom force-fields will be compared by analysing the structure and friction of organic friction modifier films using NEMD simulations. The effect of coverage and sliding velocity are also investigated.

In Chapter 6, the effect of nanoscale surface roughness on organic friction modifier film structure and friction is analysed using NEMD simulations. The effect of coverage and pressure are also investigated.

In Chapter 7, NEMD simulations are used to investigate the reduction of friction and wear by carbon nanoparticles. The effect of nanoparticle surface coverage, pressure and sliding velocity are investigated.

In Chapter 8, the effect of base oil molecular structure on nonequilibrium phase behaviour and friction are investigated using NEMD simulations. The effect of high strain rates and pressures, representative of the elastohydrodynamic lubrication regime, are studied.

Finally, conclusions from the early stages of the project, as well as the key next steps for NEMD simulations of lubricants and additives, will be outlined in Chapter 9.

Chapter 2. A Review of Classical Molecular Dynamics Simulations of Lubricants and Additives

In this chapter, the literature on classical molecular dynamics simulations of lubricants and additives. Since the thesis focusses on studies of tribological systems using nonequilibrium molecular dynamics (NEMD) simulations, first, an introduction to lubricants and additives will be given, followed by an overview of the state-of-the-art in NEMD simulations of lubricants and additives. Some parts of this review chapter have been submitted to the journal *Friction* (ref. [3]).

2.1. Lubricant Composition and Function

Lubrication is the process of reducing friction between, and wear of, contacting surfaces in relative motion to each other by introducing a lubricant between them. Effective lubrication ensures smooth, continuous operation of machine components, reduces wear, and prevents the build-up of excessive stresses. When lubrication breaks down, components can rub destructively against each other, causing excess heat, local welding, accelerated wear and ultimately component failure.

2.1.1. Regimes of Lubrication

Within automotive vehicles, mechanical components are exposed to very different contact conditions (e.g. pressure, temperature, sliding velocity) and the lubricant must be effective for all of these cases. The Stribeck curve (Fig. 1), describes the variation in the friction coefficient as a function of a dimensionless lubrication parameter (the Hersey number) [4]. The Hersey number, $H = (\eta v)/P$, where η is the dynamic viscosity (Pa s = N s m^{-2}, v is the sliding velocity (m s^{-1}), and P is the applied load per unit length (N m^{-1}). The Stribeck curve demonstrates the transition between the different lubrication regimes. The lambda ratio, $\lambda = h/RMS$, where h is the film thickness and RMS is the root-mean-square composite surface roughness. It can be used as a rough indicator of the lubrication regime.

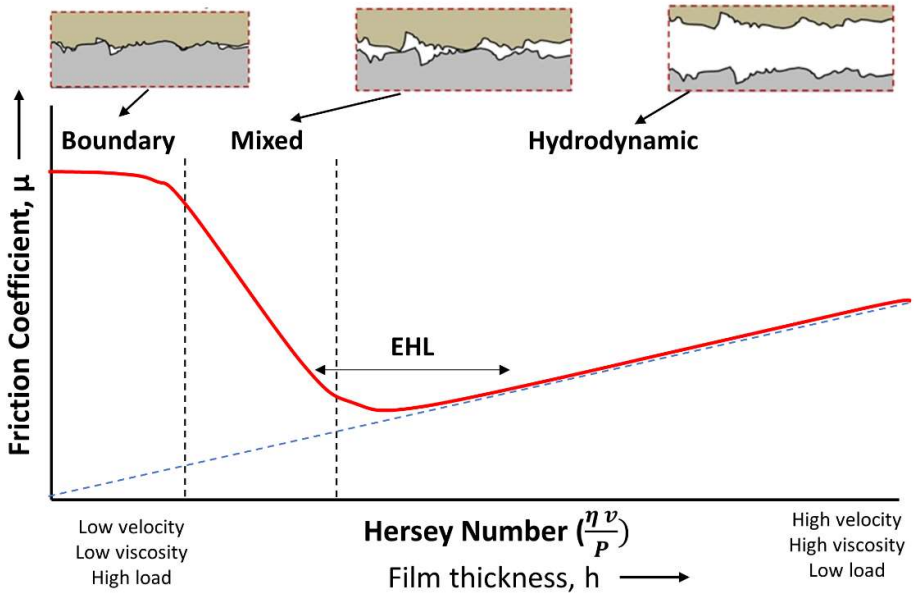

Figure 1. Generalised Stribeck Curve – adapted from ref. [5]

Each of the lubrication regimes, moving from the right to the left of the Stribeck curve, are described below [4]:

- **Hydrodynamic lubrication** occurs at high sliding speed/low pressure, where the surfaces are completely separated by a lubricant film thicker than the composite surface roughness ($5 < \lambda < 100$). Solid-solid contact is prevented through the load bearing capacity of the lubricant. In this regime, the friction coefficient is dominated by the viscosity of the lubricant and can be estimated using hydrodynamic theory [6], the basis of the Reynolds Equation [7].
- **Elastohydrodynamic lubrication (EHL)** is a specific form of hydrodynamic lubrication which occurs for non-conformal contacts which experience very high contact pressures. EHL friction calculations are similar to those for hydrodynamic lubrication but also account for the elastic deformation of surfaces, piezoviscous effects and shear thinning. Generally, EHL is the lowest friction regime, and occurs at intermediate sliding velocity, where a very thin film separates the contact surfaces ($3 < \lambda < 10$) [8].

- **Mixed lubrication** occurs when the lubricant film is not thick enough to completely separate the surfaces such that some asperities come into direct contact ($1 < \lambda < 5$). Here the load is carried by both the lubricant film as well as partial asperity contacts between the surfaces. The accuracy of hydrodynamic theory breaks down in this regime [9].
- **Boundary lubrication** is encountered at low sliding speeds and high pressures where insufficient lubricant is entrained into the contact to prevent the surfaces coming into direct contact ($\lambda < 1$). Here the lubricant film thickness is less than the composite surface roughness and thus the load is mainly supported by the surface asperities rather than the lubricant film. Without effective use of additives, this regime can result in large temperature rises and high friction and wear, the extent of which is primarily influenced by the nature of the contact surfaces [10].

Friction reduction has gained increasing attention within the automotive industry in recent years given its impact on fuel economy and thus CO_2 emissions [2]. Given that automotive lubricants are subjected to all four lubrication regimes in different components, they must be effective in all of them.

Traditionally, most lubricated engineering components in automotive applications were designed to operate under full-film (hydrodynamic or EHL) conditions, as this prevents surface contact and ensures the maximum longevity. The mixed and boundary regimes, where direct solid-solid contact leads to high friction and wear, were only encountered during low speed. However, in order to reduce energy consumption and thus CO_2 emissions, lubricant viscosity has been progressively reduced to decrease hydrodynamic losses. This means that thinner oil films separate the surfaces and more components operate in the mixed and boundary regimes. To reduce friction and wear under mixed and boundary conditions, effective additives are required [11].

2.1.2. Lubricant Formulations

The main functions of lubricants are to reduce friction and wear, to remove heat generated in moving components as well as to clean the contact surfaces. Modern automotive lubricants are composed

primarily (70-99%) of a base oil, in which a 'package' of additives is dissolved. Additive concentrations differ greatly depending upon the application, but they are generally between 1-30% [12], around half of which is usually made up of polymers to modify the viscous behaviour of the lubricant. Modern lubricants also typically include around ten other types of additives to improve different areas of lubricant performance; some of the main variants are described below.

Base oils

Base oils must meet a range of requirements to be suitable for use in lubricant formulations. They need to be sufficiently viscous to maintain a lubricant film between contacts under the operating conditions, but not overly viscous such as to unnecessarily increase hydrodynamic friction. They should also have an adequate specific heat capacity to ensure that heat is effectively removed from contacts and be stable under thermal and oxidative stresses. There are two main types of base oil available; mineral oils and synthetic oils [13].

Mineral oils are obtained from crude oil; they are composed of a combination of linear and branched hydrocarbon chains as well as aromatic and aliphatic rings. Crude oils derived from different sources and refining processes tend to vary significantly in terms of chemical structure, sulphur content and viscosity. However, regulatory and OEM specifications mean that the latter two are relatively consistent in modern refined base oils. A small amount of sulphur has been shown to improve both the friction reduction and oxidation properties of the lubricant, and can also reduce wear. However, modern automotive lubricant specifications impose strict limits on sulphur concentrations because of their detrimental effect on local emissions and after-treatment devices. Consequentially, most natural sulphur is removed in the refining process; however, certain sulphur containing additives are still added to some lubricants due to their effective friction and wear reduction properties [12]. Mineral oil viscosity depends mostly upon on the refining process, with heavier oils (higher average molecular weight) generally having higher viscosities. Even refined mineral oils have different chemical compositions; with different proportions of three main chemical structures:

- Paraffins, which are linear or branched, saturated aliphatics
- Aromatics, which are unsaturated, conjugated cyclic groups
- Naphthenes, which are saturated, cycloaliphatics

Synthetic oils are obtained through chemical synthesis, meaning that they can be designed with specific properties. They are generally more expensive than mineral oils but are commonly used in many demanding and precision applications. Synthetic oils can be classified as one of three basic types:

- Synthetic hydrocarbons (e.g. GTL, PAO)
- Synthetic oxygenates (e.g. esters, polyglycols)
- Organohalogens (e.g. PFPE)

Synthetic hydrocarbons are gaining popularity in the automotive industry as their cost falls through more efficient production processes. In fact, synthetic hydrocarbon lubricants poly-α-olefins (PAO) and Gas-To-Liquids (GTL) are now commonplace in commercial automotive lubricants [2]. PAO base oils consist of branched oligomers synthetized from olefin monomers. These monomers consist of a linear carbon chain, with an unsaturated alkene group in the α position. The presence of this α-alkene group facilitates oligomerisation to form the finished base oil. The most important characteristics of poly-α-olefins are their high viscosity, their low volatility and their good oxidative stability. The PAO acronym is followed by a number which represent the kinematic viscosity (mm^2/s at 100 °C) [12]. GTLs are produced using a process whereby natural gas is converted to syngas (CO, H_2) which is subsequently converted into long chain waxy hydrocarbons through a Fischer–Tropsch process, and then hydrocracked back to useful chain lengths to produce a range of products including diesel, kerosene and base oils [14]. A drawback with both PAO and GTL is that their low polarity and lack of aromatics make it more difficult to solubilise certain important additives.

Synthetic oxygenates, such as esters and polyglycols, are used in some automotive lubricants but are more common in other applications such as metalworking fluids, metal rolling fluids, hydraulic fluids

and greases [12]. Organohalogens, such as perfluoropolyether (PFPE), are extremely stable but are rather expensive and are therefore mainly used for extreme temperature environments [12].

It has been shown that base oil chemical structure has a direct effect on its friction behaviour [15]; this will be investigated further in this thesis.

Additives

A range of additives are dissolved in the base oil to optimise its properties and improve lubricant performance as well as to fulfil specific regulatory and OEM requirements. The most commonly used additives are presented in the following [12]:

- Antioxidants - delay the degradation of the base oil by oxidation and, therefore, extend the life expectancy of lubricant oil. High temperature and presence of oxygen from the air in automotive tribological systems activate the oxidation process. Typical additives in this class include aromatic amines, phenols and sulphur compounds as well as organo-molybdenum compounds [12].
- Detergents - ensure the cleanliness of critical engine components by preventing the formation of carbon-based deposits on contact surfaces at high temperatures. Most detergent molecules are amphiphilic surfactants and contain a polar (hydrophilic) headgroup and a non-polar (hydrophobic) tailgroup. They tend to form reverse micelles in oil solution, with alkaline headgroups at the core surrounded by the surfactant chains. These ‘over-based’ detergent reverse micelles are used to neutralise acidic compounds generated during lubricant operation [16].
- Dispersants - enable any solid impurities formed during the operation to be held in suspension in the oil. This prevents agglomeration of solid residue which could otherwise form deposits at low temperatures. They are generally also molecules with a surfactant structure; the most widely used variants are succinimides [12].

- Friction modifiers (FM) - are compounds added to reduce friction, primarily in the boundary lubrication regime [11]. Inorganic FMs such as molybdenum dithocarbonate (MoDTC) form lamellar films of MoS_2 on contact surfaces which effectively reduce friction. Organic friction modifiers (OFMs) are amphiphilic surfactant molecules, such as fatty acids, amines, amides, and esters. They adsorb onto contact surfaces to form monolayers which prevent the solid-solid contact and thus reduce friction and wear [11].
- Anti-wear additives - react with the surface and form a protective layer which ensures wear protection. They are mainly phosphorous based compounds such as zinc dialkyl dithiophosphate (ZDDP) [17].
- Corrosion inhibitors - protect the surface from reactive and oxidative species in base oil solution by adsorbing onto the surface in a similar mechanism as OFMs. Amine succinates, alkaline metal sulfonates and benzotriazole are corrosion inhibitors commonly used in lubricants [18].
- Viscosity index improvers (VII) - are added to modify the viscous behaviour of the base oil. They are generally high molecular weight polymers that increase the viscosity of the base oil, particularly at high temperatures due to steric effects. The most common examples are polyalkyl-methacrylate (PMA) and olefin copolymer (OCP) [19].
- Pour point depressants (PPD) - increase the pour point of a lubricant (the lowest temperature at which it can flow). A commonly used PPD additive is low molecular weight PMA, which interferes with the crystallization process of paraffins within the base oil, which tend to be the component that solidifies at the highest temperatures [12].
- Anti-foam additives - are used to address the foaming issues caused by dispersants and detergents in the formulation, reducing bubble formation through their low surface tension. The most common examples are high molecular weight silicon-based polymers [12].

In terms of tribological the performance of the lubricant, FMs and anti-wear additives are of most interest. In the boundary lubrication regime, the asperities are in direct contact, often leading to high

friction and wear. To reduce this phenomenon, a protective tribofilm can be formed on the friction surfaces using the additives described above. In current formulations, MoDTC and ZDDP are the most popular additives used in terms of friction and wear reduction [11]. Moreover, ZDDP is not only an excellent anti-wear additive but also an effective anti-oxidant and corrosion inhibitor [17]. Even though MoDTC and ZDDP are very powerful additives, they contain metals, sulphur and phosphorus, which are harmful to the environment and have been found to poison after-treatment catalysts [20]. As a result, the elements critical to their operation are increasingly limited in lubricant specifications. In the near future, it will be necessary to replace them with alternative additives that maintain the same efficiency in addition to being more environmentally friendly. This has resulted in a resurgence in interest in OFMs in recent times which contain only carbon, hydrogen, nitrogen, and oxygen atoms [12].

2.2. Simulation Techniques

Computational modelling is becoming an increasingly important tool in many areas of science and technology. In tribology, many different simulation techniques, from the atomic-scale right up to the continuum, have been utilised to investigate problems which may be challenging to probe with experiments alone. When selecting the most appropriate computational simulation method to use for a given problem, one must first consider the scale or scales which need to be accessed.

2.2.1. Simulation Scales

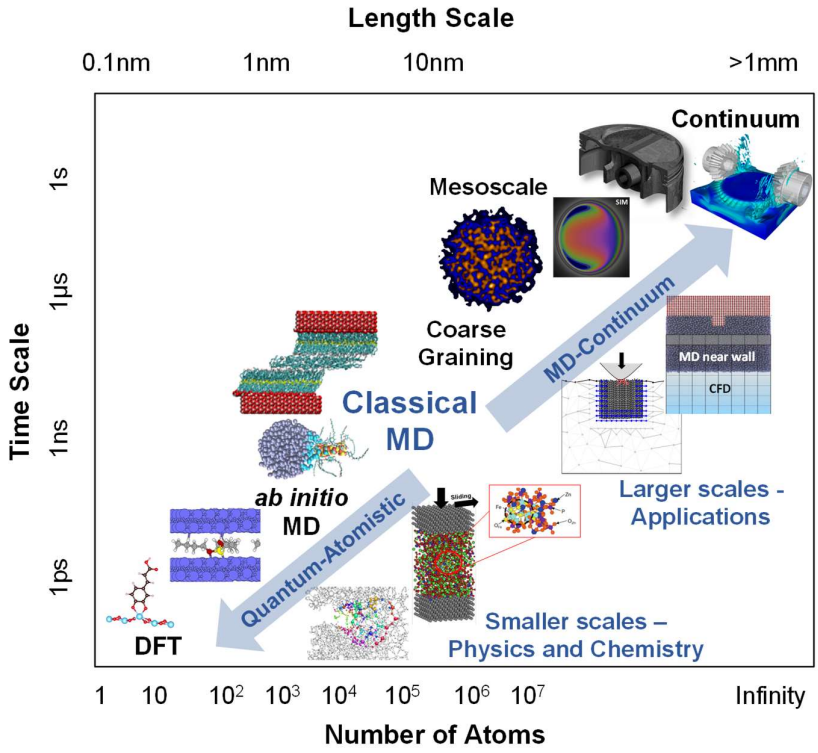

Figure 2. Accessible scales of computer simulation methods for tribological systems - from ref. [3]

Fig. 2 is a schematic representation of the range of length- and time-scales accessible to simulation methods, ranging from first principles or *ab initio* techniques, to MD, through to continuum techniques.

Macroscopic continuum methods use conservation equations along with constitutive relations in order to study fluid behaviour. The validity of these constitutive relations relies on the assumption that the fluid properties remain approximately constant across the defined volume elements. This assumption is accurate for most applications in engineering, but is invalid if there are significant variations in macroscopic quantities over smaller time- or length-scales. Furthermore, constitutive relations often provide an over-simplified model, based on empirical findings that are only valid under specific conditions. Finally, to solve the closed set of governing continuum equations, transport

coefficients need to be input into the model. This is not always easy, since that for a non-Newtonian fluid, these transport coefficients are dependent on both the thermodynamic state point of the fluid and the flow field [21].

The limitations of continuum approaches are avoided by using smaller-scale approaches, such as MD. MD simulates the movement of atoms, rather than small volume elements; the method is flexible and is the 'cheapest' method to explicitly model every atom in the system. The method continually reassigns particle positions and velocities over time from which macroscopic quantities can be calculated using statistical mechanical methods. Moreover, MD yields a plethora of structural, dynamical and chemical information that is not accessible through continuum methods. Different phases of a material can be investigated simply by changing the thermodynamic conditions, such as the temperature or pressure, without the need to alter the simulation methodology itself [21].

Molecular simulations are characterised by their relatively low cost yet good predictive ability. As with any simulation technique, they are most powerful when they are used alongside relevant experiments. For unexplored systems and properties, molecular simulations can guide experiments towards the conditions where interesting phenomena are likely to occur. Experiments can subsequently be used to validate the simulation observations. For systems and properties that have already been investigated by experiments, simulations can build understanding of the occurring phenomena from the atomic scale. Given that they provide a clean testing environment, they can also be used to determine the significance of multiple effects which can only observed collectively in macroscale experiments [22].

2.2.2. Molecular Simulation

Molecular simulation, a field of research that started in the 1950s, uses computers to generate a series of representative snapshots of a group of interacting molecules from which experimental observables can be calculated. A system of interest is simulated by a collection of individual molecules, represented at the atomic level, and the locations of the individual atoms are governed by the interaction force

laws between them. There are two main methods for performing molecular simulation, one stochastic and one deterministic [23]. The first to be developed was (Metropolis) Monte Carlo (MC), which evolves the molecules by moving (usually) one molecule at a time by a trial random displacement. This new position is accepted or rejected on the basis of the change of potential energy of the system (more specifically its exponential or the 'Boltzmann factor'). The second, and nowadays much more widely used method is Molecular Dynamics (MD), in which the atomic trajectories are generated by solving Newton's equations of motion using a finite difference scheme over a series of short time steps. Both MC and MD can be used to compute thermodynamic and other static properties such as infinite or zero frequency elastic moduli. Only MD can be used to investigate time-dependent processes and transport coefficients such as the viscosity. Therefore, MD is the most appropriate method to investigate tribological phenomena.

Molecular simulation can be viewed as both a useful testing ground for statistical mechanical theories and a quasi-experiment to explore atomic-scale phenomena that are still be difficult to probe experimentally. However, in order for such *in-silico* experiments to become useful in terms of predictive capabilities, a number of aspects must be considered, from the inherent limitation of the time and length scales that can be modelled to the accuracy of the representation of the intramolecular and intermolecular interactions.

As early as 1969, Goldstein envisaged the use of MD to study the viscosity of liquids: "*The modern molecular approach to viscosity proceeds via the formulation of the shear viscosity in terms of appropriate integrals over the stress-time correlation function in a fluid. There is no difficulty, in principle, in imagining computer experiments generating this correlation function in a finite sample of molecules set into motion according to Newton's laws. It is not yet clear how large a sample of molecules is needed, nor how long a time of study is required, to achieve the equivalent of an infinite number of molecules studied for an infinite time, but one might guess that such a calculation will be within our reach in the immediate future, for liquids having the simplest, spherically symmetric, pair*

potentials." [24]. Goldstein was percipient and the first MD study of the viscosity of a real fluid (argon) followed four years later [25]. Very significant progress has been made since then and MD simulations of complex tribological systems are now being routinely performed by researchers using high performance computer (HPC) systems that allow the interactions between millions of atoms to be treated for appreciable timescales. Yet some key questions still remain, such as: "how do we design an MD simulation to address the tribological problem at hand? Are the required system sizes and timescales accessible? What problems can be solved using classical MD in isolation, and where do other techniques need to be considered?". This chapter, after providing a historical and critical overview of the most important developments in this field of study, aims to shed light on some of the outstanding issues currently faced by researchers.

Looking at tribological applications and specifically liquid lubricants, there is considerable interest in predicting bulk transport properties of fluids under a wide range of conditions (temperature, pressure, strain rate) relevant to real components, and in understanding how fluids behave when confined by solid surfaces. One very important aspect of the molecular simulation procedure which has made it useful in studying essentially bulk systems is the use of periodic boundary conditions (PBC). The PBC creates an infinite lattice of periodically replicated molecular simulation cells that fills all space [23]. The molecules in the replicated cell follow the MC or MD scheme, and if a molecule leaves through one boundary it is reintroduced with the same velocity (in the MD case) at the same point of departure on the opposite face of the cell. This construction effectively eliminates surface effects that would dominate the behaviour of the system even if they were not deliberately included. This is because the relatively small cell would have a large surface-to-volume ratio without the PBC, so interfacial effects would dominate the molecules' behaviour. Things are different in confinement, where periodicity is effectively broken by the presence of the confining surfaces at two of the cell faces, and hence the effect of the interactions between solid walls and fluid molecules become extremely important and dominate the behaviour of the systems under consideration. This is particularly important in boundary

lubrication, where the frictional response is dominated by a few layers of molecules confined between a pair of moving surfaces. PBCs are illustrated in Fig. 1 in section 2.3.

Molecular simulation is finding increasing use in the area of tribology. The number of papers applying MD to tribological systems has increased dramatically in the last few years, for a variety of reasons. Most lubricating oils are composed of relatively large organic molecules (C_{20}-C_{40}) and simulation methodologies and force-fields that govern the internal dynamics and interactions between such molecules have now been refined to a stage where they can reproduce experimental lubricating fluids well enough to generate realistic viscous behaviour [26]. The increase in computational power over recent years, alongside the introduction of highly parallelised simulation algorithms to exploit multiprocessor HPC architectures, has enabled large molecules of tribological relevance to be modelled under experimentally realistic conditions.

MD has made a significant impact on our understanding of both dry friction, where the sliding surfaces are in intimate contact, and wet friction, where the surfaces are separated by a liquid lubricant. The focus of this article is MD simulations of wet friction, with a particular emphasis on automotive lubricants. Dong, Li and Martini [27] have given a summary of MD work on dry friction in the context of atomic force microscopy (AFM) experiments, while Sawyer et al. [28] have provided a more general overview of recent advances in dry friction including the contribution of MD. The reader should refer to these contributions for specific details on these topics.

How did we get to this point? We will now briefly summarise the stages that the subject has gone through to arrive at the present state where molecular simulation has become an important and powerful tool in the field of tribology. As with many fields of research, there were a number of key step-changing advances in the methodology which we now take for granted, but which have revolutionised the subject.

2.3. History of NEMD Simulations

MD was invented in the 1950s, using the hard sphere (HS) model in which the 'molecules' were represented as perfectly elastic and infinitely repulsive spheres ('billiard balls'). The HS MD approach is very computationally efficient (particularly at low density), and can be considered an 'event driven' method, as it follows the collisions between the spheres generated by classical mechanics in chronological order. Probably the most scientifically significant paper of this pioneering work was by Alder and Wainwright [29], who in 1957 showed that a HS liquid crystallised as the density was increased above a certain value. This discovery had wide-ranging consequences, as it was widely thought at the time that it was necessary for molecules to have an attractive component to their interaction potential to show a freezing transition and Alder and Wainwright's work showed that this was not the case. Today this would be called an 'entropy-driven' freezing transition, of which there are abundant examples in colloid and polymeric liquid systems, and its existence plays a major role in our understanding of the phase behaviour and physical properties of a wide range of soft condensed matter chemical systems [30].

The 1960s was the period in which model molecules represented by a continuous interaction potential were first simulated by MD. The first paper was by Rahman in 1964 [31], who calculated the diffusion coefficient in a system of argon atoms interacting through a Lennard-Jones (L-J) potential. This was also a ground-breaking paper in that it showed the diffusion and structural evolution of small molecules takes place by a series of small highly coordinated motions of neighbouring molecules. Until this MD paper, it had been generally held that diffusion in liquids took place through a series of rare, large distance jumps of molecules from 'lattice sites' into vacancies or 'holes' in a crystal-like lattice, the jump distance being roughly a molecular diameter. Historically, liquids were viewed as a crystal with many unoccupied sites [32], but Rahman's paper convincingly disproved this supposition. However, erratic, localised displacements have more recently been observed in the MD of supercooled liquids near the glass transition, a phenomenon known as 'heterogeneous dynamics' [33], so the defect-containing crystal view of a liquid is not entirely without merit. The diffusion coefficient

is closely related to the viscosity, indeed the 'Stokes-Einstein' relationship [34] suggests that the product of the two is almost constant in liquids. In 1970, Alder, Gass and Wainwright [35] calculated the viscosity of the HS fluid at various densities up to crystallisation. They used a mean square displacement of the shear stress route, which is now called the Einstein-Helfand method [36].

Verlet and co-workers in 1973 [25] were the first to calculate the shear viscosity of a real liquid, argon, represented by the Lennard-Jones (L-J) potential. They used a new approach called the Green-Kubo time correlation method [37,38]. The Newtonian viscosity is the integral of the shear stress relaxation function, $C_s(t)$. In the small strain rate limit, $C_s(t)$, can be shown by statistical mechanics to be the product of the shear stress at one time multiplied by its value at a later time. This function decays monotonically to zero, as liquids subjected to a step in strain can only sustain the initial jump in shear stress for a finite time. Therefore, perhaps paradoxically at first sight, the Newtonian viscosity can be calculated without actually imposing a strain rate across the system (the strain rate might be considered in this case to be a virtual perturbation via the Green-Kubo route). Near the melting line, the viscosity of the HS fluid increases rapidly because of a slowing down in the decay of the shear stress time correlation function (caused by crowding effects of the molecules packed closely together), an effect that was called the 'molasses tail' [39].

Up to the early 1970s the simulations of liquids were carried out mainly using equilibrium MD which by default follows the microcanonical ensemble (an ensemble is simply a probability distribution for the state of the system). The microcanonical ensemble is also sometimes called the NVE ensemble because the total number of particles in the system, N, the volume of the system, V, as well as the total energy in the system, E, remain constant. Then, in the early 1970s, the first nonequilibrium molecular dynamics (NEMD) simulations of imposed shear flows at large strain rates were carried out. A variety of techniques were developed, and these continue to be invented and refined today. The version perhaps most relevant to tribology is the moving wall method invented by Ashurst and Hoover in 1975 [40]. This mimics the shearing of a fluid of infinite extent in the x- and y-directions using PBC,

but the fluid is confined by bounding walls whose plane normal is in the z-direction (see Fig. 3a). The two walls, which were initially the outer regions of the fluid, were constrained to translate in opposite directions in the x-direction to shear the fluid. This was followed by simulations in later years in which solid walls confining the fluid were used to apply the shear [41]. The study of confined fluid shear flow by NEMD has undergone a rapid expansion in recent years, and is now a common geometry for simulations in many different fields of research.

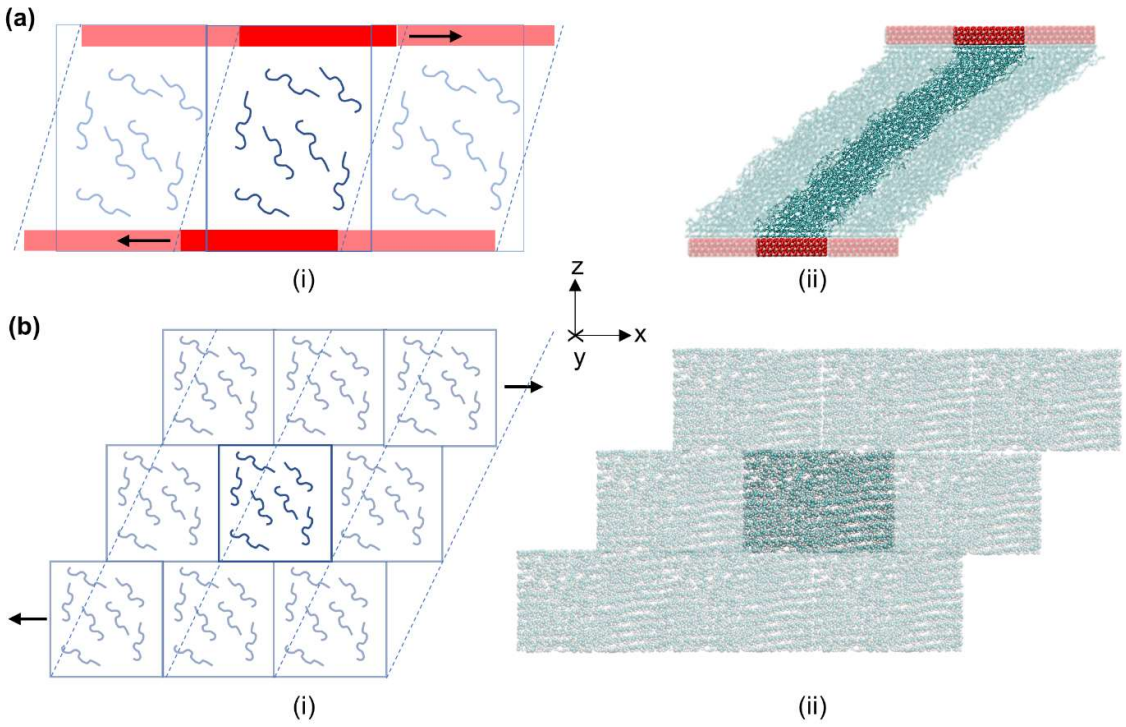

Figure 3. (a) Confined NEMD schematic (i) and an example image from an NEMD trajectory adapted from ref. [42] (ii). (b) Bulk NEMD schematic using Lees-Edwards PBC (i) and an example image from an NEMD trajectory (ii). Transparent regions show the periodic image of the simulation cell from the PBCs imposed.

Up to the end of the 1970s, NEMD simulations were quasi-2D in that they used PBCs in only two directions, but in the 1980s equations of motion for imposing shear flow in a system with PBC in all three Cartesian directions were invented. These are known as the DOLLS and SLLOD methods. By good fortune, PBCs which can accommodate shear flow of infinite extent within MD had been invented by

Lees and Edwards (LE) many years previously [43], and these new non-Hamiltonian equations of motion are compatible with this 'sliding brick' PBC arrangement (see Fig. 2b). Recent books by Evans and Morriss [44], and Todd and Daivis [45], provide a comprehensive description of the field from that time to the present. An early NEMD simulation using the LE PBC was to model the start-up of shear flow in a supercooled Lennard-Jones (L-J) fluid, performed by Heyes et al. in 1980 [46], where 'overshoot' behaviour was observed just after the initiation of shear (this phenomenon is widely seen in experimental studies of a range of polymeric and glassy systems). The importance of this period cannot be overestimated as it was then that the statistical mechanics or governing physics of liquid systems arbitrarily far from equilibrium started to be derived, largely by Evans and Morriss [44]. Since the 1980s, NEMD has progressed to a point where it has become a true predictive tool.

2.4. Methodological Developments

The computational time required for MD simulations depends on a number of factors including the computer hardware, software and force-fields used. Classical MD force-fields generally require time steps of around one femtosecond to ensure energy conservation. This means that even when performed on multiprocessor HPC systems using highly parallelised software, only nanosecond or in extreme cases, microsecond timescales are accessible in MD simulations [47] since these correspond to millions/billions of time steps. As a result, relatively high strain rates are required ($> 10^7$ s^{-1}) in NEMD simulations to ensure that the viscosity reaches a steady state within the accessible simulation time [48,49]. Moreover, at very low strain rates, the systematic nonequilibrium response becomes comparable to the equilibrium fluctuations in the phase variables of interest, resulting in a low signal-to-noise ratio [50,51]. The ability to simulate lower strain rates has been a long-term goal of NEMD simulations in order to overlap with experiments and real components [44]. For comparison, high-pressure lubricant viscosity can generally be measured up to strain rates of approximately 10^4 s^{-1} [48,49], although tribology experiments can reach up to around 10^6 s^{-1} before the temperature rise becomes too large to correct for [8] and real engine components can reach up to 10^8 s^{-1} [52].

Following the initial development of bulk and confined NEMD simulation methodologies, many aspects have been refined to allow different conditions to be studied and more accurate results obtained. Significant examples include improved temperature and pressure control methods, classical force-fields and entirely distinct simulation algorithms; these are discussed below.

2.4.1. Temperature and Pressure Control

The high shear rates that are usually imposed in NEMD simulations create heat, which must be removed to achieve a nonequilibrium steady state [44]. In parallel with the theoretical advances described above, a number of different thermostats have been invented which can be used in conjunction with the NEMD equations of motion. In bulk MD simulations, the thermostat is usually applied to all atoms in the system. The temperature in MD simulations can be controlled through a number of methods including scaling the atomic velocities (e.g. Andersen [53]), coupling atoms to an external bath (e.g. Berendsen [54]), or applying a random 'friction' force to the atoms (e.g. Langevin [55]). The Nosé-Hoover (NH) thermostat [56,57], in which a Hamiltonian with an extra degree of freedom for a heat reservoir is introduced to control the temperature, is probably the most widely used thermostat in bulk NEMD simulations. Under equilibrium conditions, the NH thermostat can be proven to generate a canonical or NVT ensemble. The NH thermostat can also be easily implemented in conjunction with the SLLOD equations of motion [58]. However, some researchers have raised concerns with thermostats, such as NH, which require a predefined flow profile (e.g. linear/Couette) to be assumed [59]. Profile-biased thermostats can result in artefacts in some systems, for example the 'string phase' which was often observed in NEMD simulations of L-J fluids [60]. Also, of course, they are incorrect for systems where the flow profile is not Couette. To overcome these problems, configurational thermostats, which make no assumptions regarding the flow profile, were developed [61,62]. These have not yet been applied in bulk NEMD simulations of lubricant-sized molecules (C_{20-40}), probably because they are more difficult to implement for large molecular systems, so the standard NH thermostat is typically still employed [48]. However, configurational thermostats may be

useful for bulk NEMD simulations under high pressure conditions, where deviations from linear velocity profiles have been observed experimentally (see section 2.2.3.).

In confined systems, alternative thermostatting strategies are required. The thermostat is usually only applied to the wall atoms [63], allowing a thermal gradient to develop through the thickness of the system, as occurs in real experiments [64]. Direct thermostatting of a confined fluid has been shown to significantly influence its behaviour [65]. For confined systems, the stochastic Langevin thermostat [55] is more popular than NH, since it removes heat more effectively [66]. Alternative thermostatting systems, which involve thermostatting only virtual atoms, rather than the confined system itself, have also been developed [67]. These are useful in large complex systems where the wall atoms can be 'frozen' to preserve structural stability and reduce the computational cost.

In bulk NEMD simulations, pressure is most commonly controlled using the Nosé-Hoover (NH) barostat [56,57], which allows the unit cell vectors, and thus the volume, to maintain a target pressure. This method can be used to sample the isothermal-isobaric or NPT ensemble in which the total number of particles in the system, N, the pressure, P, as well as the temperature, T, remain constant. For confined NEMD simulations, pressure can be controlled by setting a fixed separation distance between the confining walls, or by applying a constant normal force to one or both of the walls [68]. The latter technique is preferable since the former has been shown to lead to unphysical results in certain systems [68]. For incompressible systems, such as L-J fluids, it can also be beneficial to add a damping term to the barostat in order to prevent excessive oscillations after the force is applied [68].

2.4.2. Classical Force-fields

A common concern for classical MD simulations is that their accuracy is heavily dependent on the force-fields used to describe the intermolecular and intramolecular forces between a system of interacting molecules. The functional forms of most classical molecular force-fields are quite similar, capturing both bonded (bond stretching, bending and torsion) and non-bonded (van der Waals, electrostatic) interactions [69]. These terms are usually empirically parametrised collectively in order

to reproduce important experimental behaviour for a set of training compounds. The computational expense in classical MD simulations is dominated by modelling the van der Waals and particularly the long range electrostatic interactions between atomic partial charges. The former is usually modelled by a L-J potential and is 'cut off' at certain a distance where it tends to zero (usually around 10 Å) whilst the latter should be treated with a long-range solver, such as Ewald or particle-particle, particle-mesh (PPPM) [70].

A key target of many NEMD simulations of tribological systems is to yield realistic viscous behaviour of lubricant-sized molecules, which requires the use of highly accurate force-fields. A full discussion of the choice of force-fields for NEMD simulations of lubricants is given elsewhere [69], but a brief overview is also provided here for completeness. Most historic simulations of tribological systems including alkane molecules have employed united-atom (UA) force-fields where the nonpolar hydrogens are grouped with the carbon atoms to create CH, CH_2 and CH_3 pseudo-atoms [69]. UA force-fields have been popular primarily because they decrease the number of interaction sites by around 2/3 and computational expense by up to an order of magnitude compared to all-atom (AA) force-fields [71]. However, UA force-fields have been shown to lead to dramatic viscosity under-prediction for lubricant-sized alkanes, particularly those which are unbranched [69]. AA force-fields are more computationally expensive and, as originally developed, many resulted in anomalous solid-liquid phase behaviour for lubricant-sized alkanes [72]. Fortunately, the latter issue has been overcome by re-parameterising AA force-fields specifically for lubricant-sized alkanes [26], which has led to accurate density and viscosity prediction, even under high temperature and high pressure (HTHP) conditions [69].

2.4.3. New Simulation Algorithms

Many new algorithms have been developed over the last three decades to improve the signal-to-noise ratio of NEMD simulations, simplify their implementation, and extend them to different types of flows. Noteworthy in this set of theoretical tools is the so-called 'transient time correlation function' (TTCF)

[50,51], introduced by Morriss and Evans in the late 1980s. TTCF can be used to generalise the Green-Kubo method [37,38], which strictly is only applicable to equilibrium systems, to ones forced out of equilibrium by the imposition of an external field (e.g. strain rate). The main advantage of TTCF is that it allows very low strain rates to be simulated, comparable to those used in experiments and real components. Indeed, it has been successfully applied to study the viscosity of short alkanes (n-decane) at strain rates as low as 10^5 s^{-1} [73]. TTCF was initially used to study the rheology of bulk systems but it has also been used to study friction in confinement [74,75]. The extent to which the TTCF can be used to calculate the friction coefficient of confined fluids has been much discussed, and alternative methods have also been proposed [76–78].

In 1999, Müller-Plathe [79] introduced an alternative nonequilibrium method for calculating the shear viscosity, so-called 'reverse' NEMD or R-NEMD. The R-NEMD method reverses the cause-and-effect picture customarily used in NEMD in which the velocity gradient or strain rate is imposed and the momentum flux or stress determined, to a stress being imposed and the consequent velocities observed. The method involves a simple exchange of particle momenta, which is straightforward to implement. Moreover, it can be made to conserve the total energy as well as the total linear momentum, so no coupling to an external temperature bath is needed. The method was initially tested for a L-J fluid near its triple point and yielded a viscosity in agreement with literature results [79]. The method has since been used to predict the viscosity behaviour of simple alkanes [80] as well as more complex multicomponent systems such as lipid bilayers [81] and ionic liquids [82]. Also, R-NEMD can be used to study transport properties in bulk or confined systems, but under-predicts viscosity relative to standard NEMD at high strain rates, as discussed elsewhere [83].

Another notable advance was the extension of NEMD methodology to simulate steady state planar elongational flow (PEF) by Todd and Daivis in 1998 [84]. This is important in tribology since PEF occurs in the entrance region of high pressure elastohydrodynamic contacts [85]. Baig et al. [86] studied the rheological and structural properties of linear liquid alkanes (C_{10}, C_{12}, C_{20}) using NEMD simulations

under PEF using the p-SLLOD algorithm [87]. They showed that these molecules behave very differently to the way they do under shear flow, with strong alignment of fully stretched chains at high elongation rates suggesting the formation of a liquid-crystal-like, nematic structure. Hunt et al. [88] developed an algorithm capable of imposing mixed planar Couette flow and PEF. Furthermore, Hartkamp et al. [89] applied TTCF to these mixed flows in order to capture the behaviour of fluids at lower strain rates.

2.4. NEMD Simulations of Lubricants

Tribology problems are very well-suited to NEMD simulation since shear can be applied to systems of lubricants and additives to give insights in to their structure, flow and friction behaviour. As discussed in section 2.3., shear can be applied directly to the fluid molecules or by momentum transfer from sliding surfaces which confine the fluid (Fig. 3). While there are clearly significant differences between NEMD simulations of strongly confined, inhomogeneous systems and the bulk [90,91] (as justified below), comparisons between the methods for homogenous flows have shown good agreement [64,92,93]. Many lubricant properties, both in the bulk and under confinement, have been investigated using NEMD simulations, providing information at a scale that is difficult to access experimentally [23]. Indeed, NEMD simulations have predicted important behaviour of lubricant films many years before experimental techniques capable of providing comparisons on the same scales were developed. The following sections will discuss the use of NEMD to investigate the behaviour of lubricants in the bulk (section 2.4.1.), as well as when confined by solid surfaces (section 2.4.2.).

2.4.1. Bulk NEMD Simulations

Bulk NEMD simulations frequently investigate the change in lubricant viscosity, η, (the ratio of the shear stress, σ, to the strain rate, $\dot{\gamma}$) with strain rate, temperature and pressure. As $\dot{\gamma}$ is increased, lubricants often undergo a transition from a Newtonian regime (where η is independent of $\dot{\gamma}$) to shear thinning behaviour (where η decreases with increasing $\dot{\gamma}$). The critical strain rate transition, $\dot{\gamma}_c$, typically occurs at $\dot{\gamma} \approx \tau^{-1}$, where τ is the longest relaxation time at equilibrium (in the absence of

shear). This is usually the rotational relaxation time, τ_{rot} [48,49], which increases with molecular chain length [94]. Thus, longer simulations are required to obtain the Newtonian viscosity, η_N, from NEMD simulations of larger molecules.

Early NEMD simulations were limited to the rheology of simple L-J fluids and later short chain alkanes (≤ C_{10}) using UA force-fields [95]. Only more recently have they been applied to study lubricant-sized molecules ($C_{20\text{-}40}$). Some significant examples of bulk NEMD simulations of lubricant-sized molecules are discussed below. A list of bulk NEMD simulations applied to a wider range of fluids was compiled by Todd and Daivis [96] in 2007.

Morriss et al. in 1991 [97] were the first to simulate lubricant-sized molecules with NEMD. They used a UA model of n-eicosane (C_{20}) with a purely repulsive, Weeks, Chandler, Andersen (WCA) potential [98] and, as is common in NEMD simulations, they progressively increased the strain rate to study its effect on viscosity. At the lowest strain rates tested they observed a shear thinning regime, followed by shear thickening at higher strain rates. However, this shear thickening regime was later shown to be an artefact produced by the simplified force-field that was used [58].

Khare et al. [99] used NEMD to investigate the rheological behaviour of linear (C_{16}, C_{22}, C_{28}) and branched (5,12-dipropylhexadecane) alkanes. They employed the OPLS-UA model, which included attractive van der Waals interactions through a Lennard-Jones potential [100]. They were able to capture the Newtonian plateau and thus the zero-shear viscosity of the alkanes. The Newtonian viscosity of n-decane from the NEMD simulations was in good agreement with experiment; however, the viscosity results for longer alkanes were somewhat below the corresponding experimental values (44% for C_{28}). Nonetheless, the simple UA model employed was capable of accurately describing the pressure and temperature dependence of the viscosity, as well as its change with molecular structure (branching). Their simulation results indicated that the addition of short propyl branches to alkanes lead to a viscosity enhancement of a factor of two or more, offering interesting possibilities for lubricant design.

Moore et al. [101] performed extensive EMD and NEMD simulations of three C_{30} isomers at temperatures of 311 and 372 K, employing a UA model [102]. Using the rotational relaxation time calculated from the EMD simulation, the Rouse model [103] was used to predict the zero-shear viscosity for n-triacontane within 16% of the value determined by NEMD. Compared to experiment, NEMD with the UA model significantly under-predicted the kinematic viscosities of n-triacontane (48%) and 9-n-octyldocosane (36%) but was more accurate for squalane (15%) which contains multiple short methyl branches along its backbone. NEMD was also employed to calculate the viscosity index (VI), an important lubricant property used to characterize its change in viscosity with temperature. The VI values from the simulations for both 9-n-octyldocosane (7%) and squalane (11%) were in excellent agreement with experiment.

McCabe et al. [104] performed similar NEMD simulations of 9-octylheptadecane, a star-like isomer of C_{25}, under both ambient conditions and at GPa-level pressures, using a UA force-field [102]. Although the Newtonian viscosity was significantly underpredicted (27-66%), the viscosity number (VN) and pressure-viscosity coefficient (α) calculated from the NEMD simulations were in excellent agreement with experimental results (both within 4%) [105].

Liu et al. [106] performed NEMD simulations using a UA force-field [102] to calculate the shear viscosity of a model poly-α-olefin (PAO) base oil (1-Decene trimer) at various temperatures and pressures up to 1 GPa, in order to obtain its pressure-viscosity (α) values. Time-temperature superposition based extrapolations [107] were applied to further extend the applicability of the NEMD simulations. The α value calculated from simulations at 100 °C agreed well (7%) with experimental results [108].

Yang et al. [109] used NEMD simulations to study the rheology of heptamethylnonane (HMN) and 11-n-amylheneicosane (NAH). The Newtonian viscosity of HMN was underpredicted by 53-76% with a standard UA force-field [100]. By increasing the L-J size (σ) of the CH_3 groups attached to tertiary carbons by 4-5%, Newtonian viscosity prediction was improved to within 10% of experiment; however,

the impact of this on other fluid properties was not investigated. Using the modified UA model, Newtonian viscosity prediction of NAH was in reasonable agreement with experiment (21-31%) whilst the predicted VI was in good agreement (13%).

Cui et al. [94] used NEMD to study the rheological properties of a variety of linear (C_{10}, C_{16}, C_{24}) and branched (10-n-hexylnonadecane, squalane) alkanes, employing a UA force-field [102]. At high strain rate, the viscosity showed a power-law shear thinning behaviour over several orders of magnitude in strain rate. This power-law shear thinning was shown to be closely related to the ordering of the molecules and the molecular architecture had a significant influence on the power-law exponent. At a low strain rate, the viscosity behaviour transitioned to a Newtonian plateau and the zero-shear viscosity agreed with that from independent EMD simulations using the Green-Kubo method [37,38]. The molecular order in the low strain rate regime was similar to that of the equilibrium system, a signature of the linear response. The VI calculated for squalane with NEMD was found to be in excellent agreement with experiment (3%).

Liu et al. [110] proposed an approach to correlate shear thinning with the change in the molecular conformation, characterised by the radius of gyration of the molecule from NEMD simulations. This approach was first tested by analysing the critical strain rate for squalane and 1-decene trimer; and then extended to study the behaviours of PAO molecules with different molecular weights. A relationship between molecular weight and critical strain rate for different PAOs was observed, and the results were compared with those from the Einstein-Debye equation [111].

Bair et al. [48,49] compared bulk NEMD simulations of squalane using a UA force-field [102] with experimental measurements in both the Newtonian and shear thinning regimes. The extreme pressure and strain rate conditions studied were representative of the elastohydrodynamic lubrication (EHL) regime. This was the first comparison of the nonlinear rheology predicted by NEMD with experiment, and was thus the first experimental test of NEMD simulations in the shear thinning regime. The experimental and simulation data were separated by several orders of magnitude in strain

rate; however, they collapsed onto the same time-temperature superposition master curve [107]. This master curve was adequately fit using the Carreau shear thinning model [112].

Recently, Jadhao and Robbins [113] used NEMD simulations to determine the nonequilibrium shear response of squalane over a range of pressures and temperatures using a UA model [102]. The Newtonian viscosity values from the NEMD simulations agreed well with available experimental data. For some of the state points, their simulations extended down to low strain rates (10^5 s^{-1}) in order to capture the Newtonian plateau. The viscosity-strain rate behaviour extrapolated from the NEMD simulations agreed well with experimental data conducted at lower strain rates. The Eyring shear thinning model [114] could be used to extract an accurate prediction for the Newtonian viscosity from NEMD simulations at high strain rates as long as there is a substantial linear region in the plots of stress vs. log(strain rate). This condition was met whenever the Newtonian viscosity was ≥1 Pa s, where the fluid was in a 'glassy' regime. At lower viscosity, the response deviated from the simple Eyring form, indicating that the motion could not be described by a single activation barrier or rearrangement mechanism. The response in this 'low viscosity' regime was better described by models with a wide range of characteristic times, such as the modified power-law in the Carreau shear thinning model [112].

2.4.2. Confined NEMD Simulations

In addition to the important lubricant rheology information gained from bulk NEMD simulations, interesting insights into the behaviour of very thin lubricant films have also been obtained by confined NEMD simulations. Confined systems behave very differently from their bulk counterparts because density inhomogeneity leads to the breakdown of continuum approximations such as Navier-Stokes hydrodynamics [115]. Density oscillations in confined fluids were first identified in Monte-Carlo (MC) simulations of L-J liquids [116,117]. Shortly afterwards, surface forces apparatus (SFA) experiments by Horn and Israelachvili on confined octamethylcyclotetrasiloxane (OMCTS) [118] showed that the force between two surfaces does not evolve smoothly with the separation distance as predicted by van der

Waals theory. Instead, in films below six to ten molecular diameter thickness, the wall-wall interaction oscillated between repulsion and attraction states, with a periodicity roughly equal to the molecular diameter. This behaviour, known as the 'solvation force', was the first experimental evidence of density inhomogeneity in confined fluids. Subsequently, the first MD simulations of confined fluids agreed with earlier MC and experimental results, showing that strongly confined films have inhomogeneous density profiles across the channel [119]. NEMD simulations have also given many additional insights into the nonequilibrium response of confined fluid films, as discussed below.

Density and viscosity inhomogeneity

The first NEMD simulations of fluid films confined by solid walls were performed in 1987 by Bitsanis et al. [41]. They used the NEMD procedure developed by Ashurst and Hoover [40], but also included a 10-4 wall potential to confine the L-J fluid. They hypothesised that the inhomogeneous films could be viewed as a set of homogeneous layers and developed the local average density model (LADM), where each layer is given its own density and thus its own local viscosity. The LADM gave satisfactory results in predicting the flow of moderately-confined simple fluids [41]. However, the LADM model failed to predict many of the properties of strongly confined films, most notably the enhanced viscosity, where the density variation alone cannot explain the local dynamic properties of the film [120].

In conventional rheology models, the resistance to flow of a lubricant is characterized by its shear viscosity, η. For bulk systems, η depends purely on the fluid and its response to variations in pressure, temperature, and strain rate. Conversely, the dynamics of confined fluids are also influenced by factors that are not intrinsic to the fluid, so the definition of a bulk viscosity is not strictly appropriate [22]. However, the ratio of the shear stress to the strain rate still gives insight into the resistance to flow of confined films and can be compared directly to experiments [120]. Most experiments and NEMD simulations of confined films report this value as the 'effective' shear viscosity, η_{eff}.

When a fluid film is thicker than approximately ten molecular diameters, at which point its centre becomes a structureless medium, the experimentally measured η_{eff} is usually within around 10% of the bulk viscosity [121,122]. Experiment and NEMD simulations have shown that when the wall separation is decreased below this level, η_{eff} of confined L-J fluids [120,123], linear alkanes [124,125] as well as many other organic liquids [126] begins to increase significantly. When the film thickness is reduced to around six molecular layers, η_{eff} has been shown to increase by several orders of magnitude for a range of fluids [124–127]. For L-J fluids, this viscosity enhancement has been attributed to the crystallisation of the entire film [128,129]. Compared to L-J fluids, linear alkanes are less susceptible to crystallisation and so both a second order glass transition [128] or the formation of 'crystal bridges' [124] have been attributed to the viscosity enhancement. However, more recent all-atom MD simulations [130] have suggested that both cyclohexane and n-decane undergo a rapid, first order phase transition to a layered and ordered (i.e. crystalline) system (see Fig. 4) at surface separations equivalent to fewer than nine molecular layers. These simulations support experiments which showed an abrupt transition from liquid-like to solid-like behaviour upon increasing confinement [126,127], rather than a more gradual transition to a glassy state (vitrification) [125,131]. It is noteworthy that most evidence for vitrification originated SFA experiments which were later shown to be contaminated with platinum nanoparticles [132], which could go some way to explaining experimental discrepancies. It has also been shown through experiments [131] and NEMD simulations [128] that elevated pressure can induce such transitions, as well as the associated increase in η_{eff}, in thicker films.

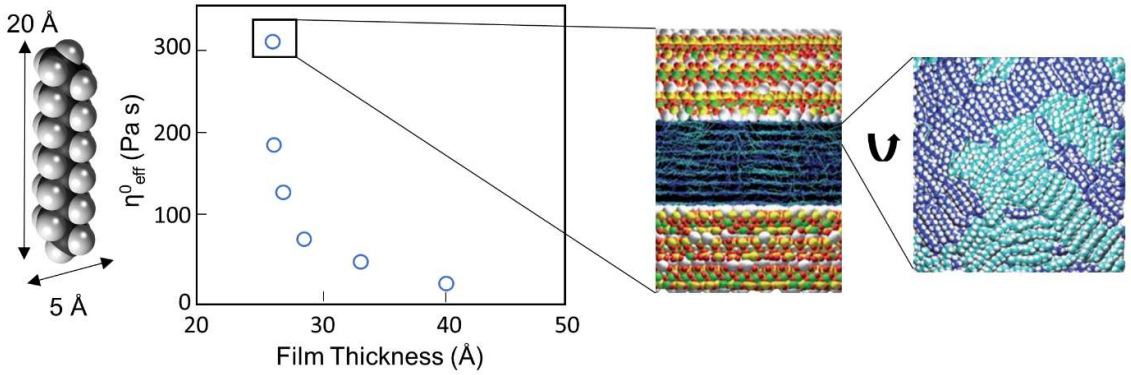

Figure 4. Viscosity enhancement with decreasing film thickness for dodecane adapted from ref. [125]. The high viscosity state has been attributed to a crystalline phase (inset image) from all-atom MD simulations in ref. [130].

The transition from liquid-like to solid-like behaviour in confined fluids also depends strongly on molecular shape and surface structure. NEMD simulations have shown that branched or flexible molecules are more resistant to solidification and remain liquid-like under more severe confinement and higher pressures compared to linear or inflexible molecules [133,134]. Thus branched molecules can give lower η_{eff} under strong confinement than linear molecules, despite their higher bulk viscosity [122]. It should also be noted most simulations of confined film behaviour employ atomically-smooth surfaces employ but it has been found that surface roughness frustrates the ordering of the neighbouring fluid molecules so that films are more liquid-like on surfaces with nanoscale roughness compared to those which are atomically-smooth [135,136].

When the film is thinner or when the pressure is increased, the Newtonian plateau is displaced to lower strain rates. Thus, at the strain rates accessible to NEMD simulations (>10^7 s^{-1}), confined fluids are often highly shear thinning [137]. A viscosity-strain rate power law was identified for L-J fluids at different pressures and thicknesses [128]. The Carreau [138] and Eyring [139] shear thinning models have both been successfully used to fit the viscosity-strain rate behaviour of confined fluids from NEMD simulations.

Martini et al. [140] used NEMD simulations to extract the thickness and velocity dependence of the viscosity of n-decane confined and sheared between atomically-smooth gold surfaces. This information was then fed into a full numerical solution for EHL problems [141] to assess the impact of these viscosity changes on the predicted film thickness.

Boundary slip

Fluid flow in confined geometries can be significantly affected by slip at the liquid/solid interface. Boundary slip occurs when the fluid cohesion is relatively stronger than its adhesion to the solid slabs [90], meaning that the slabs do not transfer sufficient momentum to fully shear the fluid [142]. The phenomenon is commonly observed in NEMD simulations of very thin fluid films confined between atomically-smooth surfaces [142–146]. Many of these studies have quantified the slip length, which is defined as an extrapolated distance into to the wall where the tangential velocity component vanishes (see Fig. 5).

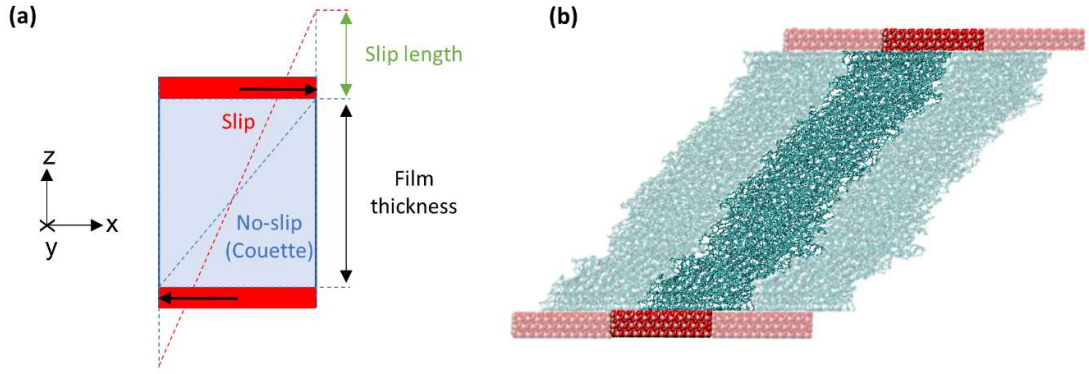

Figure 5. Schematic diagram showing the definition of the slip length from NEMD simulations (a) and image of NEMD trajectory with boundary slip with periodic images shown as translucent (b).

NEMD simulations have shown that the slip length increases with increasing sliding velocity and pressure [142–145]. An important observation is that realistic velocity-slip behaviour can only be captured when flexible, rather than rigid walls are employed [146]. The slip length also increases with

increasing molecular chain length and degree of branching, in line with the viscosity [133]. Moreover, inflexible molecules, which can conform to the surface only with a greater expense of conformational energy generally exhibit more slip [147]. Conversely, the slip length has been shown to decrease with increasing surface-fluid attraction strength and film thickness [143–145], and to be virtually eliminated in the presence of atomic-scale surface roughness [135]. This final observation is critical since experimental surfaces contain fractal roughness, even down to the atomic scale [148], which is likely to discourage boundary slip on conventional experimental surfaces. In addition, large-scale NEMD simulations of a >100 nm *n*-hexane film between atomically-smooth iron surfaces under realistic elastohydrodynamic lubrication (EHL) conditions (F_N = 1 GPa, $\dot{\gamma} = 10^5$ s^{-1}) confirmed the suitability of a macroscopic no-slip boundary condition for this particular system [144].

Pit, Hervet, and Léger were the first to show direct experimental evidence of noticeable slip at the wall for n-hexadecane flowing on a oleophobic smooth surface [149]. Boundary slip has been observed under EHL conditions for viscous polybutadiene on glass surfaces with an oleophobic coating [150]. It has also been inferred from optical interferometry experiments on glass and even steel surfaces under EHL conditions for viscous polybutadiene and polyphenyl ether (*e.g.* 5P4E) [151]. However, this phenomenon has not yet been observed experimentally for realistic lubricants on conventional surfaces [152].

Continuum approaches to study fluid flow, such as the Reynolds equation [7], generally assume a no-slip boundary condition [153]. Slip lengths extracted from NEMD simulations have been fed into a modified Reynolds equation to study the effect of slip at one [154] or both [142] of the surfaces on flow behaviour, film thickness and EHL friction. These results have shown that slip can lead to a reduction in film thickness and friction compared to the no-slip case, particularly at high strain rates.

Nonequilibrium phase transitions

In the last few years, NEMD simulations of confined L-J liquids sheared at GPa-level pressures have revealed novel nonequilibrium phase behaviour [155–157]. These simulations were designed to mimic

the conditions found in the elastohydrodynamic lubrication (EHL) regime, which is particularly important for machine components that roll and slide together, for example; rolling bearings, gears, constant velocity joints and cam/follower systems [8]. Although shear was applied in these simulations through the walls (confined NEMD), the thickness of the films was well above the ten molecular-layer limit in which fluid films experience enhanced viscosity [121,122].

At low pressure, planar Couette profiles were observed, but above a certain pressure (≈250 MPa), the NEMD simulations produced non-linear velocity profiles. Nonequilibrium phase diagrams were constructed for L-J fluids to map the changes in behaviour with pressure and strain rate (or sliding velocity). Fig. 6 shows the different types of flow behaviour which have been observed in NEMD simulations of fluids under EHL conditions. At low strain rates, shear was localised close to (but not at) the walls, while the central part of the fluid formed a solid-like region that hardly sheared. This behaviour is referred to as 'plug-slip' (PS). At higher strain rates, the localisation of shear velocity gradient moved into the centre of the film, while the fluid near the walls became solid-like. This behaviour is usually known as 'central localisation' (CL) [155–157].

In the field of tribology, shear localisation has only been experimentally observed in viscous model lubricants, such as polybutadiene and polyphenyl ethers [158–163]. However, it has also been inferred from film thickness measurements in realistic mineral oils [164,165] and there is currently a growing consensus that this phenomenon may also be important for more realistic lubricants under extreme conditions, for example those experienced in the EHL regime [152].

The discovery of such nonequilibrium phase behaviour by NEMD simulations of L-J fluids demonstrates the advantage of carrying out simulations using basic models such as hard spheres or L-J fluids. By doing so, it helps to reveal whether the phenomenon is 'universal' to the fluid state and arises for all (or at least the vast majority of) liquids under certain conditions (which vary between molecules), or is specific to certain types of molecule.

Recently, extensive NEMD simulations of confined L-J fluids under pressure have revealed that the nonequilibrium phases correlate well with corresponding friction maps [157]. The characteristics of friction on the atomic scale can deviate quite significantly from the laws of classical friction. For example, when the applied conditions yield shear localisation, the friction coefficient of L-J fluids can decrease with increasing pressure and strain rate. Such behaviour is not commonly observed experimentally for lubricants, but is more similar to how traction fluids behave [15] above their critical shear stress [152]. The nonequilibrium phase diagrams and friction maps for L-J fluids were also quite sensitive to the degree of the wall roughness on the atomic scale. Random atomic-scale roughness on both walls lead to asymmetry in the velocity profiles, with CL profiles changing to asymmetric melting (AM) where the shear is localised closer to one of the walls [152].

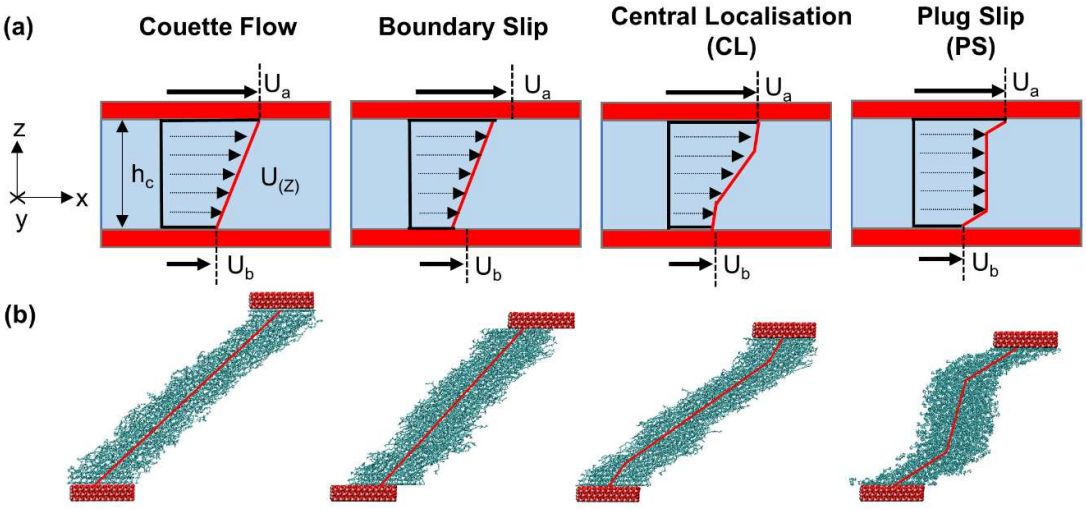

Figure 6. Schematic showing different types of flow behaviour in confined fluid films under extreme conditions for two surfaces separated by distance h_c, moving at velocities of U_a and U_b (a). Images showing examples of the flow behaviour from NEMD simulations are adapted from ref. [42] (b).

In NEMD simulations of binary mixtures of L-J particles, crystallisation was suppressed and only liquid or glassy phases were formed [156]. In these binary systems, the friction coefficient increased linearly with log(strain rate), as has commonly been observed for realistic lubricants, such as PAO, under EHL conditions [8]. In this case, the friction-strain rate behaviour can be adequately described using stress-

promoted thermal activation theory [166], according to the rheological models of Eyring [114]. It has also been suggested that the Carreau [112] and related models, which were developed for polymer shear thinning, can be used to predict the friction-strain rate behaviour of lubricants in the EHL regime [8].

An underlying assumption in current models of EHL friction is that, in the absence of thermal effects, or until a critical strain rate is reached, the rheological properties of the lubricant do not vary through its thickness. This is implicit in applying shear thinning models to predict friction in the EHL regime since they generally assume that the film is subject to planar Couette flow. Thus significant modifications of these models may be required where there are deviations from Couette flow, such as shear localisation [8]. As discussed in section 2.4.1., NEMD simulations are at the forefront of discovery in terms of the suitability of these models to predict EHL friction [113,138].

2.4.3. Summary

Bulk NEMD simulations of lubricant-sized molecules have shown how molecular structure can affect rheology. Many studies have focussed on replicating Newtonian viscosities of realistic lubricant molecules as well as its change with temperature (VII) and pressure (α). Such predictions have become more accurate and have reached a point where they can be used as a predictive tool to compare different lubricant molecular structures. Such structure-property relationships can be extremely useful in lubricant design. Bulk NEMD simulations have also given unique insights into lubricant shear thinning under extreme conditions (representative of the EHL regime) and helped to validate appropriate macroscopic models for predicting this behaviour.

Confined NEMD simulations have also proved extremely useful in understanding the behaviour of lubricants between solid surfaces. This includes building fundamental understanding of the density and viscosity inhomogeneity in confined films, as well as knowledge of important tribological phenomena such as boundary slip and nonequilibrium phase transitions. This simulation method is particularly attractive in that it mirrors the layout and physics of real tribology experiments and,

compared to bulk NEMD simulations, requires fewer assumptions with respect the flow profile and thermostatting procedure. Thus, confined NEMD simulations are being increasingly used to study relatively thick bulk-like films in tribology.

Key to any simulation methodology is validation through direct comparison with experiment. As demonstrated above, this is beginning to become possible with NEMD simulations thanks to improvements in simulation algorithms and computer hardware which have allowed lower strain rates to be investigated.

2.5. NEMD Simulations of Lubricant Additives

A more recent area of research has been the application of MD to study the behaviour of lubricant additives. The function of many lubricant additives depends on chemically reactions, which are generally not considered in classical MD simulations. Despite this, classical MD simulations have yielded unique insights into a range of lubricant additives including; detergents [16], dispersants [167], viscosity modifiers [168], anti-wear additives [169], and corrosion inhibitors [170]. By far the most widely studied class of lubricant additives are friction modifiers, which are a well-suited application of confined NEMD simulations.

The need for greater energy efficiency to reduce energy consumption has led to a shift toward lower-viscosity lubricants, which means that an increasing number of engineering components operate under boundary lubrication conditions. As a result, lubricant additives that reduce friction and wear under boundary conditions (i.e. friction modifiers) are of increasing importance [11]. Several classes of friction modifier additives exist, the main ones being organic friction modifiers (OFMs), functionalised polymers, organo-molybdenum additives and dispersed nanoparticles. An overview of the experimental advances on friction modifier additives is given in ref. [11]. Sections 2.5.1. and 2.5.2. will focus on classical MD simulations of OFMs and nanoparticle friction modifiers respectively.

2.5.1. Organic Friction Modifiers

OFMs are amphiphilic surfactant molecules that contain a nonpolar hydrocarbon tailgroup attached to a polar headgroup. Their main friction reduction mechanism involves the adsorption of the polar headgroup to metal or ceramic surfaces (Fig. 7), with strong, cumulative van der Waals forces between proximal nonpolar tails leading to the formation of incompressible monolayers that prevent contact between solid surfaces to reduce adhesion and friction [171]. Many different head and tailgroups have been tested in the literature, as discussed elsewhere [11].

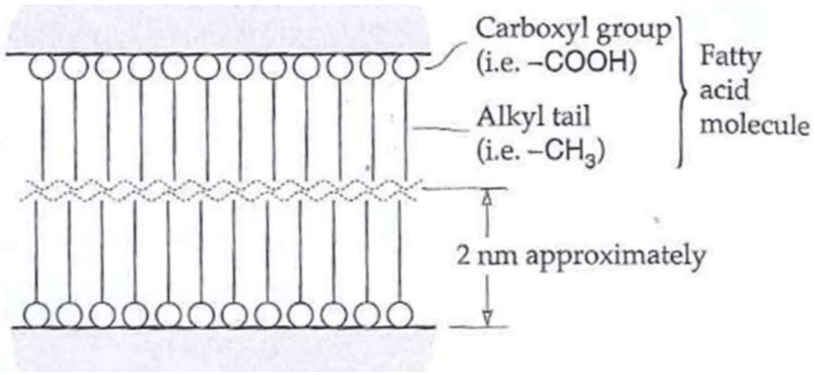

Figure 7. Schematic of OFM molecules adsorbed on opposing metal surfaces [172]

Classical NEMD simulations can be used to simultaneously probe the nanoscale structure and friction of OFM films, making them a valuable complement to experiments. Adsorption of amphiphiles from solution to solid surfaces is a relatively slow process, and close-packed monolayers can take hours to form in the absence of shear [173]. As a result, MD simulation of the adsorption process with realistic additive concentrations and accurate AA force-fields are currently unattainable. However, extensive experimental analysis has shown that OFMs do eventually form close-packed monolayers on a range of contact surfaces, and that the formation of these films is accelerated by the shearing process [173–175]. Therefore, MD simulations are generally performed with pre-formed close-packed monolayers, where additive molecule headgroups are placed on, or close to, solid surfaces at the start of the simulation. This is similar to the Langmuir-Blodgett experimental approach to quickly form films with

a controllable packing density on solid surfaces [176]. OFM simulations generally consist of monolayers of amphiphiles adsorbed on two solid surfaces, sometimes also with a layer of confined lubricant. EMD simulations have been performed to study the structure of OFM films on solid surfaces. NEMD simulations have also been performed, where the confining walls are given a lateral velocity to shear the system, and structural and friction information is then gathered. These simulations are discussed below.

Moller et al. [177] were the first to use MD simulations to study the structure of OFM films (stearic acid) on solid (graphite) surfaces. They varied the headgroup area to study its effect on the tilt angle from the surface normal. The OFM headgroup area (area units) can be viewed as the inverse of the OFM surface coverage (molecules per area units). Their simulations predicted that, under ambient conditions, OFM molecules were approximately normal to the surface at high surface coverage (headgroup area < 21 $Å^2$), but became tilted from the normal at lower surface coverage. They suggested that titling maximises the van der Waals attraction between the chains by increasing the packing efficiency [178]. The tilting transition was attributed to the packing of the hydrogen atoms belonging to methylene groups on neighbouring molecules, meaning that the correct behaviour could not be accurately reproduced using UA force-fields [177].

Glosli et al. [179] were the first to use NEMD to model the friction of OFM-like systems. Specifically, they studied the friction between two close-packed monolayers (headgroup area 17 $Å^2$) bound at their ends to two rigid substrates (similar to OFM molecules strongly absorbed to solid surfaces). Depending on the interfacial interaction strength between the two layers, energy dissipation either occurred by a discontinuous ‘plucking’ mechanism (strong interaction) or a continuous ‘viscous’ mechanism (weak interaction). Friction during the plucking mechanism followed the simple thermal activation model proposed by Briscoe and Evans from experimental friction data between opposing Langmuir-Blodgett films [176]. Friction during the viscous mechanism was generally much lower but increased at the

rotator transition temperature of the monolayers (T at which molecules become rotationally ordered in a herringbone-like pattern).

Kong et al. [180] performed NEMD simulations of adsorbed OFM (dialkylammonium chloride) monolayers between charged solid surfaces. They found that the friction coefficient decreased with increasing normal force (30-450 MPa), increased with increasing sliding velocity (1-100 m s^{-1}), and decreased with decreasing headgroup area (50-77 $Å^2$). It is worth noting that, since each dialkylammonium chloride molecule contains two alkyl tailgroups, these molecules have a similar tailgroup density to mono-alkyl surfactants with half the headgroup area. The friction between the layers correlated well with the amount of layer overlap or interpenetration, as defined by the common area under the chain density profiles. In a separate NEMD study [181], the effect of monolayers with asymmetrical ($C_{10}C_{18}$) and symmetrical ($C_{18}C_{18}$ and $C_{10}C_{10}$) tailgroups was investigated. The friction between the layers of asymmetrical surfactants was greater than that between layers of symmetrical surfactants, suggesting that films with uneven heights were less effective in reducing friction.

Greenfield et al. [182] used MD simulations to investigate the orientation of monolayers of model OFMs (headgroup area 17 $Å^2$) with and without hydrocarbon solvent and confined between atomically-smooth surfaces. The normal load, fluid layer thickness, and additive surface concentration dependencies agreed with those measured experimentally using the SFA [183]. With no solvent added, there were oscillations in normal pressure and free energy as surface separation decreased, with stable states corresponding to successive layers of OFM molecules being expelled from the region between the adsorbed films. When hydrocarbon solvent was included between the films, only a single stable position was found. The equilibrium structure was also found to depend on the headgroup structure of the OFMs. In a separate study [184], NEMD simulations were performed by shearing the same systems. The adsorbed OFM chains were found to form semi-ordered monolayers perpendicular to the surface, with distinct layering shown in the density profiles. Between these monolayers, more liquid-like layers with broader density profiles and larger fluctuations were formed by ‘free’ OFM

chains. The adsorbed monolayers remained virtually unchanged under a wide range of normal pressures (3.2-22 MPa) and sliding velocities (0.5-7.5 m s^{-1}), while the gap between the monolayers decreased with increasing pressure as the liquid-like layers were squeezed out.

Davidson et al. [20] performed EMD simulations to help elucidate structure activity relationships of mono-, di-, and tri-oleyl glyceride OFMs. These molecules contain variable numbers of OH groups and alkenyl chains and MD simulations showed the importance of intermolecular hydrogen bonding in determining the stability of the monolayer formed. Mono-glyceride molecules with two OH groups and one alkenyl chain packed more efficiently than di-glycerides which contain one OH group and two alkenyl chains. This was because the mono-glycerides occupied approximately half the area (22 $Å^2$) needed by di-glycerides (46 $Å^2$) and formed significantly more intermolecular hydrogen bonds. The density profiles showed significant mixing of the hydrophobic tailgroups with the non-polar solvent. The distribution of torsion angles in the tailgroups shows that the conformation was consistent with a liquid-like rather than a crystalline structure at room temperature. Experimentally measured friction coefficients of equimolar solutions of the glycerides showed that the efficacy as friction modifiers varied in the order mono-, di- and the tri-oleyl glyceride, which was consistent with the film formation results from the MD simulations.

Eder et al. [185] performed NEMD simulations of several OFMs on iron surfaces, varying the OFM type (stearic acid, oleic acid, methyl stearate), OFM surface coverage (2.54-4.57 nm^{-2}), the pressure (0.07-1.60 GPa), as well as the surface roughness. The resulting load versus friction behaviour was then analysed to study these parameters affected the friction coefficient and the extrapolated friction force at zero load (Derjaguin offset). A smooth-particle-based evaluation method [186] was used to visualize the sliding interface between the two OFM layers. This allowed the definition and calculation of a dimensionless normalized sliding resistance area, which was then related to the Derjaguin offset. Generally, the friction coefficient and Derjaguin offset increased with increasing surface roughness,

and decreased with increasing OFM coverage. The Derjaguin offset was eliminated by the addition of a thin n-hexadecane film between the OFM layers.

Doig et al. [187] used NEMD simulations to examine the structure and friction of stearic and oleic acid OFM films adsorbed on iron oxide surfaces and lubricated by squalane at 0.1 GPa. At high surface coverage (2.59 nm^{-2}), the measured properties of stearic acid and oleic acid films were very similar. At low (0.58 nm^{-2}) and intermediate (1.30 nm^{-2}) surface coverages, the presence of Z-unsaturation (in oleic acid) resulted in less penetration of lubricant in to the surfactant film and less layering of the lubricant near to the film. The friction coefficient increased linearly with log(strain rate) within the hydrodynamic lubrication regime, consistent with a stress-promoted thermal activation model and results from macroscale experiments [188]. Lubricant penetration and layering were found to affect the friction coefficient. The friction coefficient with oleic acid depended more weakly on surface coverage, while stearic acid allowed more lubricant penetration, and its friction coefficient increased significantly with decreasing surface coverage.

Doig et al. [189] also used NEMD simulations to gain insights into sum-frequency spectroscopy (SFS) and polarised neutron reflectometry (PNR) experiments [190] which probed the structure of hexadecylamine films adsorbed on iron oxide surfaces in dodecane and hexadecane. The simulation results showed that, at the highest surface coverage investigated (1.80 nm^{-2}), the film thickness was about 15-20 Å, and that the molecules had an average tilt angle from the surface normal of 40–50°, in agreement with experiment. The in-layer ordering of the hexadecylamine headgroup atoms was found to be dictated by the crystalline structure of the iron oxide surface, but this influence quickly diminished further along the tailgroup. The friction coefficient at 10 m s^{-1} was determined to be around 0.1, which is typical for this kind of system [188].

Bradley-Shaw et al. [191] used NEMD simulations to study reverse micelles, formed by glycerides in organic solvents [192], confined and sheared between mica surfaces. Preformed reverse micelles were found to be metastable under static conditions in all of the solvents studied. In n-heptane, under shear

conditions, with or without water, the preformed GMO reverse micelles remained intact and adsorbed onto one of the surfaces, becoming surface micelles. In dry toluene, preformed reverse micelles broke apart under shear, while in the presence of water, the reverse micelles survived and became surface micelles. Water was strongly associated with the GMO molecules, irrespective of shear or the form of the GMO added. With increasing strain rate, the GMO molecules became more flattened on the surface and the friction coefficient increased. At low strain rates ($< 10^{10}$ s^{-1}), the friction was insensitive to the form of the GMO added, whereas the presence of water was found to lead to a small reduction in friction. At high strain rates ($\geq 10^{10}$ s^{-1}), the presence of reverse micelles leads to a significant reduction in friction, whereas the presence of water increased the friction in n-heptane and decreased the friction in toluene.

Although the focus of this review is on lubricants for macroscale engineering components such as engine and transmissions, NEMD simulations of confined films have also been performed to study friction modifier additives for microelectromechanical systems (MEMS) and nanoelectromechanical systems (NEMS). In this context, NEMD simulations have been used to investigate the friction behaviour of monolayers of carboxylic/perfluorocarboxylic acids [193–195] and alkylsilanes [196–199] on silica surfaces. Model self-assembled monolayers (SAMs) such as thiols on gold surfaces have also been widely studied with NEMD [200–202]. These simulations have helped to reveal the effect of headgroup and tailgroup type on the nanoscale structure and friction behaviour of the monolayers.

2.5.2. Nanoparticle Friction Modifiers

In recent years, there has been growing interest in the possibility of using solid particles in the size range 1-500 nm as friction modifier and anti-wear additives. In principle, such particle sizes are small enough both to remain dispersed in liquids and to pass undisturbed through oil filters. Many types of nanoparticle additives have been tested, from various carbon allotropes to metals and inorganic salts. The relatively recent development of fullerenes and inorganic fullerenes has yielded particular interest

since their graphitic-like structures bear some resemblance to lamellar materials which are known to effectively reduce friction [11].

Despite this interest, there is still considerable uncertainty regarding the friction reduction mechanisms of nanoparticle additives [11]. Many different mechanisms have been proposed including; sliding (a), rolling (b), exfoliation (c), polishing (d) and mending (e), as shown in Fig. 8.

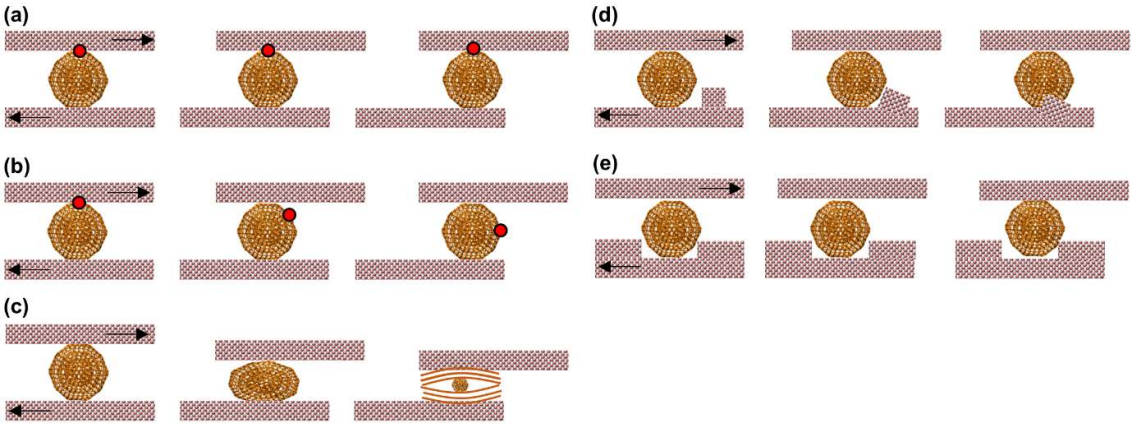

Figure 8. Schematic showing the potential mechanisms of friction reduction by the presence of nanoparticle additives pressed between sliding metal surfaces, adapted from ref. [203]. (a) Sliding, (b) rolling, (c) exfoliation, (d) polishing and (e) mending.

If nanoparticles are able to maintain separation of surface asperities they may, in principle, give large reductions in friction and wear under boundary conditions [203]. This requires nanoparticles to be sufficiently hard to not be plastically deformed under the high pressures experienced during boundary lubrication. However, if the nanoparticles are excessively hard, they may indent into the surfaces to such an extent that they no longer separate asperities. Nanoparticles that are able to prevent asperity contact may roll (Fig. 8-a) or slide (Fig. 8-b) between the surfaces in order to reduce friction. Experimental studies have suggested that unlike macroscopic systems, there is little, if any, benefit of rolling action for nanoparticles compared to sliding [204,205]. Hard nanoparticles may also reduce friction through polishing (Fig. 8-d), whereby asperities are smoothed by abrasion by the nanoparticles to reduce roughness and shift the system from boundary, towards mixed lubrication conditions [206].

While this may initially provide a large benefit, it will quickly diminish in the presence of other running-in and smoothing processes. Moreover, the potential for abrasion will remain after the initial surface roughness has been polished, potentially leading to increased wear after running-in [207]. On rough surfaces, it has been suggested that hard nanoparticles may also 'mend' the surface by filling the gaps between asperities (Fig. 8-e) [206]. For soft or layered nanoparticles, there is also the possibility that friction may be reduced through exfoliation (Fig. 8-c), whereby the nanoparticles break down into a solid lubricating film, which prevents contact between the surfaces and reduces friction by forming a low shear strength layer [208].

The prevalence of each of these mechanisms is expected to be highly situation-specific [11], and depend on variables including the nanoparticle's: material, size, shape, hardness, coverage as well as the prevailing temperature, pressure and sliding velocity. For example, *in-situ* high resolution scanning electron microscope (HRSEM) [208], high resolution transmission electron microscope (HRTEM) [209] images of inorganic fullerene (MoS_2) nanoparticles during sliding have suggested that their friction reduction mechanism consists of a mixture of sliding/rolling at low pressure and exfoliation to lamellar sheets of MoS_2 at high pressure. Exfoliation of hollow core MoS_2 fullerenes was also observed in MD simulations by Lahouij et al. [209] under uniaxial loading.

There have been a considerable number of NEMD simulations to investigate nanoparticle behaviour confined and sheared between solid surfaces. Joly-Pottuz et al. [210] conducted experiments and NEMD simulations of carbon nano-onions (2 nm diameter) between sliding diamond-like carbon (DLC) surfaces at high contact pressure (1-5 GPa). The simulations suggested that the lubrication mechanism of nano-onions is based on a coupled process of rolling and sliding inside the contact. The results suggested that carbon nano-onions remained intact under compression and sliding and do not exfoliate to graphitic planes, unlike MoS_2 fullerenes [209].

Bucholz et al. [211] further characterised the behaviour of carbon nano-onions (2 nm diameter) using NEMD simulations of their rolling and sliding action between DLC substrates. Their results indicated

that the ability of the nano-onions to roll is inhibited both by increased contact pressure and the presence of a diamond core within the nanoparticles. The transition from rolling to sliding behaviour was accompanied by a significant increase in the friction coefficient due to the formation of interfacial bonds.

Bucholz et al. [212] also used NEMD to investigate the behaviour of amorphous carbon nanoparticles between hydrogen-terminated diamond surfaces. Over the range of a-C nanoparticle diameters (2–5 nm) and hydrogenation (0-50%) considered, the simulations predicted a consistent mechanical response in which each nanoparticle was highly elastic. The simulations predicted that the transition from elastic to plastic response is directly related to an increase in the percentage of carbon-carbon crosslinking within the individual nanoparticles. The simulations also predicted that the tribological response was noticeably impacted by changes in diameter and hydrogenation. This is because during sliding, hydrogen passivates reactive carbon atoms near the surface of the nanoparticles, which prevents interfacial bond formation and allows them to roll between the surfaces. From these findings, it was demonstrated that a-C nanoparticles may provide good tribological performance for carbon surfaces only when sufficient chemical passivation of the surfaces and nanoparticles is maintained.

Hu et al. [213] investigated the effect of soft metallic copper nanoparticles (4 nm diameter) between relatively hard iron surfaces using NEMD simulations. The results suggested that the nanoparticles plastically deformed to generate a low shear strength film between the contact surfaces which accommodated the velocity gradient. The nanoparticles were most effective in reducing friction at low loads and sliding velocities (0.01 GPa, 10 m s^{-1}), but still provided a small benefit under very extreme conditions studied (0.5 GPa, 500 m s^{-1}).

Hu [214] also used NEMD simulations to investigate the tribological behaviour of hard diamond and silicon dioxide (SiO_2) nanoparticles (3 nm) between iron surfaces. At low velocity and low load (10 m s^{-1}, 0.5 GPa), the nanoparticles separated the two contact surfaces from each other and acted as “ball-

bearings", significantly reducing friction. At high velocity and high load (500 m s^{-1}, 1.0 GPa), they either plastically deformed (SiO_2) or indented into the contact surfaces (diamond), leading to smaller reductions in friction.

Eder et al. [215] simulated the abrasion process of an atomically rough iron surface with multiple hard, cubic particles (edge height 4.2 nm). By tracking the change in nanoscopic wear depth over time, the authors showed that Barwell's macroscopic wear law [216] can also be applied at the atomic scale. They found that in their multiasperity contact system, the Bowden-Tabor term, which describes the friction force as a function of the real nanoscopic contact area, accurately predicted the friction, even when wear was involved. From this, the Derjaguin-Amontons-Coulomb friction law could be recovered [217], since a linear dependence of the contact area on the applied load was observed, in accordance with Greenwood-Williamson contact mechanics [218].

2.5.3. Summary

Limitations in computational power mean that it is not yet possible to use MD simulations to observe the film formation behaviour of friction modifier additives from solution. This means that modelers still rely on experimentalists to be confident of the type of films formed by additives on solid surfaces. For surfactant molecules, such as OFMs, it has been conclusively shown from experiments that monolayers form on surfaces, meaning that 'preformed' films, similar to those from Langmuir-Blodgett experiments, provide accurate model systems. For example, NEMD simulations of several friction modifier additives have given insights into the types of films formed on solid surfaces and the way in which they alter the flow and friction behaviour under a wide range of conditions. The structure of the films formed by friction modifiers in MD simulations agree well with experimental observations. Moreover, NEMD simulations have reproduced important trends in friction behaviour seen in experiments, and helped to explained these from the atomic-scale. For other types of additive, it is not so clear from experiment how molecules arrange in a tribological contact, and so construction of a representative system for NEMD simulations is more difficult. With the advance in computational

power, and the development of more accurate force-fields, it is possible that simulations could begin to guide experiments in this area.

2.6. Conclusions

Molecular dynamics is a relatively simple simulation method, yet it has become one of the most powerful tools in science and engineering to understand the atomic scale behaviour of fluids. Historically, it has played a key role in corroborating theories of the fluid state, but it has now become capable of directly evaluating physical properties in industrially important systems [219]. Moving forwards, we expect NEMD simulations to play an increasingly important role in building a fundamental or 'bottom-up' understanding of tribological phenomena from the atomic scale. Moreover, it is reaching the point at which it can be a truly useful tool in lubricant design. Key to this process will be direct comparison of NEMD to experiment; something which is beginning to become possible thanks to improvements in simulation algorithms, classical force-fields and computer hardware as well as developments in experimental nanotribology.

Bulk NEMD simulations of lubricant-sized molecules have shown how molecular structure can affect rheology. Many studies have focussed on replicating Newtonian viscosities of realistic lubricant molecules, as well as their change with temperature and pressure. Simulations can now be used as a predictive tool to compare the viscous behaviour of lubricant molecules with different structures, providing structure-property relationships that are extremely useful for lubricant design. Bulk NEMD simulations have also given unique insights into lubricant shear thinning behaviour and helped to confirm appropriate macroscopic models for predicting it.

Confined NEMD simulations have also proved extremely useful in understanding the behaviour of lubricants between solid surfaces. They have contributed to fundamental understanding of the density and viscosity inhomogeneity in confined films, as well as knowledge of important tribological phenomena such as boundary slip and nonequilibrium phase transitions. Confined NEMD simulations are particularly useful because they more accurately reflect the layout and physical processes seen in

real tribology experiments. They also require fewer assumptions with respect the flow profile and thermostatting procedure compared to bulk NEMD simulations.

The atomic-scale behaviour of lubricant additives has also been successfully investigated with NEMD. There has been a particular focus on organic friction modifier and nanoparticle additives, in part because simulation of these additives does not necessarily need to account for chemical reactivity. NEMD simulations have shown similar friction-velocity behaviour to theory and experiment and highlighted the importance of additive coverage.

Chapter 3. Benchmarking Classical Force-Fields for Density and Viscosity Prediction of n-Hexadecane

The work described in this chapter has been partly published in *Materials* (ref. [220]).

3.1. Introduction

In this chapter, several united-atom (UA) and all-atom (AA) force-fields are benchmarked in terms of their density and viscosity prediction accuracy of n-hexadecane using equilibrium molecular dynamics (EMD) simulations at ambient and high temperature, high pressure (HTHP) conditions. These properties are significant since they govern the hydrodynamics of lubricants and directly influence their tribological behaviour. We focus on n-hexadecane because it is an important model lubricant with a wide range of industrial applications. Simulating conditions common in tribological systems, i.e., HTHP, allows the limits of the selected force-fields to be tested.

Molecular dynamics simulations using both empirically-parameterized (Class I) and *ab initio* (Class II) classical force-fields can accurately reproduce important properties of molecular systems under ambient conditions. However, these force-fields are generally poorly transferable and their accuracy decreases when the system, conditions, or properties of interest deviate from those for which they were directly parameterized. Simulations of tribological systems are particularly demanding, since most lubricants contain relatively large, complex molecules, and the conditions of interest are typically high temperatures and high pressures (HTHP). This means that force-fields should ideally be tested for these molecules and conditions prior to their application in complex simulations.

This first part of this chapter introduces the functional form of classical force-fields and discusses important differences between the available variants. It then draws attention to issues with several popular classical force-fields for MD simulations of long-chain linear alkanes, and highlights contemporary alternatives which provide far higher accuracy. The simulation of these molecules are of great interest due to their prevalence in fuels and lubricants as well as biological systems.

3.1.1. Classical Force-Fields

Force-fields are used to determine the forces acting on all particles in a system, depending on their position (equation 3). They consist of sets of parameters for use with mathematical functions which describe the potential energy of the system of atoms. Force-field functions and parameter sets can be derived by both empirical fitting with experimental data (Class I) and/or quantum mechanical calculations (Class II). It has been shown previously that Class I force-fields are far more accurate for reproducing the physical properties of alkanes in condensed phase simulations [221], and so only these are discussed further in this study.

Class I force-fields all have similar functional forms, which encapsulate both bonded terms, which describe interaction between atoms that are linked by covalent bonds, and non-bonded terms which represent the interactions between atom which are not directly bonded together:

$$V_{total} = V_{bonded} + V_{non-bonded}$$

Bonded interactions generally include terms to compute the potential energy of atoms due to bonds, angles and dihedrals. The bond and angle terms are usually modelled as harmonic oscillators. The functional form for the dihedral terms varies between force-fields, but parameters can generally be converted between different forms. The non-bonded interactions include van der Waals and electrostatic terms, which are more computationally expensive, because they involve many more interactions per atom. In order to improve computational efficiency, these interactions are often limited to only the pairwise energies [23]. The next section gives more detail with regards to the bonded and non-bonded aspects of the total potential energy calculation for the force-field.

3.1.2. Non-Bonded Interactions

In most Class I force-fields, non-bonded interactions include two types of potential, one to cover van der Waals attractive and short-range Pauli repulsive forces as well as another to represent electrostatic attraction:

$$V_{non-bonded} = V_{VDW} + V_{Coulomb} .$$

Lennard-Jones

By far the most common potential used to represent both the van der Waals attractive and Pauli repulsive forces is the Lennard-Jones (12-6) potential:

$$V_{LJ}(r_{ij}) = 4\varepsilon_{ij}\left[\left(\frac{\sigma_{ij}}{r_{ij}}\right)^{12} - \left(\frac{\sigma_{ij}}{r_{ij}}\right)^{6}\right],$$

where ε_{ij} is the well depth, effectively the maximum Lennard-Jones energy, which depends on the nature of the interacting atom and σ_{ij} is the zero point of the potential between a site of type i and a site of type j; if the interacting atoms are of the same nature, then this is also their atomic diameter. When the atoms become closer than $2^{1/6}\sigma_{ij}$, their electronic clouds superimpose and a Pauli repulsion force becomes significant. Fig. 9 shows the Lennard-Jones forces between two atoms of similar nature. Whilst the Lennard-Jones potential is a pairwise potential, it is often parameterised against experimental data, in order to implicitly include many-body effects [100]. The Lennard-Jones potential is often truncated at a distance of $2.5\sigma_{ij}$ in order to reduce computational time, at this point the energy from the potential is essentially zero (see Fig. 9).

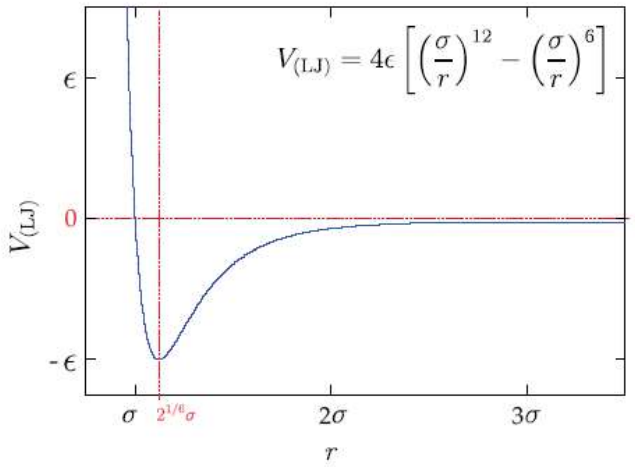

Figure 9. General Lennard-Jones curve for potential energy between two similar atoms.

For the interaction of two different types of atoms, for example hydrogen and carbon atoms, unlike interactions ε_{ij} and σ_{ij} can be calculated using mathematical mixing rules, which combine the

individual interaction parameters for the individual atoms. Many force-fields utilise geometric mean mixing rules, as shown below:

$$\varepsilon_{ij} = (\varepsilon_{ii}\,\varepsilon_{jj})^{1/2}\,,$$

$$\sigma_{ij} = (\sigma_{ii}\,\sigma_{jj})^{1/2}\,.$$

Other force-fields utilise the Lorentz-Berthelot combining rules [222,223], in which the geometric mean mixing is still used for ε_{ij}, but the arithmetic mean is used to calculate σ_{ij} as shown below:

$$\sigma_{ij} = (\sigma_{ii} + \sigma_{jj})/2\,.$$

Whilst deficiencies have been highlighted with these simple mixing rules for certain systems [224], they are generally sufficient for calculating unlike interactions.

Alternatives to Lennard-Jones

In some force-fields, the Lennard-Jones potential is simplified to the Buckingham (exp-6) potential, in which the repulsive part is exponential, it then takes the form:

$$V_{Buck}(r_{ij}) = Ae^{-\frac{r_{ij}}{\rho}} - \frac{C}{{r_{ij}}^6}\,,$$

where r_{ij} is the distance between interaction centres, A is a pre-exponential factor, ρ is an ionic-pair dependent length parameter, which governs the repulsive part of the potential, and C is a constant for the attractive part of the potential. A potential drawback of the Buckingham potential is that, because the exponential term converges to a constant as r→0 while the r-6 term diverges, the potential 'turns-over' as r becomes very small. This can be problematic when dealing with systems with very short interatomic distances, particularly charged systems, as the nuclei that cross the turn-over will become strongly (and unphysically) bound to one another at a distance of zero. The Buckingham potential is rarely used in modern force-fields, but older examples such as those developed by Tobias, Tu and Klein (TTK-AA) [225], have been shown to be effective in condensed phase simulations of alkanes.

Other alternatives to the popular 12-6 potential include various forms of the general Mie potential [226]. This is of the form:

$$V_{Mie}(r_{ij}) = C\varepsilon\left[\left(\frac{\sigma}{r}\right)^{\gamma_{rep}} - \left(\frac{\sigma}{r}\right)^{\gamma_{att}}\right]$$

where C is a function which depends on the repulsive, γ_{rep}, and attractive, γ_{rep}, exponents of the potential, and is given by:

$$C = \left(\frac{\gamma_{rep}}{\gamma_{rep} - \gamma_{att}}\right)\left(\frac{\gamma_{rep}}{\gamma_{att}}\right)^{\left(\frac{\gamma_{att}}{\gamma_{rep}-\gamma_{att}}\right)}$$

For 12-6 exponents, C is equal to 4, and hence the formula is the same as the standard Lennard-Jones potential. An alternative parameterisation is the 16-6 potential for alkanes described in ref. [227]. Here, γ_{att} = 6 and γ_{rep} = 16 and hence C = 2.388.

Coulombic Potential

If charged species are present in the system, or bonds in a molecule are polar, due to differences in electronegativity, a potential is also required to model the electrostatic interactions. The electrostatic interaction energies between atoms in polar molecules with partial charges are usually calculated using a long-range Coulombic potential:

$$V_{Coulomb} = \frac{q_i q_j}{4\pi\varepsilon_r r_{ij}},$$

where q_i and q_j are the partial atomic charges for atoms i and j separated by a distance r_{ij}. The relative dielectric constant, ε_r is usually set to one, to match the conditions for which the parameters were obtained. Coulomb interactions decay by 1/r, as opposed to 6/r for Lennard-Jones attractions, so the forces often extend beyond one simulation cell. Coulomb forces are therefore usually calculated using long range solvers such as the Ewald summation [228]. This is a technique to sum the long-range interactions between particles and all their infinite periodic images with reasonable efficiency. Luty et al. [70] offered a more efficient Fourier transform-based approach to the Ewald sum by, extending the particle-particle, particle-mesh method (PPPM or P^3M) developed by Hockney and Eastwood [229].

Partial charges arising from polar bonds can be defined in several different ways, depending on the choice of force-field. In standard non-polarizable force-fields, point charges are used which remain constant irrespective of their environment. This can be a significant over-simplification, for example when molecules are placed into a high dielectric medium such as water [230]. However, for most situations, through careful parameterisation of the force-fields to reproduce the liquid densities, the point charge model provides a reasonable representation of the forces between polar molecules.

Polarizable force-fields for the types of molecules of interest to this study have been developed [231], but they are much more computationally demanding, and are less transferable to other molecules than standard non-polarizable force-fields. Moreover, in this project, the medium for most of the simulation experiments is low dielectric alkanes, making polarisation effects less important. Hence, in this study, only non-polarizable force-fields are employed.

The definition of partial charges is another point of difference between force-fields. In the AMBER family of force-fields [232], partial charges are calculated individually for each atom depending on their environment within the molecule [233]. Conversely, in the OPLS family of force-fields [234], partial charges, like Lennard-Jones parameters, are treated as tuneable parameters and are assigned to each atom type.

Intermolecular Scaling

In most force-fields, non-bonded interactions between atoms in the same molecule separated by one bond (1-2) or two bonds (1-3) are ignored. Non-bonded interaction between atoms separated by three bonds (1-4) are usually buffered using scaling factors, in order to more accurately reproduce experimental properties (see Fig 10). In OPLS [234], the 1-4 intramolecular scaling factor is set to 0.5 for both Lennard-Jones and electrostatic interactions. In AMBER [232], the 1-4 intramolecular scaling factor is set to 0.5 for Lennard-Jones and 0.8333 for electrostatic interactions. Conversely, CHARMM [235] and GROMOS [236] include specific 1-4 intramolecular parameters for different combinations of atom types rather than using general scaling factors. Some UA force-fields, such as TraPPE [237],

completely exclude 1-4 Lennard-Jones interactions (i.e. Lennard-Jones scaling factor set to 0.0) and adjust their 1-4 dihedral parameters accordingly [238]. For polar molecules, TraPPE uses a electrostatic scaling factor of 0.5 [239].

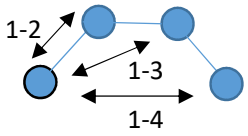

Figure 10. Schematic showing the 1-2, 1-3 and 1-4 interactions in a molecule

3.1.3. Bonded Interactions

In classical MD simulations, molecules are usually modelled as flexible chains, held together with harmonic springs. All modern force-fields include terms for, bond stretching, angle bending and torsion as shown in Fig. 11, with some also including cross-terms.

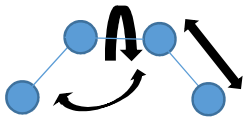

Figure 11. Schematic showing the bonded interactions in Class I force-fields

Bond Stretching and Angle Bending

Covalent bond stretching and angle bending are usually modelled with simple harmonic spring potentials:

$$V_{stretch} = \sum_{bonds} K_r (r - r_0)^2 ,$$
$$V_{bend} = \sum_{angles} K_\theta (\theta - \theta_0)^2 ,$$

where (r–r_0) and (θ–θ_0) represent the deviation from the equilibrium bond length and angle respectively. Note that for the bond and angle potentials shown, the ½ factor from Hooke's law is included in the K values, as with the original OPLS style [234].

The quantum mechanical nature of bond vibration makes the classical harmonic description used in most force-fields somewhat questionable. A more realistic description of a covalent bond at higher

stretching can be provided by the more computationally expensive Morse potential. The Morse potential energy function takes the form:

$$V_{Morse} = D(1 - e^{-\alpha(r_{ij}-r_0)})^2 ,$$

where r_{ij} is the distance between the atoms, r_0 is the equilibrium bond distance, D is the well depth (defined relative to the dissociated atoms), and α is a stiffness parameter which controls the width of the potential (the smaller α is, the larger the well). Given that bond stretching has little influence on most thermodynamic and transport properties, the additional computational expense of the Morse potential is not usually justified. Moreover, more parameters need to be collected in order to use the Morse potential, making it less extendable than the standard harmonic bond potential.

In the CHARMM force-field [235], there is an additional 1-3 term, known as the Urey–Bradley potential, which is outlined in ref. [240]. The purpose of this term is to account for steric interactions between atoms bonded to the same central atom. In most other force-fields, this effect is captured by the parameterisation for the angle potential, rather than using a separate potential.

Angle Torsion

A dihedral angle can be defined as the angle that occurs between two planes, defined by four atoms. Proper dihedrals consist of four atoms, joined linearly through bonds, these are included in all force-fields. In some force-fields, such as CHARMM [235], separate potentials for 'improper dihedrals' may also be added, to enforce the planarity of aromatic rings and other conjugated systems and to prevent molecules from flipping over to their mirror images. Other force-fields, such as OPLS [234] and AMBER [235], use a V_2 (or n = 2) term to describe improper torsions, rather than a separate potential [241].

Dihedrals can be represented with one of the following three potentials described below [54].

The Ryckaert-Bellemans (RB) potential function is a power expansion of cosines, and takes the form [242]:

$$V_{torsion}(RB) = C_0 + C_1[cos\,\phi] + C_2[cos^2(\phi)] + C_3[cos^3(\phi)] ,$$

where ϕ is the dihedral angle and Cn is the RB dihedral parameter. The related OPLS dihedral function is given as the first three or four cosine terms of a Fourier series [243]:

$$V_{torsion}(OPLS) = \frac{1}{2}V_1[1 + cos\ \phi] + \frac{1}{2}V_2[1 - cos(2\ \phi)] + \frac{1}{2}V_3[1 + cos(3\ \phi)] .$$

Trigonometric transformations give a rigorous equivalence between the 'C' and 'V' parameters from the equations above, as described in the GROMACS manual [236]. Many force-fields, such as AMBER [232] and CHARMM [235] use periodic dihedral forms:

$$V_{torsion}(AMBER) = \frac{1}{2}Vn[1 + (cos\ n\ \phi - \gamma)] ,$$

where n is the multiplicity and γ is the phase angle for torsional angle parameters. Periodic dihedral parameters can also be readily converted into the RB or OPLS forms. AMBER dihedral parameters are less specific than OPLS, and generally parameters depend only on the two central atoms (e.g. X-C-C-X), rather than all four (e.g. H-C-C-C).

3.1.4. Force-Field Complexity

For all computational simulation methods, it is necessary to make trade-offs between the accuracy and computational time required. In MD simulations of tribological systems, this is most probably evident when choosing the level of detail with which to simulate the individual molecules. In MD, there are three main methods with which to model the structure of alkane molecules: all-atom (AA), united-atom (UA) or coarse-grained (CG). AA representations explicitly model every atom in the molecule, including non-polar hydrogen atoms. In the UA representation, methyl (CH_3) and methylene (CH_2) segments are treated as single 'pseudo-atoms', with their interaction sites generally located at the centre of the carbon atoms. CG involves further simplification by combining several neighbouring atoms into larger 'beads' [244]. The main advantage of simpler UA models over AA models is their computational efficiency. Whilst CG methods further improvement in terms of efficiency, they are not considered in this study because, although they can be used to capture the key physics of bulk systems,

higher level of details are expected to be required to accurately represent, for example, friction and flow behaviour in confinement.

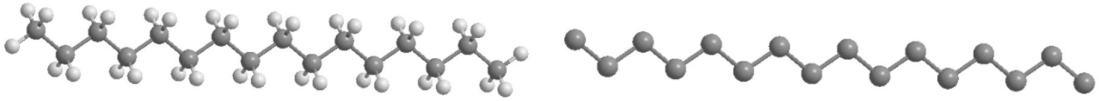

Figure 12. Snapshots of n-hexadecane molecules using All-Atom (AA) and United-Atom (UA) models.

Using *n*-hexadecane ($C_{16}H_{34}$) as an example, by using a UA force-field as opposed to an AA force-field, the number of interaction sites falls from 50 atoms to only 16 'pseudo-atoms', corresponding to the CH_2 and CH_3 units (Fig. 12). Non-bonded interactions dominate the computational time, so reducing the number of interaction sites almost by a factor of three can give savings approaching an order of magnitude [237]. This has made them very popular in tribology where the simulation of large, multicomponent systems is often required.

Currently, it is largely unclear which force-fields will yield the most accurate results in the of context tribology. Probably the most significant liquid properties in the simulation of tribological systems are the density and viscosity, since they are inherently linked to the lubricant hydrodynamics. In an MD force-field, the liquid density is mainly governed by the non-bonded (Lennard-Jones and Coulombic) interactions, whilst the viscosity is also heavily influenced by the 'stiffness' of the torsional potential [245,246]. Previous studies have compared AA and UA force-field performance in terms of their density and viscosity prediction of long-chain alkanes [246–248]; however, they have been limited to only a few variants, and have not included recent parameterizations specifically designed for long-chain molecules [26,249]. These previous comparisons have shown that UA force-fields consistently under-predict the viscosity of long-chain linear alkanes, with the prediction accuracy deteriorating when longer chain molecules or high pressures are used [246–248]. For example, under ambient conditions, UA force-fields have been shown to provide a reasonable prediction for the viscosity of C_{10} (≈ 20%); however, prediction accuracy decreases considerably for longer C_{16} molecules (≈ 50%) [248].

Although improvements to the prediction of transport properties by UA force-fields have been made by using modified forms of non-bonded interaction (other than Lennard-Jones), such changes can often have a detrimental effect on the thermodynamic properties for which the force-fields were originally parameterized [250]. It has also been shown that many popular all-atom force-fields yield a much higher melting point for long-chain alkanes than the experimental value, which in turn leads to drastically elevated density and viscosity values [26,249]. This may be critical in simulations of confined systems, where intricate phase transitions can heavily influence the tribological behaviour observed [130]. In summary, viscosity and melting point under- and over-prediction respectively will both considerably impact the simulated behaviour of long-chain molecules, which are of particular importance in tribology. Indeed, the results of several previous MD simulations of dense, multicomponent systems have suggested that the use of accurate all-atom force-fields is critical in obtaining accurate structure and friction results [130,251–254].

The following section involves the benchmarking of many popular force-fields, including recent parameterizations for long-chain molecules, in terms of their ability to predict the density and viscosity of n-hexadecane in equilibrium molecular dynamics (EMD) simulations. These properties are significant since they govern the hydrodynamics of lubricants and directly influence their tribological behaviour.

3.2. Methodology

All systems were constructed using the Materials and Processes Simulations (MAPS) platform from Scienomics SARL (Paris, France) and MD simulations were performed in LAMMPS [255]. The MD equations of motion were integrated using the velocity-Verlet algorithm with an integration time-step of 1.0 fs for all of the force-fields. Fast-moving bonds involving hydrogen atoms were constrained with the SHAKE algorithm [256].

3.2.1. Simulation Setup

In this section, many classical force-fields are benchmarked in terms of their density and viscosity prediction of n-hexadecane. The Newtonian shear viscosity is calculated using the Green-Kubo formula [37,38] applied to classical EMD simulations. Since the Green-Kubo equations allow a direct route to the Newtonian shear viscosity, it is probably the most suitable method to benchmark the considerable number of force-fields used here. Issues regarding slow convergence of the running average viscosity [257] and the potential for systems to become trapped in local minima [248] have been encountered when using this method for long-chain molecules. However, by monitoring the ensemble average viscosity over multiple-trajectories, as suggested by Payal et al. [248], and utilized here, the impact of both of these problems can be minimized. The selection of n-hexadecane as a model lubricant is justified by its extensive use in experimental and modelling tribology studies, as well as the fact that its density and viscosity are well-characterized under a range of experimental conditions. The conditions simulated in this section range between ambient (300 K, 0.1 MPa) and HTHP (423 K, 60.8 MPa; 423 K, 202.7 MPa) conditions [15], which are of direct relevance to tribological systems.

The force-fields selected for the benchmarking simulations are those developed by: Chynoweth and Michopoulos (CM-UA) [258], Nath et al. (NERD-UA) [259], Schuler et al. (GROMOS-UA) [260], Martin et al. (TraPPE-UA, 12-6) [237], Potoff and Kamath (TraPPE-UA, 16-6) [227], Mayo et al. (Dreiding-AA) [261], Cornell et al. AMBER-AA [232], Jorgensen et al. (OPLS-AA) [234], Murzyn et al. (P-OPLS-AA) [249] and Siu et al. (L-OPLS-AA) [26]. The overall functional form of these classical force-fields are quite similar (Equation (1)), with all including terms for bond stretching, bending and torsion (bonded), as well as van der Waals and Coulombic interactions (non-bonded). However, each contains unique force-field parameters and many have different forms of non-bonded and torsional potentials, non-bonded mixing rules, 1-4 non-bonded scaling factors and some utilize Coulombic parameters for alkyl C and H atoms whilst others do not.

$$V_{Total} = V_{Bond} + V_{Angle} + V_{Torsion} + V_{VDW} + V_{Coulomb}$$

A box of 130 n-hexadecane molecules was generated and periodic boundary conditions were applied in all directions (Fig. 13). The cut-off radius for Lennard-Jones interactions was fixed at 2.5σ (≈13 Å). Long-range tail corrections to the energy and pressure were included [262]. 'Unlike' interactions were evaluated using the either the Lorentz—Berthelot or geometric mean mixing rules, depending on the force-field. Long-range electrostatic interactions were not cut off, but were evaluated using the PPPM method [70] with a relative accuracy in the forces of 1 x 10^{-5}. The Nosé–Hoover thermostat and barostat [56,57,263], with relaxation constants of 0.1 and 1.0 ps, respectively, were employed to maintain the desired temperature and pressure.

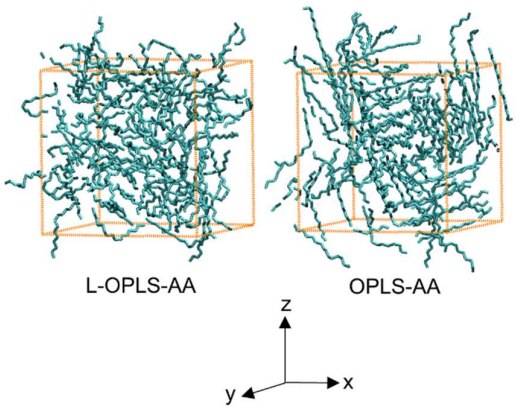

Figure 13. Equilibrated systems after 2.0 ns NPT phase (300 K, 0.1 MPa) when using OPLS (liquid) and L-OPLS (crystallized). Chain C atoms are cyan, non-polar hydrogen atoms are not shown for clarity. Periodic boundary conditions (orange dotted line) applied in all directions. Rendered using VMD [264].

3.2.2. Simulation Procedure

First, the system was energy minimised before being equilibrated in the isothermal-isobaric (NPT) ensemble until there was only negligible change in the density (2.0-10.0 ns). The densities shown in Fig. 14 were obtained from averages of the volumes of the simulation boxes during the final 1.0 ns of these NPT simulations. The simulation box volume was then fixed in order to match the average density and the system was equilibrated in the canonical ensemble (NVT) for a period of 2.0 ns. From this equilibrated system, five independent trajectories were produced through separate heat-quench

cycles. For the 300 K and 0.1 MPa simulations, the first part of the cycle consisted of 1.0 ns NVT simulations at T = 305, 310, 315, 320 and 325 K, after which the systems were quenched back to 300 K during another 1.0 ns NVT simulation. The viscosity was then calculated from subsequent 3.0 ns NVT production runs, starting from the five independent trajectories. The Newtonian viscosity was evaluated using the Green-Kubo [37,38] formula:

$$\eta(\tau) = \frac{V}{k_B T} \int_0^\infty d\tau \langle P_{\alpha\beta}(t_0) P_{\alpha\beta}(t + t_0) \rangle_{t_0} \quad \text{(Equation 1)}$$

where $\langle P_{\alpha\beta}(t_0) P_{\alpha\beta}(t + t_0) \rangle$ is the stress autocorrelation function (ACF) for the off-diagonal components of the stress tensor $P_{\alpha\beta}$, with α and β representing the *x, y,* or *z* direction in Cartesian coordinates. The running integral of the stress ACF yields the Newtonian shear viscosity (Equation 1). V is the volume of the simulation box, k_B is the Boltzmann constant, T is the temperature. For practical reasons, the upper limit in numerical calculations of the integral is set to a certain time, t_{max}, which is sufficiently long to ensure the noise-free decay of ACF, which is calculated for a limited number of consecutive time origins, t_0 [249]. Generally, t_{max} should be long enough in order to ensure convergence of the viscosity by exceeding the rotational relaxation time of the molecule [257]. In calculations of the shear viscosity, the running integrals of autocorrelation function equation 1 were evaluated for time origins, t_0, spaced by 250 ps with the off-diagonal components of the stress tensor sampled every 10 fs, and t_{max} set to 3 ns [249]. Fig. 14 shows the change in the running average of the shear viscosity with simulation time for a representative example (TraPPE-UA force-field at 423 K and 600 atm). The t_{max} and number of independent trajectories used are sufficient in order to obtain a steady state value for the average shear viscosity for all of the conditions and force-fields studied.

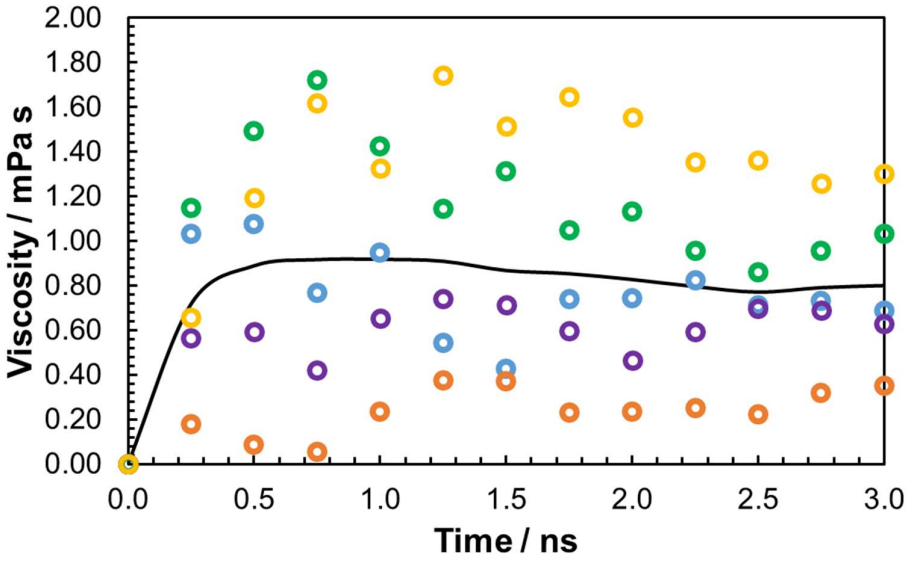

Figure 14. Variation in the running average of the shear viscosity with time for five independent trajectories, black curve shows their average. Representative example shown for TraPPE-UA force-field at 423 K and 600 atm.

It should be noted that the rotational relaxation time, required integration time and ultimately the simulation length, increases by more than an order of magnitude with a relatively modest increase in chain-length (C_{10} to C_{16}) [257]. Therefore, it is suggested that other, less direct routes to the Newtonian viscosity, such as NEMD [265] or R-NEMD [79], are used for chain-lengths greater than C_{16}. However, for n-hexadecane, the ensemble average Green-Kubo approach employed here allows sampling of a large configurational space and represents a relatively fast, accurate route to the Newtonian viscosity [248].

3.3. Results and Discussion

3.3.1. Density Prediction

Fig. 15 shows that the density prediction for n-hexadecane was generally accurate (within 15% of experiment) for all of the force-fields and conditions tested. However, there were some important differences between the performances of the force-fields under ambient and HTHP conditions.

Dreiding-AA was designed as a 'generic' force-field and it was rather inaccurate in the density prediction of n-hexadecane, yielding a consistent under-prediction of approximately 5% under all of the conditions simulated. The initial parameterisations of the popular all-atom force-fields OPLS-AA and AMBER-AA over-predicted the density by 14% and 11% respectively at ambient conditions. This density over-prediction has been observed in previous simulations of long chain alkanes using these force-fields at ambient conditions and has been attributed to crystallisation due to the over-prediction of the melting point (Fig. 13) [26,72,249]. Crystallisation did not occur at 423 K and 60.8 MPa, and both OPLS-AA and AMBER-AA under-predicted the density by around 4%. AMBER-AA also under-predicted the density by around 4% at 423 K and 202.7 MPa, whereas OPLS-AA over-predicted the density by 7%, again suggesting crystallisation. No crystallisation was observed when using P-OPLS-AA, and the density prediction under ambient conditions was significantly improved; however, a similar under-prediction of density at HTHP conditions was observed. L-OPLS-AA also suppressed crystallisation and was much more accurate (within 5%) than the other all-atom force-fields in terms of density prediction under all of the conditions simulated.

The density prediction of united-atom force-fields was generally more accurate, and all of the force-fields were within 5% of experiment under all of the conditions simulated. This is probably the result of a more comprehensive choice of molecules during parametrisation, including long-chain alkanes (up to C_{32}) [237]. The 16-6 form of TraPPE-UA was found to be less accurate in terms of density prediction relative to the conventional 12-6 form.

In summary, density prediction is significantly overestimated when using the original parameterisations of some all-atom force-fields (OPLS-AA, AMBER-AA), which will significantly affect the behaviour of long-chain alkanes in simulations. Other than these force-fields, density prediction is relatively accurate, and the small variations are unlikely to have a significant effect on simulation results.

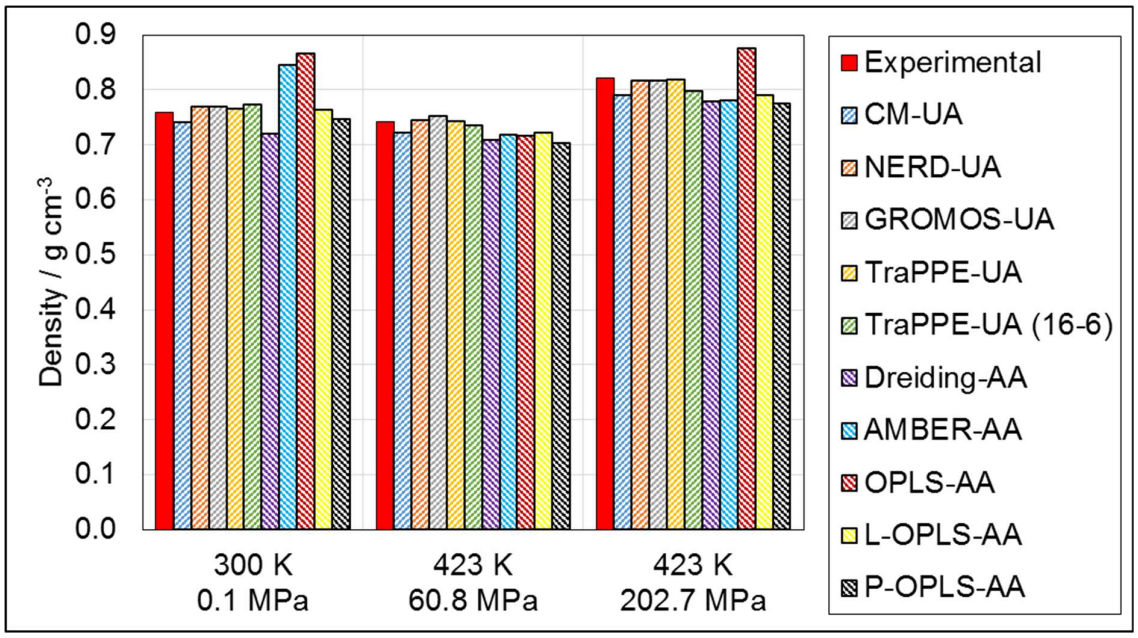

Figure 15. Simulated density (NPT) for n-hexadecane at; (a) 300 K, 0.1 MPa, (b) 423 K, 60.8 MPa, (c) 423 K, 202.7 MPa. United-atom (UA) force-fields represented by forward dashes, all-atom (AA) force-fields represented by backwards dashes. Experimental data are reproduced with permission from ref [248].

3.3.2. Viscosity Prediction

Fig. 16 shows that viscosity prediction was much less accurate for all of the force-fields tested. This is expected since, unlike the density, the transport properties are not usually directly parameterised in classical force-fields.

Given its relatively poor density prediction accuracy, the viscosity prediction of Dreiding-AA was surprisingly accurate, although it over-predicted viscosity by around 40% at 423 K and 60.8 MPa. OPLS-AA and AMBER-AA performed very poorly under ambient conditions, over-predicting the viscosity by more than two orders of magnitude, which can again be attributed to the crystallisation of n-hexadecane (Fig. 13) [26,72,249]. AMBER-AA performed rather better under HTHP conditions; however, OPLS-AA still yielded severe viscosity over-prediction at 423 K and 202.7 MPa. The updated P-OPLS-AA [249] and L-OPLS-AA [26] include modified non-bonded (Lennard-Jones and coulombic) and torsion parameters specifically to improve melting point prediction for long-chain molecules. As a result, P-OPLS-AA accurately predicts the viscosity under ambient conditions and at 423 K and 60.2

MPa; however, at 423 K and 202.7 MPa, the viscosity is under-predicted by approximately 30%. Conversely, L-OPLS-AA accurately reproduces experimental viscosities (within 15%) under all of the conditions simulated. From the density and viscosity results, it is clear that L-OPLS-AA is the most accurate all-atom force-field with which to reproduce the density, viscosity and thus the hydrodynamics of the model base oil n-hexadecane; and so it is taken forward to the AA/UA comparisons for NEMD simulations of tribological systems in the second section.

Viscosity prediction with the UA force-fields was generally rather inaccurate and they yielded a consistent under-prediction of between 10-60% depending on the conditions. Viscosity prediction was particularly poor at 423 K and 202.7 MPa, where the density is highest and the 'roughness' of individual molecules is likely to have a greater impact on the viscosity. The viscosity prediction of TraPPE-UA under ambient conditions was significantly improved through the use of a 16-6 non-bonded potential (-10% vs -30%). However, the viscosity was still significantly under-predicted (-35%) at 423 K and 202.7 MPa. This suggests that whilst the physical presence of hydrogens may not be essential in accurately predicting the viscosity of long-chain alkanes accurately under ambient conditions, at high pressures, where molecules are forced closer together, the steric clashes between hydrogen atoms on different molecules become indispensable to achieving accurate viscosity prediction. The 16-6 form for the van der Waals interactions improves the viscosity prediction of TraPPE-UA under ambient conditions; however, the different functional form of the non-bonded interactions makes it less compatible with other atom types such as those in functional groups or surfaces, and a similar under-prediction is observed under HTHP conditions. Therefore, the next best performing force-field, TraPPE-UA, was selected for the AA/UA comparisons in the second section.

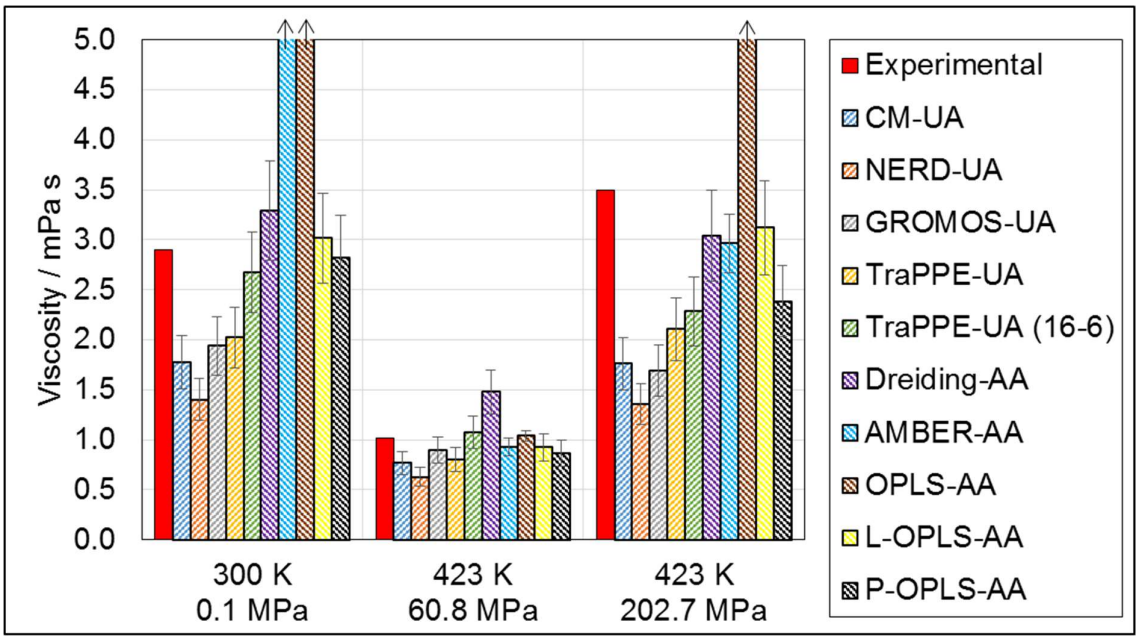

Figure 16. Simulated viscosity (NVT) for n-hexadecane at; (a) 300 K, 0.1 MPa, (b) 423 K, 60.8 MPa, (c) 423 K, 202.7 MPa. United-atom (UA) force-fields represented by forward dashes, all-atom (AA) force-fields represented by backwards dashes. Experimental data are reproduced with permission from ref [248]. Error bars show the standard deviation in the ensemble average viscosity between the five independent trajectories. Simulated viscosity bars are truncated and marked with an arrow when viscosity increased by over two orders of magnitude compared to experiment due to crystallisation.

Generally, the density and viscosity prediction of the force-fields deteriorates only slightly moving from ambient to HTHP conditions. Fig. 15 and Fig. 16 show that there is a tendency for force-fields to under-predict both density and viscosity under HTHP conditions, a factor which could be investigated further in the pursuit of force-fields specifically for HTHP simulations of long-chain molecules.

Viscosity over-prediction by the original parameterisations of popular all-atom force-fields (OPLS-AA, AMBER-AA) under ambient and HTHP conditions will have a substantial impact on the behaviour of long-chain alkanes, and they should therefore be avoided in future simulations. The viscosity under-prediction by all of the UA force-fields under ambient and HTHP conditions may also have a significant effect on simulation results. For example, in confined liquids, the friction coefficient depends greatly on the ability of individual molecules, molecular layers and solid surfaces to slide past one another

[266]. The significant under-prediction of the viscosity by UA force-fields suggests that molecules move past one another more easily than if all-atom force-fields are used, meaning that friction coefficients calculated for confined systems using UA force-fields will also be under-predicted; this effect will be explored in chapter 5.

3.4. Summary

In order to be confident that behaviour observed in NEMD simulations is representative of real dynamical systems, the selection of an accurate force-field is essential. In this study, a wide range of popular force-fields have been benchmarked for their density and viscosity prediction of n-hexadecane under ambient and HTHP conditions.

Significant issues with many popular force-fields were highlighted for the simulation of long-chain, linear alkanes. These were evident to a similar degree under both ambient and HTHP conditions. Specifically, all of the united-atom force-fields under-predicted the viscosity, and the original parameterisations of all-atom force-fields resulted in an elevated melting point for n-hexadecane, leading to anomalous density and viscosity values. Both of these problems are expected to significantly affect the behaviour in confined NEMD simulations. The most accurate force-field under the conditions tested was L-OPLS-AA, which was specifically parameterised for long-chain linear hydrocarbons.

Chapter 4. Simulations of Organic Friction Modifiers Adsorbed on Iron Oxide Surfaces

The work described in this chapter has been published in *Langmuir* (ref. [267]).

4.1. Introduction

Organic friction modifiers (OFMs) are important additives, added to reduce friction and wear particularly in the boundary lubrication regime (see section 2.5.1.). Many different amphiphiles have been tested as OFMs, and there are three main structural variables: (i) the nature of the headgroup, (ii) the length of the hydrocarbon tail, and (iii) the structure of the hydrocarbon tail, whether straight or branched and whether saturated or unsaturated [11]. Early OFMs contained carboxylic acid headgroups; however, these were soon found to cause high levels of corrosion for some bearing metals, and they were gradually replaced in most applications by less corrosive amphiphiles such as amines, amides, esters, or chelating combinations of such groups [11]. Nonetheless, most experimental and simulation tribology studies have utilised OFMs with carboxylic acid headgroups. There have been far fewer studies of the more commercially relevant amine, amide, or glyceride OFMs. Boundary friction experiments have shown that amide and glyceride OFMs can yield lower friction coefficients than their acid counterparts [188], though the reasons for this were yet to be established prior to this current study.

With respect to tailgroup selection, commercial OFMs generally utilize unbranched aliphatic tailgroups containing 12−20 carbon atoms as a result of their effective friction reduction, high base oil solubility, and availability from natural fats and oils [11]. These natural fats and oils contain mixtures of molecules with saturated as well as mono and polyunsaturated tailgroups which are generally used collectively rather than being separated into individual tailgroup types [11]. The most widely studied components in the literature are saturated C18 chains (stearyl) and monounsaturated C_{18} chains with an unsaturated Z-alkene at the C_9 position (oleyl) [11]. Boundary friction experiments at equal concentration showed that OFMs with saturated tails, such as stearic acid and glycerol monostearate,

gave low friction coefficients which increased linearly with log(sliding velocity) [188]. Conversely, OFMs with Z-unsaturated tails, such as oleic acid and glycerol monooleate, yielded significantly higher friction coefficients that remained relatively constant with sliding velocity [188]. One aspect of this current study is to establish whether these observations are due to differences in the nanoscale structure of the film or simply arise from a lower surface coverage at a given concentration as a result of the "kinks" from the Z-alkene in the middle of the tailgroup.

In order to understand how the head and tailgroups influence the performance of OFMs, it is necessary to obtain a clear picture of (i) the structure of the OFM film and its modification of the interface between the polar metal oxide surface and the hydrocarbon lubricant and (ii) the effect that this has on the friction coefficient. Detailed structural information on OFM films at the surface–lubricant interface can be obtained from experimental techniques such as sum frequency spectroscopy (SFS) [268], polarized neutron reflectometry (PNR) [175], the surface force apparatus (SFA) [173], and *in situ* atomic force microscopy (AFM) [174,269]. These methods can be used to monitor monolayer formation and gather information such as the OFM film thickness and tilt angle. The friction behaviour of OFM films can also be investigated using AFM [174,269] and SFA [173] as well as macroscopic boundary friction experiments [188]. These tests employ low sliding velocities (mm s^{-1}) and high pressures (GPa) in order to minimize lubricant entrainment and thus maintain boundary lubrication conditions. Classical molecular dynamics simulations can be used to simultaneously probe the nanoscale structure and friction of OFM films, as summarised in section 2.5.1.

The aim of this chapter is to use NEMD simulations to shed light on the nanoscale structure of OFM films adsorbed on iron oxide surfaces and separated by a thin layer of hexadecane to calculate the friction coefficient as a function of coverage and sliding velocity and to fully explore links between the structure and friction. A wide range of OFMs are explored in order to better understand the influence of headgroup type and tailgroup Z-unsaturation on structure and friction. In addition, the use of OFM

films with a wide range of coverages, including close to the theoretical limit, should indicate the significance of the formation of close-packed monolayer films in the reduction of boundary friction. The velocity dependence of the friction coefficient for different OFMs and coverages will also be analysed and compared to boundary friction experiments.

The structure of the remainder of this section will now be outlined. First, the general system setup for all of the simulations is introduced, followed by the specific methodology for the preliminary squeeze-out and compression and sliding simulations. This is followed by the results of the preliminary squeeze-out simulations and finally the structure and friction results from the compression and sliding simulations are discussed in detail.

4.2. Methodology

4.2.1. System Setup

A representative example of the systems simulated in this study is shown in Fig. 17-a. It consists of a thin layer of hexadecane lubricant confined between two OFM monolayers adsorbed on iron oxide slabs. All structures were constructed using the Materials and Processes Simulations (MAPS) platform from Scienomics SARL. Three different OFM headgroups (carboxylic acid, amide, and glyceride) and two different tailgroups (stearyl and oleyl) are considered in these simulations. Acid OFMs were selected to allow comparison to previous experiments and simulations, whereas amide and glyceride OFMs are more commercially relevant [11]. Specifically, NEMD simulations were used to compare the structure and friction of stearic acid (SA), oleic acid (OA), stearic amide (SAm), oleamide (OAm), glycerol monostearate (GMS), and glycerol monooleate (GMO) films over a range of surface coverages and sliding velocities (Fig. 17-b). Hexadecane was chosen as a model lubricant because its properties are well-defined, and it is commonly employed in both experimental [174,188,269] and modelling [185,189] tribology studies. Given that charge separation is unfavourable in the low-polarity hexadecane solvent, all OFM molecules were assumed to be in their electronically neutral form.

Classical MD simulations were performed using LAMMPS [255]. In all of the MD simulations, (100) slabs of α-iron(III) oxide (hematite) [270] with dimensions (xyz) of approximately 55 × 55 × 12 Å were used as the substrates, representing a single asperity contact. Periodic boundary conditions were applied in the x and y directions. Care was taken to cleave the surface in a manner such that the Fe/O ratio remained at 2:3 in order to ensure that surfaces with no overall charge were produced. OFM molecules were oriented perpendicular to, and initially 3 Å from, the interior surfaces of two such slabs (Fig. 17-a). This produced OFM films similar to those formed by the Langmuir−Blodgett experimental procedure, e.g., ref [176]. Hexadecane molecules were then randomly distributed between the OFM films.

If one assumes a monodentate binding mode for the glycerides, then the limiting headgroup area for all of the OFMs is around 22 $Å^2$ [170]. The surface coverage or packing density can be quantified as the number of headgroups per area of surface, Γ. A high surface coverage (Γ = 4.32 nm^{-2}), close to the maximum theoretical value [170], is simulated by adsorbing 132 OFM molecules on each 3000 $Å^2$ slab to form a close-packed monolayer. Two other surface coverages are considered: a medium coverage (Γ = 2.88 nm^{-2}), which is approximately two-thirds of the maximum coverage, and a low coverage (Γ = 1.44 nm^{-2}), which is around one-third of the maximum coverage. The high-coverage simulation has been achieved experimentally on steel surfaces for acids and amides [170] but has not been reported for glycerides. However, previous MD simulations [20] as well as experimental results at the air−water interface [271] suggest that the high coverage employed should also be possible for glycerides. In tribology experiments, the OFM concentration in the lubricant is generally used rather than surface coverage because it is far easier to measure and control. Adsorption and PNR experiments of stearic and oleic acid [175] suggest that only stearic acid can form high coverage films, whereas oleic acid can only form low coverage films due to steric effects from the kink in its tail group.

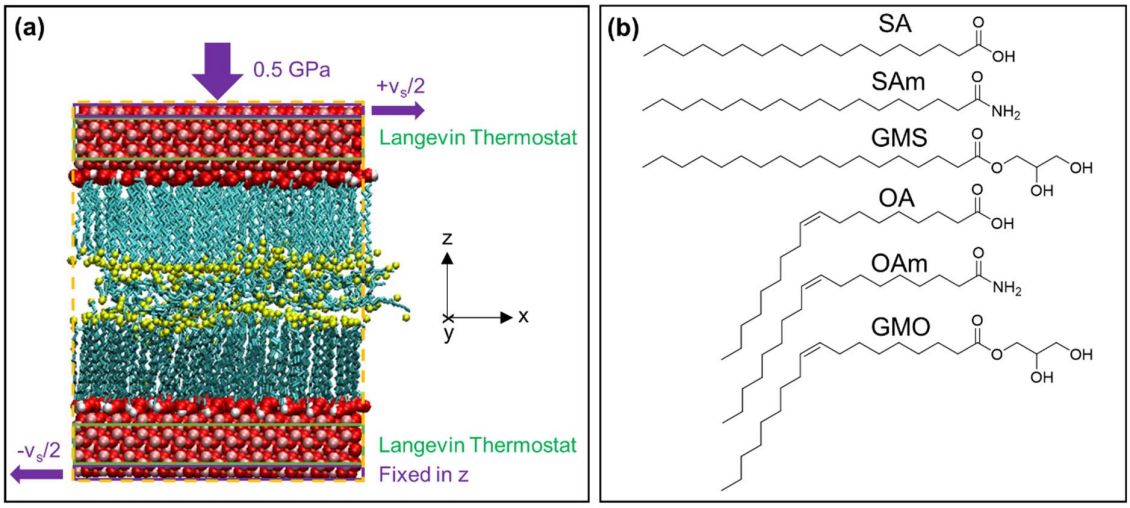

Figure 17. Simulation details: setup for compression and sliding simulations (a). Example shown for SA at high coverage after compression, before sliding. Headgroups are shown with O in red and H in white, terminal C in yellow, and the other tailgroup C in cyan. Hydrogen atoms in the tailgroups are omitted for clarity. In the slab, Fe atoms are shown in pink. Periodic boundary conditions (yellow dotted line) are applied in the x and y directions. Rendered using VMD [264]. Chemical structures of OFMs simulated in this study (b): stearic acid (SA), stearic amide (SAm), glycerol monostearate (GMS), oleic acid (OA), oleamide (OAm), and glycerol monooleate (GMO).

A combination of several updated versions of the OPLS all-atom force field [234] were used to represent both hexadecane and the OFM molecules; full details can be found in Appendix A. The OPLS family of forcefields was chosen for three main reasons: (i) the inclusion specific parameters for all of the functional groups required [234,272], (ii) the all-atom representation that is expected to be critical in accurately modelling friction in this system [220] (for quantitative comparisons see Chapter 6), and (iii) recent parametrizations available which allow far more accurate representations of long-chain hydrocarbons [26]. The final point is critical because the original OPLS parametrization has been shown to misrepresent the liquid−solid phase behaviour of long-chain alkanes [26,249], an issue which would certainly impact the behaviour observed in these simulations. Lennard-Jones interactions were cut off at 10 Å, and “unlike” interactions were evaluated using the geometric mean mixing rules, as prescribed in the OPLS force field [234]. Electrostatic interactions were not cut off but rather evaluated

using a slab implementation [273] of the PPPM algorithm [70] with a relative accuracy in the forces of 1×10^{-5}.

Surface−lubricant and surface−OFM interactions were represented by the Lennard-Jones and Coulomb potentials; the hematite surface parameters selected were developed by Berro et al. [169], which are outlined in Appendix A. The hematite slab atoms were restrained in the corundum crystal by harmonic bonds between atoms within 3 Å. The force constant of these bonds was chosen to be 130 kcal mol^{-1} $Å^{-2}$, which has been shown previously to keep the surface structure suitably rigid but not to adversely affect the thermostatting [169].

The MD equations of motion were integrated using the velocity Verlet algorithm with an integration time step of 1.0 fs. Fast-moving bonds involving hydrogen atoms were constrained with the SHAKE algorithm [256]. The Langevin thermostat [55], with a time relaxation constant of 0.1 ps, was used in all of the simulations in order to maintain a temperature, T = 300 K. The pressure (Pz = 0.5 GPa) was controlled by applying a constant normal force to the outermost layer of atoms in the upper slab, keeping the z coordinates of the outermost layer of atoms in the lower slab fixed, as previously proposed [68,187] (Fig. 17-a).

4.2.2. Squeeze-out Simulations

To estimate the thickness of the central hexadecane film under the applied pressure, preliminary squeeze-out simulations were performed prior to the compression and sliding simulations. Previous simulations [274,275] and AFM experiments [276] of hydrocarbon squeeze-out between solid surfaces showed that there was a significant energy barrier to overcome when squeezing out each molecular layer. The size of this barrier increased when longer chains with a higher viscosity were used and also increased progressively when fewer molecular layers remained in the contact [274–276]. Hence, a relatively large pressure was required to squeeze out the last few molecular layers of fluid. From these previous results, it was expected that an equilibrium thickness of between 1 and 3 molecular layers of hexadecane would remain in the contact under the simulation conditions (P_z = 0.5 GPa, T = 300 K).

Starting from the system described above, 50 Å of vacuum was added in the x and y directions to allow hexadecane molecules to be squeezed out of the contact, and the strongly adsorbed OFM molecules remained on the surface. Periodic boundary conditions were maintained outside of this extended system. At this stage, the thermostat was applied to the entire system. Hexadecane molecules (200) were randomly distributed between the OFM-covered slabs, corresponding to roughly 5 molecular layers for this contact area (~3000 $Å^2$). The slabs were moved closer together by applying a velocity (10 m s^{-1}) to the top slab until the density of the OFM and hexadecane region was similar to that of liquid hexadecane (0.75 g cm^{-3}) and the system was then energy-minimized. Pressure (Pz = 0.5 GPa) was then applied until the average slab separation reached equilibrium, after approximately 250 ps (Fig. 18). The number of hexadecane molecules remaining in the contact was estimated by dividing the number of hexadecane carbon atoms between the slabs by 16. This residual number of hexadecane molecules was used for the following compression and sliding simulations. The addition of vacuum to the edge of the system may mean that so-called finite-size effects [277] influence the residual number of hexadecane molecules. Therefore, squeeze-out simulations were also conducted with system sizes two and four times as large as those used in the compression and sliding simulations to ensure consistency. Indeed, the squeeze-out data presented in the results and discussion section scaled well with system size, with the same number of hexadecane layers remaining inside the contact in the larger systems (see Appendix A).

4.2.3. Compression and Sliding Simulations

The compression and sliding simulations used systems containing a residual number of hexadecane molecules from the squeeze-out simulations, with the same three coverages of OFM molecules as outlined previously but with the vacuum in the x and y directions removed. A density similar to that of liquid hexadecane (0.75 g cm^{-3}) was reached by moving the top slab down at 10 m s^{-1} prior to energy minimization. The system was then pressurized (P_z = 0.5 GPa), thermostatted in directions perpendicular to the compression (x and y), and allowed to equilibrate at 300 K. Initially, the slab separation varied in a damped harmonic manner, so sliding was not applied until a constant average

slab separation was obtained and the hydrostatic pressure within the hexadecane film was close to its target value [169]. These compression simulations were generally around 200 ps in duration. During the compression stage, there was a collective tilting of the OFM molecules toward the surface in a random direction. The sliding direction (x) was chosen to be perpendicular to the orientation of this initial tilt (y). Previous NEMD simulations of self-assembled monolayers in intimate contact, with the tilt orientated parallel to the sliding direction (x), have shown high friction and stick−slip behaviour due to the high commensurability of the interface [185,201]. However, the presence of a thin, separating layer of hexadecane in previous NEMD simulations has been shown to maintain low friction [185]. Hence, the consistently low friction observed in boundary friction experiments [188] is expected to be reproduced in these simulations due to the presence of the hexadecane layer between the OFM films. Additional simulations with the sliding direction completely aligned with the initial tilt were also conducted to confirm that the initial orientation of the tilt did not influence the friction results obtained.

After compressive oscillation became negligible, a velocity of $v_x = \pm v_s/2$ was added in the x direction to the outermost layer of atoms in each slab (Fig. 17-a), and sliding simulations were conducted for 0.5−10 ns, depending on the sliding velocity, vs. The values of vs applied were 1, 2, 5, 10, and 20 m s^{-1}, and all simulations were run for long enough to yield a sufficient sliding distance (10 nm) to obtain representative values for the friction coefficients (uncertainty <10%). Although lower sliding velocities are desirable to match those used in boundary friction experiments (typically mm s^{-1}), they are not yet accessible using all-atom NEMD simulations on this scale [187]. During the sliding simulations, any heat generated was dissipated using a thermostat acting only on the middle 10 Å of both iron oxide slabs (Fig. 17-a), applied in the direction perpendicular to the both the sliding and compression (y) [92]. This is known to be advantageous over direct thermostatting of the fluid, which has been shown to significantly affect the behaviour of confined fluids under sliding conditions [65]. The boundary thermostatting method applied here has been shown previously to be effective in controlling the temperature of similar systems and sliding velocities [278]. At the onset of sliding, an expansion due

to the increase in temperature by shear heating was expected, so it was ensured that steady-state sliding had been attained before sampling for the friction coefficient began [169]. The time taken to achieve steady-state sliding decreased with increasing sliding velocity but always equated to approximately 2 nm of sliding distance.

The kinetic friction coefficient, μ, was obtained using the extended Amontons−Coulomb law under the high load approximation [187]: $F_L/F_N = F_0/F_N + \mu \simeq \mu$. F_L and F_N are respectively the average total lateral and normal forces acting on each slab, and F_0 is the load-independent Derjaguin offset representing adhesive surface forces. The validity of this approximation was confirmed for two test cases (SA and GMO) by ensuring that a linear fit of F_L as a function of F_N gave an insignificant value of F_0 and the same result for μ within the statistical uncertainty. An insignificant value of F_0 was expected from previous simulations, which included a thin layer of lubricant confined between the monolayers [185]. In general, the assumption of $\mu \simeq F_L/F_N$ is appropriate for systems with low adhesion (small F_0) or under high applied loads (large F_N) [279]; both of these are applicable to these simulations.

4.3. Results and Discussion

The results are presented as follows. Results of the preliminary squeeze-out simulations are outlined first. This is followed by a detailed analysis of the structure of the film at different coverages under sliding conditions. The friction results at different coverages and sliding velocities are then described and linked to the structural variations in the films. In what follows, some properties are expressed as functions of the distance from the surface, denoted by z; this is taken as the distance from the innermost layer of atoms on the bottom slab.

4.3.1. Squeeze-out Simulations

Simulations to establish the appropriate thickness of a boundary film of hexadecane under high pressure (P_z = 0.5 GPa) were performed first. The variation of the overall slab separation and of the number of confined hexadecane molecules from the beginning of the simulation is shown for a representative OFM (SA) in Fig. 18. As expected, the slab separation distance (Fig. 18-a) decreases

asymptotically to reach an equilibrium value [275]. Changes in gradient due to layer−layer transitions [275] are most easily observed at low coverage, where the deformation of the OFM film has a less significant effect on the change in slab separation than at medium and high coverage. The equilibrium slab separation decreases from 30 Å at high coverage to 20 Å at low coverage. All of the OFM films deform considerably, leading to significantly thinner equilibrium slab separations than those in subsequent compression and sliding simulations, where no vacuum is present in the x or y direction.

Fig. 18-b shows how the number of hexadecane molecules inside the contact volume decreases with time. Before 25 ps, there is little change in this value as the OFM film is compressed, but after this point, the number of molecules decreases asymptotically as expected [275]. The number of hexadecane molecules stabilizes at around 70 at all coverages, which corresponds to approximately two horizontally oriented molecular layers. Thus, these simulations suggest that the equilibrium number of hexadecane molecules remaining inside the contact volume is essentially independent of OFM coverage. This two-layer limit agrees well with extrapolations from previous squeeze-out simulations for C3−C14 hydrocarbons between gold surfaces [274] as well as experimental AFM data for hexadecane between graphite surfaces, which suggest that the 2 → 1 layer transition occurs only above 0.6 GPa [276]. These results did not vary significantly between the different types of OFMs, so the subsequent compression and sliding simulations were based on systems containing 70 hexadecane lubricant molecules (2 molecular layers) for all types and coverages of OFM.

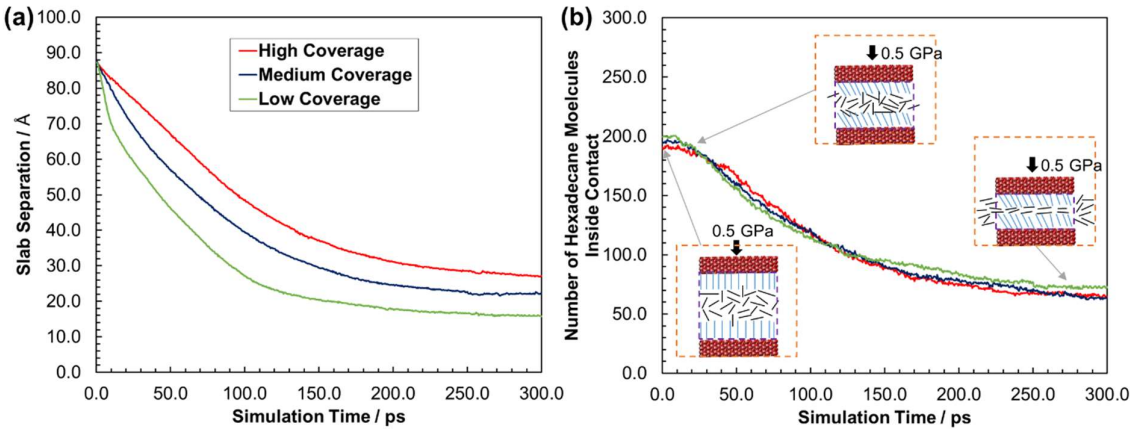

Figure 18. Results of squeeze-out simulations for representative OFM (SA) at different coverages: variation in the slab separation (a) and the number of hexadecane molecules within the contact volume (b), over 300 ps, Pz = 0.5 GPa. Inset schematics in (b) show the structure of the initial system, followed by compression of the OFM film and the squeeze out of hexadecane. Blue lines represent OFM molecules, and black lines represent hexadecane. The orange dotted line shows periodic boundaries, and the purple dotted line shows the contact volume.

4.3.2. Structure

Classical MD simulations of the OFM−hexadecane system under sliding conditions can yield important information regarding both the atomistic structure of the confined films and their friction behaviour. Fig. 19 shows simulation snapshots for a representative OFM (SA) at low, medium, and high surface coverages after 500 ps of sliding at 10 m s^{-1}.

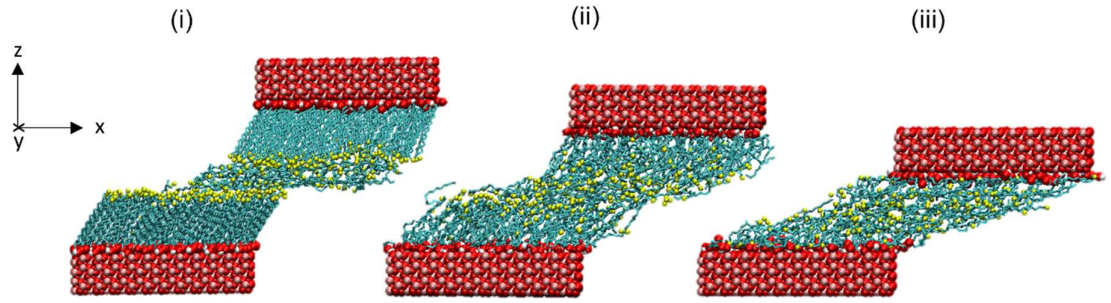

Figure 19. Simulation snapshots of representative OFM (SA) after 500 ps of sliding at high coverage (i), medium coverage (ii), and low coverage (iii), with P_z = 0.5 GPa and vs = 10 m s^{-1}. Oxygen atoms are shown in red; headgroup hydrogen atoms, in white; terminal carbon atoms, in yellow; the other tailgroup carbon atoms, in cyan; and iron atoms, in pink. Hydrogen atoms in the tailgroups are omitted for clarity. Periodic images and boundaries are not shown. Rendered using VMD [264].

The structure of the confined films has been studied under sliding conditions (v_s = 10 m s^{-1}) by analysing their atomic mass density profile, atomic position probability profile, radial distribution function, hydrogen-bonding network, velocity profile, and centre of mass and tilt angle. In general, the structure of the films remains very similar after the compression phase and during the sliding phase (see Appendix A), which is consistent with previous NEMD simulations [184,187,189]. However, the film structure changes significantly with OFM coverage and to a much lesser extent between different headgroups and tailgroups.

The overall thickness and layering of the system in the z direction and the interdigitation of the OFM and hexadecane layers can be observed through mass density profiles, ρ(z) (Fig. 20), and atom position probability profiles, p(z) (Fig. 21). Data are shown for the saturated and unsaturated acids (SA and OA) and glycerides (GMS and GMO); amides (SAm and OAm) are an intermediate case between the two other headgroups, so data for them are shown in Appendix A.

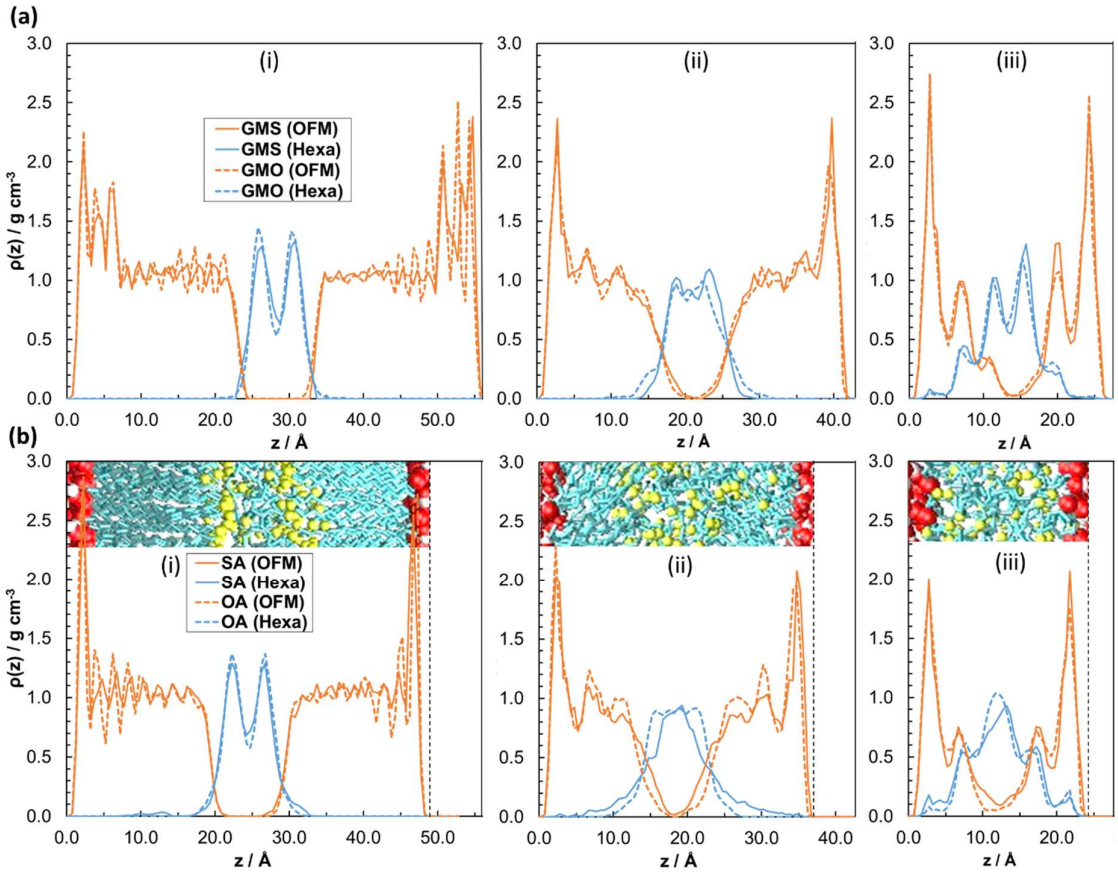

Figure 20. Atomic mass density profiles in z, ρ(z), of OFM (orange) and hexadecane (blue) for (a) glyceride (GMS and GMO) and (b) carboxylic acid (SA and OA) headgroups with stearyl (solid) and oleyl (dotted) tailgroups at high (i), medium (ii), and low (iii) coverages. The vertical black dotted line in (b) shows the position of the top slab. Image overlay shows a section of the SA OFM film at corresponding coverages to help illustrate the interdigitation.

Sharp, intense peaks on the far-left and right-hand sides of Fig. 20 indicate the adsorption of OFM headgroups on the surface, and the less intense peaks which extend further from the surface are due to the tailgroups. The OFM films become substantially thicker and more structured with increasing coverage. At high coverage (Γ = 4.32 nm^{-2}), the slabs are separated by approximately 50−55 Å, with up to 10 small peaks which indicate layering of the tailgroup carbon atoms. Comparing profiles from OFMs with stearyl (solid) and oleyl (dotted) tailgroups, it is clear that the presence of Z unsaturation does not significantly alter either the peak positions or the slab separations. The high-coverage slab separations agree well with SFA experimental observations, which found that SA films on opposing mica surfaces in hexadecane (46−54 Å) were of similar thickness to those formed by OA (50−55 Å)

when an elevated concentration of OA was used [173]. At medium coverage (Γ = 2.88 nm^{-2}), the slabs are separated by approximately 40 Å and the OFM tailgroups show much less layering. At low coverage (Γ = 1.44 nm^{-2}), the slabs are separated by just 25 Å and the OFM displays only two clear peaks: a large peak at the surface incorporating both the headgroup and tailgroup atoms close to the surface and a smaller peak which extends to approximately 5 Å from the surface. The slab separation is greater for glycerides (Fig. 20-a) than for acids (Fig. 20-b) and amides as a result of the larger headgroup size, with the greatest difference being at high coverage (5 Å).

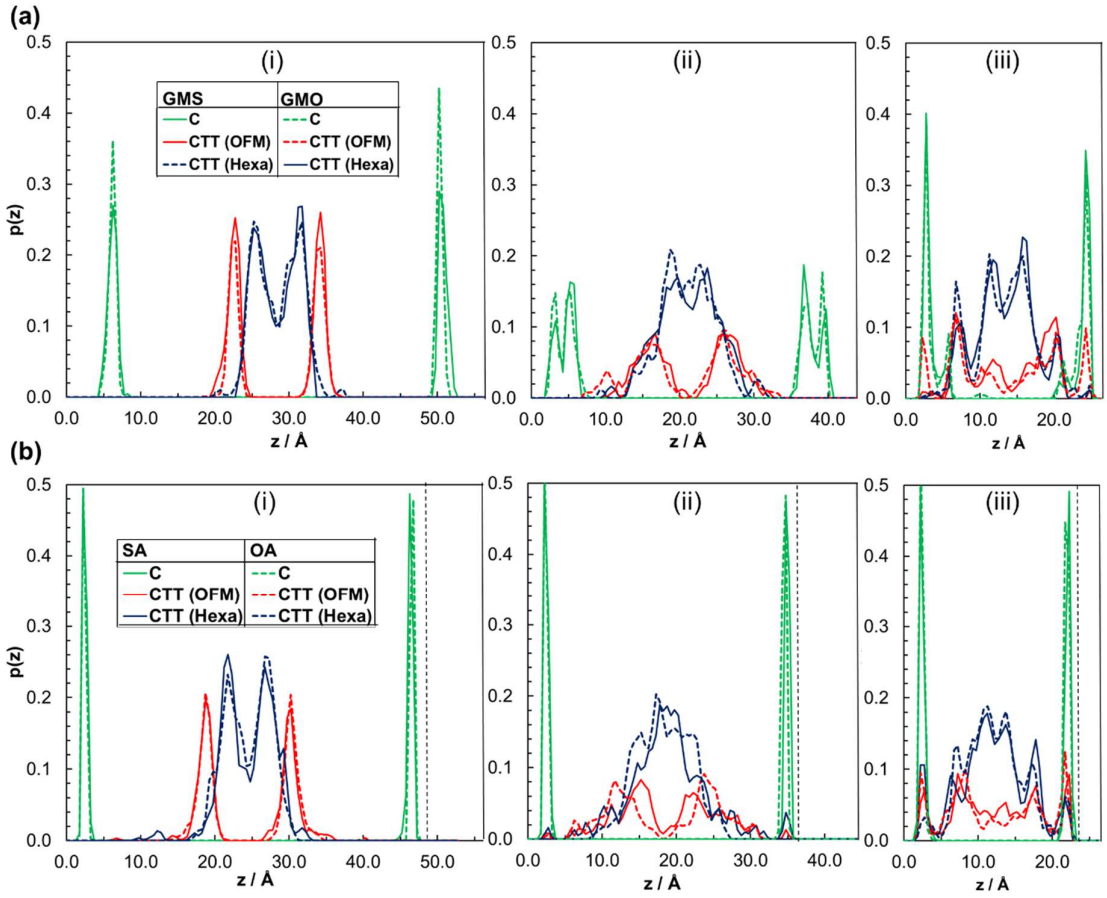

Figure 21. Atomic position probability profiles in z, p(z), for carbonyl C (green), hexadecane terminal CTT (blue), and OFM terminal CTT (red) atoms in GMS and GMO (a) and SA and OA (b) at high (i), medium (ii), and low (iii) coverages. The black dotted line in (b) shows the position of the top slab.

The height of the individual OFM films can be estimated by measuring the distance of the terminal carbon in the OFM tail, CTT, from the surface, as shown in Fig. 21. At high surface coverage, glyceride film heights are approximately 21 Å (Fig. 21-a-i), whereas for acids (Fig. 21-b-i) and amides they are closer to 19 Å, which agrees well with experimentally measured film thicknesses from *in situ* AFM experiments [174]. At medium coverage, the average position of the OFM CTT peak is broader and shifted slightly closer to the surface (approximately 12 Å). At low surface coverage, there are two sharper OFM CTT peaks just 2 and 7 Å from the surface. The intense carbonyl, C, peaks close to the surface in Fig. 21 indicate that the headgroup positions are also localized in z. At low coverage, the C peaks are only 2 Å from the surface for all of the OFMs. For glyceride OFMs (Fig. 21-a), this suggests that most headgroups are bound in a bidentate mode, with both alcohol groups bound to the surface. At medium coverage, the glyceride C profiles are significantly different from those for acids and amides, with a second peak of equal intensity appearing 5 Å from the surface. This suggests that, at medium coverage, around half of the molecules are bound in a bidentate mode with the C atoms close to the surface and half are bound in a monodentate mode with C atoms further from the surface. For high-coverage glyceride films, there is only a peak at 5 Å, suggesting that all molecules are now bound in a monodentate mode. The C peaks for acids (Fig. 21-b) and amides are generally far sharper than for glycerides (Fig. 21-a) due to the closer proximity of the C atoms to the surface.

Fig. 20 and Fig. 21 also reveal important information regarding the level of interdigitation of the OFM films and the hexadecane lubricant, which is indicated by the penetration of the hexadecane profile into the OFM profile. The amount of penetration is influenced significantly by both the coverage and the headgroup type. For all of the OFMs tested, at high coverage two distinct hexadecane peaks form which correspond to well-separated layers. In Fig. 20 and Fig. 21, the outer limits of the hexadecane peaks extend only to around 1 Å into the OFM peaks for glycerides (a-i), which increases to 3 Å for acids (b-i), indicating more interdigitation for the latter. At medium coverage, there is less layering of the lubricant, with only one broad hexadecane peak, the outer limits of which extend much further into the OFM film: 5 Å for glycerides (a-ii) and 10 Å for acids (b-ii). At low coverage, there is even more

penetration of the hexadecane and OFM profiles, with a nonzero value for the OFMs in the center of the film, indicating that films on opposing slabs are directly interdigitated. In fact, at low coverage the hexadecane and OFM peaks directly overlap, suggesting that they form mixed layers which are likely to behave similarly to thin films of pure hexadecane [266]. The glyceride profiles at low coverage (a-iii) contain a larger number of better defined peaks than those for acids (b-iii) and amides (six vs five), suggesting more numerous well-separated layers.

The ordering within the OFM films was examined further by calculating separate radial distribution functions (RDFs), g(r), for the headgroup carbon (C) and the terminal carbon (CTT). In Fig. 22, the C RDFs are shifted upward by 10 units for clarity.

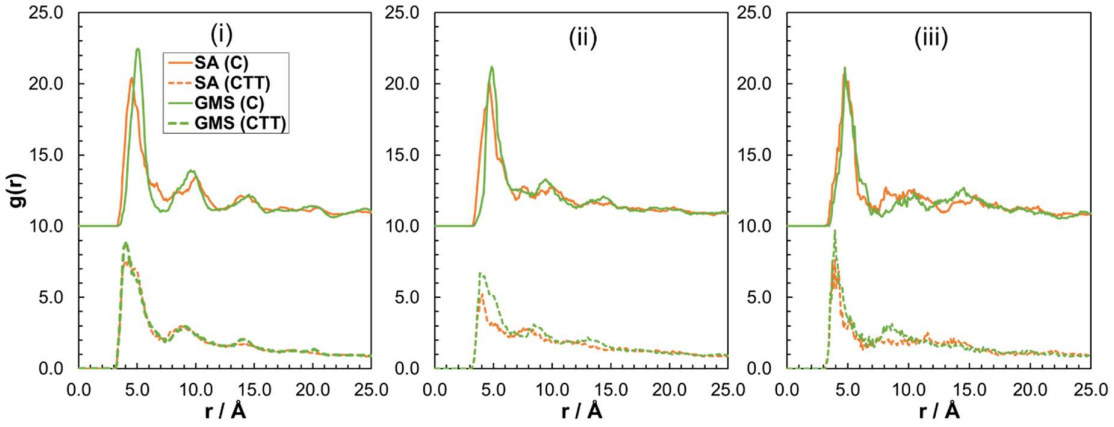

Figure 22. Radial distribution function (RDF) describing the ordering of the terminal CTT (dotted) and carbonyl C (solid) atoms for SA (orange) and GMS (green) at high (i), medium (ii), and low (iii) coverages. The C RDFs are shifted upward by 10 units for clarity.

In Fig. 22, the carbonyl carbon, C, shows long-range order for all OFMs and coverages, with the major peaks occurring at multiples of r = 5 Å. This corresponds to the unit-cell dimension of the hematite surface [270], confirming that the surface structure dictates the headgroup packing in the OFM films [187]. Although the C peak at 5 Å is of similar intensity at all coverages, at high coverage, there are sharper peaks at 10, 15, and 20 Å, indicating increased long-range ordering and more solid-like films. At all coverages, the terminal CTT peaks are at least 25% less intense than the carbonyl C peaks,

suggesting that the tailgroup positions are less ordered. However, at high coverage, there are still identifiable CTT peaks at 10, 15, and 20 Å, suggesting that the films remain solid-like at the interface between the OFM film and the hexadecane lubricant. At medium coverage, all of the CTT peaks are less sharp and intense than at high coverage, suggesting that the film is more amorphous with less correlation between the carbonyl and terminal carbon positions. At low coverage, the CTT peak at 5 Å is more intense than at medium coverage because the terminal carbon atoms are close enough to the surface such that it influences their packing. Overall, there appears to be a correlation between the intensity and long-range order of C and CTT peaks, suggesting that more ordered headgroup atoms can lead to more ordered tailgroup atoms. The peaks for GMS (Fig. 22-a) are generally sharper and more intense than those for SA (Fig. 22-b) at all coverages, suggesting that the former yields more ordered, solid-like films. OFMs with amide headgroups represent an intermediate case between acid and glyceride headgroups.

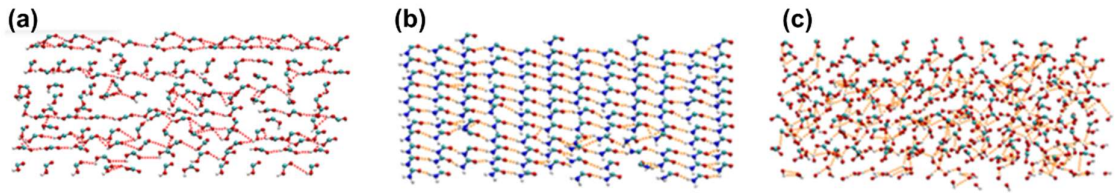

Figure 23. Snapshots of hydrogen bonding between OFM headgroups at high coverage 500 ps into a sliding simulation: SA (a), SAm (b), and GMS (c). Headgroups: oxygen shown in red; hydrogen, in white; nitrogen, in blue; and carbon, in cyan. Tailgroups are omitted for clarity, and hydrogen bonds [280] are shown in orange.

The differences in the phase of and level of interdigitation between films formed from different OFM headgroups are postulated to be due to variations in the hydrogen-bonded networks, which are shown for the high-coverage case in Fig. 23. These networks were analysed in VMD [264] using standard criteria for hydrogen bonding [280], i.e., a bond length cut-off of 3.9 Å and an angle cut-off of 90°. Intermolecular hydrogen bonding between the headgroups appears to have an effect on the structure of the OFM-lubricant interface, through inducing a more solid-like film in glycerides than in

acids. Amide OFMs are an intermediate case between acid and glyceride OFMs. Indeed, excluding those formed between the OFM and the surface, high-coverage GMS films contain approximately three intermolecular hydrogen bonds per molecule: SAm, two such bonds per molecule; and SA, one per molecule. The presence of unsaturation in the tailgroup has no effect on acid or amide OFMs; however, GMO forms only approximately two hydrogen bonds per molecule, perhaps explaining the greater levels of interdigitation in its films compared to those in GMS.

To understand flow within the confined films during sliding, velocity profiles, $v_x(z)$, for a representative OFM (SA) are shown in Fig. 24. Velocity profiles are overlaid onto mass density profiles, $\rho(z)$, and a snapshot of the system in order to aid the interpretation of the results. Atom velocities are computed for 0.5 Å spatial bins which are averaged over 100 ps time blocks during the sliding phase. The velocity profiles at all coverages show that there is no slip at the surface, as expected for the strongly absorbed OFM headgroups. The OFM tailgroups move at a similar velocity as the slab to which they are absorbed (± 5 m s^{-1}) until the region where they become interdigitated with the hexadecane lubricant. For SA at high coverage (i), these interfaces are at approximately 20 and 28 Å, at which points the gradient increases as the interface is sheared. At 22 and 26 Å, there is a flattening of the velocity profile, corresponding to the two hexadecane peaks in the mass density profile, with another increase in the velocity gradient at 24 Å between the two hexadecane layers. This suggests that these two hexadecane layers move as 'plugs' between the OFM films, with three separate slip planes, i.e., at the OFM−hexadecane interfaces as well as between the two hexadecane layers. At medium coverage (ii), the slip plane becomes more difficult to define, and there appears to be significant shearing within the portion of the OFM tailgroup which is interdigitated with hexadecane. The velocity profile passes through zero at the centre of the hexadecane layer, with a shallower gradient than at high coverage. The low-coverage velocity profile (iii) is more typical of conventional planar Couette flow, with a nearly linear velocity profile of the liquid between the slabs. However, the velocity profile still contains steps which indicate partial plug flow between combined OFM−hexadecane layers. Such stepped velocity

profiles have also been observed in previous NEMD simulations of pure hexadecane films of similar thickness [266].

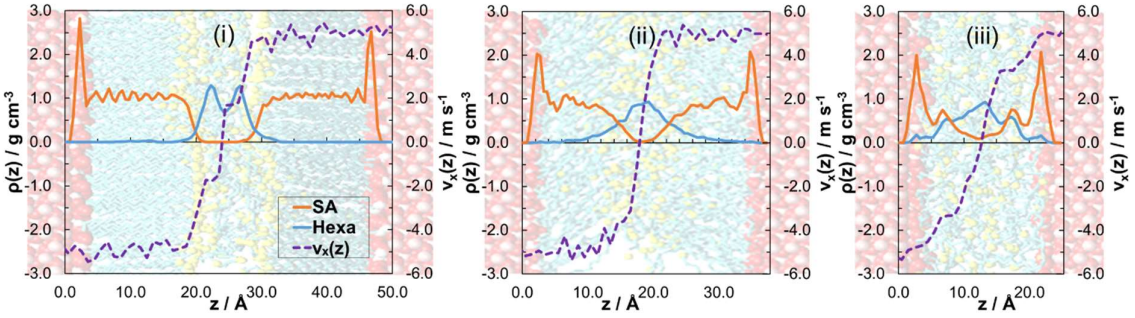

Figure 24. Profile of atom x velocities from 0.5 Å spatial bins in z, vx(z), overlaid on the mass density profile, ρ(z), and a snapshot of representative OFM system (SA) at high (i), medium (ii), and low (iii) coverage. Pz = 0.5 GPa and vs = 10 m s^{-1}.

The extension and orientation of the OFM films during sliding are further analyzed by calculating the average center of mass with respect to the z-coordinate, zCoM (Fig. 25-a) and also the tilt angle, θ, defined as the angle between a vector from the carbonyl C atom to the carbon atom halfway up the chain (C9) and the surface normal (Fig. 25-b).

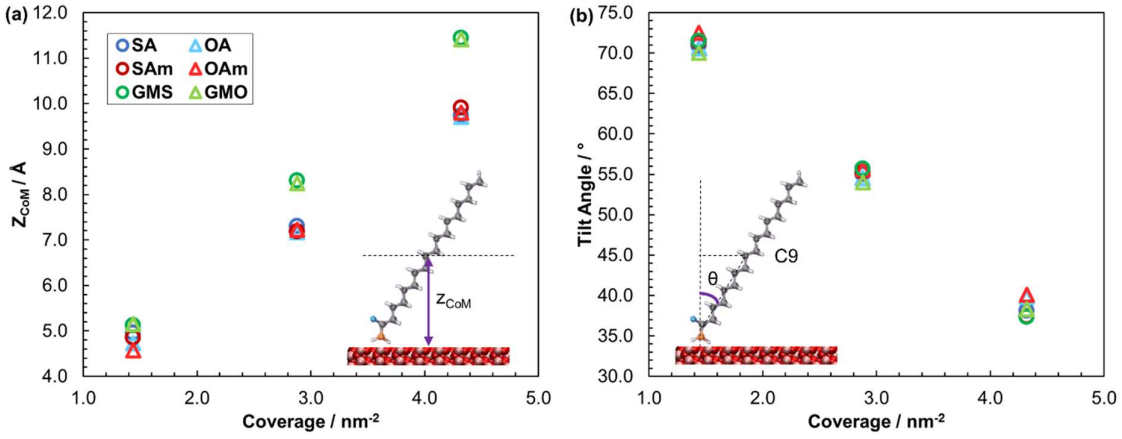

Figure 25. OFM film extension and orientation: average z_{CoM} of OFMs as a function of coverage (a), average C1–9 tilt angle as a function of coverage under sliding conditions (b), P_z = 0.5 GPa, v_s = 10 m s^{-1}. Error bars not shown as within the symbol size. Circles represent OFMs with saturated tailgroups; triangles represent OFMs with tailgroup Z-unsaturation.

At low coverage, zCoM ≈ 5 Å and θ ≈ 70°, indicating that most molecules are lying almost flat on the surface. zCoM increases linearly with coverage, at two different gradients depending on the headgroup. For acid (SA and OA) and amide (SAm and OAm) headgroups, zCoM reaches a maximum of approximately 10 Å at high coverage, and for glyceride headgroups, the maximum is 11.5 Å as a result of the larger headgroup size. This means that, for the same tailgroup, glyceride OFMs yield slightly thicker films than acids or amides. OFMs with saturated and Z-unsaturated tailgroups have similar zCoM values, though saturated films are very slightly more extended (<0.2 Å). The tilt angle, θ, decreases linearly with coverage at the same rate for all of the OFMs, to approximately 55° at medium coverage and 40° at high coverage. The high-coverage value agrees reasonably well with tilt angles estimated from in situ AFM experiments, around 50° for SA [174] and stearyl amine [269] monolayers. Possible explanations for the 10° higher tilt angle in the experiments relative to these simulations include the fact that a higher pressure (1.6 GPa) was used in the experiments or that the experiments obtained a lower coverage than the highest used in these simulations. It is worth noting that both of these simulations and the in situ AFM experiments yield a significantly larger tilt than that observed in PNR experiments of stearyl amine on iron oxide surfaces under ambient conditions (θ ≈ 22°) [190] because of additional tilting under compression. In these simulations, θ appears to be independent of headgroup and tailgroup type, suggesting that once the molecules are subjected to high pressure (0.5 GPa), all of the molecules pack in a similar fashion regardless of headgroup type or tailgroup Z-unsaturation. This view is supported by previous high-pressure (0.3 GPa) simulations of close-packed alkanethiol monolayers on gold surfaces [201] which yielded a similar tilt angle (θ ≈ 35°); the slightly lower tilt angle can be rationalized through the lower applied pressure.

The fact that θ remains similar moving from compression to sliding conditions indicates that this angle is determined solely by the film response in supporting the applied pressure, whereas the applied sliding simply rotates the preferred tilt orientation toward the sliding direction. The partial alignment of the molecular tilt with the sliding direction does not have a significant effect on the friction coefficient, the 100 ps block average of which remains relatively constant throughout the course of

the sampling period for all of the OFMs and coverages simulated (see Appendix A). Indeed, a simulation with the initial tilt aligned parallel to the sliding direction ($\Phi \approx 0°$) yielded a friction coefficient within the statistical uncertainty of that when the initial tilt was perpendicular to the sliding direction. Previous NEMD simulations of direct monolayer−monolayer [201] and monolayer−surface [281] systems showed an increase and decrease in friction, respectively, when the tilt was aligned with the sliding direction. The fact that friction appears to be independent of the orientation of the tilt angle in these NEMD simulations suggests that a thin lubricant layer between the OFM films is critical to maintain a consistently low friction coefficient on atomically-smooth surfaces [185].

4.3.3. Friction

The influence of surface coverage on the friction coefficient was probed at a sliding velocity, v_s = 10 m s^{-1} and a pressure, P_z = 0.5 GPa for acids, amides, and glycerides (Fig. 26-a). The variation in the friction coefficient with sliding velocity was also examined for acids and glycerides at a pressure P_z = 0.5 GPa (Fig. 26-b). The results indicate that the friction coefficient varies significantly with OFM coverage, headgroup type, and sliding velocity. Fig. 26-a shows that for all OFMs considered, at 10 m s^{-1}, the friction coefficient at high coverage is around 30% lower than at medium coverage and approximately 25% less than at low coverage. On the basis of the structural information gathered at different coverages, this reduction in friction can be attributed to the formation of clear slip planes between the OFM films and the hexadecane lubricant, as observed through density (Fig. 20), probability (Fig. 21), and velocity profiles (Fig. 24) as well as simulation snapshots (Fig. 19). These slip planes are facilitated through the close-packing of the OFM tailgroups, which leads to a solid-like, coherent monolayer film which allows very little interdigitation with the hexadecane lubricant or with each another. Indeed, large decreases in friction have also been observed for close-packed monolayers relative to loose-packed monolayers in previous NEMD simulations [180,282] and AFM experiments [283,284], supporting the postulate that the formation of close-packed monolayers is important for the effective friction reduction of OFMs [188].

The performance of the OFMs with respect to friction reduction is as follows: OA ≈ SA < OAm ≈ SAm ≈ GMO < GMS. As with the variation in coverage, the differences in film structure can also be used to explain the relative performance of the various OFM molecules; however, the differences are more subtle. Contrary to some previous suggestions regarding the action of glycerides as friction modifiers [285], these simulations suggest that glycerides are able to act independently as friction modifiers on steel surfaces rather than merely serving as a reservoir for the acid. This hypothesis is supported by high-frequency reciprocating rig (HFRR) experimental results on steel surfaces, which showed higher friction coefficients for the disubstituted and trisubstituted glyceride than for the monosubstituted variant [20], suggesting that the molecule as a whole is responsible for reducing friction, rather than its hydrolysis products. In fact, GMS is the most effective additive in reducing friction at all coverages in these simulations, and this is consistent with the structural information in Fig. 20 and 21, which indicates less interdigitation between the OFM film and hexadecane for glyceride compared to acid and amide as a result of increased intermolecular hydrogen bonding (Fig. 23). At low coverage, the reduced friction coefficient for glycerides relative to that for acids and amides is probably primarily due to increased layering [266] of the OFM−hexadecane system rather than reduced interdigitation. These results agree with boundary friction experiments which have shown that amides [286] and glycerides [188] with saturated tailgroups yield lower friction coefficients than do acids. However, a smaller benefit of glycerides and amides relative to acids has been observed experimentally rather than being found in these simulations. This is probably due to lower glyceride and amide binding energies relative to that of the acid, which lead to lower surface coverage at equivalent concentrations.

To probe the effect of sliding velocity, v_s, on the friction of the OFM films, simulations with v_s = 1, 2, 5, 10, and 20 m s^{-1} were also conducted, as shown in Fig. 26-b. The chosen sliding velocities lie at the upper end of the range of experimentally relevant values while still being computationally feasible and reliably thermostattable [278]. Because experimental boundary friction data on steel surfaces at different velocities are available in the literature only for acids and glycerides [188], amides are not

included in these comparisons. It is noteworthy that, other than the orientation of the tilt angle mentioned previously, the film structures remained essentially unchanged through the course of the simulations over the entire range of sliding velocities simulated.

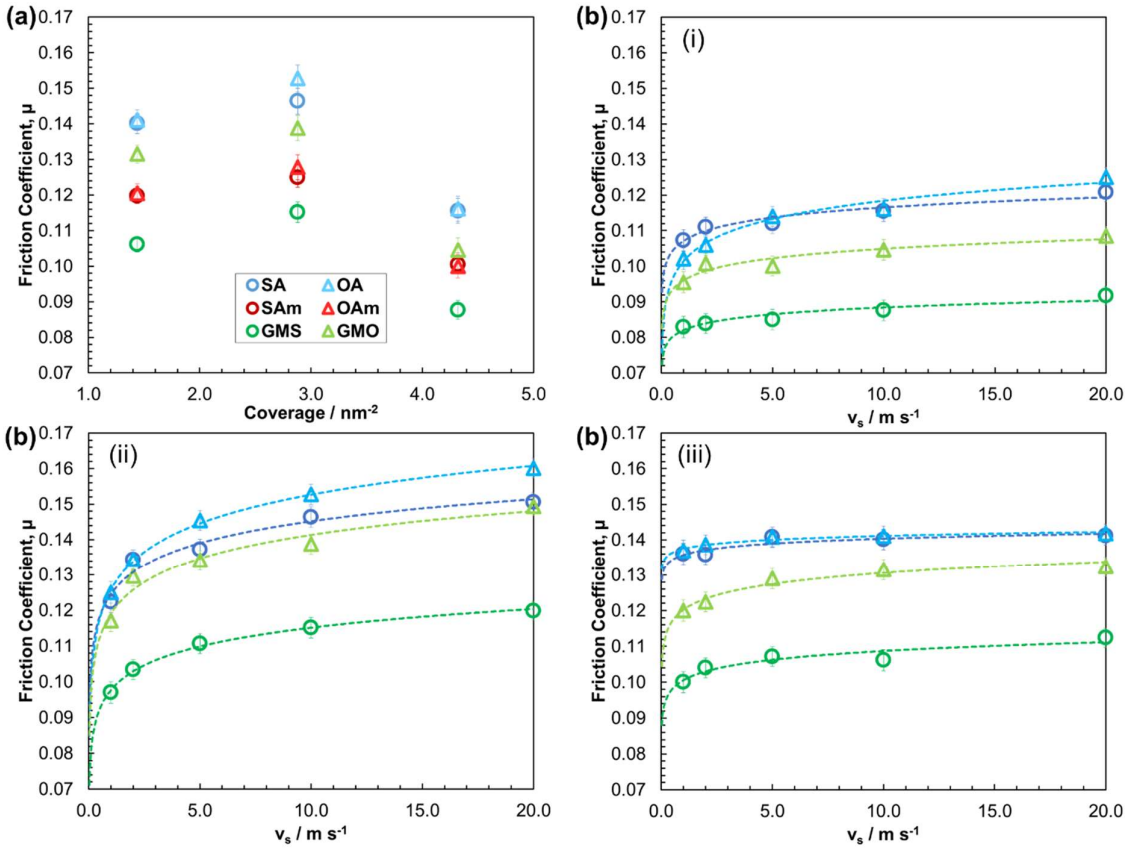

Figure 26. Friction coefficient: as a function of coverage at v_s = 10 m s^{-1} (a) and as a function of sliding velocity (b) at high coverage (i), medium coverage (ii), and low coverage (iii). The dotted line is a logarithmic fit of the friction–velocity data for each OFM. Error bars were calculated from the standard deviation between block averages from 100 ps time windows.

It is clear from the fitting curves in Fig. 26-b that the friction coefficient increases linearly with log(sliding velocity) for all of the OFMs and coverages, in accord with experimental results [188,286] and stress-promoted thermal activation theory [166,176]. The observed increase in friction with sliding velocity can be rationalized in the following way; as two atoms approach in the interdigitated region, they experience a repulsive force. At low sliding velocities and/or high temperatures, the molecules can adjust their geometry by thermally induced translation, rotation, and conformational

changes in order to avoid increasing the repulsive force as the surfaces move past one another [279]. At high sliding velocities and/or low temperatures, thermal molecular adjustment alone becomes too slow and must be increasingly augmented by shear stress-promoted adjustments and thus the friction coefficient increases with sliding velocity [180]. Stress-promoted thermal activation models such as this yield a linear relationship between log(sliding velocity) and the friction coefficient [176,188]. At high coverage, the barriers to interfacial sliding are small because there is very little interdigitation of the OFM film and the hexadecane lubricant (Fig. 26-i), leading to a low friction coefficient which is only weakly influenced by the sliding velocity (Fig. 26-b-i). This behaviour mirrors that observed in SFA experiments on high-coverage monolayer films of other surfactants [287]. At medium coverage, the amorphous OFM monolayers are more interdigitated by the lubricant (Fig. 26-ii) and molecular adjustment is relatively slow because molecules are closely spaced. This means that activation barriers are both higher and more numerous, leading to a high friction coefficient which varies significantly with sliding velocity (Fig. 26-b-ii). At low coverage, the film is more liquid-like, and although the films are even more interdigitated (Fig. 26-iii), the widely spaced OFM molecules are relatively free to rearrange in order to reduce the barrier height regardless of the sliding velocity [288]. This means that low coverage films display a high friction coefficient which is almost independent of the sliding velocity (Fig. 26-b-iii).

At high velocity (v_s = 10 m s^{-1}), the friction coefficient increases by around 5% for all OFMs between low and medium coverage (Fig. 26-a) before decreasing by 30% between medium and high coverage. This pattern has been observed in SFA experiments using monolayer films formed from other surfactants in which friction increased as the film moved from a liquid-like to an amorphous film and then decreased when a solid-like film was formed [288].This is because, at high velocity, the closely spaced molecules in medium-coverage films have insufficient time to adjust their positions without augmenting the shear stress. At low velocity (v_s = 1 m s^{-1}), the friction coefficient at medium coverage decreases to a value in between those at low coverage and high coverage (Fig. 26-b). This is because the molecules in medium-coverage films now have sufficient time to adjust their positions without

significantly increasing the shear stress. Boundary friction experiments are always carried out at relatively low velocity, explaining why a steady reduction in friction is observed in these experiments when the concentration of the OFM is increased [289,290].

The effect of tailgroup unsaturation on friction has been a topic of interest in many experimental [173,175,188,291] and simulation [187,292] studies of OFMs. The current simulation results suggest that, at equal coverage, the structure (Fig. 20 and Fig. 21) and friction (Fig. 26) of acid and amide OFMs with Z-unsaturated tailgroups are very similar to their saturated counterparts. Thus, experimentally observed differences between acid and amide OFMs with saturated and Z-unsaturated tailgroups are likely to have arisen from differences in their level of adsorption and thus surface coverage at the tested concentration, rather than from nanoscale structural differences. Although the binding energy of the OFM is not expected to change upon moving from saturated to Z-unsaturated tailgroups [292], the kink in the chain results in a larger kinetic barrier for the formation of a high-coverage film due to steric effects [293]. Indeed, in situ AFM experiments [174] have shown that, unlike SA, OA does not form close-packed monolayers on mica surfaces at equal concentration. Similarly, SFA experiments on steel surfaces have indicated that OA is able form close-packed monolayers, but only when it is added at much higher concentrations than SA [173]. This suggests that, in boundary friction experiments [188], OFMs with saturated tailgroups are more likely to form high-coverage films whereas OFMs with Z-unsaturated tailgroups probably form low coverage films. In these simulations, one can observe a 25% reduction in the friction coefficient upon moving from low to high coverage (Fig. 26-a). This level of reduction agrees well with experimentally observed differences between the friction coefficients of Z-unsaturated and saturated acid OFMs [188]. Moreover, the experimental friction coefficient for OFMs with saturated tailgroups increases linearly with log(sliding velocity) whereas the friction remains almost constant for OFMs with Z-unsaturated tailgroups [188]. This friction– velocity behaviour is also replicated in these simulations, with the friction of high-coverage (saturated) films increasing linearly with log(sliding velocity) (Fig. 26-b) and low coverage (Z-unsaturated) films displaying a friction coefficient which has only a very weak dependence on sliding velocity (Fig. 26-d).

The simulations still show a very slight increase for low-coverage films as opposed to complete invariance observed experimentally. This difference can be explained through the possibility of a small amount of lubricant entrainment in the higher boundary friction experiment velocities [286], which, at low coverage, may be sufficient to cancel the slight increase observed in these simulations.

The influence of the tailgroup Z-unsaturation on glyceride OFMs is different from that for acids and amides; specifically, saturated GMS is significantly (10%) more effective at reducing friction than Z-unsaturated GMO at all coverages and sliding velocities. This is mirrored by the fact that GMS films are less interdigitated by hexadecane, as shown in Fig. 20-a and Fig. 21-a. The cause of these differences in structure and friction is postulated to be a disruption of the hydrogen-bonding network due to the kink in the tailgroup.

4.4. Summary

In this study, classical MD simulations with an all-atom force field have been used to investigate the structure and friction of films consisting of a range of model (SA and OA) and commercially relevant (SAm, OAm, GMS, and GMO) OFMs adsorbed on iron oxide surfaces and lubricated by a thin layer of hexadecane. The primary aim was to determine the effects of surface coverage and sliding velocity as well as headgroup and tailgroup type on the properties of interest. We have shown that NEMD simulations with accurate all-atom force fields are capable of describing the structure and friction of a complex multicomponent system when care is taken in the simulation setup. Indeed, we have found very good agreement between our results for aspects of the film structure and friction and experimental results reported in the literature.

Preliminary squeeze-out simulations demonstrate that, even at low coverage, OFM films are able to support a thin hexadecane film and prevent solid−solid contact at high pressure (P_z = 0.5 GPa). As the coverage is increased, the equilibrium film thickness increases; however, the amount of lubricant trapped in this film remains constant regardless of coverage and corresponds to two molecular layers

of hexadecane. This thin layer of hexadecane appears to be critical in maintaining consistent low friction between high-coverage films.

Compression simulations indicate that the OFM molecules tilt under the applied pressure (P_z = 0.5 GPa) to an extent that depends on the coverage. At low coverage, the average tilt angle was 70°, but this dropped to 40° at high coverage. The latter angle and the high-coverage slab separation (50−55 Å) agree well with the experimental results. When sliding is applied, the average tilt angle does not change significantly, but the orientation of the tilt changes from being aligned perpendicular to predominantly, though not wholly, parallel with the sliding direction.

The simulations demonstrate the key role of OFM coverage in film structure and thus in boundary friction. At low coverage, the hexadecane molecules penetrate the OFM monolayers, leading to a loosely ordered film that responds under shear in a viscous, almost Couette-like fashion. By contrast, at high coverage the OFM monolayers form ordered, solid-like structures with negligible interdigitation between their methyl groups and the separating hexadecane layer. In these high coverage films, shear is accommodated by slip planes between the well-defined OFM−hexadecane and hexadecane−hexadecane layers. Consequently, the friction coefficient is considerably lower at high coverage than at low coverage. The medium-coverage case gives an amorphous film structure which, at v_s = 10 m s^{-1}, leads to the highest friction of the three studied because it lacks both the fluidity of the low-coverage case and the clear slip plane formation that occurs at high coverage.

Amide and particularly glyceride OFMs yield lower friction coefficients than acid OFMs at all coverages in these simulations, as has been observed experimentally. This is achieved through the formation of intermolecular hydrogen bonds between proximal headgroups, which results in more cohesive films, thus allowing less lubricant interdigitation. These simulations suggest that glyceride OFMs are effective at reducing friction in their own right, and thus hydrolysis to the carboxylic acid may not be required in order to reduce boundary friction, as is sometimes proposed.

A linear increase in the friction coefficient with log(sliding velocity) is confirmed for all of the OFMs at all coverages, although the dependence is greatest for medium-coverage (amorphous) monolayers and very slight for low-coverage (liquid-like) monolayers. The results of the simulations suggest that differences in friction between high-coverage (solid-like) and medium-coverage (amorphous) OFM films will be relatively small under experimentally relevant boundary sliding velocities, whereas a 25% reduction is predicted when moving from low coverage to high coverage, as has been observed experimentally.

The simulation results provide strong evidence to suggest that the experimentally observed benefits of OFMs with saturated tailgroups over those containing Z-unsaturation originate not primarily from the inherent structures of their films but rather from the ability to form films with a higher surface coverage. As a result, saturated OFMs should be used where possible to facilitate the formation of close-packed monolayers and maximize friction reduction in the boundary regime.

Chapter 5. Comparison of All-Atom and United-Atom Force-Fields for Simulations of OFM Structure and Friction

The work described in this chapter has been partly published in *Materials* (ref. [220]).

5.1. Introduction

As discussed in detail in chapter 3, the choice of force-field for long chain molecules can significantly affect the accuracy of results obtained from MD simulations. In this chapter, united-atom and all-atom force-fields are compared in confined NEMD simulations which probe the structure and friction of stearic acid adsorbed on iron oxide and separated by a thin layer of n-hexadecane.

5.2. Methodology

5.2.1. Simulation Setup

The simulation setup is essentially the same as for Section 4.2. only united-atom and all-atom force-fields are compared. Thus, to avoid repetition, the methodology for this section is described briefly here and in more detail in Section 4.2. A representative example of the systems simulated in this study is shown in Fig. 17-a. It consists of a thin layer of n-hexadecane lubricant confined between two stearic acid (OFM) monolayers adsorbed on iron oxide slabs.

Two (100) slabs of α-iron(III)-oxide [270] (hematite) with dimensions (*xyz*) of approximately 55 Å × 55 Å x 12 Å were used as the substrates, representing a single asperity contact. Periodic boundary conditions were applied in the *x* and *y* directions. Stearic acid molecules were oriented perpendicular to, and initially 3 Å from, the interior surfaces of the two slabs (Fig. 17-a). Two horizontally-orientated molecular layers (70 molecules) of n-hexadecane were then randomly distributed between the stearic acid films. This thickness of n-hexadecane was determined from previous squeeze-out simulations using the same systems, as described in ref [267].

Three coverages of stearic acid are considered; a high surface coverage (Γ = 4.32 nm^{-2}) close to the maximum theoretical value; a medium coverage (Γ = 2.88 nm^{-2}) approximately 2/3 of the maximum

coverage; and a low coverage (Γ = 1.44 nm^{-2}) around 1/3 of the maximum coverage. This corresponds to 132, 88 and 44 stearic acid molecules on each 30 nm^2 slab respectively. The highest coverage simulated has been observed experimentally for stearic acid on iron oxide surfaces [170].

The n-hexadecane and stearic acid molecules were represented by either; i) L-OPLS-AA [26,234] (all-atom) or, ii) TraPPE-UA [237,294] (united-atom) force-fields. Lennard-Jones interactions were cut-off at 10 Å and 'unlike' interactions were evaluated using either the geometric mean (L-OPLS-AA) or Lorentz—Berthelot (TraPPE-UA) mixing rules. Electrostatic interactions were evaluated using a slab implementation [273] of the PPPM algorithm [70] with a relative accuracy in the forces of 1 x 10^{-5}. Surface-hexadecane and surface-stearic acid interactions were represented by the Lennard-Jones and Coulomb potentials; the hematite surface parameters selected were developed by Berro *et al.* [169]. The hematite slab atoms were restrained in the corundum crystal structure by harmonic bonds between atoms within 3 Å. The force constant of these bonds was chosen to be 130 kcal mol^{-1} Å^{-2}, which has been shown previously to keep the surface structure suitably rigid, but not to adversely affect the thermostatting [187].

A temperature of 300 K is maintained using a Langevin thermostat [55], with a time relaxation constant of 0.1 ps. The pressure (P_z = 0.5 GPa) was controlled by applying a constant normal force to the outermost layer of atoms in the upper slab, keeping the *z*-coordinates of the outermost layer of atoms in the lower slab fixed, as is common in confined NEMD simulations (Fig. 17-a).

5.2.2. Simulation Procedure

First, a density similar to that of liquid n-hexadecane (0.75 g cm^{-3}) was achieved by moving the top slab down at 10 m s^{-1}, prior to energy minimisation. The system was then pressurised (P_z = 0.5 GPa), thermostatted in the directions perpendicular to the compression (*x* and *y*), and allowed to equilibrate at 300 K. Initially, the slab separation varied in a damped harmonic manner, so sliding was not applied until a constant average slab separation was obtained and the hydrostatic pressure within the n-

hexadecane film was close to its target value. These compression simulations were generally around 200 ps in duration.

After compressive oscillation became negligible, a velocity of $v_x = \pm v_s/2$ was added in the *x* direction to the outermost layer of atoms in each slab (Fig. 17-a) and sliding simulations were conducted for 0.5-10.0 ns, depending on the sliding velocity. The values of v_s applied were 1.0, 2.0, 5.0, 10.0 and 20.0 m s^{-1} and all simulations were run for long enough to yield a sufficient sliding distance (10 nm) to obtain representative values for the friction coefficients (uncertainty <10%). While lower sliding velocities are desirable to match those used in boundary friction experiments (typically mm s^{-1}), they are not yet accessible using NEMD simulations of this scale [187]. During the sliding simulations, any heat generated was dissipated using a thermostat acting only on the middle 10 Å of both iron oxide slabs (Fig. 17-a), applied in the direction perpendicular to the both the sliding and compression (*y*) [92]. This is known to be advantageous over direct thermostatting of the fluid which has been shown to significantly affect the behaviour of confined fluids under sliding conditions [65]. The boundary thermostatting method applied here has been shown previously to be effective in controlling the temperature of similar systems and sliding velocities [278]. At the onset of sliding, an expansion due to the increase of temperature by shear heating was expected so it was ensured that steady state sliding had been attained before sampling began for the friction coefficient [169]. The time taken to achieve steady state sliding decreased with increasing sliding velocity but always equated to approximately 2 nm of sliding distance.

The kinetic friction coefficient, μ, was obtained using the extended Amontons−Coulomb law under the high load approximation: $F_L/F_N \simeq \mu$. F_L and F_N are respectively the average total lateral and normal forces acting on the entire slab. The friction coefficients presented are the average of those calculated for the top and bottom slabs. The validity of the high load approximation has been confirmed from previous NEMD simulations of stearic acid layers with a thin, separating layer of n-hexadecane [185,187].

5.3. Results and Discussion

The results in section two describe differences between L-OPLS-AA (all-atom) and TraPPE-UA (united-atom) in terms of their description of the structure and friction of iron oxide surfaces, covered by stearic acid monolayers, confining a thin layer of n-hexadecane, during NEMD simulations. These results demonstrate the crucial role of force-field selection on the reproduction of experimental friction behaviour in multicomponent tribological systems. Differences in the structure of the films obtained with the two force-fields are described first, followed by variations in their frictional behaviour. The structures of the films as calculated with the two force fields are very similar; however, marked differences are visible in the system's dynamic properties, such as the velocity profile and the friction coefficient. In what follows, some properties are expressed as functions of the distance from the surface, denoted by *z*; this is taken as the distance from the innermost layer of atoms on the bottom slab.

5.3.1. Structure

Fig. 27 shows the variation in the molecular tilt angle, θ, defined as the angle between a vector from the carbonyl carbon atom (C) to the terminal carbon atom (CTT) and the surface normal. The high coverage tilt angle of the stearic acid film agrees relatively well with values estimated from *in-situ* AFM experiments (50° at 1.6 GPa) [174] for both the all-atom and united-atom force-fields. However, similar to previous MD simulations of thiol monolayers on gold [251], united-atom force-fields yielded reduced tilt angles, owing to the slightly lower area that each chain occupies, allowing molecules to lie flatter to the surface. The difference is most apparent at high coverage, where the molecules represented by the united-atom force-field are almost 5° more tilted than those represented by the all-atom force-field.

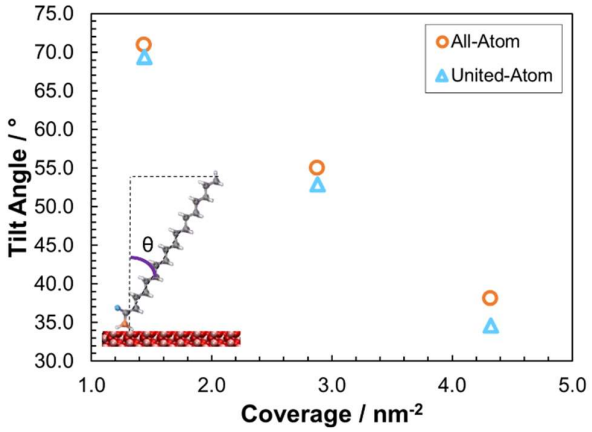

Figure 27. Variation in the average $C_{1\text{-}18}$ tilt angle to surface normal, θ, as a function of coverage for all-atom and united-atom force-fields under sliding conditions, P_z = 0.5 GPa, v = 10 m s^{-1}.

Fig. 28 shows the ordering within the high coverage stearic acid films through separate radial distribution functions (RDFs), g(r), for the carbonyl carbon, C, and the terminal carbon, CTT. The C RDFs are shifted upwards by 10 units for clarity. RDFs from previous simulations have shown that the films move from liquid-like to amorphous to solid-like with increasing coverage [267]. The C RDFs show a large peak at r = 5 Å, which indicates ordering of the stearic acid molecules to the unit-cell dimension of the hematite surface [270]. There are also distinguishable C and CTT peaks at higher multiples of r = 5 Å indicating long-range order and a solid-like film. The united-atom and all-atom systems have very similar C and CTT RDFs, suggesting the united-atom force-field also yields a solid-like film at high coverage. The C peaks are better defined in the all-atom case, perhaps due to the non-polar hydrogens

'locking' the molecules in place and leading to a slightly more solid-like film.

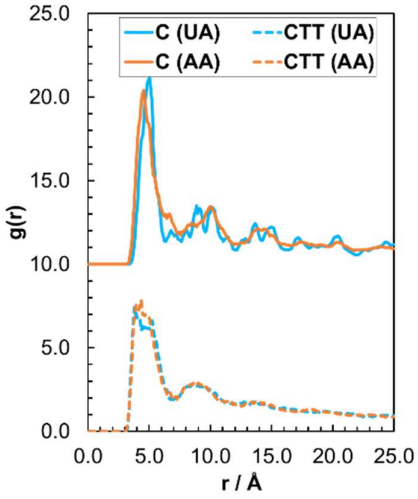

Figure 28. Radial Distribution Function (RDF), g(r), which describes the ordering of the terminal CTT (dotted) and carbonyl C (solid) atoms for all-atom (orange) and united-atom (blue) at high coverage. The C RDFs are shifted upwards by 10 units for clarity.

The mass density profiles, ρ(z), in Fig. 29 show the layering and interdigitation of the all-atom and united-atom systems. In order to uncover differences in the flow within all-atom and united-atom systems during sliding, velocity profiles, $v_x(z)$, are also shown. Atom velocities are computed for 0.5 Å spatial bins which are averaged over 100 ps time blocks during the sliding phase.

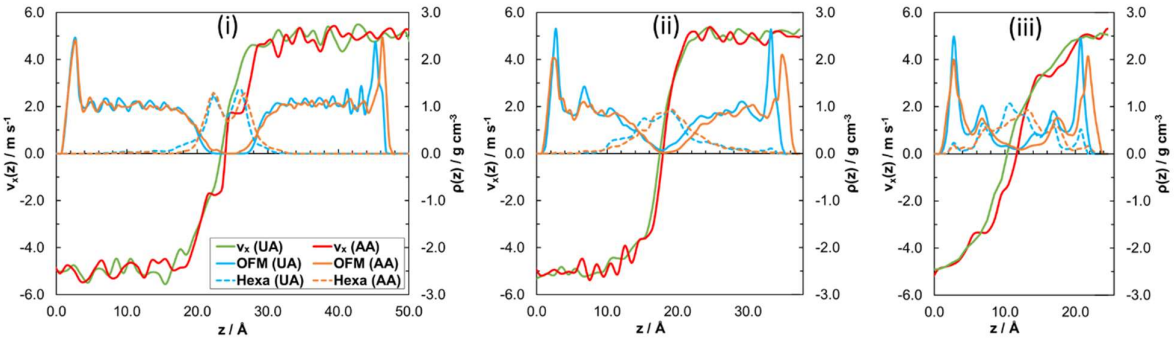

Figure 29. Profile of atom *x* velocities from 0.5 Å spatial bins in *z*, $v_x(z)$, overlaid on to atomic mass density profile in *z*, ρ(z), at high (i), medium (ii) and low (iii) coverage. P_z = 0.5 GPa, v_s = 10 m s^{-1}.

Sharp, intense peaks at the far left and right-hand side of the mass density profiles in Fig. 29 indicate adsorption of carboxylic acid headgroups on the surface, whilst the less intense peaks, which extend further from the surface, are due to the tailgroups. The stearic acid films become substantially thicker and more structured with increasing coverage. Moreover, the level of interdigitation, indicated by the overlap of the solid and dotted lines, decreases with increasing coverage [267]. Fig. 29 shows that the layering and interdigitation of the films are very similar between united-atom and all-atom models; however, the slab separation is slightly greater in the all-atom systems since the volume of each molecule is marginally greater than in the united-atom systems. The thickness of the stearic acid films [174], and the system as a whole [173], agree well with experiment for both the all-atom and united-atom systems at high coverage.

The velocity profiles indicate that there is no slip at the surface in any of the systems, as expected for the strongly absorbed headgroups. The tailgroups move at a similar velocity as the slab to which they are absorbed (± 5 m s^{-1}) until the region where they become significantly interdigitated with the n-hexadecane lubricant. At this point, the velocity profile becomes Couette-like, indicating shear within the interdigitated region. The flow within the system changes slightly moving from an all-atom force-field to a united-atom force-field. For the all-atom system at high coverage (Fig. 29-i), almost the entire stearic acid molecule moves with the wall, with multiple slip planes between the well-defined stearic acid and n-hexadecane layers. Although these layers seem equally well-defined in the united-atom mass density profile, the velocity profile has a shallower gradient and includes only one slip plane in the centre of the system. This is more similar to the all-atom velocity profile at medium coverage (Fig. 29-ii). The low coverage velocity profile (Fig. 29-iii) is more typical of conventional planar Couette flow, with a near linear velocity profile of the liquid between the slabs, rather than the region between the stearic acid tailgroups. In the all-atom case, the low coverage velocity profile contains steps which indicate partial plug-flow between combined stearic acid-hexadecane layers [154]. These steps are less evident in the united-atom case, where the velocity profile is almost linear throughout the fluid. Collectively, the united-atom and all-atom velocity profiles suggest that the flow within the film

changes depending on whether a united-atom or all-atom force-field is used. Generally, the flow is more Couette-like and there is less variation with coverage in the united-atom systems; specifically there is an absence of steps and more similar gradients in the velocity profiles.

5.3.2. Friction

The influence of surface coverage on the friction coefficient was probed at a sliding velocity, v_s = 10.0 m s^{-1} and a pressure, P_z = 0.5 GPa (Fig. 30-a). The variation in the friction coefficient with sliding velocity (v_s = 1-20 m s^{-1}) was also examined at high, medium and low coverage and a pressure, P_z = 0.5 GPa (Fig. 30-b). The high coverage friction-velocity behaviour is then compared directly to experiments (Fig. 31). The results indicate that the all-atom and united-atom systems yield considerably different friction behaviour.

Friction-coverage behaviour for the all-atom system is described first. At 10.0 m s^{-1}, the friction coefficient increases by 5% between low and medium coverage (Fig. 30-a); which can be rationalised as follows. In the liquid-like, low coverage system, there is a very high level of interdigitation (Fig. 29) but molecular rearrangement is also fast, because the stearic acid molecules are widely spaced. This means that the shear stress is not significantly augmented as molecules from opposing slabs slide past one another. In the amorphous, medium coverage film, interdigitation is decreased; however, molecular rearrangement is much slower, due to stearic acid molecules being packed more closely; this results in increased shear stress and thus a higher friction coefficient [267].

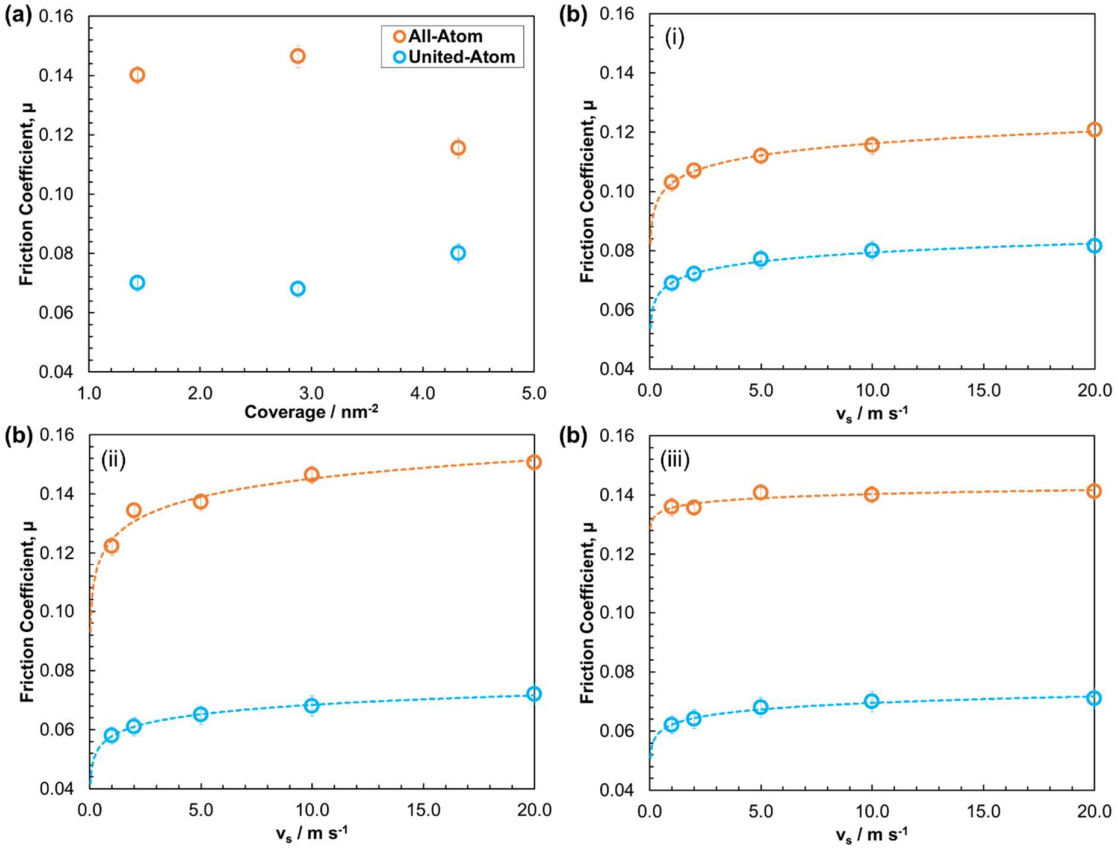

Figure 30. Friction coefficient: as a function of coverage at v_s = 10 m s^{-1} (a) and as a function of sliding velocity (b) at high coverage (i), medium coverage (ii) and low coverage (iii). Dotted line is a logarithmic fit of the friction-velocity data. Error bars calculated from standard deviation between block averages from 100 ps time windows.

The friction coefficient at high coverage is around 30% lower than at medium coverage, and approximately 25% less than at low coverage. Based on the structural changes with coverage, this reduction in friction can be attributed to the formation of clear slip planes between the stearic acid films and the n-hexadecane lubricant, as observed through atomic mass density and velocity profiles (Fig. 29). These slip planes are facilitated through the close-packing of the tailgroups, which leads to a solid-like, coherent monolayer film which allows very little interdigitation with the n-hexadecane lubricant or with each another. The increase in friction coefficient between low and medium coverage and then decrease between medium and high coverage (Fig. 30-b) observed at high velocity (v_s = 10.0 m s^{-1}) has been observed in AFM experiments of different surfactant films [288]. At low velocity (v_s =

1.0 m s^{-1}), the friction coefficient at medium coverage decreases to a value in between those at low coverage and high coverage (Fig. 30-b), since molecules have more time to rearrange relative to the sliding velocity [267]. Boundary friction experiments are always carried out at relatively low velocity, explaining why a steady reduction in friction is observed when the concentration of stearic acid is increased [289].

In the united-atom systems, the structural changes with coverage are similar; however, the friction-coverage behaviour is very different. Firstly, the friction coefficient is significantly lower in the united-atom systems for all of the coverages simulated. This is probably due to the artificial smoothness of the hydrogen-free united-atom molecules which leads to a reduction in the steric barriers to interfacial sliding. Moreover, the friction-coverage trend (Fig. 30-a) is the opposite of that observed in the all-atom NEMD simulations as well as AFM [288] and boundary friction experiments [188]. In the all-atom systems, in accordance with experiment, increasing coverage leads to reduced interdigitation and a significant reduction in the friction coefficient. This behaviour is not replicated for united-atom systems, since the smoother molecules can slide over one another more easily, so the level of interdigitation has less influence on the friction coefficient. This means that the increased viscous contribution to friction from the thicker, high coverage film becomes more significant than any reduction due to slip plane formation. Therefore, the united-atom friction coefficient increases with increasing coverage of stearic acid, despite the reduced interdigitation.

It is clear from the fitting curves in Fig. 30-b that the friction coefficient increases linearly with log(sliding velocity) at all coverages, in accord with experimental results and stress-promoted thermal activation theory [188]. The friction coefficient is much lower in the united-atom systems; the greatest difference (-45%) is at low and medium coverage and the smallest difference (-30%) is at high coverage, where there is significantly less interdigitation. This further suggests that the contribution to friction due to interdigitation is severely under-predicted when using a united-atom force-field. The rate of increase in friction coefficient with increasing sliding velocity is also slightly less for united-

atom systems and there is less variation between the different coverages. For example, the steep increase in the friction coefficient evident in the medium coverage all-atom system is not so prominent in the united-atom system.

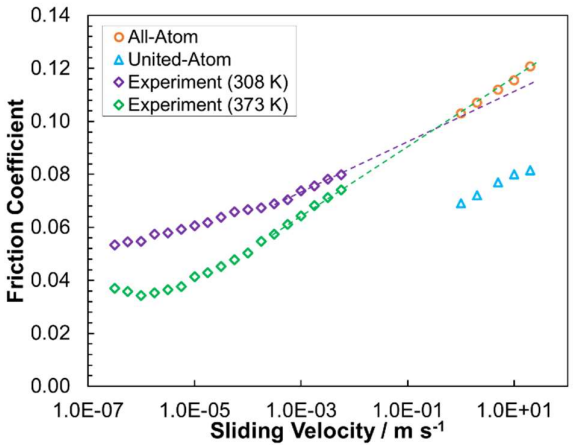

Figure 31. Variation in the friction coefficient with sliding velocity (logarithmic *x*-axis) for high coverage all-atom and united-atom systems as well as experiment. Experimental data (P_z = 0.69 GPa) are reproduced with permission from ref [188]. Dotted line extrapolation from point at which experimental data shows a constant gradient (5 x 10^{-4} m s^{-1}) to sliding velocities accessible in NEMD simulations.

Fig. 31 shows that the friction coefficients from the high coverage all-atom system agrees extremely well with extrapolations from boundary friction experiments [188] conducted at lower sliding velocities (3.0 x 10^{-7} - 5.0 x 10^{-3} m s^{-1}), whereas united-atom friction coefficients are around 30% lower than these extrapolations. The linear extrapolation of the experimental data to higher sliding velocities is justified since this linear increase in the friction coefficient with log(sliding velocity) is predicted by stress-promoted thermal activation theory [188]. The all-atom simulation data (boundary thermostatted to 300 K) appear to show slightly better agreement with the experimental data collected at 373 K than data collected at 308 K. Experimentally, the temperature may influence the level of interdigitation and speed of molecular rearrangement within the films, as well as the surface coverage [188]. Since the exact coverage is not known in the experimental systems, it is not possible to determine the relative significance of these factors on the friction coefficient; this could be

investigated in future simulations where coverage and temperature are varied independently. The friction under-prediction using united-atom force-fields is evident from the comparison shown in Fig. 31. This under-prediction is expected to be relevant in all NEMD simulations of long-chain molecules, and will be particularly severe when the molecules are densely packed but not clearly layered, for example the medium coverage films in these simulations (Fig. 30-b-ii). In line with the viscosity [101], friction under-prediction is expected to be much more severe for linear molecules, than those with significant branching.

5.4. Summary

The most effective united-atom (TraPPE-UA) and all-atom (L-OPLS-AA) force-fields from chapter 3 were applied in confined NEMD simulations of a test system. In particular, a multicomponent tribological system where high pressures are especially relevant, was chosen in order to compare the differences between the force-fields in terms of their prediction of structure and friction.

Both all-atom and united-atom force-fields accurately reproduce the experimental structure of stearic acid films adsorbed on iron oxide surfaces and separated by a thin layer of n-hexadecane. However, differences are observed in the flow within the films under sliding, with steeper, more stepped velocity profiles for the all-atom systems. The friction behaviour is also very different between the all-atom and united-atom systems. In the all-atom systems, friction generally decreases with increasing coverage, in accord with experimental results. This is due to reduced interdigitation and the formation of clear slip planes between the stearic acid and n-hexadecane layers. In the united-atom systems, the friction coefficient is much lower, and generally increases with increasing coverage, suggesting that interdigitation is less critical to the friction coefficient, which appears to be dominated by the viscous contribution due to shearing within the film.

United-atom force-fields are able to reproduce the linear increase with log(sliding velocity) predicted by stress-promoted thermal activation theory and captured by all-atom simulations and experiments.

However, while the high coverage all-atom results fit extremely well with experimental extrapolations, the friction coefficient is under-predicted by 30% in the united-atom system.

The results from the first section suggest that an accurate, all-atom force-field, such as L-OPLS-AA is required in order to accurately predict the experimental viscosity of long-chain molecules. Moreover, results from the second section indicate that experimental friction behaviour of confined, multicomponent tribological systems is only captured using and accurate, all-atom force-field.

United-atom force-fields have been, and will likely continue to be useful to capture trends in tribological simulations of very large, complex systems due to their relatively low computational expense. However, systematic under-prediction of the viscosity and friction of long-chain, linear molecules make them less accurate for NEMD simulations of tribological systems. Thus it is recommended that all-atom force-fields, specifically L-OPLS-AA, are used in future MD simulations of tribological systems containing long-chain, linear molecules where computational resources allow.

Chapter 6. Effect of Nanoscale Roughness on the Structure and Friction of OFM Films

The work described in this chapter has been published in *Tribology International* (ref. [295]).

6.1. Introduction

The effect of surface roughness on the performance of OFMs is not fully understood [11]. Most previous NEMD simulations of OFM films on metal surfaces have utilised atomically-smooth slabs, with only atomic corrugation [69,187,267,292,293,296], although the influence of artificial asperities placed on top of atomically smooth slabs have also been considered [185,186,297]. The presence of nanoscale roughness has been shown to significantly influence the adhesion of solid surfaces through both MD simulations and AFM experiments [298]. The effect of 3D nanoscale fractal roughness on the friction between sliding surfaces has also been investigated for both dry sliding [299–301] and in the presence of lubricant molecules [302–304] in large-scale NEMD simulations. These previous simulations suggested that the friction coefficient depends on how effectively the lubricant is able to prevent the direct contact of asperities on opposing surfaces [303]. Nonpolar lubricant molecules can be easily squeezed-out from between asperities [275,305], but strongly-adsorbed OFMs are expected to be more difficult to remove, making them more effective in reducing asperity contact and thus friction in the boundary lubrication regime [267]. Other NEMD simulations of alkanes between amorphous and crystalline surfaces have shown that layering of lubricant films is strongly suppressed on the rougher amorphous surfaces, resulting in a more liquid-like film [135]. This may have significant implications regarding the ability of OFM films to separate opposing solid surfaces with nanoscale roughness.

The kinetic friction coefficient in nanotribological systems can be obtained using the extended Amontons-Coulomb law: $F_L = \mu F_N + F_0$, where F_L and F_N are, respectively, the average total lateral and normal forces acting on the outermost layer of atoms in each of the slabs and F_0 is the Derjaguin offset, the friction force at vanishing load, which is generally attributed to adhesive forces [185,187,306].

Recent SFA experiments of palmitic acid OFMs in PAO base oil highlighted F_0 as a significant contribution to F_L under relatively low applied pressures (<10 MPa) [306]. Previous NEMD simulations showed that the Derjaguin offset increased with increasing surface roughness, decreased with increasing stearic acid coverage, and became negligible when sufficient lubricant was present to separate the stearic acid films [185]. In our previous NEMD simulations, we demonstrated that the friction coefficient is reduced at high coverage of stearic acid, due to the formation of solid-like monolayers which allow very little interdigitation and yield slip planes between well-defined molecular layers [267]. In this study, we will probe the effect of; (i) higher pressures (0.5-2.0 GPa), in order to test the limits of operability of OFMs, and (ii) surfaces with different levels of 3D root mean square (RMS) roughness (0.2, 0.5, 0.8 nm), in order to assess the effect of nanoscale roughness on the structure and tribological behaviour of OFM films. The roughness added in this study is expected to be similar to that found on experimental surfaces, since it is added using a random midpoint displacement (RMD) algorithm, which generates surfaces with a quantifiable RMS roughness [299]. Conversely, in previous confined NEMD simulations of stearic acid, the roughness was varied by changing the size of artificial roughness features [185,186,297].

The 'smooth' steel surfaces used in tribological experiments generally have a RMS roughness of approximately 10 nm [307,308], though other surfaces, such as gold, can be produced with a RMS roughness well below 1 nm [309]. Therefore, all of the RMS roughness values used in this study represent an extremely smooth experimental surface; however, accurate representation of larger RMS roughness values would require prohibitively large simulation areas [135]. Moreover, the roughness features considered here are on a similar scale to the OFM molecules, probably giving them the most potential to weaken OFM films by disrupting intermolecular forces between neighbouring molecules. The current simulations will highlight the effect of changes in the nanoscale structure within the film due to changes in surface roughness on both the friction coefficient and the Derjaguin offset. The results obtained with stearic acid will also be directly compare to results for *n*-hexadecane

under similar conditions [303], in order to highlight the reasons for the differences in their friction reduction performance in the boundary lubrication regime [188,310].

6.2. Methodology

6.2.1. Simulation Setup

A representative example of the systems simulated in this study is shown in Fig. 32-a. It consists of two stearic acid monolayers adsorbed on α-iron slabs with 3D nanoscale RMS roughness (Fig. 32-b). The α-iron slabs are chosen as a model for steel, which is of significant academic and industrial interest. Though α-iron oxide would be a more accurate representation of a steel surface [267], no classical MD force-field is currently available which can accurately model its deformation under the high pressures applied in these simulations. Stearic acid was chosen as a model OFM, an important class of boundary lubricant additive, which has been used in numerous previous experiments [173–175,188,310] and MD simulations [69,185–187,267,292,293,296,297]. Our previous NEMD study showed that whilst there were significant variations in the structure and friction of stearic acid films and those formed by other types of OFM (amides and glycerides), all gave the same general trends [267]. Unlike in our previous study [267], no lubricant molecules were added between the stearic acid films. Preliminary squeeze-out simulations showed that only two molecular layers of *n*-hexadecane remained between stearic acid films at 0.5 GPa [267], and since higher pressures (0.5–2.0 GPa) were applied in the current simulations, very few *n*-hexadecane molecules were expected to remain between the asperities. A more complete understanding of lubricant squeeze-out in the presence of OFM films would certainly be an interesting target of future MD simulations and AFM experiments, but is beyond the scope of this current study. All structures were constructed using the Materials and Processes Simulations (MAPS) platform from Scienomics SARL.

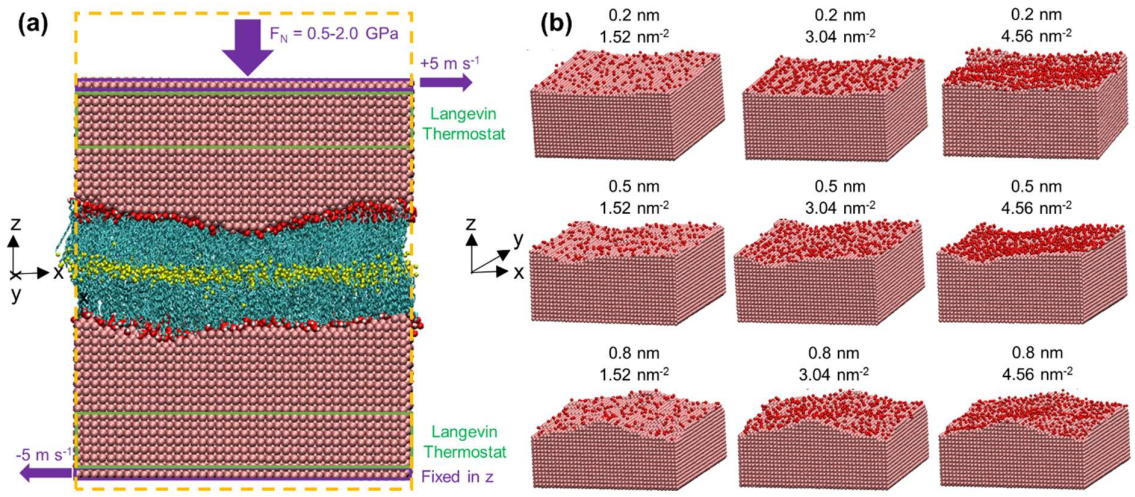

Figure 32. Setup for compression and sliding simulations. (a) Shows a representative system (0.8 nm roughness, 4.56 nm^{-2} coverage) after compression (1.0 GPa), before sliding; periodic boundary conditions (yellow dashed line) are applied in the *x* and *y* directions. (b) Shows only the bottom slab to demonstrate the different levels of RMS roughness; the headgroup positions are highlighted to indicate the different surface coverages of stearic acid. Rendered using VMD [264]; Fe atoms are shown in pink, O in red, H in white, terminal C in yellow, and the other C in cyan; H atoms in the tailgroups are omitted for clarity.

Most surfaces have roughness on several length scales, including the nanoscale, that can be described by a self-affine fractal scaling law [299,311]. Here, the Hurst exponent and the root mean square (RMS) roughness can be used to quantify the amount of roughness [300]. Using the random midpoint displacement (RMD) algorithm, rough surfaces can be generated which are periodic across their boundaries [300]. The RMD algorithm, with a Hurst exponent of 0.8, was used to independently generate the same RMS nanoscale roughness (0.2, 0.5 or 0.8 nm) in the top and bottom slabs [299,303]. In order to avoid generating only a few large asperities, the RMD algorithm did not start from the centre of only one square (entire slab), but rather four smaller, equally sized squares [300]. The slabs themselves had approximate *x, y, z* dimensions of 11, 11, 5 nm. Periodic boundary conditions were applied in the *x* and *y* directions. The dimensions of the solid surfaces confining the stearic acid films are much larger in the current simulations than those used in many previous NEMD studies [69,185–187,267,297], in order to provide a more faithful representation of the statistical distribution

of the heterogeneous surface morphology [135]. On experimental surfaces, the typical height of a roughness feature is expected to be approximately 2–3 orders of magnitude smaller than its lateral dimensions [312]. To replicate this in NEMD simulations would require a prohibitively large system size and hence the 'steepness' of the roughness features in these and previous NEMD simulations [299,312] is expected to be somewhat exaggerated. Nonetheless, the use of an RMD algorithm provides a more realistic representation of nanoscale surface roughness than harmonic [266] or other artificially introduced [185] roughness features.

Stearic acid molecules were oriented perpendicular to, and initially 3 Å from, the interior surfaces of the two slabs (Fig. 32-a). The surface coverage, Γ, can be defined as the average number of stearic acid molecules present in a given surface area (nm^{-2}). Three coverages of stearic acid were considered; a high surface coverage (Γ = 4.56 nm^{-2}) close to the maximum theoretical value [170]; a medium coverage (Γ = 3.04 nm^{-2}) approximately 2/3 of the maximum coverage; and a low coverage (Γ = 1.52 nm^{-2}) around 1/3 of the maximum coverage (Fig. 32-b). Note that the Γ values assume an atomically smooth surface. The high, medium and low coverages correspond to 600, 400, and 200 stearic acid molecules adsorbed on each of the 131.6 nm^2 slabs respectively. The highest coverage simulated has also been observed experimentally [170]. Simulations with no stearic acid molecules between the slabs were also conducted for comparison.

Classical MD simulations were performed using LAMMPS [255]. The MD equations of motion were integrated using the velocity-Verlet algorithm with an integration time-step of 1.0 fs. Fast-moving bonds involving hydrogen atoms were constrained with the SHAKE algorithm [256]. The stearic acid molecules were represented by the L-OPLS-AA force-field [26]. This is an updated form of the OPLS-AA force-field [234] which was explicitly parameterised for long-chain molecules. We have shown previously that the use of accurate all-atom force-fields is critical to obtain accurate tribological behaviour in confined systems which include long-chain molecules [69]. Lennard-Jones interactions were cut-off at 10 Å and 'unlike' interactions were evaluated using the geometric mean mixing rules

[234]. Electrostatic interactions were evaluated using a slab implementation [273] of the PPPM algorithm [70] with a relative accuracy in the forces of 1 x 10^{-5}. Fe-stearic acid interactions were represented by the Lennard-Jones potential; the parameters for iron were developed by Savio *et al.* [266] for the adsorption of alkanes. The α-iron slabs contain no partial charges so there is no electrostatic interaction between the stearic acid molecules and the α-iron slab; however, there is still preferential adsorption of the headgroups due to the stronger Fe-O interactions (ε ≈ 0.06 eV) relative to the Fe-C interactions (ε ≈ 0.01 eV) [185]. Fe-Fe interactions within the slabs are represented by the many-body Embedded Atom Model (EAM) [313], which can accurately model deformation of the slabs under the high pressures applied [303]. Iron and steel surfaces quickly become oxidised when exposed to air, which significantly reduces the adhesion force between contact surfaces in experimental systems [303]. Therefore, a Lennard-Jones potential was used for Fe–Fe interactions between atoms in opposing slabs (Fig. 32-a) in order to mimic the reduced adhesion between oxidised surfaces [299]. The Lennard-Jones parameters, ε = 0.02045 eV and σ = 0.321 nm, were used for this interaction, as have been successfully utilised in previous NEMD simulations of tribological systems [203,303].

6.2.2. Simulation Procedure

The systems were initially energy minimized and then compressed (F_N = 0.5, 1.0, 1.5, 2.0 GPa), thermostatted (300 K) in the directions perpendicular to the compression (*x* and *y*), and allowed to equilibrate. During the compression stage, the temperature is controlled using a global Langevin thermostat [92], with a time relaxation constant of 0.1 ps. The pressure was controlled by applying a constant normal force to the outermost layer of atoms in the upper slab, keeping the z-coordinates of the outermost layer of atoms in the lower slab fixed (Fig. 32-a), as is common in confined NEMD simulations [185,186,297,302–304]. The slab separation initially varied in a damped harmonic manner, so sliding was not applied until a constant average slab separation was obtained and the hydrostatic pressure within the stearic acid film was close to its target value. The compression simulations were approximately 0.5 ns in duration.

A velocity of +5 m s^{-1} was then added in the *x* direction to the outermost layer of atoms in the top slab and -5 m s^{-1} to the bottom slab (total sliding velocity = 10 m s^{-1}), as shown in Fig. 32-a, and sliding simulations were conducted for 2.0 ns. All simulations were run for long enough to yield a sufficient sliding distance (20 nm) to obtain representative values for the lateral (friction) forces (uncertainty < 10%). While lower sliding velocities are desirable to match those used in boundary friction experiments (typically mm s^{-1}), they are not yet accessible using NEMD simulations of this scale [187,267].

During the sliding simulations, any heat generated by shearing of the molecules was dissipated using a Langevin thermostat, with a time relaxation constant of 0.1 ps, which acted only on the 10 Å of α-iron slabs closest to the fixed layers (Fig. 32-a), and was applied in the direction perpendicular to both the sliding and compression (*y*) [92]. This is known to be advantageous over direct thermostatting of the fluid, which has been shown to significantly alter the behaviour of confined fluids under sliding conditions [65]. This boundary thermostatting method is common in confined NEMD simulations [185,186,297,302–304] and has been shown to be effective in controlling the temperature of similar systems at the sliding velocity applied applied here (10 m s^{-1}) [278]. At the onset of sliding, an expansion due to the increase of temperature by shear heating was expected, so it was ensured that steady state sliding [187] had been attained before sampling of the lateral and normal forces began. The time taken to achieve steady state sliding equated to approximately 0.5 ns (5 nm of sliding).

6.3. Results and Discussion

Variations in the nanoscale structure within the films with nanoscale RMS roughness and stearic acid coverage were monitored through visualised trajectories, atomic mass density profiles, velocity profiles, and radial distribution functions. Thermal and mechanical equilibration were confirmed before sampling began. The tribological behaviour of the stearic acid films were probed by examining the change in lateral forces on the outer layer of atoms in the slabs, F_L, with normal pressure, F_N. A linear plot of F_L against F_N was then used to establish the Derjaguin offset, F_0, and the friction

coefficient, μ, for each of the surface roughness and coverages combinations simulated. The variation in F_0 and μ with RMS surface roughness and coverage was then plotted in order to establish the relative influence of each.

6.3.1. Structure

Fig. 33 shows the variation in the interface between the stearic acid films on the top and bottom slabs with surface coverage and RMS roughness. Even with the exaggerated steepness of the nanoscale roughness features [312], and high pressures applied in these simulations, the stearic acid films maintain separation of the asperities at all coverages, which demonstrates the robustness of the films.

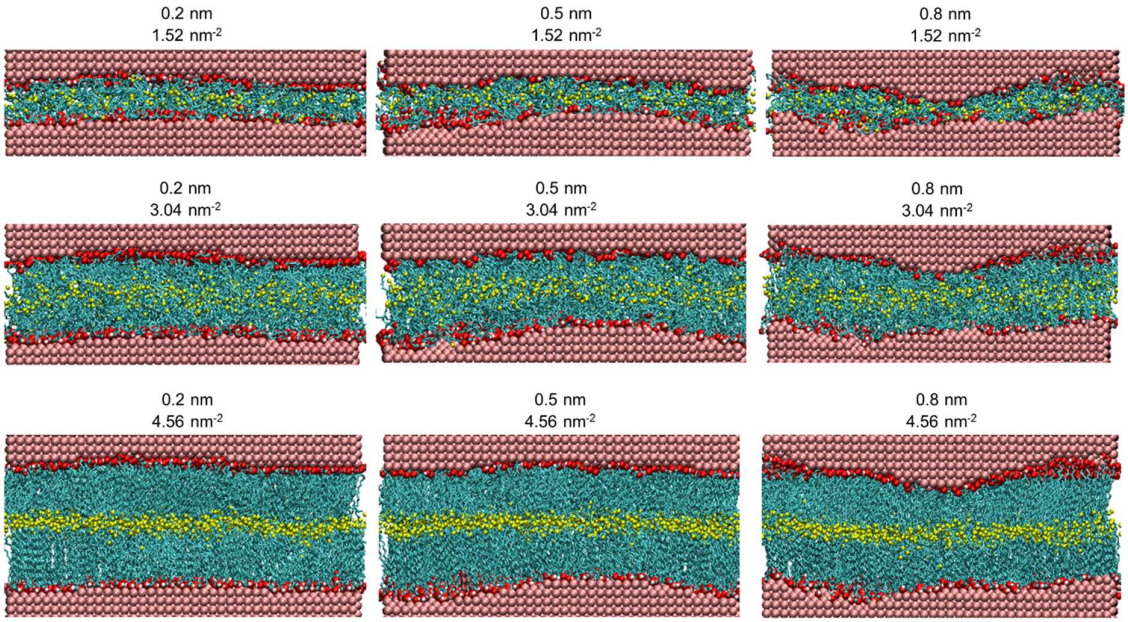

Figure 33. Images showing the interface between the stearic acid films on the top and bottom slabs at all levels of RMS roughness and coverages considered; after compression (1.0 GPa), before sliding. Rendered using VMD [264]; Fe atoms are shown in pink, O in red, H in white, terminal C in yellow, and the other C in cyan; H atoms in the tailgroups are omitted for clarity.

These results are in contrast to those obtained for similar coverages of *n*-hexadecane, which allowed direct contact of asperities under the same conditions [303]. At increasing stearic acid coverage, there is a larger separation between the opposing slabs. Moreover, the terminal carbon atoms, highlighted in yellow, form more ordered layers, resulting in a smoother interface between the films adsorbed on

the upper and lower slabs. Increased RMS surface roughness seems to supress this layering somewhat and leads to more disordered interfaces; however, these changes appear to be less significant than the dependence on surface coverage.

Fig. 34 shows the change in the atomic mass density profiles for all atoms in the stearic acid molecules in z, $\rho(z)$, and x-velocity profile in z, $v_x(z)$, with coverage at 0.2, 0.5 and 0.8 nm RMS roughness. The velocity profiles at all levels of coverage and roughness show that there is no slip at the surface, as expected for the strongly absorbed carboxylic acid headgroups [187,267]. The tailgroups also move at equal velocity to the slabs to which they are absorbed (±5 m s^{-1}), but only up to the region where they become interdigitated with the other film, at which point the atoms move slower as the interface is sheared [267]. In common with results from atomically smooth slabs [267], there is a decrease in the interdigitation between films adsorbed on opposing slabs as the coverage of stearic acid is increased, as indicated by reduced overlap of the mass density profiles. Therefore, the interface is more ordered in the 4.56 nm^{-2} coverage systems, resulting in steeper velocity profiles compared to those at lower coverage. This suggests the presence of slip planes between the films adsorbed to the top and bottom slabs, which leads to less shearing of the film and thus a lower viscous contribution to the friction coefficient [267]. On slabs with greater RMS surface roughness, there is more interdigitation between films adsorbed on opposing slabs; although this effect is less significant than the change with coverage. The velocity profiles are similar at all levels of RMS surface roughness, though they are generally steeper at 0.2 nm, suggesting a clearer slip plane due to a smoother interface. At 0.2 nm RMS roughness, the mass density profiles are very similar to those observed on atomically smooth α-iron oxide surfaces [267]; however, as the surface roughness increases, the outermost headgroup peaks (closest to the iron surface) become considerably less intense. This is similar to what has been highlighted previously for linear alkanes, where less ordered, more liquid-like films were observed on surfaces with greater nanoscale roughness [135]. This is explored further for stearic acid through the film radial distribution function (RDF) in Fig. 35.

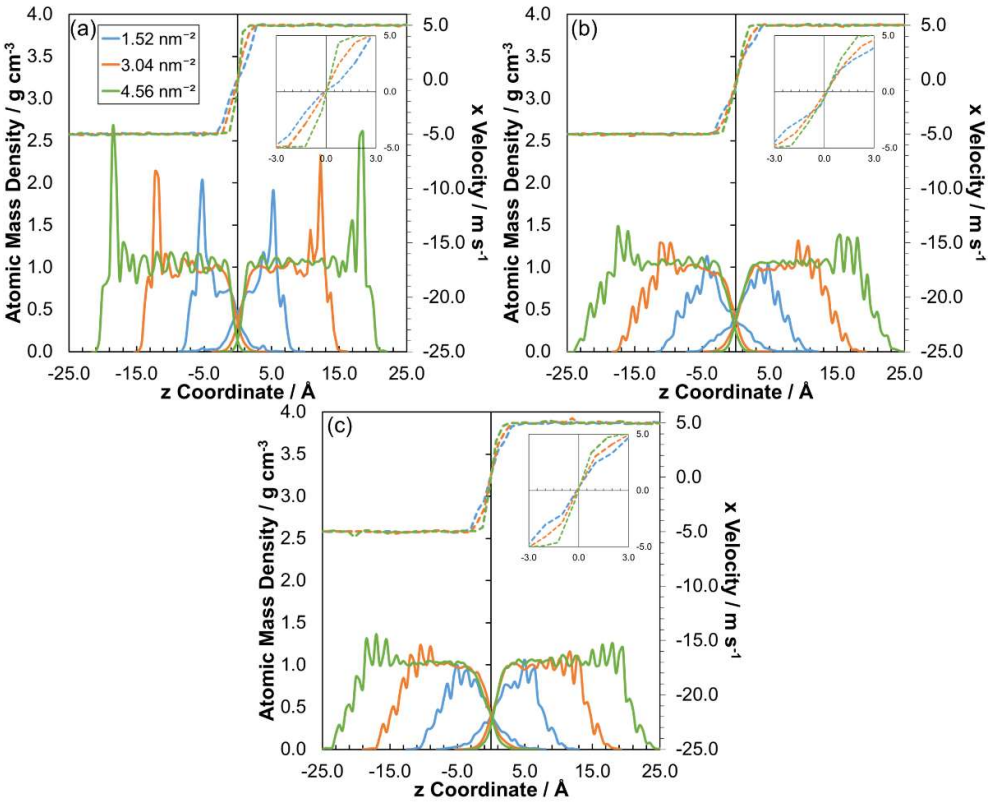

Figure 34. Atomic mass density profiles in *z* (solid line), ρ(*z*), and *x*-velocity profile in z (dashed line), $v_x(z)$, at: 1.0 GPa; 1.52, 3.04, 4.56 nm^{-2} coverage; (a) 0.2 nm (b) 0.5 nm (c) 0.8 nm RMS roughness. Atomic mass densities and velocities are computed for 0.5 Å spatial bins and averaged for the final 200 ps of the sliding phase. The profiles are shifted such that a *z*-coordinate of zero is at the centre of the interface between the films adsorbed on the top and bottom slabs. Magnified inset highlights the change in velocity profile with coverage.

Fig. 35 shows the change in the radial distribution function (RDF) for the carbonyl carbon and terminal carbon atoms with coverage at 0.2, 0.5 and 0.8 nm RMS roughness. In Fig. 35, the carbonyl carbon shows long-range order for all levels of RMS roughness and coverages, with the major peaks occurring at multiples of r = 4 Å. This slightly exceeds the unit-cell dimension of the α-iron surface (2.86 Å) [313], suggesting that, while the surface structure determines the headgroup packing of the stearic acid films on α-iron oxide [267], on α-iron, the limiting headgroup area [170] is too large to occupy every lattice site. The carbonyl peak at 4 Å is of similar intensity at all coverages; however, at 4.56 nm^{-2}, there are sharper, more intense peaks at 8 and 12 Å, indicating long-range ordering of the headgroups and more solid-like films. The terminal peaks at 4, 12 and 16 Å are most intense at 4.56 nm^{-2} coverage, suggesting

that the tailgroups remain solid-like at the interface [267]. The change in the RDFs with coverage is similar at 0.2 nm RMS roughness as on atomically smooth α-iron oxide surfaces [267]; however, there is much less variation on the RDFs with coverage at 0.8 nm RMS roughness. Films on surfaces with larger RMS roughness generally have weaker carbonyl and terminal peaks, particularly at 8 and 12 Å, indicating less long-range order and more liquid-like films.

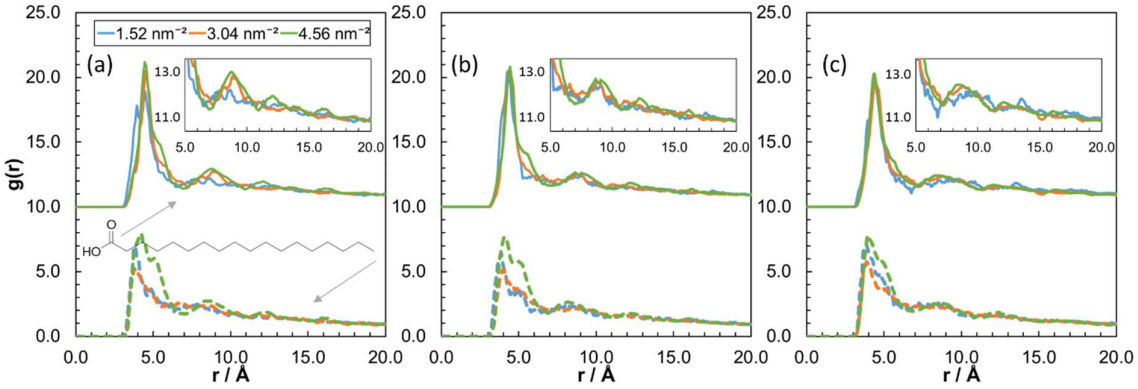

Figure 35. Radial distribution function (RDF) for the terminal (dashed line) and carbonyl (solid line) carbon atoms at: 1.0 GPa; 1.52, 3.04, 4.56 nm^{-2} coverage; (a) 0.2 nm (b) 0.5 nm (c) 0.8 nm RMS roughness. The carbonyl RDFs are shifted upward by 10 units for clarity. Magnified inset highlights the change in RDF with coverage and RMS roughness.

6.3.2. Friction

Fig. 36 shows the change in average total lateral force, F_L, with average total normal force, F_N, for all of the roughness and coverage combinations considered. The normal and the lateral force on the outer layer of atoms in the slabs (Fig. 32-a) are both time-averaged over the data acquisition period (1.5 ns). This approach is commonplace in confined NEMD simulations of tribological systems [69,185–187,267,297] and is similar how these forces are measured experimentally [188,310]. All of the combinations in Fig. 36 yield a linear increase in F_L with F_N and a non-zero intercept, indicating that all of the systems follow the extended Amontons-Coulomb friction law [185]. A steeper gradient in Fig. 36 indicates a greater friction coefficient while a larger intercept shows a larger Derjaguin offset, F_0, which represents load-independent adhesive forces [187].

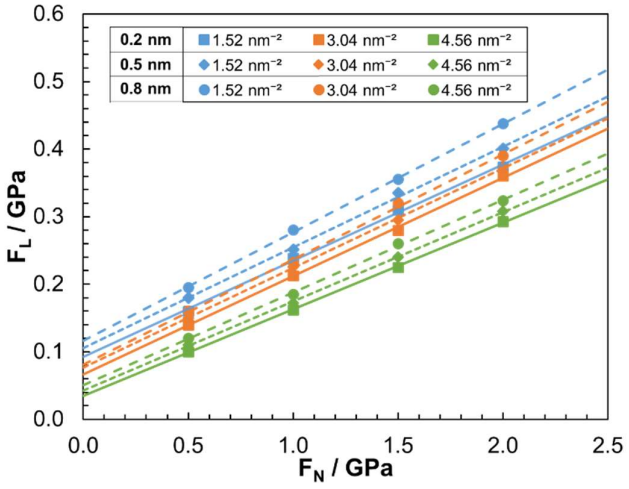

Figure 36. Variation in the average total lateral force, F_L, with the total normal force, F_N, on the outer layer of atoms in the top and bottom slabs, at: 1.52, 3.04, 4.56 nm^{-2} coverage; 0.2 nm, 0.5 nm, 0.8 nm RMS roughness. The intercept of each line represents the Derjaguin offset, F_0, and gradient is the friction coefficient, μ. Error bars, calculated from the standard deviation between the trajectory time-averages, are omitted for clarity, but are of a similar size to the symbols.

Generally, as the surface coverage of stearic acid increases, there is a reduction in lateral force through a reduction in both the gradient (μ) and intercept (F_0). Conversely, as the RMS surface roughness increases, there is an increase in lateral forces due to an increase in both gradient (μ) and intercept (F_0). The variation in the F_0 and μ values (determined from Fig. 36) with surface coverage and RMS roughness are presented in Fig. 37 and Fig. 38 respectively.

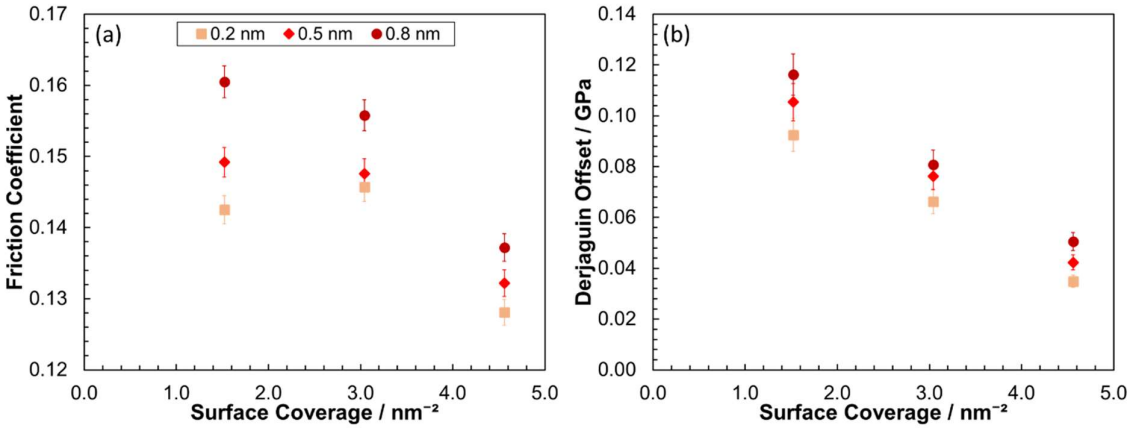

Figure 37. Variation in the friction coefficient, μ, (a) and Derjaguin offset, F_0, (b) with coverage at: 0.2 nm, 0.5 nm, 0.8 nm RMS roughness. Error bars represent the variation between approximate and exact solutions of the Amontons-Coulomb equation.

Fig. 37-a shows that the variation of the friction coefficient, μ, with coverage depends on the RMS surface roughness. At 0.2 nm RMS roughness, the friction coefficient increases by 3% between 1.52 nm^{-2} and 3.04 nm^{-2} coverage and then decreases by 12% between 3.04 nm^{-2} and 4.56 nm^{-2} coverage. This is the same pattern observed in NEMD simulations of stearic acid adsorbed on atomically smooth α-iron oxide surfaces at high sliding velocity (10 m s^{-1}) [267]. However, even with only 0.2 nm RMS roughness, the friction coefficient is higher, and is reduced by less between low and high coverage, than on atomically smooth surfaces [267]. The friction-coverage behaviour changes at 0.5 nm RMS roughness, where the friction coefficient at 1.52 nm^{-2} and 3.04 nm^{-2} are virtually identical, but there is still a decrease of 11% between 3.04 nm^{-2} and 4.56 nm^{-2} coverage. At 0.8 nm RMS roughness, there is a continuous decrease in friction coefficient with increasing coverage, by 5% between 1.52 nm^{-2} and 3.04 nm^{-2} and by 12% between 3.04 nm^{-2} and 4.56 nm^{-2}. The general reduction in the friction coefficient with increasing coverage can be explained through the reduction in interdigitation between stearic acid films on the upper and lower slabs (Fig. 34). The reduction in interdigitation means that the stearic acid molecules do not need to rearrange as much in order to facilitate sliding of the surfaces, resulting in a reduction in lateral force [180]. The increase in friction coefficient between 1.52 nm^{-2} and 3.04 nm^{-2} at 0.2 nm roughness is due to slower rearrangement of the more

closely-packed stearic acid molecules, which leads to a higher friction coefficient at high sliding velocity (10 m s^{-1}) [267]. At higher roughness, the films generally become more liquid-like (Fig. 34 and Fig. 35) and hence molecular rearrangement is faster, leading to a reduction in the friction coefficient at 3.04 nm^{-2}.

Fig. 37-b shows that F_0 decreases linearly with increasing surface coverage to a similar degree at all levels of RMS surface roughness. There is a decrease in F_0 of approximately 40% between 1.52 nm^{-2} and 3.04 nm^{-2} as well as between 3.04 nm^{-2} and 4.56 nm^{-2}. Previous NEMD simulations [185] also observed a similar decrease in F_0 with increasing coverage on atomically smooth slabs; however, there was much less change in F_0 on slabs which contained nanoscale roughness features. Analysis using the smooth particle method (SPM) showed that F_0 was exponentially related to the interface contact area between the upper and lower films [185]. In the current simulations, the interdigitation between the upper and lower films is reduced at increasing coverage regardless of the RMS surface roughness (Fig. 34). This is because the smoother interface (Fig. 33) results in a smaller contact area and thus a lower F_0. The discrepancy between the changes in F_0 with coverage at different levels of roughness may arise from differences in the method used to impose the surface roughness, or perhaps even the force-field applied; this is discussed further below.

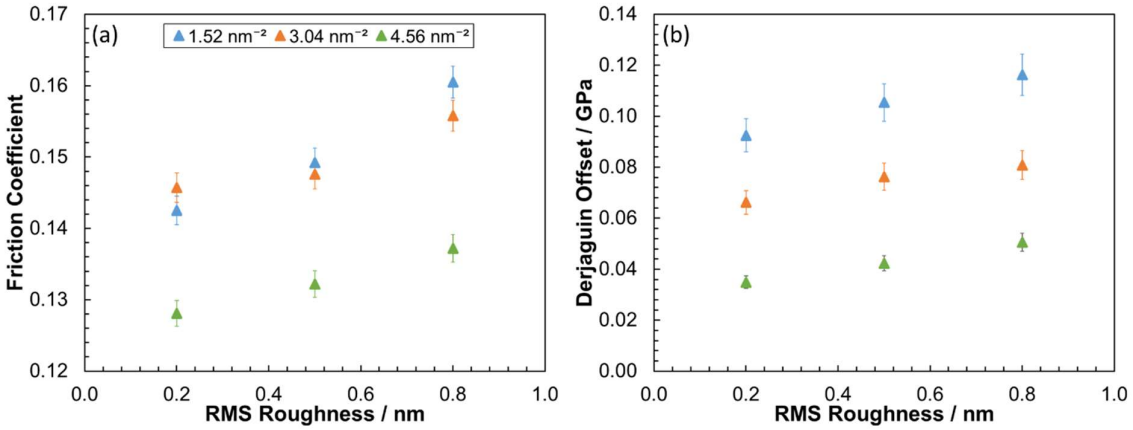

Figure 38. Variation in the friction coefficient, μ, (a) and Derjaguin offset, F_0, (b) with RMS roughness at: 1.52, 3.04, 4.56 nm^{-2} coverage. Error bars represent the variation between approximate and exact solutions of the Amontons-Coulomb equation.

Fig. 38 shows that both μ and F_0 increase linearly with increasing RMS surface roughness. From Fig. 33 and Fig. 34, as well as previous SPM analysis [185], this can be attributed to an increase in interdigitation, leading to increased interface contact area and thus increased adhesion and resistance to sliding. It is not due to local breakdown of the OFM film or solid-solid contact (Fig. 33). The gradients of the increase in μ and F_0 with RMS roughness are similar at all coverages. The gradient for the change in F_0 with RMS roughness suggests a value of just 0.03 GPa at 4.56 nm^{-2} and 0.08 at 1.52 nm^{-2} coverage on atomically smooth surfaces, which agrees well with previous NEMD simulations [185]. However, ref. [185] found that, at low coverage, the change in μ and F_0 were less dependent on roughness than at high coverage. This was explained through the fact that, in solid-like, high coverage films, roughness features below the film are almost perfectly reproduced on top of it; whereas in liquid-like, low coverage films, the stearic acid molecules have more freedom to rearrange themselves according to the surface features of the slab, filling the troughs between asperities and ensuring a more even sliding interface [185]. However, Fig. 33 and Fig. 34 demonstrate that on these larger slabs, which provide a more faithful representation of the statistical distribution of the heterogeneous surface morphology [135], the interface is much smoother at higher coverage, even at 0.8 nm RMS roughness. Another factor to the differences between the current and previous results may be the force-field used to represent the stearic acid molecules. Ref. [185] represented stearic acid with the OPLS-AA force-field [234], which has been shown to yield elevated melting points for long-chain molecules [69]. The use of OPLS-AA [234] may lead to more solid-like films than when a more accurate force-fields for long-chain molecules, such as L-OPLS-AA [26] are used (as they are in the current simulations). Therefore, the use of OPLS-AA [234] may result in high coverage films which are less deformable, leading to rougher interfaces and thus more adhesion and resistance to interfacial sliding at high coverage than if L-OPLS-AA [26] were employed.

From these simulations, it is clear that μ and F_0 are generally decreased with increasing stearic acid coverage and decreased by increasing nanoscale RMS roughness. Generally, the gradients in Fig. 38 are shallower than those in Fig. 37, suggesting that μ and F_0 are influenced more heavily by stearic

acid coverage than nanoscale RMS surface roughness. Moreover, comparing Fig. 37-a to Fig. 38-a and Fig. 37-b to Fig. 38-b, it seems that F_0 is more susceptible to changes in stearic acid coverage and nanoscale RMS roughness than μ (note that the μ *y*-axis is truncated).

Relating these simulations to experiments, the lateral (friction) force measured in OFM-lubricated systems is likely to be heavily influenced by F_0 at lower F_N, i.e. lower applied loads and thus contact pressures (<0.5 GPa) [306]. However, in this case, there is likely to be a significant number of lubricant molecules present which separate the OFM films; and this has been shown to eliminate F_0 [185,267]. Conversely, when F_N is high, as in the boundary lubrication regime, the lateral force experienced is more heavily influenced by changes in μ, and any variation in F_0 becomes less significant (Fig. 36). Therefore, the extended Amonton-Coulomb law under the high load approximation [187,267], $\mu \approx F_L/F_N$, should provide an accurate estimation of the friction coefficient in OFM-lubricated systems in the boundary regime.

The μ value observed with no stearic acid molecules present between the α-iron slabs decreases with increasing RMS roughness; from 0.2 nm (μ = 0.28), to 0.5 nm (μ = 0.25) and 0.8nm (μ = 0.24), which agrees well with previous NEMD simulations using the same α-iron force-field and similar conditions [303]. This trend is due to the reduction in solid-solid contact area at higher roughness. In these previous simulations, slabs with 0.5 nm RMS roughness lubricated with *n*-hexadecane reduced the friction coefficients by 10% at 1.48 nm^{-2} (μ = 0.22) and 30% at 2.96 nm^{-2} (μ = 0.17) compared to the unlubricated case [303]. In the current simulations, at 0.5 nm RMS roughness, a similar coverage of stearic acid yielded friction coefficients reduced by 40% at 1.52 nm^{-2} (μ = 0.149) and 47% at 4.56 nm^{-2} (μ = 0.132) compared to the unlubricated case. The μ value obtained with *n*-hexadecane is both higher and more sensitive to changing coverage than when stearic acid is used. This is because when the rough surface is lubricated with *n*-hexadecane, direct contact of asperities on opposing surfaces occurs; however, this is avoided when the rough surfaces are lubricated by stearic acid, even at low

coverage. This can be attributed to the strong adsorption of the carboxylic acid headgroup to the α-iron surface, which prevents molecules being squeezed out from between asperities [267,306].

In High Frequency Reciprocating Rig (HFRR) experiments [310], μ has also been observed to decrease with an increasing concentration of stearic acid. The concentration of OFMs in a lubricant is generally used as the variable in tribology experiments rather than surface coverage, because it is far easier to measure and control [267]; however, recent depletion isotherm experiments have shown that stearic acid adsorption follows the Langmuir isotherm model [175]. In HFRR experiments on steel surfaces, a reduction in μ with an increasing concentration of stearic acid in *n*-hexadecane has been observed; from 0 mmol dm^{-3} (μ = 0.25), to 0.1 mmol dm^{-3} (μ = 0.18), to 1 mmol dm^{-3} (μ = 0.12), and 10 mmol dm^{-3} (μ = 0.10) [310]. These results agree well with the decrease in μ with increasing coverage of stearic acid observed in these NEMD simulations. The μ values from the simulations are somewhat higher than those from the experiments due to the higher sliding velocities employed (10 vs. 0.05 m s^{-1}) [188], as predicted by stress-promoted thermal activation theory [69,310].

There is much interest in the different friction behaviour of saturated OFMs and those with *Z*-unsaturation in their tailgroups [173–175,188]. Mixtures of these are generally used collectively in commercial additive formulations [11], which may affect their friction reduction performance [188,267]. Our previous NEMD simulations [267] showed that, at a given coverage, films of *Z*-unsaturated OFMs, such as oleic acid, actually had very similar nanoscale structures as those formed by saturated OFMs, such as stearic acid. However, by comparing the friction-velocity behaviour from NEMD simulations and experiments, it was suggested that OFMs with *Z*-unsaturated tailgroups yield lower coverage films than saturated OFMs on steel surfaces [267]. Specifically, in the NEMD simulations low coverage films gave higher friction coefficients which were independent of sliding velocity [267], as experimentally observed for oleic acid [188], whereas high coverage films yielded a low friction coefficient which increased linearly with log(sliding velocity) [267], as experimentally observed for stearic acid [188]. This postulation has recently been confirmed using depletion isotherm

experiments [175] which showed a much lower plateau coverage for oleic acid ($\Gamma \approx 2$ nm^{-2}) than stearic acid ($\Gamma \approx 4$ nm^{-2}) on iron oxide from *n*-hexadecane. Therefore, assuming a high experimental concentration, the low coverage films in these simulations are representative of those observed experimentally for oleic acid, whist the high coverage films are comparable to stearic acid. The structure of the stearic acid films varied less with coverage in the presence of nanoscale RMS roughness (Fig. 34 and Fig. 35); however, the high coverage films gave lower lateral forces (Fig. 35), through reductions in both μ and F_0 (Fig. 37 and Fig. 38). This suggests that OFMs with *Z*-unsaturation will be significantly less effective in reducing friction than those with completely saturated tails on surfaces with nanoscale RMS roughness as well as atomically smooth ones.

6.4. Summary

In this study, we have used large-scale nonequilibrium molecular dynamics (NEMD) simulations to examine the nanoscale structure and friction of stearic acid, a model organic friction modifier (OFM), adsorbed on iron surfaces with 3D nanoscale RMS roughness. Three different coverages of stearic acid (1.52, 3.04, 4.56 nm^{-2}) were adsorbed between iron slabs with three different levels of RMS roughness (0.2, 0.5, 0.8 nm). High (0.5-2.0 GPa) pressures, as experienced between asperities in the boundary lubrication regime, were simulated in order to investigate the robustness of stearic acid monolayers under these rather extreme conditions.

The stearic acid films were able to maintain separation of asperities on opposing surfaces under even the highest RMS roughness (0.8 nm) and lowest coverage (1.52 nm^{-2}) systems simulated, due to strong adsorption of the headgroups which prevented squeeze-out. As a result, the friction coefficient was reduced by more than 40% compared to when no stearic acid molecules were present between the slabs. Moreover, comparing the results of the current study to previous NEMD simulations [303], the stearic acid films were found to be significantly more effective than *n*-hexadecane in reducing friction on surfaces with 0.5 nm RMS roughness. The decrease in friction coefficient moving from *n*-hexadecane to stearic acid is consistent with that observed in boundary friction experiments.

The results of this study suggest that the lateral (friction) force measured experimentally is likely to be heavily influenced by the Derjaguin offset at lower pressure (<0.5 GPa). However, in this case, there is likely to be lubricant present to separate the stearic acid films, which eliminates the Derjaguin offset. Conversely, when the pressure is high, as in the boundary lubrication regime, the lateral force experienced is more heavily influenced by changes in the friction coefficient, and any variation in the Derjaguin offset becomes less significant.

These simulations reiterate the key role of OFM coverage in the film structure and boundary friction reduction. On surfaces with nanoscale roughness, systems with a higher coverage of stearic acid generally yielded lower lateral (friction) forces due to reductions in both the friction coefficient and Derjaguin offset. This is due to the formation of solid-like films, which allow little interdigitation with the opposing film, resulting in smooth interfaces and low resistance to interfacial sliding.

Surfaces that have greater levels of nanoscale RMS roughness have more disordered, liquidike stearic acid films; however, the friction coefficients and Derjaguin offsets is only slightly increased, despite the rather extreme steepness of the roughness features. Therefore, these results suggest that OFMs are only slightly less effective in reducing friction on surfaces with nanoscale roughness as those which are atomically smooth.

This study showed no evidence of any collapse of stearic acid films at asperity tips even at the highest contact pressures; the changes in friction observed with pressure and coverage originated solely from changes in the structure of the OFM films. Since the surface roughness simulated was considerably steeper than the level expected in real engineering components, this suggests that such OFM film collapse between asperities is unlikely on engineering surfaces under the conditions studied.

Chapter 7. Investigation of Friction and Wear of Carbon Nanoparticles Between Iron Surfaces

The work described in this chapter has been partly published in *Tribology Letters* (ref. [203]).

7.1. Introduction

Since the discovery of Buckminster Fullerene (C_{60}), tribologists have been enthused about the possibility of utilising spherical molecules as 'nanoscale ball-bearings' to reduce friction and wear [314]. They are attractive as additives since they have a high degree of structural stability and are chemically unreactive. Moreover, they do not contain elements such as sulphur, phosphorus, and certain metals which can be environmentally harmful and also poison engine exhaust after-treatment devices. Although C_{60} fullerene additives have been shown to reduce friction and wear under specific conditions [206,315–317] their action as molecular ball bearings has been widely disputed [204,205] and their overall performance as potential lubricant additives has been somewhat disappointing [11,204,205]. However, larger carbon nanoparticle additives have shown more promise with regards to boundary friction and wear reduction; specifically carbon nano-diamonds (CND), and carbon nano-onions (CNO) [11]. CNDs can be formed from detonation experiments which yield extremely smooth, spherical particles with a diameter between 1-20 nm [318]. CNDs contain predominantly sp^3 carbons and have a mainly polycrystalline diamond structure. CNOs consist of nested icosahedral fullerenes, with each layer containing $60n^2$ carbon atoms, where n is an integer [319]. They can be formed by electron-beam irradiation of amorphous carbon [319] as well as annealing of CNDs [320], which results in progressive graphitization (sp^3 to sp^2) from the surface to the core of the particle.

Both CND [318,321–326] and CNO [210,211,327–333] have been shown to significantly reduce friction and wear of steel surfaces under boundary lubrication conditions. Specifically, CNO has been shown to reduce the friction coefficient by ≈85% when used as a solid lubricant [331]. Friction coefficient reductions of ≈50% have also been observed compared to a pure base oil when CNO [210] and CND [321] were used as additives. Under high pressure boundary lubrication conditions, much of the base

oil is squeezed out from between asperities [267,275], leading to contact of opposing surfaces and high friction and wear. Large friction and wear benefits can still be observed when CNO and CND are used as additives, suggesting that they are able to reduce the contact of asperities more effectively than the base oil alone [321]. In comparative studies, CNO additives have yielded both lower [210,328] and higher [326] friction and wear than CND additives, though the reasons for this disparity are, prior to this study, yet to be elucidated.

Despite considerable research, there is still much uncertainty as to the friction reduction mechanisms of carbon-based, and indeed most, nanoparticle friction modifier additives [11]. Many different mechanisms have been proposed as discussed in Section 4.2.2. and shown in Fig. 8.

The aim of this study is to use atomistic NEMD simulations to shed further light on the friction reduction mechanisms of carbon nanoparticle additives on α-iron surfaces, chosen as a model for steel which is generally used in experiments and applications. Two types of nanoparticle will be simulated; i) a CNO, modelled by four layers of nested fullerenes ($C_{60}@C_{240}@C_{540}@C_{960}$), with a diameter of approximately 3 nm, ii) a CND, modelled by a diamond sphere, also with a diameter of approximately 3 nm. These particle diameters, although rather small due to computational constraints, still lie well within the experimentally relevant range [318]. Simulating both CND and CNO allows us to assess their relative effectiveness under identical conditions, as well as to uncover any differences in their friction reduction mechanisms.

The NEMD simulations will be conducted under a wide range of conditions, with variables including surface coverage, applied normal pressure and sliding velocity. This should reveal a more complete picture of how carbon nanoparticle additives operate at the nanoscale under boundary lubrication conditions. The fact that NEMD simulations are limited to the nanoscale means that it is not feasible for them to recreate all situations where the nanoparticles may provide a reduction in friction and wear (e.g. Fig. 8-d); however, they can yield unique insights into the nanoscale tribological behaviour of the nanoparticles confined between asperities, which are inaccessible to experiments [215]. The

remainder of this manuscript will be presented as follows; first, details of the simulation methodology are given, this is followed by discussion of the results in the context of the application of CNO and CND as lubricant additives, before final conclusions are drawn.

7.2. Methodology

Classical NEMD simulations were performed in LAMMPS [255]. In all of the simulations, two atomically smooth (100) slabs of α-iron with dimensions (*xyz*) of approximately 9.0 × 9.0 x 3.0 nm were used as the substrates, representing a single asperity contact (Fig. 39-a). Nanoparticles were confined between the two slabs and periodic boundary conditions were applied in the *x* and *y* directions (Fig. 39-c). No base oil molecules were included in these simulations since, under high pressure, boundary conditions, we can assume that most of them will be squeezed out from between asperities [267,275], and thus the nanoparticles will support the majority of the load. Adding an arbitrary number of base oil molecules in these simulations would be counterproductive, since the periodic boundary conditions mean that molecules cannot be squeezed out from between asperities as they would be in experimental systems and they would therefore provide additional, unphysical load support.

The C-C interactions in CNO and CND are modelled using an updated version of the adaptive intermolecular reactive empirical bond order (AIREBO) potential [334], known as AIREBO-M [335]. AIREBO-M uses the same functional form as the hydrocarbon second generation REBO2 potential [336] for covalent C-C interactions, with an additional Morse term to represent the van der Waals interactions. The Morse potential is 'switched off' at the onset of C-C bond formation in order to prevent disruption of the REBO2 energies. The Morse potential replaces the Lennard–Jones potential used in the original AIRBEO, which has been shown to yield unphysical results for carbon systems subjected to high pressures [335]. The use of AIREBO-M rather than AIREBO is expected to more accurately reproduce the interlayer distances in the CNO nanoparticles, as well as interactions between neighbouring carbon nanoparticles, under the high normal pressures applied.

In order to accurately model plastic deformation within the slab, the Fe–Fe interactions are modelled using the embedded atom model (EAM) potential [313]. Iron and steel surfaces quickly become oxidized when exposed to air, which significantly reduces the adhesion force between contact surfaces in experimental systems [303]. Therefore, a Lennard–Jones potential was used for Fe–Fe interactions between atoms in opposing slabs (Fig. 39-a) in order to mimic the reduced adhesion between oxidized surfaces [300]. The Lennard–Jones parameters, ε = 0.02045 eV and σ = 3.21 Å, were used for this interaction, as have been successfully utilised in previous tribological NEMD simulations [300,303].

The Fe–C van der Waals interactions are also modelled using a Lennard–Jones potential. The Lennard-Jones parameters used here, ε = 0.02495 eV and σ = 3.70, were parameterised for MD simulations of carbon nanotube growth on iron surfaces [337] and have since been successfully applied in tribological NEMD simulations of CNDs between iron surfaces [214] as well as nano-scratching of iron by diamond tips [338,339].

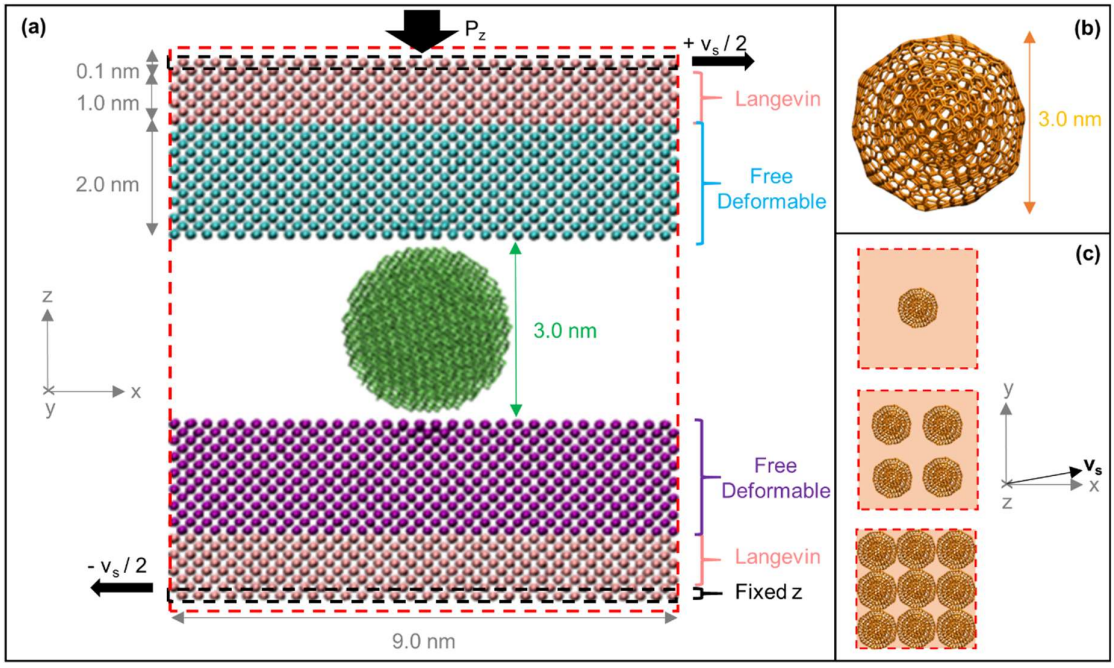

Figure 39. (a) Image of representative system set up for NEMD simulations (CND, θ = 0.11). Carbon-carbon bonds are shown in green for CND and orange for CNO, Fe atoms are shown in pink for the thermostatted and fixed atoms and cyan (top) or purple (bottom) for the deformable atoms. The red dotted lines indicate periodic boundaries. Rendered using VMD [264]. (b) Image of four-layer CNO particle (C_{60}@C_{240}@C_{540}@C_{960}). (c) Schematic showing the nanoparticle coverages simulated; θ = 0.11, 0.44 and 1.00. Velocity, v_s, applied at 10° to the *x*-axis of the periodic box.

All systems were constructed using the Materials and Processes Simulations (MAPS) platform from Scienomics SARL. A representative example of the systems simulated in this study is shown in Fig. 39-a.

The MD equations of motion were integrated using the velocity-Verlet algorithm with an integration time-step of 1.0 fs. A Langevin thermostat [55], with a time relaxation constant of 0.1 ps was used in all of the simulations in order to maintain a temperature of 300 K. The thermostat acted only on the atoms in the outer 10 Å (*z*) of each slab (Fig. 39-a) and was applied in the direction perpendicular to the both the sliding and compression (*y*) [214,267]. This method is known to be advantageous over direct thermostatting of systems in confinement, which has been shown to significantly affect their behaviour during sliding [65].

A wide phase-space was mapped in order to capture any changes in the friction reduction mechanism of the nanoparticles under boundary conditions. Specifically, the fractional coverage of the nanoparticles, θ, the applied normal pressure, P_z, and sliding velocity, v_s, were all varied independently. A maximum coverage (θ = 1.00) was simulated by including nine nanoparticles in direct contact with each other in a primitive cubic arrangement between the slabs. A medium (θ = 0.44) and low (θ = 0.11) coverage were also simulated by including four and one nanoparticles between the slabs respectively. The nanoparticles were initially positioned to give maximum possible separation from one another (Fig. 39-c). A simulation with no nanoparticles between the sliding surfaces was also conducted in order to estimate the percentage friction reduction achieved with CNO and CND.

The nanoparticles were initially positioned 3 Å from the slabs prior to energy minimisation. The systems were energy minimised, compressed and equilibrated before sliding was applied. After energy minimisation, the outer-shell of CNO became slightly faceted (Fig. 39-b) [320], whereas CND remained entirely spherical (Fig. 39-a). The normal pressure, P_z = 1.0, 2.0, 3.0, 4.0 and 5.0 GPa was applied to the slab by adding a constant force in the *z*-direction to the outermost layer of atoms in the top slab whilst keeping the outermost layer of atoms in the bottom slab fixed in the *z*-direction, as is

common in confined NEMD simulations [214,267]. The target pressure was reached gradually by increasing the normal force from that corresponding to $P_z/100$, $P_z/20$, $P_z/10$, $P_z/2$ and finally P_z during 100 ps increments. As the normal pressure was increased, the slab separation initially varied in a damped harmonic manner, so sliding was not applied until a constant average slab separation was obtained at the target pressure, P_z.

A range of sliding velocities, v_s = 5, 10 and 20 m s^{-1}, were applied in order to monitor any change in the friction coefficient as well as the rolling/sliding motion of the nanoparticles. While lower sliding velocities are desirable to match those used in boundary friction experiments (typically mm s^{-1}), they are not yet accessible using atomistic NEMD simulations of this scale [267]. When compressive oscillation became negligible, a velocity of $v = \pm v_s/2$ was added to the outermost layer of atoms in each slab (Fig. 39-a). In the low coverage and high pressure simulations, the nanoparticles ploughed through the surface to produce nanoscale wear tracks. Therefore, when the sliding velocity was applied parallel to the *x*-axis of the periodic box yield, the nanoparticles reworked their own wear tracks as they passed through periodic boundaries, leading to an unphysical decrease in the friction coefficient. Consequentially, for all of the results given below, the sliding velocity was applied at a 10° angle from the *x*-axis of the periodic box (Fig. 39-c), which was sufficient to prevent the nanoparticles from reworking their own wear tracks after passing through the periodic boundary [215]. Sliding simulations were conducted for 10-40 ns, depending on the sliding velocity. All simulations were run for long enough to yield a sufficient sliding distance (20 nm) in order to obtain a steady state friction coefficient, with an uncertainty less than 10%. This uncertainty was estimated as the standard deviation between the block average friction coefficient values, which were calculated every 0.5 nm after 2.0 nm of sliding. It was also confirmed for a representative sample that the standard deviation between ensemble average friction coefficients from three independent trajectories yielded a similar level of uncertainty.

7.3. Results and Discussion

In this study, we use NEMD to provide unique insights into the nanoscale friction and wear reduction mechanism of carbon nanoparticles CND and CNO. The kinetic friction coefficient, μ, was obtained using the extended Amontons−Coulomb law under the high load approximation: $\mu = F_L/F_N$, where F_L and F_N are respectively the average total lateral and normal forces acting on the outer layer of atoms in each slab. Variations of the friction coefficient with sliding distance are presented for CND and CNO under a range of coverages, pressures and sliding velocities. The variation in the average friction coefficient with pressure and indentation depth are also presented and linked to macroscopic predictions. The indentation depth of the nanoparticles into the slabs, temperature profiles of the systems during sliding, and angular velocities which indicate whether the nanoparticles are rolling or sliding, are also included in order to gain more insight into the friction reduction mechanisms of the nanoparticles. All results are presented as block averages, calculated every 0.5 nm of sliding. Simulation snapshots are included to enable visualisation of important changes in behaviour under different simulation conditions. The results section is divided into three sections corresponding to the variation in friction and wear due to the three main variables investigated in this study; the nanoparticle coverage (3.1), the normal pressure (3.2) and the sliding velocity (3.3).

7.3.1. Effect of nanoparticle coverage

Results for NEMD simulations with no nanoparticles between the slabs are presented first in order to enable estimation of the benefits of different coverages of CNO and CND.

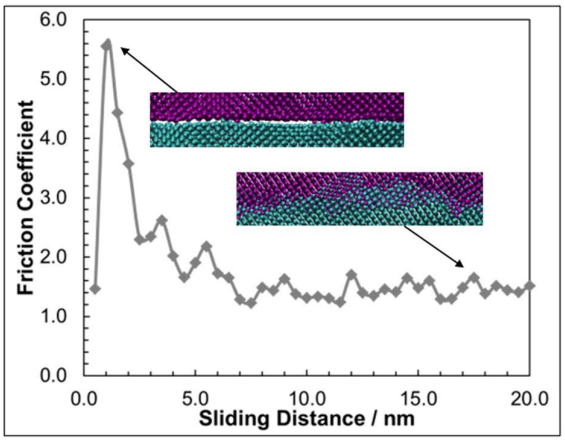

Figure 40. Dry sliding of α-iron slabs, variation in the friction coefficient with sliding distance. For P_z = 1.0 GPa and v_s = 10 m s^{-1}. Inset images show interface after 200 and 2000 ps (2 and 20 nm of sliding).

Fig. 40 shows that when α-iron slabs are slid against one another without nanoparticles between them, the friction behaviour varies significantly with sliding distance. Initially, there is a sharp increase to a high friction coefficient ($\mu > 5$) as a result of the very high commensurability of the opposing surfaces which 'locks' them together (Fig. 40). After around 1 nm of sliding, a transfer film forms between the opposing surfaces (Fig. 40) [214]. Here, the friction coefficient decreases [213,303] and reaches a steady state of $\mu \approx 1$, which is comparable to the experimentally observed value for the dry sliding of steel surfaces [331,340], thus validating this surface model for the reproduction of experimental friction coefficients.

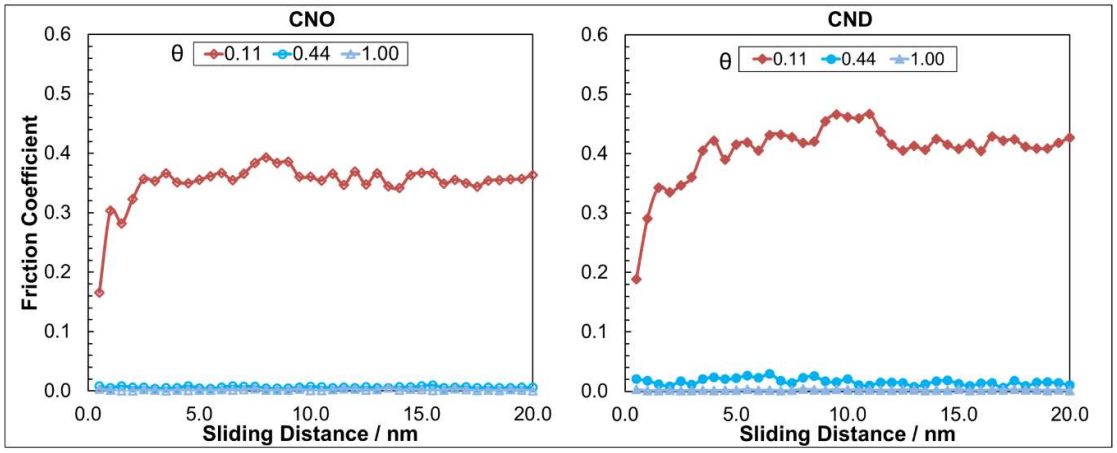

Figure 41. Effect of carbon nanoparticle coverage, θ, on the friction coefficient. For P_z = 1.0 GPa and v_s = 10 m s^{-1}.

Fig. 41 shows the change in the friction behaviour when CNO and CND nanoparticles are present at various coverages when P_z = 1.0 GPa. Comparing Fig. 40 to Fig. 41 indicates that the friction coefficient is reduced considerably in the presence of CNO and CND at all nanoparticle coverages considered. Fig. 41 also shows that the friction coefficient varies significantly with nanoparticle coverage. Since the apparent contact area decreases at lower coverages, the local pressure on each particle increases. The nanoparticles do not indent into the slabs at 0.44 coverage and 1.00 coverage (Fig. 42), which leads to very low friction coefficients (<0.05) that remain relatively constant through the course of the sliding simulation (Fig. 41). Here, the friction coefficient arises purely from resistance to rolling/sliding due to van der Waals interactions between the nanoparticle and the slabs, which dislodges surface atoms from their lattice positions, thus increasing the shear stress. At 0.11 coverage, the friction coefficient sharply increases to around 0.35 for CNO and 0.40 for CND and then reaches a steady state after approximately 2 nm of sliding. This is because, at 0.11 coverage, there is significant indentation of the nanoparticles into the surface, which plough nanoscale wear tracks during sliding (Fig. 42). The ploughing action of the nanoparticles causes plastic deformation within the slab, leading to an additional, much larger, contribution to the friction coefficient [341]. As has been observed experimentally [210,328], CNO yields a lower friction coefficient than CND in these simulations.

Experiments which have shown CND to be more effective in reducing friction [326] probably achieved better dispersion of CND than CNO, leading to a higher surface coverage.

The 0.11 coverage CNO and CND systems show a slight increase in the friction coefficient after one pass of the surface (≈9 nm), due to contact of the nanoparticles with wear debris ejected during the first pass of the surface. However, after ≈2 nm more sliding, the friction coefficient returns to the same as value before passing through the periodic boundary, suggesting that any atomic-scale roughness present on the surface will be removed by the nanoparticles and will have a negligible influence on the friction coefficient. This also indicates that surface polishing due to the presence of CNO and CND may be another contributor to low friction, as has been suggested previously from experimental results [321,325].

The friction-coverage behaviour agrees well with boundary friction experiments which, at low concentrations, show a decrease in friction coefficient when the concentration of CND or CNO is increased [330,332]. At 0.11 coverage (Fig. 41), the friction coefficient is reduced by approximately 75% relative to when no nanoparticles are present (Fig. 40). This percentage friction reduction agrees broadly well with results of boundary friction experiments which used carbon nanopearls (larger, ≈150 nm layered nanoparticles) as a solid lubricant (≈85%) [331], as well as when CNO and CND are used as additives in a base oil (≈50%) [210,321]. The very low friction coefficients and zero wear observed at 0.44 and 1.00 coverage in these simulations have not been detected in boundary friction experiments of CNO and CND. Whilst this can partly be attributed to the lack of viscous friction from the presence of a base oil in these simulations, it also suggests that high nanoparticle coverages were probably not reached in the experiments. This is because, although nanoparticle coverage intially increases with concentration, at higher concentrations the nanoparticles begin to agglomerate and become too large to enter the contact, leading to a reduction in surface coverage [324]. Therefore, CNO and CND nanoparticles may be even more effective in reducing boundary friction and wear should better dispersion methods to be developed in order to yield high surface coverages.

Fig. 42-a shows the indentation depth, d(z), of the nanoparticles into each of the α-iron slabs. This is monitored throughout the sliding simulation by subtracting the *z*-extension of the nanoparticle, Part(z), from the *z*-separation of the outer layer of undisturbed atoms in the top and bottom slabs, Slab(z), and dividing this value by two, as shown in Fig. 42-b. Slab(z) excludes slab atoms which form part of the wear debris during the ploughing of the nanoparticles (Fig. 42-b) [215]. Part(z) remains relatively constant through the course of the simulation for both nanoparticles, but is fractionally lower for CNO (28 Å) than CND (30 Å), suggesting that the CNO particles compress slightly under the applied normal pressure (1.0 GPa).

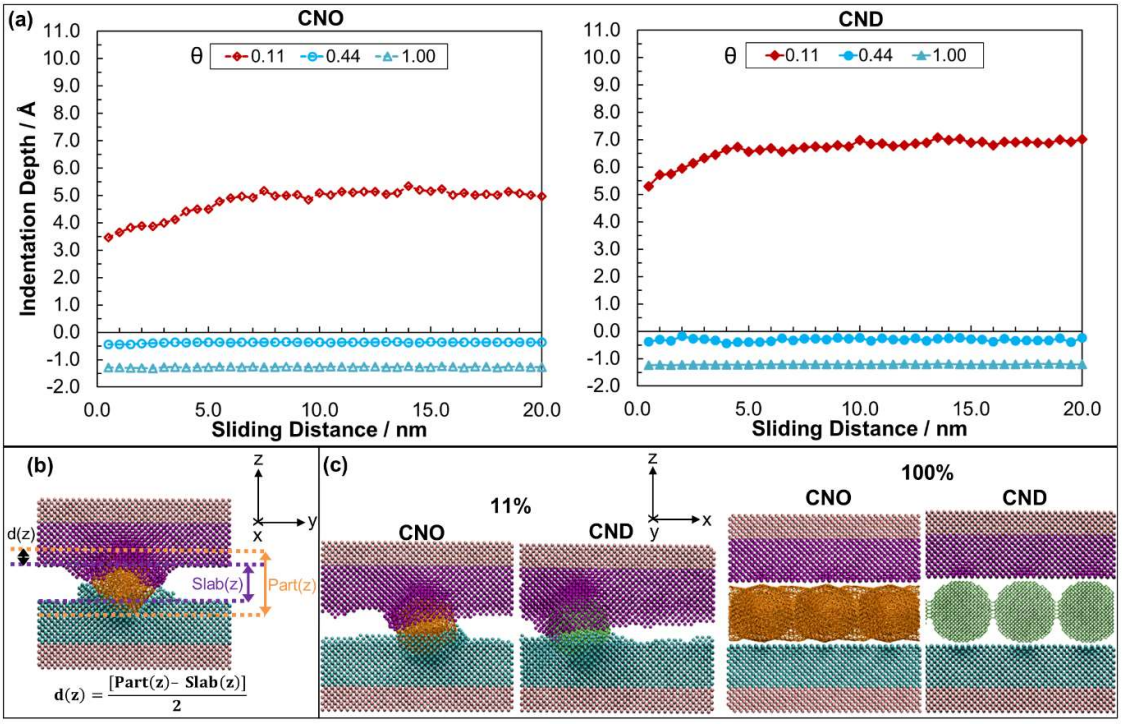

Figure 42. (a) Effect of nanoparticle coverage, θ, on the indentation depth, d(z), of nanoparticles into slabs. For P_z = 1.0 GPa and v_s = 10 m s^{-1}. (b) Schematic viewed along *x* showing the ploughing of the wear track by CNO after 10 nm of sliding; indicating definitions of Slab(z), Part(z) and d(z). (c) Images of 0.11 and 1.00 coverage systems along *y* after 10 nm of sliding.

When θ = 0.44 and θ = 1.00, the indentation depth value in Fig. 42-a is negative, indicating that there is no overlap of the average z-positions of the outermost layer of atoms in the nanoparticles and the

slabs. This results in zero wear and a very low friction coefficient (Fig. 41). The average position of the nanoparticles is slightly closer to the slabs when θ = 0.44 than when θ = 1.00, as well as for CND relative to CNO, leading to stronger slab-nanoparticle van der Waals interactions and somewhat higher friction coefficients (Fig. 41). At 0.11 coverage, there is significant indentation of the α-iron slabs by the nanoparticles, which plough atomic-scale wear tracks during sliding (Fig. 42). The nanoparticles are indented into the slabs even before the onset of sliding; CND (5 Å) to a slightly greater extent than CNO (3 Å). As the nanoparticles plough through the slabs, indentation increases slightly, with CND (7 Å) remaining more indented than CNO (5 Å). This suggests that the lower friction coefficient for CNO relative to CND at 0.11 coverage (Fig. 41) is a result of reduced indentation into the slab (Fig. 42), due to its softer layered structure.

An important observation is that for both CNO and CND nanoparticles when θ = 0.11, plastic deformation of the surface around the nanoparticle occurs rather than plastic deformation of the nanoparticle itself. There was no evidence of exfoliation of CNO in any of the simulations, which is consistent with HRTEM images taken after boundary friction experiments [210] and high-pressure Raman spectroscopy [342,343] which suggest very high compressive strength owing to the concentric, nested structure of CNO.

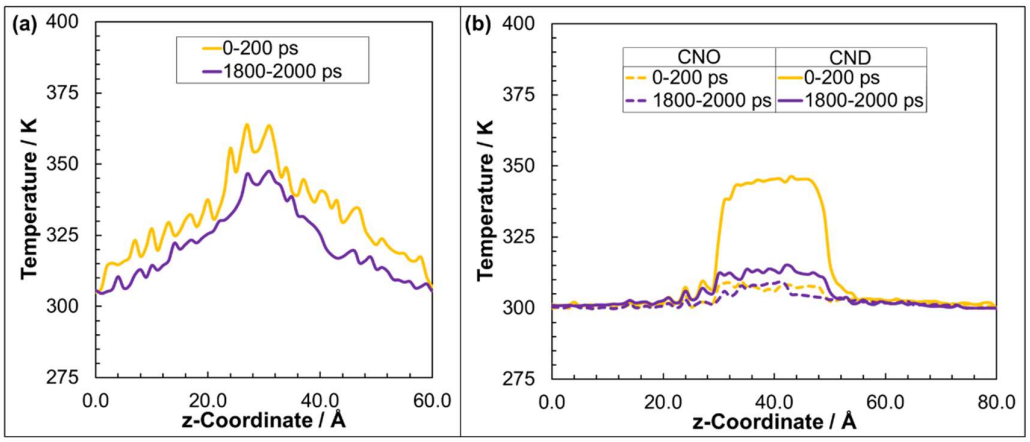

Figure 43. Time-averaged temperature profile in *z* for the system after 200 ps and 2000 ps (2 nm and 20 nm of sliding) for when no nanoparticle is present (a) and for θ = 0.11 CNO and CND (b), for P_z = 1.0 GPa and v_s = 10 m s^{-1}.

In boundary lubrication, contact between opposing surfaces leads to adhesion and high friction, which can in turn lead to an increase in surface temperature. Temperature profiles in *z* are shown for when no nanoparticle is present (Fig. 43-a) and with CNO and CND at 0.11 coverage (Fig. 43-b), at the start (0-200 ps) and end (1800-2000 ps) of the sliding simulations. The temperature profiles show the expected parabolic shape for boundary-thermostatted systems during sliding, with a maximum temperature in the centre of the system [156]. Both nanoparticle systems exhibit lower maximum temperatures (CND 315 K, CND 305 K) compared to when no nanoparticle is present (350 K) at the end of the sliding simulation. The CND system showed a large initial increase in temperature within the nanoparticle due to the high thermal conductivity of diamond; however, the maximum temperature at the end of the sliding simulation is similar to that for CNO, and much lower than when no nanoparticle is present. It should be noted that the exclusion of electronic effects in classical MD simulations leads to an underestimation of metal thermal conductivity, and is responsible for the relatively high temperature gradients within these systems [215]. Nonetheless, a similar reduction in surface temperature as found in these simulations has also been observed in previous experimental studies. For example, Ivanov *et al.* [323] observed a reduction in surface temperature from approximately 400 K to 340 K for formulations which included CND compared to a pure base oil. From these simulations, this reduction in surface temperature can be attributed to the reduction in contact of opposing surfaces, which leads to a decrease in frictional heating, as exemplified in by the lower friction coefficients in the nanoparticle-containing systems (Fig. 40 vs. Fig. 41). The slight reduction in the maximum temperatures of systems containing CNO relative to CND at the end of the sliding simulation can be rationalised using the same arguments (Fig. 41).

7.3.2. Effect of pressure

In order to further probe the friction and wear behaviour of CNO and CND from the onset of indentation, variable pressure simulations were also conducted. Fig. 44 shows the variation in the friction coefficient with sliding distance when $\theta = 0.44$ and for pressures between 1.0 and 5.0 GPa. The slight increase in the friction coefficient after 9 nm is not identifiable in the 0.44 coverage results (Fig.

44) because there are multiple particles which pass through periodic boundaries after different sliding distances. From Fig. 44, it is clear that CND yields a higher friction coefficient than CNO at all pressures simulated. Moreover, the friction behaviour suggests that the onset of indentation at 0.44 coverage occurs at lower pressure for CND (2.0 GPa) than for CNO (3.0 GPa).

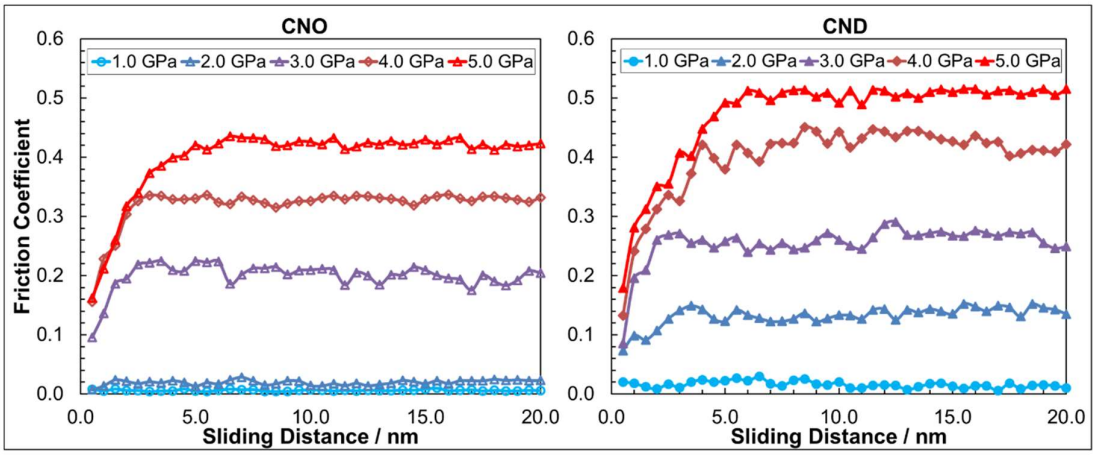

Figure 44. Effect of contact pressure, P_z, on the friction coefficient. For P_z = 1.0 – 5.0 GPa, θ = 0.44 and v_s = 10 m s^{-1}.

Fig. 45 clearly indicates the differences in nanoparticle indentation depth between the CNO and CND systems. For example, at 2.0 GPa, the CND nanoparticles become indented into the slabs while the softer CNO nanoparticles do not. At 3.0 GPa and above, both CND and CNO nanoparticles become indented into the slab; however, CND nanoparticles to a greater extent than CNO. Even at the highest pressure (5.0 GPa), the undisturbed layers of atoms in the opposing slabs remain well-separated (Slab(z) ≈ 10 Å), though some wear debris atoms ejected from opposing slabs do come in to contact. This contact seems to have only a minimal effect on the friction coefficient (Fig. 44), and ploughing of the nanoparticles remains the dominant factor. The contribution to friction from adhesion between atoms in opposing slabs may become more significant at higher pressures, or lower coverages than those simulated here, when the nanoparticles are no longer able to maintain separation of opposing slabs.

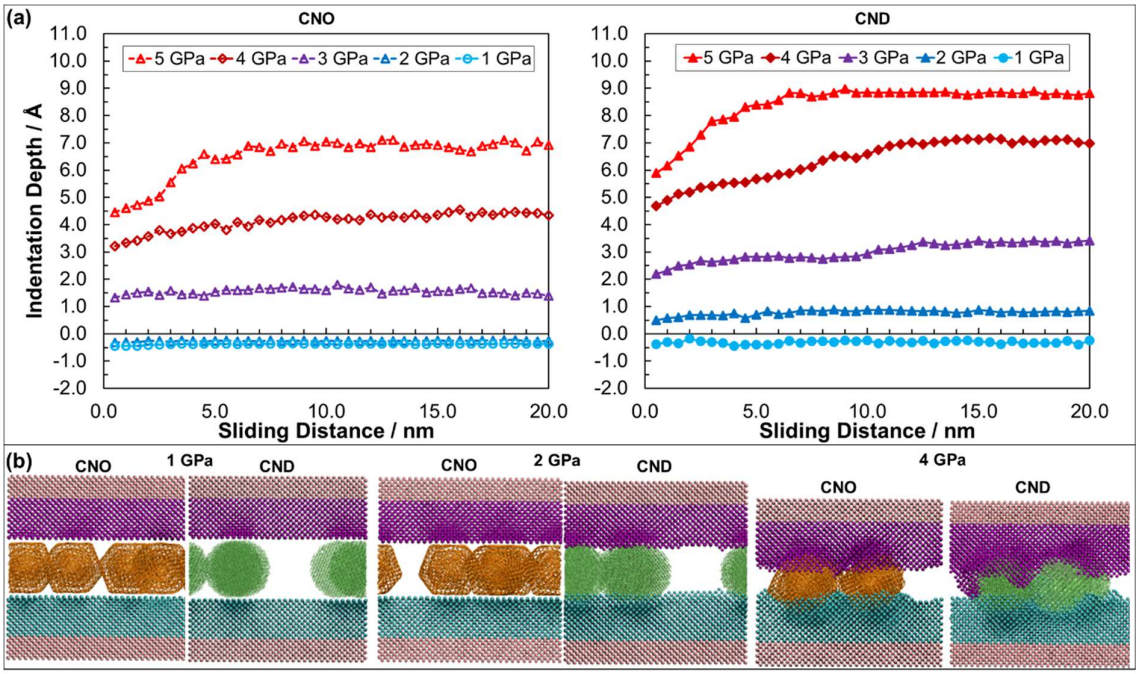

Figure 45. (a) Effect of pressure, P_z, on the indentaion depth, d(z). For P_z = 1.0 GPa to 5.0 GPa, θ = 0.44, v_s = 10 m s^{-1}. (b) Images of 0.44 coverage systems along *y* after 10 nm of sliding at different pressures.

The 0.44 coverage at 4.0 GPa (Fig. 44) and the 0.11 coverage at 1.0 GPa (Fig. 42) are equivalent in terms of the force on each nanoparticle. The differences in the friction and wear behaviour between these two cases shows that the effect of pressure and coverage are subtly different. At 0.44 coverage, there is slightly less indentation into the surface than at θ = 0.11 due to a more even distribution of the force over the slabs. This leads to a very slightly (5%) lower friction coefficient at 0.44 than at 0.11 coverage at equivalent pressure per nanoparticle.

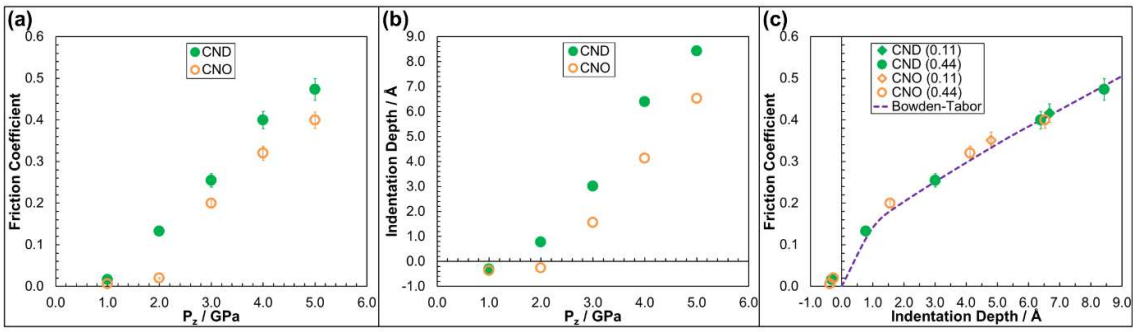

Figure 46. (a) Variation in the friction coefficient with normal force. (b) Variation in the indentation depth with normal force. (c) Variation in the friction coefficient with the indentation depth. The dotted line in (c) indicates the Bowden-Tabor prediction from Equation 2. Error bars indicate the standard deviation between block average friction coefficient values.

Fig. 46-a shows the variation in the average friction coefficient with pressure. Above 2.0 GPa for CNO and 1.0 GPa for CND, the friction coefficient increases rapidly with pressure due to increasing indentation of the nanoparticles. This increase in friction coefficient with pressure has been also observed in previous NEMD simulations of hard nanoparticles [215] as well as in nano-scratching simulations of α-iron surfaces by diamond tips [338,339]. This relationship has also been observed experimentally for CNO additives [330,333]; however, other boundary friction experiments have shown increasing wear, but decreasing friction, with increasing pressure [210]. In these experiments, the decrease in friction with increasing pressure was evident both in the presence or absence of nanoparticles in a base oil [210]. This is probably because, at higher pressure, there is increased contact of asperities, which become smoothed over experimental timescales, resulting in increased wear but decreased friction. This experimentally observed decrease in friction coefficient with increasing pressure may sometimes supersede the increase which has been observed in these and previous [215] NEMD simulations of hard nanoparticles.

From Fig. 46-b it is clear that, after the onset of indentation, the nanoparticle indentation depth increases almost linearly with pressure, as is anticipated from previous nanoindentation experiments [344] and simulations [338,339]. In these current simulations, CND indents more than CNO at equal

pressure, which may be due to higher hardness. The normal hardness of a material, H_N, can be directly related to its indentation depth through: $H_N = F_N / A_N$, where A_N can be estimated for a spherical indenter through $A_N = \pi[R^{*2} – (R^* – d(z))^2]$. Here R* is the apparent indenter radius, given by: $R^* = R + r_c$, where R is the radius of the nanoparticle (15 Å), r_c is the cut-off for the repulsive part of the C-Fe potential (3.8 Å) [339] and d(z) is the indentation depth. Note that the cut-off for the van der Waals C-Fe potential is used here purely to assign the radius of the indenter, and no attractive or repulsive forces are considered. Conventionally, this relationship is used to calculate the hardness of the substrate rather than the indenter, but given that the hardness of the α-iron slab is the same in both cases, the difference between the contact areas estimated from the indentation depths for CNO and CND at a given pressure can be used to give an approximation of their relative hardness. CND nanoparticles are generally around 25% more indented than CNO (Fig. 46-c), suggesting that CND nanoparticles are approximately 25% harder than CNO. This 25% difference in hardness is much less than the difference in hardness between diamond and graphite, suggesting that the relatively high hardness of CNO is mainly due to its concentric, nested structure.

The ploughing of wear tracks in these simulations represents a nanoscale wear process, with the amount of wear being proportional to the nanoparticle indentation depth [215]. Purely through the difference in indentation depths in these simulations, 25% more wear in systems lubricated by CND than systems lubricated by CNO would be expected at equal coverage and pressure. Indeed, this difference is similar to that which has been observed experimentally [210]. It is important to note that both nanoparticles are expected to reduce wear compared to systems not containing nanoparticles, because maintaining separation of opposing slabs and reducing contact of asperities has been shown to be more significant than the nanoscale wear caused by the indentation of the nanoparticles [210,318,326,328]. However, since these processes occur on different length-scales, it is not possible to quantify this difference using the current simulations.

Fig. 46-c shows the relationship between the indentation depth and the friction coefficient for all of the 0.44 and 0.11 coverage data. The observed relationship is well predicted by the analytical expression (Equation 2) developed by Bowden and Tabor [345] to describe the friction coefficient of spherical indenters. The expression assumes that the same material hardness applies in both the normal and lateral directions; which has been confirmed in previous simulations of α-iron [339]. This means that the friction coefficient, μ, can be predicted through the ratio of the nanoparticle areas 'seen' by the substrate in the normal and lateral direction, given by:

$$\mu = A_n/A_L = [2\theta_s - \sin(2\theta_s)]/[\pi \sin^2(\theta_s)] \quad \text{(Equation 2)}$$

where θ_s is the semi-angle at the centre of the nanoparticle subtended by the groove and is obtained from: $\cos(\theta_s) = (R^* - d)/R^*$. Equation 2 predicts that the friction coefficient will increase with indentation depth since the projected lateral area (A_L) increases faster than the normal area (A_N). Using Equation 2, we calculate the friction coefficient as a function of indentation depth, see the dashed line in Fig. 46-c. The simulation results agree well with the calculated friction coefficient values for the range of indentation depths encountered. This suggests that, at the small indentation depths which occur in these simulations, the assumptions of Bowden and Tabor [345] are fulfilled and that the evolution of the friction coefficient with depth for the spherical nanoparticle can be well predicted from purely geometric considerations. This finding agrees with previous NEMD simulations of fixed hard abrasive particles on atomically-rough α-iron surfaces [215]. The simulated friction data lies slightly above the Bowden-Tabor prediction, particularly at low indentation depths, suggesting another contribution to the friction coefficient. This contribution can be attributed to the van der Waals force between the opposing slabs and the nanoparticles. Although the indentation depth is greater at each pressure for CND than CNO, the friction coefficient is almost identical at equal indentation depth.

The friction coefficient results obtained in these simulations generally agree well with experimentally observed values for CNO and CND boundary friction experiments using base oils containing CNO and

CND. These generally yield friction coefficients of ≈ 0.1 [210,321–331] , though higher (≈ 0.3) values have also been observed [318]. The frictions coefficients obtained experimentally suggest that nanoparticles are indented into the surface because friction coefficients from simulations with no nanoparticle indentation (high coverages and low pressures) are much lower (< 0.05). This is supported by HRTEM images of the wear track after sliding which show indentation of the nanoparticles into the surface for both CNO [210] and CND [321]. Comparing experimentally observed friction coefficients (≈ 0.1) to Fig. 46-c suggests a relatively small indentation depth (≈ 1 Å). These simulations also indicate that indentation depth is very sensitive to nanoparticle coverage and pressure, meaning that indentation depth probably varies significantly around this value within a macroscopic contact, depending on the local conditions.

The relatively small amount of indentation observed experimentally and in these simulations may actually be important to the effective lubrication of hard nanoparticles such as CND and CNO. It has been argued previously that some adhesion with the surface must be necessary in order to maintain an adequate coverage of nanoparticles to maintain separation of contact surfaces [11]. The high specific surface area of CND and CNO, up to 400 $m^2 g^{-1}$, results in reasonably strong surface-active and adsorption properties [318]. However, given that CND and CNO are non-polar and only have relatively weak short-ranged van der Waals interactions with the surface, they probably show less surface-activity than, for example, conventional amphiphilic organic friction modifier additives. As a consequence, some indentation into the surfaces could ensure that nanoparticles remain on the surface following compression rather than returning into the oil. This may be crucial in order to maintain an adequate coverage to effectively separate contact surfaces and reduce friction and wear [11].

The α-iron slabs used in these simulations are softer than carbon steel and iron oxide, the most relevant surfaces experimentally and industrially, meaning that indentation is more pronounced in these simulations than might be expected experimentally. For example, recent nanoindentation

experiments suggested that Fe hardness increases linearly with C content, by up to an order of magnitude for pure Fe_3C (cementite) [346]. However, both CND and CNO nanoparticles are harder than carbon steel and hence the high boundary pressure is expected to be accommodated in the same manner, with the slab deforming around the nanoparticle. That said, for a given surface coverage and pressure, the indentation depth of the nanoparticle into the slab will be less in carbon steel than α-iron. This in turn will result in reduced wear and a lower friction coefficient; *i.e.* points on Fig. 46-c would be shifted towards the bottom left region of the curve. Nonetheless, assuming that the normal and lateral hardness are equal, the dotted line in Fig. 46-c should still predict the friction coefficient of nanoparticles between harder surfaces. Conversely, on softer surfaces [207], such as tribofilms formed from the anti-wear additive zinc dialkyldithiophosphate (ZDDP), the indentation depth may be greater at a given coverage and pressure than suggested by these simulations. In this case, these hard nanoparticles may cause high friction and accelerated wear by abrading tribofilms which are reformed, and then abraded again; this is the same mechanism which has been proposed for increased wear from model diesel soot (carbon black) in ZDDP-containing formulations [347]. This contrasts to experimental studies using diesel soot as an additive in the absence of ZDDP, where a significant decrease in friction and wear was observed [348,349]. These findings suggest that CNO and particularly CND may lead to increased friction and wear in the presence of ZDDP, a possibility which should certainly be investigated experimentally.

7.3.3. Effect of sliding velocity

Under the range of sliding velocities simulated (v_s = 5, 10, 20 m s^{-1}), there was negligible change in the friction and wear behaviour. This is shown for at high pressure (P_z = 4.0 GPa) when the nanoparticles indent into the surface in Fig. 47-a, though the same trends are evident at lower pressure (P_z = 1.0 GPa) where the nanoparticles do not indent. However, the average angular velocity of the nanoparticles, which indicates their rolling motion, did change with the sliding velocity (Fig. 47-b). In Fig. 47-b, a value of zero for the angular velocity indicates that the nanoparticles are sliding, a positive

value indicates that the nanoparticles are rolling with the sliding direction, whilst a negative value indicates that the nanoparticles are rolling against it.

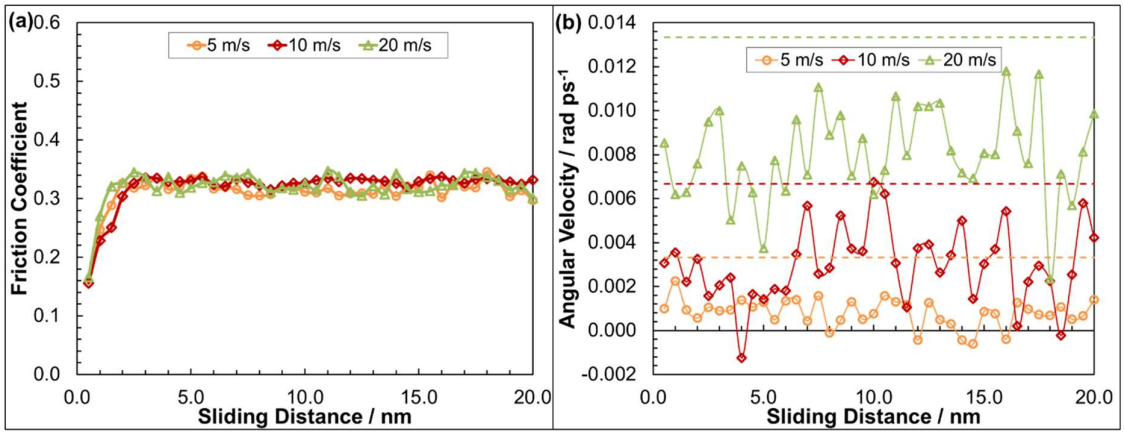

Figure 47. (a) Effect of the sliding velocity, v_s, on the friction coefficient. (b) Average angular velocity of one of the nanoparticles with sliding velocities at different sliding velocities, v_s = 5, 10, 20 m s^{-1}. Data are shown for CNO at θ = 0.44, P_z = 4.0 GPa. Horizontal dotted lines in (b) represent angular velocity expected for 100% rolling (0% sliding).

There has been much interest in determining whether carbon nanoparticles act as nanoscale ball-bearings, *i.e.* that the rolling motion of the nanoparticles contributes to low friction [210,211,321]. At the macroscale, rolling resistance is generally much lower than sliding friction since it provides an additional velocity accommodation mechanism [204,205]. However, at the atomic scale, experimental studies of C_{60} fullerene films actually yielded slightly higher friction when molecules were allowed to roll as opposed to when they were fixed in place and forced to slide [204,205]. Indeed, in these simulations, the angular velocity of the nanoparticles seems to have a minimal effect on the friction coefficient obtained. The nanoparticles undergo short periods of sliding and rolling through the course of the simulations (Fig. 47-b), yet there is minimal change in the friction coefficient (Fig. 47-a). Moreover, the friction coefficient at 1.00 coverage, where the nanoparticles do not roll due to the proximity of other nanoparticles, is actually lower than at 0.44 coverage, where rolling occurs. In previous NEMD simulations of CNO between DLC surfaces, lower friction coefficients have been attributed to the rolling motion of the nanoparticles relative to sliding [210,211]. However, from the

results of these simulations, it is suggested that the differences in the friction coefficients during rolling (low pressure) and sliding (high pressure) may have originated from an increase in adhesive forces, due to surface-nanoparticle bond formation, rather than changes to the motion of the nanoparticles. In summary, for the range of conditions simulated here, it seems that rolling motion is not a significant contributor to the low friction achieved by CNO and CND additives, as has been confirmed experimentally for C_{60} [204,205].

7.4. Summary

In this study, NEMD simulations with accurate atomistic potentials have been successfully utilised to shed light on the lubrication mechanisms of two carbon nanoparticles; CNO and CND. The simulations have analysed the effects of nanoparticle type and coverage, as well as the local pressure and sliding velocity, on the friction coefficient and the indentation (wear) depth.

Both CNO and CND nanoparticles appear to be promising boundary lubricant additives, which yield low friction by maintaining separation of asperities as a result of their high compressive strength and hardness. These simulations indicate that the friction and wear behaviour is highly dependent on the coverage of the nanoparticle and the contact pressure. In order to maximise friction and wear reduction, a high coverage of nanoparticle is required between asperities. This suggests that effective dispersion methods, to avoid agglomeration, is critical to the effective performance of these additives so that they may enter the contact at the requisite coverage.

At high coverage and low pressure, the nanoparticles do not indent into the slabs, leading to a low friction coefficient which arises purely from van der Waals interactions between the nanoparticles and the slabs. At low coverage and high pressure, which are likely to be encountered in boundary lubrication, nanoparticles indent into, and plough through the slabs during sliding, leading to atomic-scale wear and a much higher friction coefficient. After the onset of indentation, both the indentation (wear) depth of the nanoparticles and the friction coefficient increase linearly with pressure. However, even at the highest pressures and lowest coverages simulated, both types of nanoparticle are able to

maintain separation of opposing slabs and reduce friction by approximately 75% compared to when no nanoparticle is present, in accord with experimental results. The contribution to the friction coefficient due to indentation can be well predicted through purely geometric considerations using an expression developed for macroscopic indentation by Bowden and Tabor. Friction coefficients observed experimentally for CNO and CND suggest ≈1 Å of indentation of the nanoparticles into the surface. This relatively small indentation depth may actually be important to the effective performance of these additives by maintaining a higher coverage between asperities.

As a result of their layered structure, CNO nanoparticles are softer, and indent less into the α-iron surface than CND at the same coverage and pressure. This reduced indentation depth leads to an approximately 25% reduction in both the indentation (wear) depth and the friction coefficient in these NEMD simulations. This agrees well with differences observed experimentally in boundary friction experiments for CNO and CND. Therefore, both these simulations and most experimental studies suggest that CNOs are more attractive as boundary lubricant additives.

The indentation depths observed on the α-iron slabs used in these simulations are expected to be more pronounced than would occur on the harder carbon steel and iron oxide surfaces more commonly encountered experimentally. However, the same pressure-indentation, pressure-friction and indentation-friction trends are expected to remain the same.

Whilst rolling of the nanoparticles can be observed during these simulations, it does not appear to be critical in reducing the friction coefficient. There is no detectable difference in the friction coefficient in periods where nanoparticles roll or slide, and simulations where more rolling occurs often do not yield a lower friction coefficient. This suggests that the separation of the contact surfaces is the critical factor in the friction reduction of nanoparticles rather than the motion of the nanoparticles themselves.

Chapter 8. Effect of Confined Fluid Molecular Structure on Nonequilibrium Phase Behaviour and Friction

The work shown in this chapter has been published in *Physical Chemistry Chemical Physics* (ref. [42]).

8.1. Introduction

Many lubricated engineering components include elements that roll and slide together, for example; rolling bearings, gears, constant velocity joints and cam/follower systems [8]. In these components, much of the friction loss is in the elastohydrodynamic lubrication (EHL) regime, where a very thin (< μm) lubricant film is sheared at very high strain rate (10^4-10^{10} s^{-1}) and pressure (0.5-2.0 GPa) between non-conforming contact surfaces [156]. Generally, low friction is desirable in order to increase efficiency; however, in some components, such as traction drives, high friction is required and can be obtained using bulky 'traction fluid' molecules [15]. Despite extensive research, the prediction of friction in the EHL regime remains a considerable challenge, primarily because the combination of extreme pressure and strain rate which need to be reproduced, without an uncontrollable temperature rise. As a result, there is still disagreement regarding the most appropriate rheological model to describe the behaviour of lubricant films in rolling-sliding contacts under EHL conditions [8].

Friction in the EHL regime is significantly affected by the molecular structure of the base fluid [15]. To predict EHL friction, one must also consider how the extreme conditions affect the behaviour of the lubricant molecules. Increasing the applied hydrostatic pressure generally increases the viscosity of confined lubricants [156]. High viscosity, in combination with high strain rate, leads to very high shear stresses and this can also significantly affect the lubricant rheology through, for example, shear thinning [8]. There is also growing evidence to suggest that very high shear stresses can lead to nonequilibrium phase transitions which result in deviations from Couette flow [152,164,165]. However, such phase transitions have proved difficult to capture experimentally and neither the physical driving force behind them, nor their influence on the friction behaviour, is yet well understood [152,156].

Confined nonequilibrium molecular dynamics (NEMD) simulations have proved a valuable tool with which to investigate the friction behaviour of thin films of a range of fluids [82,267,350–353]. Significant advantages of confined NEMD simulations include the fact that atomic-scale effects (*e.g.* phase transitions) can be identified and that the friction behaviour emerges naturally from the simulation, rather than being parameterised into the model [156]. Also, thermostats can be applied to control the large local temperature rises [278] which complicate experimental investigations [8]. Confined NEMD simulations of Lennard-Jones fluids have revealed that liquids can transform, at steady state, into ordered, solid-like regions in coexistence with disordered, liquid-like regions [354,355]. Such systems exhibit non-affine flow, whereby the solid-like and liquid-like regions have different average strain rates; a phenomenon known as 'shear localisation' or 'shear banding' [156].

Comprehensive parameter studies have revealed many forms of shear localisation in single-component Lennard-Jones fluid, with different locations of the liquid-like and solid-like regions depending on the applied conditions [155–157]. When the applied conditions yield shear localisation, the friction coefficient of Lennard-Jones fluids no longer shows the usual increase with strain rate; an observation which has also been made for traction fluids above their limiting shear stress [356]. In addition to Lennard-Jones fluids, shear localisation has also been observed in experiments and NEMD simulations of a range of systems [357], including granular beads [358], glasses [359,360], colloids [361,362], and polymer melts [363,364]. In the field of tribology, shear localisation has only been experimentally observed in very viscous model lubricants, such as polybutadiene and polyphenyl ethers (*e.g.* 5P4E) [150,158–163]. However, there is currently a growing consensus that the phenomenon may also be important for more realistic lubricants under extreme conditions, for example those experienced in the EHL regime [152,164,165].

In NEMD simulations of binary mixtures of Lennard-Jones particles, crystallisation was suppressed and only liquid or glassy phases were formed [156]. In these binary systems, the friction coefficient increased linearly with log(sliding velocity) [156], as is frequently observed for realistic lubricants, such

as polyalphaolefin (PAO), under EHL conditions [8,356]. In this case, the friction-strain rate behaviour can be adequately described using stress-promoted thermal activation theory [166], according to the rheological models of Eyring [114]. It has also been suggested that the Carreau [112] or Carreau–Yasuda models, [112,365] which were developed for polymer shear thinning, can be used to predict the friction-strain rate behaviour of lubricants in the EHL regime [8].

An underlying assumption in current models for EHL friction is that, in the absence of thermal effects, or until a critical strain rate is reached, the rheological properties of the lubricant do not vary through its thickness. This is implicit in applying the Eyring [114] or Carreau–Yasuda [112,365] shear thinning models to predict friction in the EHL regime since they generally assume that the film is subject to Couette shear (*i.e.* the strain rate is the same as the macroscopic velocity gradient). Thus significant modifications of these models may be required where there are deviations from planar Couette flow, such as shear localisation [8].

In this study, tribometer experiments and NEMD simulations have been used to investigate the effect of base fluid molecular structure, pressure and strain rate on nonequilibrium phase behaviour and friction in the EHL regime. NEMD can simultaneously probe both the friction and flow behaviour within the EHL film, but is limited to high strain rates ($>10^7$ s^{-1}) to achieve a satisfactory signal to noise ratio within the available computational resources [48,267]. Experimental friction data serves the dual purpose of providing insights into the behaviour at lower strain rates ($<10^7$ s^{-1}) as well as some validation of the NEMD results. This study represents an important step towards utilising NEMD simulations, supported by experiments, to provide information which is critical to; i) improve macroscale models for EHL friction, and ii) design new molecules to control EHL friction [8].

8.2. Methodology

8.2.1. Tribometer Experiments

Note that the experimental work described in section 8.2.1. was not performed by the author, but rather by Jie Zhang and Hugh Spikes (also Imperial College London). Thanks are expressed for their permission to include their contributions here.

Test Fluids

In this study, two model lubricants were compared with two traction fluids. Squalane (2,6,10,15,19,23-hexamethyltetracosane) is a linear C_{24} alkane with six methyl branches that has commonly been employed as a model lubricant in both experiments and NEMD simulations [48,49,108]. Bis[2-ethylhexyl]decanedioate or diethylhexyl sebacate (DEHS) is an example of a synthetic ester oil [366] and its alkyl groups can be varied in order to modify its friction behaviour [15]. 2,3-Dimethyl-2-[(3-methylbicyclo[2.2.1]hept-2-yl)methyl]bicyclo[2.2.1]heptane (DM2H) and 2-methy-2,4-dicyclohexylpentane (DCMP) are both traction fluids, which have been specifically designed to give high friction even at low speed in traction drives [15]. Squalane (Sigma Aldrich), DEHS (Sigma Aldrich), DM2H (Idemitsu Kosan) and DCMP/Santotrac 2000 (SantoLubes LLC) are all well-characterised, monodisperse fluids which are free of any additives; their molecular structures are shown in Fig. 48. In this manuscript, the term ‘lubricants’ is used to refer to fluids chosen to generally give low friction (squalane, DEHS), while ‘traction fluids’ will be used to refer to molecules chosen to give high friction (DM2H, DCMP). It should, however, be noted that traction fluids also serve a lubricating function.

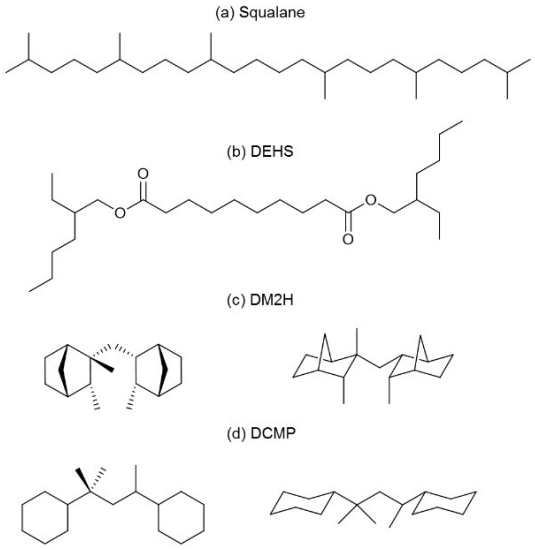

Figure 48. Molecular structures of the base fluids investigated; lubricants - squalane (a), DEHS (b) and traction fluids - DM2H (c), DCMP (d)

Methodology

Rolling-sliding EHL friction tests were carried out using a minitraction machine (MTM2, PCS Instruments, UK). In this tribometer, a ball is loaded and rotated against the flat surface of a rotating disc immersed in lubricant at a controlled temperature. The ball and disc are driven by independent motors to enable any combination of sliding and rolling. The drive motors, applied load and temperature are all computer-controlled, and friction is measured from a load cell attached to the ball drive shaft [356].

Table 1. Conditions for tribometer experiments

Entrainment Speed, U	2.5 m s^{-1}
Slide-Roll Ratio, SRR	0-0.5
Film Thickness, h	80-500 nm
Strain Rate, $\dot{\gamma}$	10^4-10^7 s^{-1}
Temperature, T	30-120 °C
Mean Pressure, F_N	0.55-1.75 GPa

The main test conditions are listed in Table 1. The choices of load, entrainment speed and slide-roll ratio are explained further below. The MTM2 has a maximum load of 75 N and at this load the mean

Hertz pressure in steel/steel contacts cannot exceed 0.8 GPa using a ball-on-flat contact with the smallest ball that can be accommodated. In order to obtain higher contact pressures in a ball-on-flat contact, tests were therefore carried out using tungsten carbide (WC) balls and discs whose high elastic modulus gives a significantly higher contact pressure than steel at the same applied load [356]. Details of the materials, diameter, applied loads and corresponding mean Hertz pressures for ball-on-flat contact are shown in Table 2. An EHL ball-on-flat contact produces a pressure distribution that is close to ellipsoidal, with a maximum pressure in the centre of the contact that is 1.5 times the mean pressure.

Table 2. Contact materials, ball diameter, loads and corresponding mean Hertz pressures for ball-on-flat contact

Materials	Ball Diameter / mm	Applied Load / N	Mean Pressure / GPa
Steel/steel	19.05	20.0	0.55
Steel/steel	19.05	50.0	0.75
WC/WC	19.05	15.0	1.01
WC/WC	19.05	30.0	1.27
WC/WC	12.70	22.7	1.50
WC/WC	19.05	75.0	1.73

In each test, the fluid temperature was increased from 30°C to 120°C in 10°C increments and at each temperature a 'traction curve' was measured. This consisted of measuring the friction while progressively increasing the slide-roll ratio (SRR) from 0 to 0.5 in 24 stages. The SRR is the ratio of the sliding speed, v_s, to the entrainment speed, U. If v_1 and v_2 are the speeds of the ball and disc surfaces respectively, v_s is the difference in speed between the two surfaces, (v_1-v_2) while U, which was held constant at 2.5 m s^{-1}, is the mean speed of the surfaces with respect to the contact, (v_1+v_2)/2. In EHL, the lubricant film thickness depends on U, but not on v_s, so a traction curve describes how EHL friction increases with sliding speed at a fixed film thickness [356]. The traction curves can be very simply converted to a curve of shear stress *versus* strain rate by dividing the measured friction by the applied load to obtain the mean shear stress, and dividing v_s by the film thickness, h, to determine the strain rate. In this study, only the data at 80 °C were used for comparison with NEMD results. Measurements

at other temperatures were made to enable correction of the influence of shear heating on friction, as described below.

A feature of EHL contacts is that, because of the combination of high strain rate and high pressure, a large amount of energy is dissipated within the lubricant film and this can lead to large rises in local film temperature [367,368]. This should be accounted for when interpreting EHL friction results and was achieved here by calculating the mean fluid film temperature rise due to shear and then correcting the measured friction data back to their bulk test temperature values [8]. Because sets of shear stress vs. strain rate data were collected at several test temperatures for each fluid and load, these could be combined to determine the dependence of the shear stress on temperature at a fixed strain rate. From this information, it was possible to correct the measured shear stresses back to the bulk test temperature [8,369]. Further details of the interpolation thermal correction procedure are shown in Appendix B. It is important to note that the correction was not used to determine values of shear stress at the bulk test temperature *a priori* but only to correct the original shear stress measurement. Moreover, the correction is generally relatively minor for the small temperature rises that are considered in this study (maximum thermal correction accounted for was 10°C) [8,369].

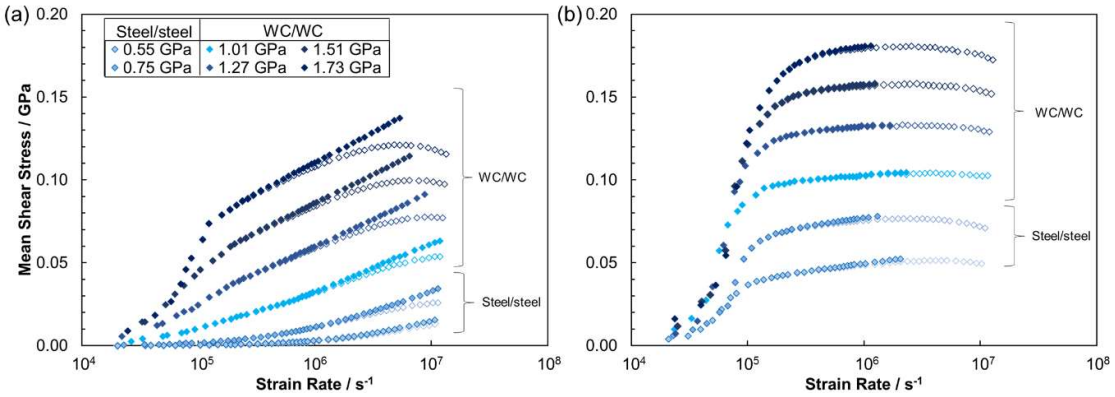

Figure 49. Thermally-corrected (filled symbols) and raw (open symbols) mean shear stress versus $\log_{10}$(strain rate) for; a representative lubricant, squalane (a) and a traction fluid, DM2H (b) at 80 °C. The thermal correction was only applied when calculated fluid film temperature rise was <10°C.

Fig. 49 shows sets of raw and thermally-corrected mean shear stress *versus* strain rate curves for squalane and DM2H at 80 °C. The minor thermal corrections applied significantly alter the friction behaviour of the lubricants, maintaining a linear increase in the shear stress with log(strain rate), which would otherwise tail off as a result of shear heating [8]. Conversely, the same thermal correction procedure does not significantly change the shear stress in the traction fluids, since their shear stress is almost independent of temperature [15,356].

The composite surface roughness was 12 nm for the steel ball and disc and 16 nm for the WC ball and disc. For all four fluids tested, the EHL film thickness was greater than 80 nm at the entrainment speed of 2.5 m s^{-1} and a temperature of 80 °C (Table 1). Therefore, the film thickness was always at least five times greater than the composite surface roughness, ensuring a full EHL fluid film with negligible asperity contact [15,356].

8.2.2. NEMD Simulations

Model Details

Classical, all-atom NEMD simulations were performed using LAMMPS [255]. The MD equations of motion were integrated using the velocity-Verlet algorithm with a time step of 1 fs. All the systems were constructed using the Materials and Processes Simulations (MAPS) platform from Scienomics SARL. The systems consisted of a lubricant film confined between atomically-smooth iron oxide (α-Fe_2O_3 [100]) slabs, a representative model for steel contact surfaces [142]. It is important to note that the shear localisation behaviour critical to this study can only be captured in NEMD simulations if the shearing process is boundary-driven, rather than imposed directly on the fluid molecules [363]. WC surfaces were not considered in the NEMD simulations since the high pressures, which necessitated the use of WC surfaces in the accompanying experiments, could be readily achieved using iron oxide slabs, for which well-tested, accurate MD parameters are available [142]. The *x*, *y*, *z* dimensions of the slabs were approximately 5.5 x 5.5 x 1.5 nm.

An example system is shown in Fig. 50. The systems contained a fixed number of molecules (600-1040 depending on fluid) to give a film thickness of approximately 15 nm at the lowest pressure considered (0.5 GPa). The total number of atoms in these systems was approximately 60,000. To make this wide parameter study (Table 3) computationally feasible, the simulated film thickness was much lower than in the accompanying experiments (Table 1). However, in this study, the results from the experiments and NEMD simulations are expected to be directly comparable. This is because, apart from for very small film thicknesses [353], and in the absence of boundary slip [135,142–146], the shear stress measured in bulk and confined NEMD simulations are virtually indistinguishable [90,142,350]. Thus the difference in film thickness between the simulations and experiments is not expected to influence the shear stress results. To ensure the validity of this approach, some of the systems were also tested with half and double the normal film thickness. At equal strain rate, these systems gave the same shear stress result within the statistical uncertainty, as shown in Appendix B.

The α-Fe_2O_3 slabs were restrained in the corundum crystal structure using harmonic bonds with a spring constant of 25 kcal mol^{-1} [142]. Forces between the iron oxide and fluid atoms were governed by Lennard-Jones and electrostatic interactions; the Fe and O parameters used were similar to those developed by Savio et al. [142] and Berro et al. [169] to study the behaviour of alkane films confined between α-Fe_2O_3 surfaces, and are given in Appendix B.

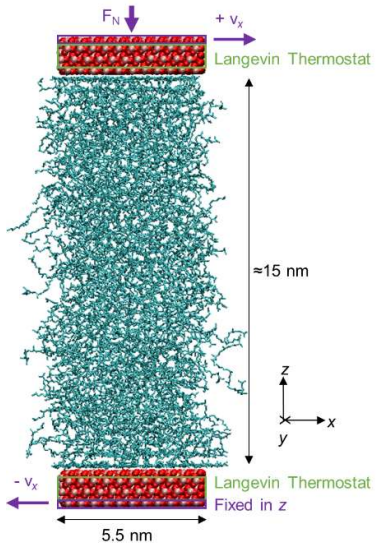

Figure 50. Representative system setup for the confined NEMD simulations of squalane at 80 °C, after compression (1.0 GPa), before sliding. Iron atoms are shown in pink, oxygen in red, carbon in blue and hydrogen atoms are not shown for clarity. Rendered using VMD [264].

Interactions between the liquid molecules were represented with an updated form of the all-atom 'optimized potential for liquid simulations' force-field [234], L-OPLS-AA [26]. In L-OPLS-AA, both bonded and non-bonded parameters have been updated for several atom types to provide a more realistic description of long-chain alkanes [26] and, more recently, alcohols and esters [370]. More details of the molecular dynamics force-field used, as well as validation for the molecules used here, are shown in Appendix B. Fast-moving bonds involving hydrogen atoms were constrained with the SHAKE algorithm [256]. Lennard-Jones interactions were cut off at 12 Å [26] and electrostatic interactions were evaluated using a slab implementation [273] of the PPPM algorithm [70] with a relative force accuracy of 10^{-5}. 'Unlike' interactions were evaluated using the geometric mean mixing rules [234]. Although the computational expense of all-atom force-fields is much greater than for simplified united-atom variants, it has been shown that they are critical for obtaining accurate experimental viscosities of long-chain alkanes [69]. It is therefore expected that the friction behaviour of these molecules will only be accurately reproduced by all-atom force-fields.[26] Moreover, all-atom

force-fields have also been shown to be critical to obtain liquid-solid phase transitions in strongly confined fluids which agree with experimental observations [130].

Simulation Procedure

First, fluid molecules (600-1040) were randomly inserted between the slabs to achieve a density comparable to the fluids under ambient conditions using the 'Amorphous Builder' tool in MAPS. The entire system was then energy minimised. The pressure was increased by giving a normal force to the outer layer of atoms in the top slab while keeping the outer layer of atoms in the bottom slab fixed in *z* (purple box in Fig. 50). The pressures, F_N, considered were between 0.5-2.0 GPa, to provide an envelope for the experimental data, with upper and lower limits slightly above and below those covered in the experiments (Table 1). During the compression phase, a global Langevin thermostat [55] with a damping coefficient of 0.1 ps was applied in all directions and the systems were allowed to equilibrate at 80 °C in order to match the experiments. Initially, the slab separation varied in a damped harmonic manner, so sliding was not applied until a constant average slab separation was obtained and the average hydrostatic pressure within the liquid film reached its target value [267]. These compression simulations were generally around 2 ns in duration.

Table 3. Conditions for NEMD simulations

Sliding Speed, v_s	0.5-100 m s^{-1}
Film Thickness, h	12-16 nm
Strain Rate, $\dot{\gamma}$	10^7-10^{10} s^{-1}
Temperature, T	80 °C
Mean Pressure, F_N	0.50-2.0 GPa

After compressive oscillation became negligible, a shear velocity gradient was imposed on the system by means of a constant velocity, $v_x = \pm v_s/2$ applied to the outermost layer of atoms in each slab (purple box in Fig. 50) in the *x* direction [156]. Sliding simulations were conducted until the mean shear stress reached a steady state. The necessary simulation time was between 2-50 ns, with lower sliding velocities, v_s, requiring longer simulations. For all of the sliding velocities considered, the shear stress reached a steady state after 5-10 nm of sliding distance (see Appendix B). The values of v_s applied

were between 0.5-100 m s^{-1} [90], yielding strain rates of approximately 10^7-10^{10} s^{-1} for the film thickness simulated (Table 4). Although lower NEMD strain rates are desirable to overlap with those used in the tribometer experiments (<10^7 s^{-1}), they are not yet practical for extensive parameter studies using accurate all-atom force-fields [267]. Heat generated during the sliding simulations was dissipated using a Langevin thermostat [55] acting only on the middle 1 nm of the iron oxide slabs (green box in Fig. 50), applied in the spanwise direction (*y*) *i.e.* perpendicular to both sliding and compression [92]. This approach is known to be more physically meaningful than applying the thermostat directly to the confined fluid, which has been shown to significantly affect its behaviour under sliding conditions [65]. In the context of temperature rise in experimental EHL conditions, this approach is similar to removing the effect of bounding surface flash temperature rise, but leaving the effect of temperature rise within the lubricant film due to finite thermal conductivity [8] (see Appendix B). However, for the thin films simulated here (h ≈ 15 nm), the latter was also relatively small and only became significant at the highest strain rates considered [278].

Previous NEMD studies have shown that the boundary thermostatting method applied here was effective in controlling the temperature of confined molecular fluids at similar sliding velocities [66,278]. However, the NEMD shear stress data can only be considered as isothermal at up to sliding velocities of 20 m s^{-1} ($\dot{\gamma} \approx 10^9$ s^{-1}), where there is no observable temperature rise within the film above the thermal noise [66]. The temperature in the centre of the film [155] increased by approximately 10 °C at 40 m s^{-1} and around 30 °C higher at 100 m s^{-1}; these temperature rises depended only weakly on the pressure and fluid. For the lubricants (squalane, DEHS), this temperature increase lead to a decrease in the shear stress at the highest sliding velocities considered (open circles in Fig. 51). Conversely, for the traction fluids (DM2H, DCMP), the temperature rise had a negligible effect on the shear stress, which is more weakly dependent on temperature [15,356].

8.3. Results and Discussion

8.3.1. Friction Behaviour

The variation in mean shear stress with pressure and strain rate was measured in both tribology experiments and in NEMD simulations, allowing a much wider parameter space to be covered than would be possible through either technique independently. The shear stress in the NEMD simulations was monitored through the mean lateral (friction) force acting on the outer layer of atoms in the top and bottom slabs in response to the fluid [169,371].

Fig. 51 shows the variation in the mean shear stress with log(strain rate) for the lubricants (squalane, DEHS) and traction fluids (DM2H, DCMP) at 80 °C, under several applied mean pressures. Note that experimental data have been thermally-corrected to isothermal conditions as described in the Methodology (Fig. 49) and Appendix B. NEMD data with filled symbols are isothermal whilst those at the highest strain rates, with a detectable film temperature rise, are shown as open circles.

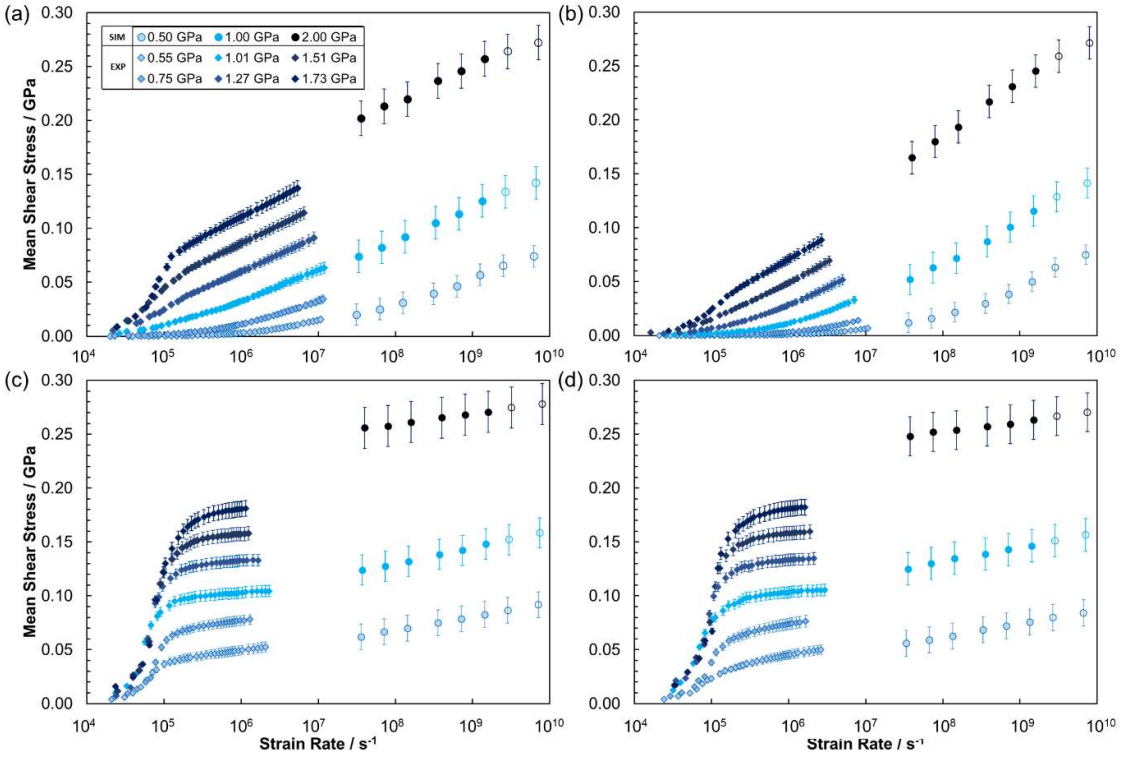

Figure 51. Mean shear stress versus $\log_{10}$(strain rate) for the fluids at: 80 °C and 0.5-2.0 GPa; squalane (a), DEHS (b), DM2H (c), DCMP (d). Thermally-corrected experimental data shown as filled diamonds. Isothermal NEMD data shown as filled circles, NEMD data with a temperature rise shown as open circles. NEMD data time-averaged for the final 10 nm of sliding. Error bars for NEMD data represents maximum variation between independent trajectories for some state points. Error bars for experimental data represent the uncertainty from the thermal correction. Data from higher applied pressures are shown in darker colours.

Fig. 51 suggests good agreement between the thermally corrected experimental data ($\dot{\gamma} < 10^7$ s^{-1}) and the NEMD simulation data ($\dot{\gamma} > 10^7$ s^{-1}) for most of the fluids and applied conditions studied. In the experiments, there will be significant variation in the conditions within the macroscopic contact [372,373], which cannot all be captured in a NEMD simulation limited to the nanoscale [152]. However, the general agreement found between the experimental and NEMD mean shear stress results for the fluids and conditions studied here suggests that NEMD simulations performed under average conditions for the contact are sufficient to reproduce the important trends. Similar conclusions have been drawn from experimental comparisons between microscopic local viscosity

measurements and more conventional global average viscosity measurements for contacts under EHL conditions [372,373].

Fig. 51 shows that the mean shear stress varies significantly with the applied load as well as the strain rate for all of the fluids studied. The friction behaviour is markedly different between the lubricants and the traction fluids. For the lubricants (Fig. 51-a and Fig. 51-b), the thermally-corrected experimental data and NEMD mean shear stress data are in excellent agreement. Generally, the lubricants show a linear increase in shear stress with log(strain rate), as predicted by the Eyring model [114]. This behaviour has been consistently observed in previous experiments and NEMD simulations of lubricants [8,15,156,371]. At the highest pressures considered (>1.5 GPa), there is a sharp increase in experimentally measured shear stress with log(strain rate) at low strain rates ($<10^5$ s^{-1}), due to viscoelastic accommodation of strain by the surface in the entry zone of the contact, in response to the very steep friction increase in this region [15,374]. However, at higher strain rates ($>10^5$ s^{-1}), the experimental shear stress shows the same linear increase with log(strain rate) as observed at lower pressure.

The traction fluids (Fig. 51-c and Fig. 51-d) give much higher shear stress than the lubricants, particularly at low strain rates; however, the slope of the shear stress with log(strain rate) is shallower than for the lubricants. In both the simulations and the experiments, the slope of the shear stress with log(strain rate) (*i.e.* the Eyring stress) generally increases with increasing pressure for the lubricants, and decreases with increasing pressure for the traction fluids, as has been noted previously [374]. At low strain rates ($<10^5$ s^{-1}), the traction fluids also show a sharp increase in shear stress with log(strain rate) due to viscoelastic accommodation of strain [15,374], but this occurs at lower pressure (0.55 GPa) than for the lubricants. There is good agreement between the experimental and NEMD simulation mean shear stress data for the traction fluids at low pressure (≤0.55 GPa). At higher pressure, the trends in the NEMD and experiments are similar, but the mean shear stress value, as

well as the slope of the shear stress with log(strain rate), are overestimated in the NEMD simulations relative to the experiments. Possible reasons for these discrepancies are discussed later.

The critical strain rate transition, $\dot{\gamma}_c$, above which shear thinning is observed, and below which there is a Newtonian plateau (i.e. where the viscosity, η, is independent of $\dot{\gamma}$), typically occurs at $\dot{\gamma} \approx \tau^{-1}$, where τ is the longest relaxation time at equilibrium (in the absence of shear). This is usually τ_{rot}, the rotational relaxation time [48]. The experimental data probes both the Newtonian plateau and the shear thinning regime for the fluids and conditions considered. The high strain rate NEMD data are mostly in the shear thinning regime, but the transition to the Newtonian plateau can be seen for the lubricants at 0.5 GPa at the lowest strain rates considered (≈ 10^7 s^{-1}).

The variation in the friction coefficient with strain rate is also shown to make comparisons between different applied pressures easier [156]. The friction coefficient, μ, was obtained using the extended Amontons−Coulomb law under the high load approximation: $F_L/F_N = F_0/F_N + \mu \simeq \mu$. F_L and F_N are respectively the mean lateral (friction) force and normal force acting on the outer layer of atoms in each slab, and F_0 is the load-independent Derjaguin offset representing adhesive surface forces. The validity of this approximation was confirmed by ensuring that a linear fit of F_L as a function of F_N gave an insignificant value of F_0 [267]. The trends evident in Fig. 52 are statistically significant; when reproducing some of the NEMD simulations with different starting configurations, but the same parameters, the maximum difference between the friction coefficient between independent trajectories was approximately 10%. Error bars are omitted from Fig. 52 for clarity.

The friction coefficients for the lubricants (Fig. 52-a and Fig. 52-b) generally increase linearly with log(strain rate) and also increases with the applied pressure. This type of behaviour is commonly observed in experiments and NEMD simulations of lubricants under EHL conditions [8,15,156,371]. Interestingly, the slope of the friction coefficient with log(strain rate) decreases with increasing pressure, as has been observed in NEMD simulations of binary Lennard-Jones mixtures [156]. Similar observations have also been made in recent NEMD simulations of *n*-hexadecane confined between α-

Fe_2O_3 slabs at high pressure [371]. Consequently, the friction coefficient at 0.5 GPa exceeds that at 2.0 GPa at very high strain rates (>2 x 10^9 s^{-1}).

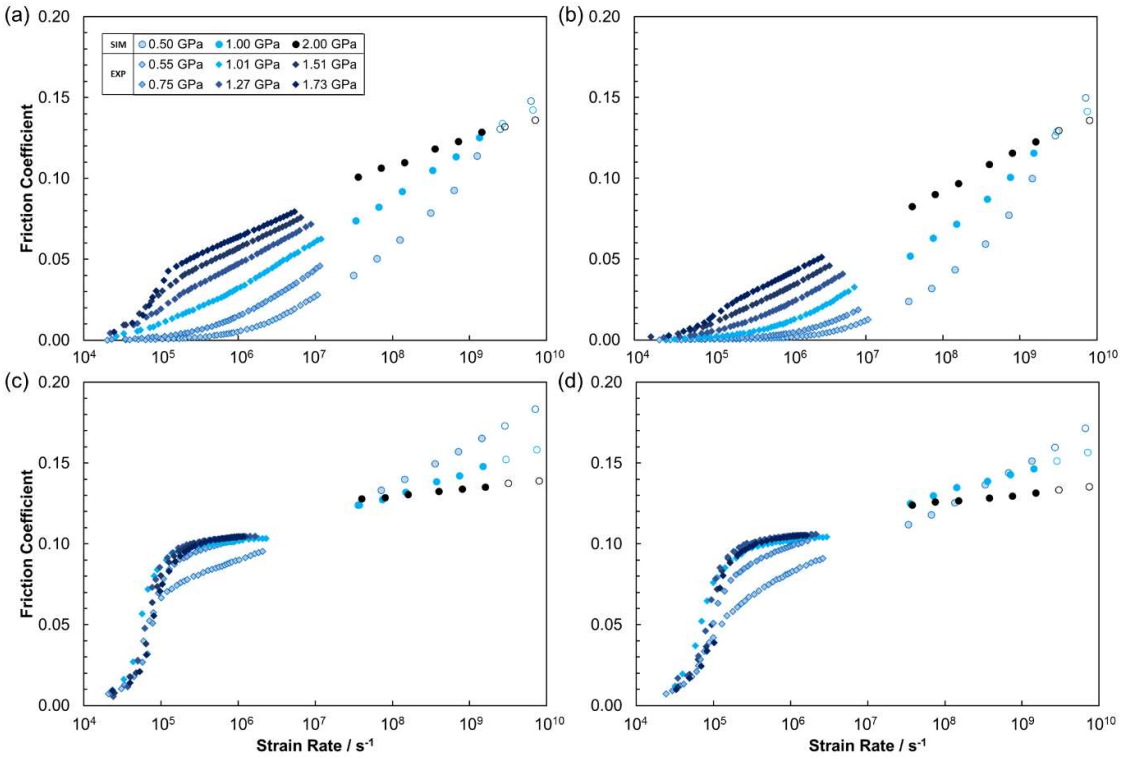

Figure 52. EHL friction coefficient versus $\log_{10}$(strain rate) for the fluids at: 80 °C and 0.5-2.0 GPa; squalane (a), DEHS (b), DM2H (c), DCMP (d). Thermally-corrected experimental data shown as filled diamonds. Isothermal NEMD data shown as filled circles, NEMD data with a temperature rise shown as open circles. NEMD data time-averaged for the final 10 nm of sliding. Error bars are omitted for clarity. Data from higher applied pressures are shown in darker colours.

Although the friction coefficient of the traction fluids (Fig. 52-c and Fig. 52-d) also increases linearly with log(strain rate), it does so with a much lower slope than for the lubricants. This behaviour is similar to that observed in NEMD simulations of single-component Lennard-Jones fluids subjected to high pressures [155–157]. The traction fluids generally gave much higher friction coefficients than lubricants, particularly at low strain rate. The friction coefficient at 0.5 GPa exceeds that at 2.0 GPa at much lower strain rates (>10^8 s^{-1}) for the traction fluids than for the lubricants (>2 x 10^9 s^{-1}). The high friction from the traction fluid molecules can be attributed to interlocking of the bulky cyclohexane and bicyclo[2.2.1]heptyl groups DCMP and DM2H respectively [375]. This, coupled with their internal

molecular stiffness [376], increase energy barriers for neighbouring molecules to slide over one another [114], leading to high friction [15].

8.3.2. Flow Behaviour

The physical state of fluids in the EHL regime is still largely unresolved, owing to experimental difficulties in probing the contact zone under the extreme conditions [156]. The nonequilibrium phase behaviour of the fluids can be directly probed using velocity and atomic mass density profiles from the NEMD simulations [155–157]. Although not part of this current study, experimental velocity profiles for these fluids are also currently under investigation using recently developed techniques [150,161–163]. The NEMD velocity and atomic mass density profiles are spatially and time averaged to improve their signal to noise ratio. The profiles are both shifted such that a *z*-coordinate of zero is at the centre of the fluid film. The velocity profiles generally reach a steady state after 5-10 nm of sliding, depending on the fluid and conditions.

Fig. 53 shows how the *x*-velocity profile in the *z*-dimension, $v_x(z)$, and the atomic mass density profile in the *z*-dimension, changes with the applied pressure for a representative lubricant, squalane. At 0.5 GPa (Fig. 53-a), a Couette flow profile develops, with a linear velocity gradient between the two slabs. The outer molecular layer of fluid moves at the same velocity as the wetting α-Fe_2O_3 slabs, indicating that no boundary slip occurs (see Appendix B). The oscillatory atomic mass density profile indicates strong layering of the squalane molecules close to the surface and weaker layering in the centre of the film. These profiles are similar to those from NEMD simulations of thin *n*-hexadecane films confined by α-Fe_2O_3 slabs at high pressure [352,371]. At 1.0 GPa (Fig. 53-b), there is stronger layering of the fluid extending further from the slabs, suggesting the formation of an ordered, solid-like region close to the slabs, with a liquid-like region in the centre of the film. The flow profiles in Fig. 53 confirm the transition to a 'central localisation' (CL) phase, with the solid-like regions of the fluid moving at the same velocity as the slabs and a steeper velocity gradient within the central liquid-like region than for the Couette flow case. CL is one of the nonequilibrium phases identified in previous confined NEMD

simulations of Lennard-Jones fluids [155–157], and has also been observed experimentally for 5P4E [158–160,163]. At 2.0 GPa (Fig. 53-c), the molecular layering is even more pronounced, and extends further into the centre of the film. Thus, the system shows stronger CL, with thicker solid-like regions moving with the slab and a steeper velocity gradient in the central liquid-like region. It is important to note that the strong layering extends much further into fluid than is directly influenced by the solid slab (Lennard-Jones interactions cut off at 12 Å). It is not possible from these simulations to definitively show the physical state of the solid-like region, whether glassy or fully crystalline; this will be investigated in future studies. The change in the velocity profiles with pressure, moving from Couette-like to increasingly strong CL, is similar to that observed experimentally for viscous 5P4E at lower temperature, strain rate, and pressure [163].

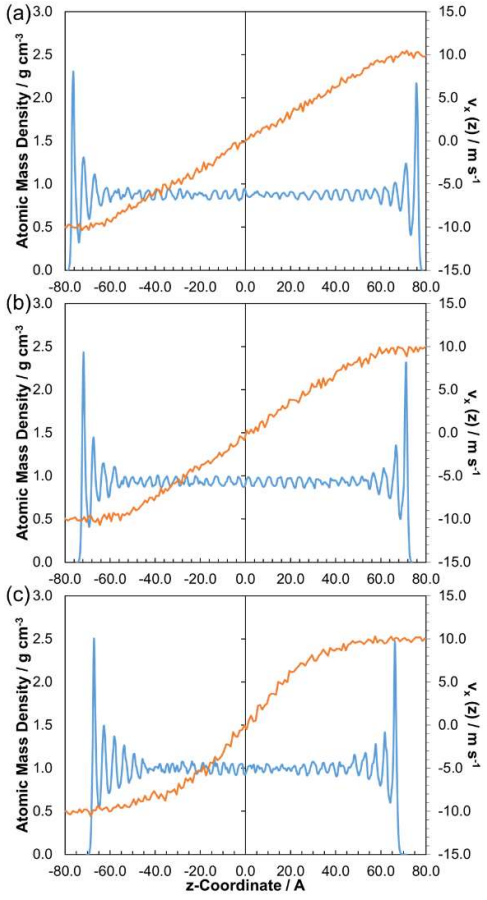

Figure 53. Atomic mass density (blue) and velocity (orange) profiles for squalane at: 80 °C, 20 m s^{-1} ($\dot{\gamma} \approx 10^9$ s^{-1}), and; 0.50 GPa (a), 1.00 GPa (b), 2.00 GPa (c). Time-averaged for the final 5 nm of sliding.

Fig. 54 shows how the *x*-velocity profile in the *z*-dimension, $v_x(z)$, and the atomic mass density profile in the *z*-dimension, change with the applied pressure for a representative traction fluid, DM2H. The trends for the traction fluids are similar to those for the lubricants, but they show greater divergence from Couette flow under the same conditions. Even at 0.5 GPa (Fig. 54-a), DM2H shows weak CL, with layering of the molecules close to the surface resulting in a sinusoidal velocity profile. At 1.0 GPa (Fig. 54-b), the traction fluids show much stronger CL, which is similar to the lubricants at 2.0 GPa (Fig. 53-c). At 2.0 GPa (Fig. 54-c), the traction fluids show 'plug slip' (PS), another phase identified in confined NEMD simulations of Lennard-Jones fluids [155–157]. Here, the velocity profile shows that shear localises close to the slabs and the density profile indicates strong layering throughout the film.[157] During PS, the first molecular layer still moves at the same speed as the slab and 'slip planes' form within the second and third layers [157]. Note that PS is distinct from the boundary slip behaviour, which is commonly observed in NEMD simulations of very thin films [352] (see Appendix B). PS has been observed experimentally for viscous polybutadiene [161,162] and has also been inferred from film thickness measurements in realistic mineral oils [164,165].

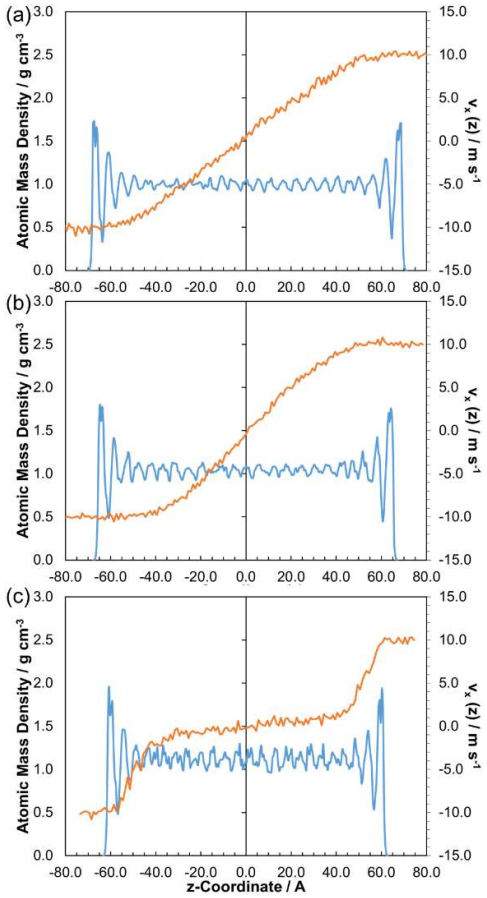

Figure 54. Atomic mass density (blue) and velocity (orange) profiles for DM2H at: 80 °C, 20 m s^{-1} ($\dot{\gamma} \approx 10^9$ s^{-1}), and; 0.50 GPa (a), 1.00 GPa (b), 2.00 GPa (c). Time-averaged for the final 5 nm of sliding.

Fig. 55 shows the change in the velocity profile with sliding velocity for a representative fluid, DM2H. The width of the central liquid-like region increases with sliding velocity from 5-100 m s^{-1}, as has been observed previously for Lennard-Jones fluids undergoing CL [155–157]. This is intuitive given that, at higher sliding velocities (strain rates), there is increased shear heating in the centre of the film [155]. At the lowest sliding velocities considered (0.5-2.0 m s^{-1}), the lower signal to noise ratio in the velocity profiles makes it difficult to definitively state the flow behaviour.

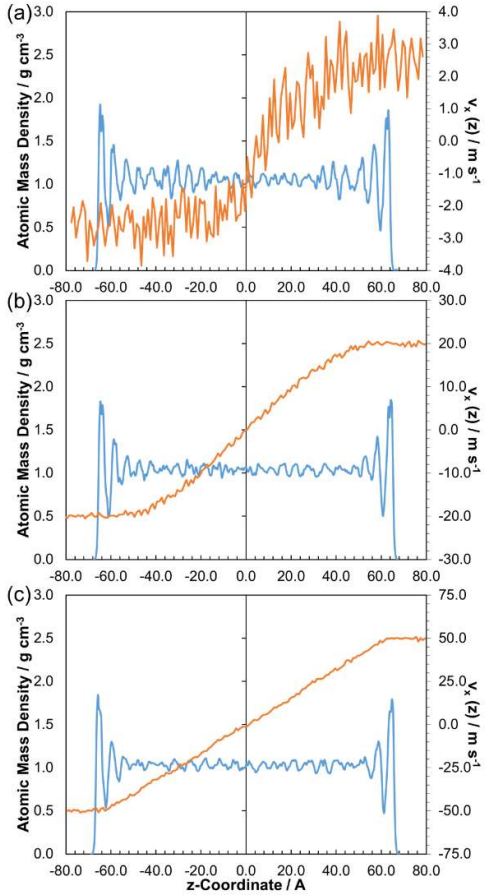

Figure 55. Atomic mass density (blue) and velocity (orange) profiles for DM2H at: 80 °C, 1.0 GPa, and; 5 m s^{-1} (a), 40 m s^{-1} (b), 100 m s^{-1} (c). Time-averaged for final 5 nm of sliding.

In the confined molecular fluids simulated here, the nonequilibrium phase behaviour is broadly similar to that observed in NEMD simulations of Lennard-Jones fluids [155–157]. As the pressure is increased, molecules are forced closer together, and eventually localisation of the shear becomes energetically favourable to global shearing of the film. Under the relatively high strain rates accessible through NEMD, this generally manifests as CL, but the transition to PS was also observed for the traction fluids at the highest pressures considered [155]. The results of this study suggest that, precluding excessive shear heating, shear localisation will arise in any confined molecular fluid providing that the pressure is sufficiently high [156].

The shear bands form parallel to the confining walls in these and, to our knowledge, all previous NEMD simulations which have investigated this phenomenon [152]. Conversely, bands have been observed at a 20° angle to the confining surfaces in experiments using 100 µm thick 5P4E films [159], which was later supported by theoretical predictions [160]. The bands in the NEMD simulations probably form parallel to the surfaces rather than at an angle because relatively thin films are used with periodic boundary conditions in the *x* and *y* directions in order to make the simulations computationally feasible [152,155].

8.3.3. Relationship Between Flow and Friction

Given the fact that shear localisation occurs for a wide range of condensed phase materials (see Introduction), it might be reasonably expected that a common principle applies across the range of different types [357]. The critical question to consider is: why would a fluid film shear inhomogeneously rather than with a linear velocity gradient? The principle of least work or minimisation of heat production may go some way to explain this effect, which is encapsulated in basic form in the following equation, for a fluid undergoing Couette flow:

$$\dot{q} = \eta \dot{\gamma}^2 \mathrm{h} S^2 \qquad \text{(Equation 3)}$$

where $\dot{q}$ is the rate of heat production, η is the shear viscosity, $\dot{\gamma}$ is the strain rate, and S is a cross-sectional dimension. For Couette flow, $\dot{\gamma} = v_s/h$, where v_s is the difference in velocity between the slabs and h is the measured thickness of the lubricant film. If there is shear localisation, for a thickness, Δh, then, assuming the solid-like region is not sheared, the 'actual' strain rate is $v_s/\Delta h$. The localisation thickness, Δh, can range from near zero to h, the measured film thickness. The product of the actual strain rate and the localisation thickness, $\dot{\gamma}\Delta h$, must be constant to a first approximation (the exact value of Δh can be difficult to specify). Hence, from Equation 3:

$$\dot{q} \propto \eta(\gamma)\dot{\gamma} \qquad \text{(Equation 4)}$$

There is an energetic advantage, therefore, in having localisation of the shear as if the actual strain rate is larger than the Couette case, and the fluid is shear thinning [48], then the rate of heat production (or equivalently work performed) will be reduced in proportion to the decrease in viscosity due to enhanced shear thinning [157]. Moreover, the solid-like region will have an increased thermal conductivity [15], leading to more efficient thermal dissipation when the shear is localised. A combination of these factors mean that, at high pressure shear localisation can reduce the magnitude of the friction coefficient relative to Couette flow.

The slope of the friction coefficient with log(strain rate) is also reduced when fluids undergo shear localisation. This is intuitive since the region in which the shear is localised can be viewed as a strongly shear thinning liquid or, in extreme cases, as a slip plane between two solid-like layers [157]. In the former case, because the thickness of the liquid-like region grows with increasing strain rate (see Fig. 55), the actual strain rate, and thus the friction coefficient, becomes less sensitive to the applied strain rate. In the latter case, invariance of the friction coefficient to the applied strain rate is expected, as it is for sliding between elastic-plastic solids [374].

Recall that increased pressure generally lead stronger shear localisation (Fig. 53 and Fig. 54), an increase in the magnitude of the friction coefficient, but a reduction in the slope of the friction coefficient with log(strain rate) (Fig. 52). Thus, although the reduction in the slope from stronger shear localisation can clearly be observed in Fig. 52, the decrease in the magnitude of the friction coefficient must be masked by other effects. Specifically, increasing the pressure also increases the fluid viscosity, leading to higher friction [8]. Although the magnitude of the friction coefficient increases in systems at higher pressure, which show more shear localisation, it is lower than would be expected were Couette flow to be enforced under the same conditions.

When the limiting shear stress is reached, the friction coefficient becomes insensitive to both strain rate and pressure [152]. The results of this study (Fig. 52) suggest that this will only occur for bulky traction fluid molecules at high pressure, which show significant deviation from Couette flow, *i.e.*

strong shear localisation (Fig. 54). Thus, these results support strong shear localisation as the physical origin of the limiting shear stress, one of several proposed explanations in the literature [152,377]. One might also tentatively suggest that the limiting shear stress is reached upon the transition from CL to PS [152], although more research is needed to confirm this.

The experimental results suggest that the limiting shear stress was approximately 0.1 GPa for both DM2H and DCMP at 1.0 GPa and 80 °C, which is similar to that reported from earlier experiments for the latter [374]. The NEMD simulations (Fig. 52-c and Fig. 52-d) suggest a higher limiting shear stress (approximately 0.25 GPa); at 1.0 GPa applied pressure, the friction coefficient still increases with log(strain rate). This discrepancy, along with the overestimated friction coefficient for the traction fluids at high pressure (Fig. 52-c and Fig. 52-d) may have at least two explanations. Firstly, the phase transitions critical to the friction behaviour, may occur under different conditions in the simulations (dependant on the MD force-field) [26] than in the experiments. Specifically, the results suggest that shear localisation, which reduces both the magnitude of the friction coefficient and its slope with log(strain rate), occurs under milder conditions, and to a greater degree, in the experiments compared to the NEMD simulations. Secondly, the thinner NEMD film thickness ($h \approx 15$ nm) relative to the experiments ($h \approx 150$ nm), could lead to differences in the relative sizes of the solid-like and liquid-like regions under equivalent conditions as well as variations in thermal dissipation. It should be noted, however, that there is generally good agreement between the results of the tribology experiments and NEMD simulations.

The differences in the friction behaviour between the two lubricants are clear in both the experiments and the NEMD simulations. Squalane (Fig. 52-a) gives a consistently higher friction than DEHS (Fig. 52-b) under all the conditions studied. Molecular factors that promote low EHL friction include linear chains and flexible groups, such as ester linkages, that reduce energy barriers for neighbouring molecules to slide over one another [15]. Both molecules include linear backbones of the same length (24 atoms); however, squalane includes several methyl branches, while DEHS has two ethyl branches

as well as two flexible ester linkages (Fig. 48). This additional flexibility and molecular 'smoothness' leads to a significantly lower friction for DEHS than squalane. In future studies, more molecular structures could be compared and similar methodologies to those used here could be used to design new molecules with specific levels of EHL friction.

The differences between the two traction fluids are far more subtle. At low pressure (≤0.55 GPa), the shear stress of DCMP (Fig. 52-d) has a slightly steeper slope with log(strain rate) than for DM2H (Fig. 52-c). This difference can be explained through the NEMD simulations, where DCMP has a more Couette-like profile at 0.50 GPa (see Appendix B) while DM2H shows some central localisation (Fig. 54-a). At higher pressures (>0.55 GPa), DM2H and DCMP have virtually identical friction and flow behaviour in both the experiments and NEMD simulations. Both traction fluids have similar molecular structures (Fig. 48), with cyclohexane groups in their chair confirmation meaning that they have steric bulk in three dimensions.

An increased knowledge of the friction and flow behaviour of confined fluids from tribology experiments and NEMD simulations, as used in this study, could help to accelerate the design of both new lubricants which give lower friction, and new traction fluids that give higher friction. For example, lubricants which are more susceptible to shear localisation under EHL conditions could lead to lower friction. Shear localisation could perhaps be promoted by using strongly layered lubricants, such as ionic liquids [82,378,379]. Conversely, including a mixture of different traction fluid molecules to supress the formation of solid-like regions and thus shear localisation should increase EHL friction, particularly at high strain rates.

8.4. Summary

A combination of tribometer experiments and confined NEMD simulations has been used to investigate the effect of molecular structure on friction and nonequilibrium phase behaviour. An extensive parameter study, including several lubricant and traction fluid molecules subjected to

pressures (0.5-2.0 GPa) and strain rates (10^4-10^{10} s^{-1}) typical of the EHL regime, suggests clear relationships between the friction and flow behaviour.

In both the tribometer experiments and NEMD simulations, lubricant molecules generally give a low friction coefficient which increases with both strain rate and pressure. Conversely, traction fluid molecules give a high friction coefficient which has a much weaker dependence on strain rate and pressure. This behaviour can be rationalised through analysis of flow profiles from the NEMD simulations which suggest significant shear localisation, particularly in the traction fluids.

Nonequilibrium phase changes, which were first identified in NEMD simulations of simple Lennard-Jones fluids, have also been observed here, for the first time, in well-characterised molecular fluids. All of the fluids investigated display some shear localisation at high pressure. Both lubricants and traction fluids show central localisation, where the regions of the fluid close to the slab become solid-like and only the central, liquid-like region is sheared. At very high pressure, the traction fluids also show plug slip, where the centre of the film becomes solid-like and the shear occurs close to, but not at, the walls. The traction fluid molecules, which have bulky cycloaliphatic groups, show a higher propensity for shear localisation, and only exhibit Couette flow at low pressure or very high strain rate. Higher pressure induced more pronounced shear localisation, whilst increasing the strain rate resulted in a widening of the sheared, liquid-like region. Shear localisation generally leads to a decrease in both the magnitude of the friction coefficient and the slope of its increase with log(strain rate) compared to Couette flow.

For most of the fluids and conditions considered, the variation in the shear stress with log(strain rate) in the NEMD simulations is in good agreement with tribometer experiments conducted at lower strain rates. This study has important implications with respect to utilising tribometer experiments and NEMD simulations to predict and control EHL friction. Specifically, they suggest that a range of molecules show significant deviations from planar Couette flow under EHL conditions, meaning that macroscale models currently used to predict friction in this regime may require modification to

account for this. Moreover, the techniques applied here show significant potential to accelerate the design of new lubricant and traction fluid molecular structures.

Chapter 9. Conclusions and Further Work

In this chapter the main conclusions which can be drawn from this project are elucidated and topics of further work are suggested.

9.1. Conclusions

1. It has been demonstrated that the use of an accurate, all-atom force-field is critical in order to accurately predict important fluid properties of long-chain, linear molecules. Several united-atom and all-atom force-fields were benchmarked with respect to their how accurately they predicted the density and viscosity of n-hexadecane compared to experiment. These comparisons used the Green-Kubo method in equilibrium molecular dynamics (EMD) simulations under both ambient and high temperature, high pressure conditions. Whilst united-atom force-fields accurately reproduced experimental density, the viscosity was significantly under-predicted compared to all-atom force-fields and experiments. Moreover, some all-atom force-fields yielded elevated melting points, leading to significant overestimation of both the density and viscosity. Recently all-atom force-fields specifically parameterised for long-chain alkanes accurately predicted density and viscosity under ambient and high temperature, high pressure conditions.
2. Nonequilibrium molecular dynamics (NEMD) simulations showed that united-atom force-fields can provide an accurate representation of the structure of confined organic friction modifier (OFM) films; however, friction coefficients were significantly under-predicted. Moreover, their friction-velocity and particularly friction-coverage behaviour deviates from that obtained with all-atom force-fields and experiments. These observations had important implications regarding force-field selection for NEMD simulations of tribological systems; specifically, it was recommended that accurate all-atom potentials, such as L-OPLS-AA are used.

3. NEMD simulations of OFM films with a thin layer of confined n-hexadecane lubricant were performed. They indicated that, at low and medium coverage, OFMs form liquid-like and amorphous monolayers, respectively, which are significantly interdigitated with the confined hexadecane, resulting in high friction coefficients. At high coverage, solid-like monolayers were formed which facilitated slip between the well-defined OFM and hexadecane layers, yielding a marked reduction in the friction coefficient.
4. When present at equal surface coverage, OFMs with saturated and Z-unsaturated tailgroups were found to yield similar structure and friction behaviour. In boundary friction experiments, OFMs with saturated tailgroups showed similar friction behaviour to the high coverage NEMD results, whereas OFMs with Z-unsaturated tailgroups resembled the low coverage NEMD results. This suggests that OFMs with saturated tailgroups form close-packed monolayers under boundary lubrication layers whilst steric effects prevent this for OFMs with Z-unsaturated tailgroups. This postulation has since been supported by adsorption experiments.
5. OFMs with glyceride headgroups yielded significantly lower friction coefficients than amide and particularly carboxylic acid headgroups. This was shown to be due to the formation of intermolecular hydrogen bonded networks which yielded a more coherent, solid like film, reduced interdigitation as well as the friction coefficient.
6. For all of the OFMs and coverages simulated, the friction coefficient was found to increase linearly with log(sliding velocity). This observation is in agreement with experiment and can be rationalised through stress-promoted thermal activation theory. The slope of the increase in friction with log(sliding velocity) depends on the coverage, with medium coverage films being most sensitive to changes in sliding velocity.
7. Surfaces with random nanoscale roughness led to more liquid-like OFM films due to frustration of the ordering of the molecules. However, the friction coefficient and firction force at zero-load (Derjaguin offset) were only slightly increased by the levels of surface

roughness studied. This suggests that OFM films are almost as effective on contact surfaces with nanoscale roughness compared to those which are atomically-smooth.

8. NEMD simulations of carbon nano-diamonds (CNDs) and carbon nano-onions (CNOs) showed that, at high coverage and/or low pressure, the nanoparticles do not indent into the iron slabs during sliding, leading to zero wear and a low friction coefficient. At low coverage and/or high pressure, the nanoparticles indent into, and plough through the slabs during sliding, leading to atomic-scale wear and a much higher friction coefficient. This contribution to the friction coefficient was well predicted by an expression developed for macroscopic indentation by Bowden and Tabor. Even at the highest pressures and lowest coverages simulated, both nanoparticles were able to maintain separation of the opposing slabs and reduce friction by approximately 75 % compared to when no nanoparticle was present, which agrees well with experimental observations. CNO nanoparticles yielded a lower indentation (wear) depth and lower friction coefficients at equal coverage and pressure with respect to CND, making them more attractive friction modifier additives.
9. A combination of tribological experiments and confined NEMD simulations revealed clear relationships between the friction and flow behaviour. Lubricants, which are flexible, broadly linear molecules, gave low friction coefficients that increased with strain rate and pressure in both the experiments and the simulations. Conversely, traction fluids, which are based on inflexible cycloaliphatic groups, gave high friction coefficients that only weakly depended on strain rate and pressure. The observed differences in friction behaviour were rationalised through the stronger shear localisation which is observed for the traction fluids in the simulations. Higher pressures lead to more pronounced shear localisation, whilst increased strain rates lead to a widening of the sheared region.

9.2. Further Work

The work carried out in this thesis involved applying confined NEMD simulations to a range of diverse problems in tribology. Rather than focussing on identifying further applications of the same methods

to different problems, this section will focus on new methodologies which can give different information. Some parts of this section have been submitted to the journal *Friction* (ref. [3]).

Molecular simulations have made remarkable advances in the past few decades both in terms of methodology development and application-driven research. Despite this, for a more general approach to modelling in the context of lubrication and tribology, new tools and knowledge are required to describe complex phenomena that govern the macroscopic experimental behaviour. Our understanding of some complex tribology problems (e.g. tribochemistry, triboemmission, adhesion, plasticity), would benefit from models which span multiple scales with multiple levels of complexity. Multiscale/multiphysics modelling can be used to calculate material properties or system behaviour at one level, using information or models from different levels. At each level, different approaches are used to describe the system. The following levels are usually distinguished: quantum mechanical models (electronic scale), MD models (atomic scale), coarse-grained models (mesoscopic scale), and finally continuum models. Each level addresses a phenomenon over a specific window of length and time.

Critical to these advances will be to link MD with simulations performed at the top and bottom of the scales (see Fig. 2). In doing so, modelling strategies can be produced that will minimise the computational resources required while maximising the insight provided by simulations performed simultaneously or sequentially at different scales. The emphasis remains on lubricants and additives in the next two sub-sections. An outlook is provided which describes the most promising multiscale/multiphysics techniques currently available to link MD simulations to quantum mechanics (section 9.2.1.) and continuum models (section 9.2.2.).

9.2.1. Linking MD to Smaller Scales

The function of many lubricant additives depends on chemical reactivity both in solution and at solid surfaces. Modelling chemical reactivity is beyond the capabilities of classical MD simulations; however, techniques which allow this have been developed and applied to study lubricant additives.

One promising technique is the use of 'reactive' force-fields, such as ReaxFF [380] which can approximate chemical reactivity in classical MD simulations through bond order terms [381]. A drawback of this approach is the limited availability of reliable parameter sets for the materials, conditions, and properties of interest. The generation of high-quality ReaxFF parameter sets is a very difficult and time consuming task due to the huge number of parameters which need to be fitted [382]. Despite this, parameters have been developed which can be used to investigate some important lubricant additives, such as carboxylic acid OFMs [383], phosphoric acids [384] and MoS_2 [385]. Using such force fields, relatively large molecular systems (nm) can be compressed and sheared [384] in a similar manner to conventional confined NEMD simulations, and consequent chemical reactions monitored over a reasonable simulations time (ns).

Alternatively, the reactivity of lubricant additives can be explicitly modelled using first principles or *ab initio* MD techniques. Examples of this include Car-Parrinello MD (CP-MD) [386–390] and tight-binding quantum chemical MD (TB-QCMD) [391–395], which have given important insights into the reactivity of common friction modifier (molybdenum disulphide - MoS_2, molybdenum dithiocarbamate - MoDTC) and anti-wear (zinc dialkyldithiophosphate - ZDDP) additives. *Ab intito* NEMD simulations have also been performed on additive systems subjected to confinement and shear. For example, TB-QCMD has been used to investigate OFM adsorption on iron oxide surfaces under sliding conditions [292,293,296]. While these techniques allow more accurate reactivity behaviour, they are orders of magnitude more expensive than classical MD simulations, meaning that the system sizes and timescales accessible are rather limited. One potential solution, for confined NEMD where the 'reactive' region is well-defined, is spatial coupling of classical MD for the 'non-reactive' region to *ab initio* MD for the 'reactive' region.

9.2.2. Linking MD to Larger Scales

As shown in Fig. 7, the next scale up from atomistic MD is coarse-grained MD (CG-MD), which involves grouping of multiple atoms together to form 'beads' to reduce the number of interaction sites. It is

commonly used to simulate large polymers, where monomers or even a combination of monomers can be represented as a single CG bead. CG-MD has not been extensively applied in tribology; however, it has been used to study friction in polymer brushes [396,397], model friction modifier additives [398] and ionic liquids [399]. The use of CG-MD in tribology is likely to remain rare in tribology, since the importance of atomic detail has been highlighted in representing a range of processes accurately. Possible applications of CG-MD in tribology are very large polymer additives or the study of relatively slow processes such as surfactant self-assembly at solid surfaces whose timescales are inaccessible to study using atomistic force-fields.

Most tribological processes are governed by physical and chemical phenomena localised in an interfacial layer which controls the macroscopic behaviour of the system. With this is mind, an attractive possibility is to capture the interfacial laws of friction, heat transfer, and other relevant phenomena at small, accurate scales and pass this information to continuum models to study entire tribological systems. Choosing how to pass information across the scales is not always straightforward; some issues concern what assumptions can be made and the accuracy required in linking the two levels. Two options are usually available, depending whether it is possible to establish scale-separation between the atomic level and the continuum. If such separation exists, then a hierarchical (or sequential) multiscale model is acceptable, otherwise a hybrid (or concurrent) scheme is required. Both of these MD-continuum coupling methods have already been applied to a variety of problems in tribology. Hierarchical coupling involves using MD simulations to gain information about the boundary conditions and constitutive laws to input into separate continuum models [400]. This method is relatively straightforward to implement, but requires careful planning to establish which regions of phase space can be reliably probed with MD to provide useful inputs for the continuum models. For example, Martini et al. [140] and Savio et al. [142,154] used local viscosity and slip information obtained using MD simulations to improve continuum predictions of film thickness and friction for strongly confined systems. These are examples of phenomena that can be studied at a single relevant scale and integrated at a larger scale in a hierarchical manner.

Alternatively, the MD and continuum models can be run concurrently on different spatial regions; this is the preferred method when atomic interactions dictate the observed macroscopic tribological behaviour but are themselves affected by the whole macroscopic domain. Modelling surfaces with realistic levels of roughness lubricated by a fluid is a case in point. Such a problem is still beyond the scales accessible to full MD simulation. Alternatively, atomistic details of the surface topography and fluid close to the walls can be explicitly modelled and intimately linked to the macroscopic response of the fluid further from the walls. In this case MD-continuum coupling strategies involve the transfer of information between the MD and continuum regions, and particular care must be taken when the two descriptions merge [401,402]. A number of schemes exist for this [403–406], with various procedures enabling hybrid coupling [407].

Models dealing with concurrent coupling are generally far more complex than their hierarchical alternatives, but are of high importance in understanding the physics of certain phenomena in contact interfaces, such as the effect of surface roughness, surface coatings and additive layers on fluid flow. One major limitation of concurrent coupling techniques is that the simulation time step is limited to the shortest timescale which needs to be modelled at the smallest scale. Despite this, considerable performance enhancements can be achieved compared to modelling the entire system at the atomic level [405]. The future success of concurrent coupling schemes will depend on the development of efficient coupling libraries and algorithms that facilitate hybrid coupling simulations and support their implementation on different HPC platforms (see *e.g.* a recent software made available by the Imperial College Tribology Group [408]).

9.2.3. Summary

Classical NEMD simulations have already given unique insights into the atomic-scale behaviour of lubricants and additives, but are for computational reasons limited to the study of relatively small systems and timescales. This continues to limit their ability to adequately model situations of specific engineering significance. For reactive lubricant additives, classical MD is deficient in its inability to

model chemical reactivity. Moving forwards, we expect classical MD simulations to be supplemented by coupling techniques to *smaller* scales, to study tribochemistry, as well as *larger* scales, to represent entire tribological systems. Tribology is an ideal subject for such multiscale/multiphysics models since many macroscopic tribological phenomena have been shown to driven by atomic-scale processes. Such tools will shed further light on these processes and could even transform lubricant formulation by identifying process-structure-property relationships as it has in other fields of research.

References

1. Holmberg, K.; Andersson, P.; Erdemir, A. Global energy consumption due to friction in passenger cars. *Tribol. Int.* **2012**, *47*, 221–234.

2. Taylor, R. I. Tribology and energy efficiency: from molecules to lubricated contacts to complete machines. *Faraday Discuss.* **2012**, *156*, 361–382.

3. Ewen, J. P.; Heyes, D. M.; Dini, D. Advances in molecular dynamics simulations of lubricants and additives. *Friction* **2017**, *Submitted*.

4. Lu, X. B.; Khonsari, M. M.; Gelinck, E. R. M. The Stribeck curve: Experimental results and theoretical prediction. *J. Tribol. Asme* **2006**, *128*, 789–794.

5. Hutchings, I. M. *Tribology: Friction and Wear of Engineering Materials*; Elsevier Butterworth Heinemann: London, 1992.

6. Hori, Y. *Hydrodynamic Lubrication*; Springer: Tokyo, 2006.

7. Reynolds, O. On the theory of lubrication and its application to Mr. Beauchamp Tower's experiments, including an experimental determination of the viscosity of olive oil. *Proc. Roy. Soc. Lond.* **1886**, *40*, 191–203.

8. Spikes, H.; Zhang, J. History, Origins and Prediction of Elastohydrodynamic Friction. *Tribol. Lett.* **2014**, *56*, 1–25.

9. Spikes, H. A. Mixed lubrication — an overview. *Lubr. Sci.* **1997**, *9*, 221–253.

10. Spikes, H. A. Boundary Lubrication and Boundary Films. In *Thin Films in Tribology*; Leeds, 1993; Vol. 25, pp. 331–346.

11. Spikes, H. Friction Modifier Additives. *Tribol. Lett.* **2015**, *60*, 5.

12. Loehle, S. Understanding of adsorption mechanism and tribological behaviors of C18 fatty acids on iron-based surfaces: A molecular simulation approach, l'Ecole Centrale de Lyon, 2014.

13. Jackson, A. Synthetic versus Mineral Fluids in Lubrication. In *International Tribology Conference*; 1987; p. 10.

14. Clark, R.; Wedlock, D.; Cherrillo, R. Future fuels and lubricant base oils from Shell Gas to Liquids (GTL) technology. *SAE Tech. Pap.* **2005**, *2005-01–21*, 1–16.

15. Zhang, J.; Tan, A.; Spikes, H. Effect of Base Oil Structure on Elastohydrodynamic Friction. *Tribol. Lett.* **2017**, *65*, 13.

16. Bodnarchuk, M. S.; Heyes, D. M.; Breakspear, A.; Chahine, S.; Dini, D. A molecular dynamics study of CaCO3 nanoparticles in a hydrophobic solvent with a stearate co-surfactant. *Phys. Chem. Chem. Phys.* **2015**, *17*, 13575–13581.

17. Spikes, H. The history and mechanisms of ZDDP. *Tribol. Lett.* **2004**, *17*, 469–489.

18. Gattinoni, C.; Michaelides, A. Understanding corrosion inhibition with van der Waals DFT methods: the case of benzotriazole. *Faraday Discuss.* **2015**, *180*, 439–458.

19. Ghosh, P.; Das, M. Study of the influence of some polymeric additives as viscosity index improvers and pour point depressants - Synthesis and characterization. *J. Pet. Sci. Eng.* **2014**, *119*, 79–84.

20. Davidson, J. E.; Hinchley, S. L.; Harris, S. G.; Parkin, A.; Parsons, S.; Tasker, P. A. Molecular dynamics simulations to aid the rational design of organic friction modifiers. *J. Mol. Graph. Model.* **2006**, *25*,

495–506.

21. Hartkamp, R. A molecular dynamics study of non-newtonian flows of simple fluids in confined and unconfined geometries, University of Twente, 2013.

22. Berro, H. A Molecular Dynamics Approach to Nano-scale Lubrication, l'Ecole de Central de Lyon, 2010.

23. Allen, M. P.; Tidesley, D. J. *Computer Simulation of Liquids*; Clarendon Press: Oxford, 1989.

24. Goldstein, M. Viscous Liquids and the Glass Transition: A Potential Energy Barrier Picture. *J. Chem. Phys.* **1969**, *51*, 3728–3739.

25. Levesque, D.; Verlet, L.; Kurkijar.J Computer "Experiments" on Classical Fluids. IV. Transport Properties and Time-Correlation Functions of the Lennard- Jones Liquid near its Triple Point. *Phys. Rev. A* **1973**, *7*, 1690–1700.

26. Siu, S. W. I.; Pluhackova, K.; Bockmann, R. A. Optimization of the OPLS-AA Force Field for Long Hydrocarbons. *J. Chem. Theory Comput.* **2012**, *8*, 1459–1470.

27. Dong, Y.; Li, Q.; Martini, A. Molecular dynamics simulation of atomic friction: A review and guide. *J. Vac. Sci. Technol. A,* **2013**, *31*, 30801.

28. Sawyer, W. G.; Argibay, N.; Burris, D. L.; Krick, B. A. Mechanistic Studies in Friction and Wear of Bulk Materials. *Annu. Rev. Mater. Res.* **2014**, *44*, 395–427.

29. Alder, B. J.; Wainwright, T. E. Phase Transition for a Hard Sphere System. *J. Chem. Phys.* **1957**, *27*, 1208–1209.

30. Frenkel, D. Entropy-driven phase transitions. *Physica A* **1999**, *263*, 26–38.

31. Rahman, A. Correlations in the Motion of Atoms in Liquid Argon. *Phys. Rev.* **1964**, *136*, 405–411.

32. Eyring, H.; Ree, T. Significant Liquid Structures, VI. The Vacancy Theory of Liquids. *Proc. Natl. Acad. Sci.* **1961**, *47*, 526–537.

33. Ediger, M. D. Spatially Heterogeneous Dynamics in Supercooled Liquids. *Annu. Rev. Phys. Chem.* **2000**, *51*, 99–128.

34. Hansen, J.-P.; McDonald, R. I. *Theory of Simple Liquids*; 4th ed.; Academic Press: Amsterdam, 2014.

35. Alder, B. J.; Gass, D. M.; Wainwright, T. . Studies in Molecular Dynamics. VIII. The Transport Coefficients for a Hard-Sphere Fluid. *J. Chem. Phys.* **1970**, *53*, 3813–3826.

36. Hefland, E. Transport Coefficients from Dissipation in a Canonical Ensemble. *Phys. Rev.* **1960**, *570*, 1.

37. Green, M. S. Markoff Random Processes and the Statistical Mechanics of Time-Dependent Phenomena. II. Irreversible Processes in Fluids. *J. Chem. Phys.* **1954**, *22*, 398–413.

38. Kubo, R. Statistical-Mechanical Theory of Irreversible Processes. I. General Theory and Simple Applications to Magnetic and Conduction Problems. *J. Phys. Soc. Jpn.* **1957**, *12*, 570–586.

39. Ladd, A. J. C.; Alley, W. E.; Alder, B. J. Structural relaxation in dense hard-sphere fluids. *J. Stat. Phys.* **1987**, *48*, 1147–1156.

40. Ashurst, W. T.; Hoover, W. G. Dense-fluid shear viscosity via nonequilibrium molecular dynamics. *Phys. Rev. A* **1975**, *11*, 658–678.

41. Bitsanis, I.; Magda, J. J.; Tirrell, M.; Davis, H. T. Molecular dynamics of flow in micropores. *J. Chem.*

Phys. **1987**, *87*, 1733–1750.

42. Ewen, J.; Gattinoni, C.; Zhang, J.; Heyes, D. M.; Spikes, H. A.; Dini, D. On the Effect of Confined Fluid Molecular Structure on Nonequilibrium Phase Behaviour and Friction. *Phys. Chem. Chem. Phys.* **2017**, *19*, 17883.

43. Lees, A. W.; Edwards, S. F. The computer study of transport processes under extreme conditions. *J. Phys. Part C Solid State Phys.* **1972**, *5*, 1921-.

44. Evans, D. J.; Morriss, G. P. *Statistical Mechanics of Nonequilibrium Liquids*; 2nd ed.; Cambridge University Press: Cambridge, 2008.

45. Todd, B. D.; Daivis, P. J. *Nonequilibrium Molecular Dynamics*; Cambridge University Press: Cambridge, 2017.

46. Heyes, D. M.; Kim, J. J.; Montrose, C. J.; Litovitz, T. A. Time dependent nonlinear shear stress effects in simple liquids: A molecular dynamics study. *J. Chem. Phys.* **1980**, *73*, 3987–3996.

47. Gotz, A. W.; Williamson, M. J.; Xu, D.; Poole, D.; Le Grand, S.; Walker, R. C. Routine Microsecond Molecular Dynamics Simulations with AMBER on GPUs. 1. Generalized Born. *J. Chem. Theory Comput* **2012**, *8*, 1542−1555.

48. Bair, S.; McCabe, C.; Cummings, P. T. Comparison of nonequilibrium molecular dynamics with experimental measurements in the nonlinear shear-thinning regime. *Phys. Rev. Lett.* **2002**, *88*, 58302.

49. Bair, S.; McCabe, C.; Cummings, P. T. Calculation of viscous EHL traction for squalane using molecular simulation and rheometry. *Tribol. Lett.* **2002**, *13*, 251–254.

50. Morriss, G. P.; Evans, D. J. Application of transient correlation functions to shear flow far from equilibrium. *Phys. Rev. A* **1987**, *35*, 792–797.

51. Evans, D. J.; Morriss, G. P. Transient-time-correlation functions and the rheology of fluids. *Phys. Rev. A* **1988**, *38*, 4142–4148.

52. Taylor, R.; de Kraker, B. Shear rates in engines and implications for lubricant design. *Proc. Inst. Mech. Eng. Part J J. Eng. Tribol.* **2017**, *231*, 1106–1116.

53. Andersen, H. C. Molecular Dynamics Simulations at Constant Pressure and/or Temperature. *J. Chem. Phys.* **1980**, *72*, 2384–2393.

54. Berendsen, H. J. C.; Postma, J. P. M.; Vangunsteren, W. F.; Dinola, A.; Haak, J. R. Molecular dynamics with coupling to an external bath. *J. Chem. Phys.* **1984**, *81*, 3684–3690.

55. Schneider, T.; Stoll, E. Molecular-dynamics study of a three-dimensional one-component model for distortive phase-transitions. *Phys. Rev. B* **1978**, *17*, 1302–1322.

56. Nosé, S. A Molecular-Dynamics Method for Simulations in the Canonical Ensemble. *Mol. Phys.* **1984**, *52*, 255–268.

57. Hoover, W. G. Canonical Dynamics: Equilibrium Phase-Space Distributions. *Phys. Rev. A* **1985**, *31*, 1695–1697.

58. Mundy, C. J.; Siepmann, J. I.; Klein, M. L. Decane under shear: A molecular dynamics study using reversible NVT-SLLOD and NPT-SLLOD algorithms. *J. Chem. Phys.* **1995**, *103*, 10192–10200.

59. Delhommelle, J.; Petravic, J.; Evans, D. J. On the effects of assuming flow profiles in nonequilibrium simulations. *J. Chem. Phys.* **2003**, *119*, 11005–11010.

60. Delhommelle, J.; Petravic, J.; Evans, D. J. Reexamination of string phase and shear thickening in

simple fluids. *Phys. Rev. E. Stat. Nonlin. Soft Matter Phys.* **2003**, *68*, 31201.

61. Delhommelle, J.; Evans, D. J. Configurational temperature profile in confined fluids. II. Molecular fluids. *J. Chem. Phys.* **2001**, *114*, 6236.

62. Braga, C.; Travis, K. P. A configurational temperature Nosé-Hoover thermostat. *J. Chem. Phys.* **2005**, *123*, 134101.

63. Yong, X.; Zhang, L. T. Thermostats and thermostat strategies for molecular dynamics simulations of nanofluidics. *J. Chem. Phys.* **2013**, *138*.

64. Khare, R.; de Pablo, J.; Yethiraj, A. Molecular simulation and continuum mechanics study of simple fluids in non-isothermal planar couette flows. *J. Chem. Phys.* **1997**, *107*, 2589.

65. Bernardi, S.; Todd, B. D.; Searles, D. J. Thermostating highly confined fluids. *J. Chem. Phys.* **2010**, *132*, 244706.

66. Berro, H.; Fillot, N.; Vergne, P.; Tokumasu, T.; Ohara, T.; Kikugawa, G. Energy dissipation in non-isothermal molecular dynamics simulations of confined liquids under shear. *J. Chem. Phys.* **2011**, *135*, 134708.

67. De Luca, S.; Todd, B. D.; Hansen, J. S.; Daivis, P. J. A new and effective method for thermostatting confined fluids. *J. Chem. Phys.* **2014**, *140*, 15.

68. Gattinoni, C.; Mackowiak, S.; Heyes, D. M.; Branka, A. C.; Dini, D. Boundary-controlled barostats for slab geometries in molecular dynamics simulations. *Phys. Rev. E* **2014**, *90*, 13.

69. Ewen, J. P.; Gattinoni, C.; Thakkar, F. M.; Morgan, N.; Spikes, H.; Dini, D. A Comparison of Classical Force-Fields for Molecular Dynamics Simulations of Lubricants. *Materials.* **2016**, *9*, 651.

70. Luty, B. A.; Davis, M. E.; Tironi, I. G.; Vangunsteren, W. F. A comparison of particle-particle, particle-mesh and Ewald methods for calculating electrostatic interactions in periodic molecular-systems. *Mol. Simul.* **1994**, *14*, 11–20.

71. Fischer, J.; Paschek, D.; Geiger, A.; Sadowski, G. Modeling of aqueous poly(oxyethylene) solutions: 1. Atomistic Simulations. *J. Phys. Chem. B* **2008**, *112*, 2388–2398.

72. Ye, X. G.; Cui, S. T.; de Almeida, V. F.; Khomami, B. Effect of varying the 1-4 intramolecular scaling factor in atomistic simulations of long-chain N-alkanes with the OPLS-AA model. *J. Mol. Model.* **2013**, *19*, 1251–1258.

73. Pan, G.; McCabe, C. Prediction of viscosity for molecular fluids at experimentally accessible shear rates using the transient time correlation function formalism. *J. Chem. Phys.* **2006**, *125*, 9.

74. Delhommelle, J.; Cummings, P. T. Simulation of friction in nanoconfined fluids for an arbitrarily low shear rate. *Phys. Rev. B* **2005**, *72*, 4.

75. Bernardi, S.; Brookes, S. J.; Searles, D. J.; Evans, D. J. Response theory for confined systems. *J. Chem. Phys.* **2012**, *137*, 7.

76. Bocquet, L.; Barrat, J. L. Hydrodynamic boundary conditions, correlation functions, and Kubo relations for confined fluids. *Phys. Rev. E* **1994**, *49*, 3079–3092.

77. Petravic, J.; Harrowell, P. On the equilibrium calculation of the friction coefficient for liquid slip against a wall. *J. Chem. Phys.* **2007**, *127*, 174706.

78. Bocquet, L.; Barrat, J. L. On the Green-Kubo relationship for the liquid-solid friction coefficient. *J. Chem. Phys.* **2013**, *139*.

79. Muller-Plathe, F. Reversing the perturbation in nonequilibrium molecular dynamics: An easy way to calculate the shear viscosity of fluids. *Phys. Rev. E* **1999**, *59*, 4894–4898.

80. Bordat, P.; Muller-Plathe, F. The shear viscosity of molecular fluids: A calculation by reverse nonequilibrium molecular dynamics. *J. Chem. Phys.* **2002**, *116*, 3362–3369.

81. Muller, T. J.; Muller-Plathe, F. Determining the Local Shear Viscosity of a Lipid Bilayer System by Reverse Non-Equilibrium Molecular Dynamics Simulations. *ChemPhysChem* **2009**, *10*, 2305–2315.

82. Voeltzel, N.; Giuliani, A.; Fillot, N.; Vergne, P.; Joly, L. Nanolubrication by ionic liquids: molecular dynamics simulations reveal an anomalous effective rheology. *Phys. Chem. Chem. Phys.* **2015**, *17*, 23226–23235.

83. Tenney, C. M.; Maginn, E. J. Limitations and recommendations for the calculation of shear viscosity using reverse nonequilibrium molecular dynamics. *J. Chem. Phys.* **2010**, *132*, 14103.

84. Todd, B. D.; Daivis, P. J. Nonequilibrium molecular dynamics simulations of planar elongational flow with spatially and temporally periodic boundary conditions. *Phys. Rev. Lett.* **1998**, *81*, 1118–1121.

85. Bair, S. Rheology and high-pressure models for quantitative elastohydrodynamics. *Proc. Inst. Mech. Eng. Part J J. Eng. Tribol.* **2008**, *223*, 617–628.

86. Baig, C.; Edwards, B. J.; Keffer, D. J.; Cochran, H. D. Rheological and structural studies of liquid decane, hexadecane, and tetracosane under planar elongational flow using nonequilibrium molecular-dynamics simulations. *J. Chem. Phys.* **2005**, *122*, 1–2.

87. Baig, C.; Edwards, B. J.; Keffer, D. J.; Cochran, H. D. A proper approach for nonequilibrium molecular dynamics simulations of planar elongational flow. *J. Chem. Phys.* **2005**, *122*, 14.

88. Hunt, T. A.; Bernardi, S.; Todd, B. D. A new algorithm for extended nonequilibrium molecular dynamics simulations of mixed flow. *J. Chem. Phys.* **2010**, *133*, 7.

89. Hartkamp, R.; Bernardi, S.; Todd, B. D. Transient-time correlation function applied to mixed shear and elongational flows. *J. Chem. Phys.* **2012**, *136*, 7.

90. Stevens, M. J.; Mondello, M.; Grest, G. S.; Cui, S. T.; Cochran, H. D.; Cummings, P. T. Comparison of shear flow of hexadecane in a confined geometry and in bulk. *J. Chem. Phys.* **1997**, *106*, 7303–7314.

91. Zhang, J.; Todd, B. D.; Travis, K. P. Viscosity of confined inhomogeneous nonequilibrium fluids. *J. Chem. Phys.* **2004**, *121*, 10778–10786.

92. Liem, S. Y.; Brown, D.; Clarke, J. H. R. Investigation of the homogeneous-shear nonequilibrium-molecular-dynamics method. *Phys. Rev. A* **1992**, *45*, 3706–3713.

93. Todd, B. D.; Evans, D. J.; Travis, K. P.; Daivis, P. J. Comment on “Molecular simulation and continuum mechanics study of simple fluids in nonisothermal planar Couette flows” [J. Chem. Phys. 107, 2589 (1997)]. *J. Chem. Phys.* **1999**, *111*, 10730.

94. Cui, S. T.; Cummings, P. T.; Cochran, H. D.; Moore, J. D.; Gupta, S. A. Nonequilibrium molecular dynamics simulation of the rheology of linear and branched alkanes. *Int. J. Thermophys.* **1998**, *19*, 449–459.

95. Mundy, C. J.; Balasubramanian, S.; Bagchi, K.; Siepmann, J. I.; Klein, M. L. Equilibrium and non-equilibrium simulation studies of fluid alkanes in bulk and at interfaces. *Faraday Discuss.* **1996**, *104*, 17–36.

96. Todd, B. D.; Daivis, P. J. Homogeneous non-equilibrium molecular dynamics simulations of viscous flow: techniques and applications. *Mol. Simul.* **2007**, *33*, 189–229.

97. Morriss, G. P.; Daivis, P. J.; Evans, D. J. The rheology of normal alkanes: Decane and Eicosane. *J. Chem. Phys.* **1991**, *94*, 7420–7433.

98. Weeks, J. D.; Chandler, D.; Andersen, H. C. Role of Repulsive Forces in Determining the Equilibrium Structure of Simple Liquids. *J. Chem. Phys. 54*, 5237–5247.

99. Khare, R.; dePablo, J.; Yethiraj, A. Rheological, thermodynamic, and structural studies of linear and branched alkanes under shear. *J. Chem. Phys.* **1997**, *107*, 6956–6964.

100. Jorgensen, W. L.; Madura, J. D.; Swenson, C. J. Optimized intermolecular potential functions for liquid hydrocarbons. *J. Am. Chem. Soc.* **1984**, *106*, 6638–6646.

101. Moore, J. D.; Cui, S. T.; Cochran, H. D.; Cummings, P. T. Rheology of lubricant basestocks: A molecular dynamics study of C-30 isomers. *J. Chem. Phys.* **2000**, *113*, 8833–8840.

102. Siepmann, J. I.; Karaborni, S.; Smit, B. Simulating the critical behavior of complex fluids. *Nature* **1993**, *365*, 330–332.

103. Rouse, P. E. A Theory of the Linear Viscoelastic Properties of Dilute Solutions of Coiling Polymers. *J. Chem. Phys* **1953**, *21*, 1272.

104. McCabe, C.; Cui, S. T.; Cummings, P. T.; Gordon, P. A.; Saeger, R. B. Examining the rheology of 9-octylheptadecane to giga-pascal pressures. *J. Chem. Phys.* **2001**, *114*, 1887–1891.

105. McCabe, C.; Cui, S. T.; Cummings, P. T. Characterizing the viscosity-temperature dependence of lubricants by molecular simulation. *Fluid Phase Equilib.* **2001**, *183*, 363–370.

106. Liu, P. Z.; Yu, H. L.; Ren, N.; Lockwood, F. E.; Wang, Q. J. Pressure-Viscosity Coefficient of Hydrocarbon Base Oil through Molecular Dynamics Simulations. *Tribol. Lett.* **2015**, *60*, 9.

107. Bird, R. B.; Armstrong, R. C.; Hassager, O. *Dynamics of Polymeric Liquids: Fluid Mechanics*; John Wiley and Sons: New York, 1987.

108. Bair, S. The High Pressure Rheology of Some Simple Model Hydrocarbons. *Proc. Instn. Mech. Engrs. Part J J Eng. Tribol.* **2002**, *216*, 139–149.

109. Yang, Y.; Pakkanen, T. A.; Rowley, R. L. NEMD simulations of viscosity and viscosity index for lubricant-size model molecules. *Int. J. Thermophys.* **2002**, *23*, 1441–1454.

110. Liu, P.; Lu, J.; Yu, H.; Ren, N.; Lockwood, F. E.; Wang, Q. J. Lubricant shear thinning behavior correlated with variation of radius of gyration via molecular dynamics simulations. *J. Chem. Phys.* **2017**, *147*, 84904.

111. Bair, S.; Winer, W. O. A quantitative test of the Einstein-Debye relation using the shear dependence of viscosity for low molecular weight liquids. *Tribol. Lett.* **2007**, *26*, 223–228.

112. Carreau, P. J. Rheological Equations from Molecular Network Theories. *J. Rheol.* **1972**, *16*, 99.

113. Jadhao, V.; Robbins, M. O. Probing large viscosities in glass-formers with nonequilibrium simulations. *Proc. Natl. Acad. Sci.* **2017**, *114*, 7952–7957.

114. Eyring, H. Viscosity, plasticity, and diffusion as examples of absolute reaction rates. *J. Chem. Phys.* **1936**, *4*, 283–291.

115. Travis, K. P.; Todd, B. D.; Evans, D. J. Departure from Navier-Stokes hydrodynamics in confined liquids. *Phys. Rev. E* **1997**, *55*, 4288–4295.

116. Abraham, F. F. The interfacial density profile of a Lennard-Jones fluid in contact with a (100) Lennard-Jones wall and its relationship to idealized fluid/wall systems. *J. Chem. Phys.* **1978**, *68*, 3713.

117. Snook, I. K.; Megen, W. Van Solvation forces in simple dense fluids. I. *J. Chem. Phys.* **1980**, *72*, 2907.

118. Horn, R. G.; Israelachvili, J. N. Direct measurement of structural forces between two surfaces in a nonpolar liquid. *J. Chem. Phys.* **1981**, *75*, 1400.

119. Magda, J. J.; Tirrell, M.; Davis, H. T. Molecular dynamics of narrow, liquid-filled pores. *J. Chem. Phys.* **1985**, *83*, 1888–1901.

120. Bitsanis, I.; Somers, S. A.; Davis, H. T.; Tirrell, M. Microscopic dynamics of flow in molecularly narrow pores. *J. Chem. Phys.* **1990**, *93*, 3427–3431.

121. Israelachvili, J. N. Measurement of the viscosity of liquids in very thin films. *J. Colloid Interface Sci.* **1986**, *110*, 263–271.

122. Gee, M. L.; McGuiggan, P. M.; Israelachvili, J. N.; Homola, A. M. Liquid to solid-like transitions of molecularly thin-films under shear. *J. Chem. Phys.* **1990**, *93*, 1895–1906.

123. Somers, S. A.; Davis, H. T. Microscopic dynamics of fluids confined between smooth and atomically structured solid surfaces. *J. Chem. Phys.* **1992**, *96*, 5389–5407.

124. Jabbarzadeh, A.; Harrowell, P.; Tanner, R. I. Crystal bridge formation marks the transition to rigidity in a thin lubrication film. *Phys. Rev. Lett.* **2006**, *96*, 206102.

125. Granick, S. Motions and relaxations of confined liquids. *Science.* **1991**, *253*, 1374–1379.

126. Klein, J.; Kumacheva, E. Simple liquids confined to molecularly thin layers. I. Confinement-induced liquid-to-solid phase transitions. *J. Chem. Phys.* **1998**, *108*, 6996–7009.

127. Klein, J.; Kumacheva, E. Confinement-induced phase transitions in simple liquids. *Science.* **1995**, *269*, 816–819.

128. Thompson, P. A.; Grest, G. S.; Robbins, M. O. Phase transitions and universal dynamics in confined films. *Phys. Rev. Lett.* **1992**, *68*, 3448–3451.

129. Gao, J. P.; Luedtke, W. D.; Landman, U. Layering transitions and dynamics of confined liquid films. *Phys. Rev. Lett.* **1997**, *79*, 705–708.

130. Docherty, H.; Cummings, P. T. Direct evidence for fluid-solid transition of nanoconfined fluids. *Soft Matter* **2010**, *6*, 1640–1643.

131. Van Alsten, J.; Granick, S. Molecular tribometry of ultrathin liquid films. *Phys. Rev. Lett.* **1988**, *61*, 2570–2573.

132. Zhu, Y.; Granick, S. Reassessment of solidification in fluids confined between mica sheets. *Langmuir* **2003**, *19*, 8148–8151.

133. Jabbarzadeh, A.; Atkinson, J. D.; Tanner, R. I. The effect of branching on slip and rheological properties of lubricants in molecular dynamics simulation of Couette shear flow. *Tribol. Int.* **2002**, *35*, 35–46.

134. Gupta, S. A.; Cochran, H. D.; Cummings, P. T. Shear behavior of squalane and tetracosane under extreme confinement .2. Confined film structure. *J. Chem. Phys.* **1997**, *107*, 10327–10334.

135. Gao, J. P.; Luedtke, W. D.; Landman, U. Structures, solvation forces and shear of molecular films in a rough nano-confinement. *Tribol. Lett.* **2000**, *9*, 3–13.

136. Jabbarzadeh, A.; Atkinson, J. D.; Tanner, R. I. Effect of the wall roughness on slip and rheological properties of hexadecane in molecular dynamics simulation of Couette shear flow between two

sinusoidal walls. *Phys. Rev. E* **2000**, *61*, 690–699.

137. Cui, S. T.; McCabe, C.; Cummings, P. T.; Cochran, H. D. Molecular dynamics study of the nano-rheology of n-dodecane confined between planar surfaces. *J. Chem. Phys.* **2003**, *118*, 8941–8944.

138. Voeltzel, N.; Vergne, P.; Fillot, N.; Bouscharain, N.; Joly, L. Rheology of an Ionic Liquid with Variable Carreau Exponent: A Full Picture by Molecular Simulation with Experimental Contribution. *Tribol. Lett.* **2016**, *64*, 25.

139. Spikes, H. A. Comment on: Rheology of an Ionic Liquid with Variable Carreau Exponent: A Full Picture by Molecular Simulation with Experimental Contribution, by Nicolas Voeltzel, Philippe Vergne, Nicolas Fillot, Nathalie Bouscharain, Laurent Joly, Tribol. Lett. (2017). *Tribol. Lett.* **2017**, *65*, 72.

140. Martini, A.; Liu, Y.; Snurr, R. Q.; Wang, Q. J. Molecular dynamics characterization of thin film viscosity for EHL simulation. *Tribol. Lett.* **2006**, *21*, 217–225.

141. Hu, Y.-Z.; Zhu, D. A Full Numerical Solution to the Mixed Lubrication in Point Contacts. *J. Tribol.* **1999**, *122*, 1–9.

142. Savio, D.; Fillot, N.; Vergne, P.; Zaccheddu, M. A Model for Wall Slip Prediction of Confined n-Alkanes: Effect of Wall-Fluid Interaction Versus Fluid Resistance. *Tribol. Lett.* **2012**, *46*, 11–22.

143. Fillot, N.; Berro, H.; Vergne, P. From Continuous to Molecular Scale in Modelling Elastohydrodynamic Lubrication: Nanoscale Surface Slip Effects on Film Thickness and Friction. *Tribol. Lett.* **2011**, *43*, 257–266.

144. Washizu, H.; Hyodo, S.; Ohmori, T.; Nishino, N.; Suzuki, A. Macroscopic No-Slip Boundary Condition Confirmed in Full Atomistic Simulation of Oil Film. *Tribol. Online* **2014**, *9*, 45–50.

145. Jabbarzadeh, A.; Atkinson, J. D.; Tanner, R. I. Wall slip in the molecular dynamics simulation of thin films of hexadecane. *J. Chem. Phys.* **1999**, *110*, 2612–2620.

146. Martini, A.; Hsu, H. Y.; Patankar, N. A.; Lichter, S. Slip at high shear rates. *Phys. Rev. Lett.* **2008**, *100*, 4.

147. Vadakkepatt, A.; Dong, Y. L.; Lichter, S.; Martini, A. Effect of molecular structure on liquid slip. *Phys. Rev. E* **2011**, *84*, 11.

148. Majumdar, A.; Bhushan, B. Role of Fractal Geometry in Roughness Characterization and Contact Mechanics of Surfaces. *ASME J. Tribol.* **1990**, *112*, 205–216.

149. Pit, R.; Hervet, H.; Leger, L. Direct experimental evidence of slip in hexadecane: Solid interfaces. *Phys. Rev. Lett.* **2000**, *85*, 980–983.

150. Ponjavic, A.; Wong, J. S. S. The effect of boundary slip on elastohydrodynamic lubrication. *RSC Adv.* **2014**, *4*, 20821–20829.

151. Wong, P. L.; Li, X. M.; Guo, F. Evidence of lubricant slip on steel surface in EHL contact. *Tribol. Int.* **2013**, *61*, 116–119.

152. Martinie, L.; Vergne, P. Lubrication at Extreme Conditions: A Discussion About the Limiting Shear Stress Concept. *Tribol. Lett.* **2016**, *63*, 21.

153. Zhu, Y.; Granick, S. Limits of the Hydrodynamic No-Slip Boundary Condition. *Phys. Rev. Lett.* **2002**, *88*, 106102.

154. Savio, D.; Fillot, N.; Vergne, P.; Hetzler, H.; Seemann, W.; Morales-Espejel, G. E. A Multiscale Study on the Wall Slip Effect in a Ceramic-Steel Contact With Nanometer-Thick Lubricant Film by a Nano-to-Elastohydrodynamic Lubrication Approach. *J. Tribol* **2015**, *137*, 31502.

155. Heyes, D. M.; Smith, E. R.; Dini, D.; Spikes, H. A.; Zaki, T. A. Pressure dependence of confined liquid behavior subjected to boundary-driven shear. *J. Chem. Phys.* **2012**, *136*, 134705.

156. Gattinoni, C.; Heyes, D. M.; Lorenz, C. D.; Dini, D. Traction and nonequilibrium phase behavior of confined sheared liquids at high pressure. *Phys. Rev. E* **2013**, *88*, 52406.

157. Maćkowiak, S.; Heyes, D. M.; Dini, D.; Brańka, A. C. Non-equilibrium phase behavior and friction of confined molecular films under shear: A non-equilibrium molecular dynamics study. *J. Chem. Phys.* **2016**, *145*, 164704.

158. Bair, S.; Winer, W. O. The high-pressure high shear-stress rheology of liquid lubricants. *J. Tribol.* **1992**, *114*, 1–9.

159. Bair, S.; Qureshi, F.; Winer, W. O. Observations of shear localization in liquid lubricants under pressure. *J. Tribol.* **1993**, *115*, 507–514.

160. Bair, S.; McCabe, C. A study of mechanical shear bands in liquids at high pressure. *Tribol. Int.* **2004**, *37*, 783–789.

161. Ponjavic, A.; Chennaoui, M.; Wong, J. S. S. Through-Thickness Velocity Profile Measurements in an Elastohydrodynamic Contact. *Tribol. Lett.* **2013**, *50*, 261–277.

162. Ponjavic, A.; di Mare, L.; Wong, J. S. S. Effect of Pressure on the Flow Behavior of Polybutene. *J. Polym. Sci. B Polym. Phys.* **2014**, *52*, 708–715.

163. Galmiche, B.; Ponjavic, A.; Wong, J. S. S. Flow measurements of a polyphenyl ether oil in an elastohydrodynamic contact. *J. Phys. Condens. Matter* **2016**, *28*, 134005.

164. Sperka, P.; Krupka, I.; Hartl, M. Evidence of Plug Flow in Rolling-Sliding Elastohydrodynamic Contact. *Tribol. Lett.* **2014**, *54*, 151–160.

165. Sperka, P.; Krupka, I.; Hartl, M. Lubricant flow in thin-film elastohydrodynamic contact under extreme conditions. *Friction* **2016**, *4*, 380–390.

166. Spikes, H.; Tysoe, W. On the Commonality Between Theoretical Models for Fluid and Solid Friction, Wear and Tribochemistry. *Tribol. Lett.* **2015**, *59*, 14.

167. Tomlinson, A.; Danks, T. N.; Heyes, D. M. Interfacial Characterization of Succinimide Surfactants. *Langmuir* **1997**, *7463*, 5881–5893.

168. Ramasamy, U. S.; Lichter, S.; Martini, A. Effect of Molecular-Scale Features on the Polymer Coil Size of Model Viscosity Index Improvers. *Tribol. Lett.* **2016**, *62*, 1–7.

169. Berro, H.; Fillot, N.; Vergne, P. Molecular dynamics simulation of surface energy and ZDDP effects on friction in nano-scale lubricated contacts. *Tribol. Int.* **2010**, *43*, 1811–1822.

170. Ramachandran, S.; Tsai, B. L.; Blanco, M.; Chen, H.; Tang, Y. C.; Goddard, W. A. Self-assembled monolayer mechanism for corrosion inhibition of iron by imidazolines. *Langmuir* **1996**, *12*, 6419–6428.

171. Beltzer, M.; Jahanmir, S. Role of dispersion interactions between hydrocarbon chains in boundary lubrication. *ASLE Trans.* **1987**, *30*, 47–54.

172. Stachowiak, G.; Batchelor, A. *Engineering Tribology*; 3rd ed.; Elsevier Inc., 2005.

173. Lundgren, S. M.; Ruths, M.; Danerlov, K.; Persson, K. Effects of unsaturation on film structure and friction of fatty acids in a model base oil. *J. Colloid Interface Sci.* **2008**, *326*, 530–536.

174. Campen, S.; Green, J. H.; Lamb, G. D.; Spikes, H. A. In Situ Study of Model Organic Friction Modifiers Using Liquid Cell AFM; Saturated and Mono-unsaturated Carboxylic Acids. *Tribol. Lett.* **2015**,

57, 1–20.

175. Wood, M. H.; Casford, M. T.; Steitz, R.; Zarbakhsh, A.; Welbourn, R. J. L.; Clarke, S. M. Comparative Adsorption of Saturated and Unsaturated Fatty Acids at the Iron Oxide/Oil Interface. *Langmuir* **2016**, *32*, 534–540.

176. Briscoe, B. J.; Evans, D. C. B. The shear properties of Langmuir-Blodgett layers. *Proc. R. Soc. A* **1982**, *380*, 389.

177. Moller, M. A.; Tildesley, D. J.; Kim, K. S.; Quirke, N. Molecular Dynamics Simulation of a Langmuir-Blodgett Film. *J. Chem. Phys.* **1991**, *94*, 8390–8401.

178. Daillant, J.; Bosio, L.; Benattar, J. J.; Study, R.; Helm, C. A.; Abed, A. El; Ionov, R.; Schmitz, P.; Gruler, H. Effect of Chain Conformation on the Tilt Behaviour in Langmuir Monolayers. *Eur. Lett.* **1994**, *27*, 467.

179. Glosli, J. N.; McClelland, G. M. Molecular dynamics study of sliding friction of ordered organic monolayers. *Phys. Rev. Lett.* **1993**, *70*, 1960–1963.

180. Kong, Y. C.; Tildesley, D. J.; Alejandre, J. The molecular dynamics simulation of boundary-layer lubrication. *Mol. Phys.* **1997**, *92*, 7–18.

181. Kong, Y. C.; Tildesley, D. J. The effect of molecular geometry on boundary layer lubrication. *Mol. Simul.* **1999**, *22*, 149–168.

182. Greenfield, M. L.; Ohtani, H. Molecular dynamics simulation study of model friction modifier additives confined between two surfaces. *Tribol. Lett.* **1999**, *7*, 137–145.

183. Ruths, M.; Ohtani, H.; Greenfield, M.; Granick, S. Exploring the “friction modifier” phenomenon: nanorheology of n-alkane chains with polar terminus dissolved in n-alkane solvent. *Tribol. Lett.* **1999**, *6*, 207–214.

184. Greenfield, M. L.; Ohtani, H. Packing of simulated friction modifier additives under confinement. *Langmuir* **2005**, *21*, 7568–7578.

185. Eder, S. J.; Vernes, A.; Betz, G. On the Derjaguin Offset in Boundary-Lubricated Nanotribological Systems. *Langmuir* **2013**, *29*, 13760–13772.

186. Eder, S.; Vernes, A.; Vorlaufer, G.; Betz, G. Molecular dynamics simulations of mixed lubrication with smooth particle post-processing. *J. Physics-Condensed Matter* **2011**, *23*, 12.

187. Doig, M.; Warrens, C. P.; Camp, P. J. Structure and Friction of Stearic Acid and Oleic Acid Films Adsorbed on Iron Oxide Surfaces in Squalane. *Langmuir* **2014**, *30*, 186–195.

188. Campen, S.; Green, J.; Lamb, G.; Atkinson, D.; Spikes, H. On the Increase in Boundary Friction with Sliding Speed. *Tribol. Lett.* **2012**, *48*, 237–248.

189. Doig, M.; Camp, P. J. The structures of hexadecylamine films adsorbed on iron-oxide surfaces in dodecane and hexadecane. *Phys. Chem. Chem. Phys.* **2015**, *17*, 5248–5255.

190. Wood, M. H.; Welbourn, R. J. L.; Charlton, T.; Zarbakhsh, A.; Casford, M. T.; Clarke, S. M. Hexadecylamine Adsorption at the Iron Oxide-Oil Interface. *Langmuir* **2013**, *29*, 13735–13742.

191. Bradley-Shaw, J. L.; Camp, P. J.; Dowding, P. J.; Lewtas, K. Molecular Dynamics Simulations of Glycerol Monooleate Confined between Mica Surfaces. *Langmuir* **2016**, *32*, 7707–7718.

192. Bradley-Shaw, J. L.; Camp, P. J.; Dowding, P. J.; Lewtas, K. Glycerol Monooleate Reverse Micelles in Nonpolar Solvents: Computer Simulations and Small-Angle Neutron Scattering. *J. Phys. Chem. B* **2015**, *119*, 4321–4331.

193. Koike, A.; Yoneya, M. Molecular dynamics simulations of sliding friction of Langmuir-Blodgett monolayers. *J. Chem. Phys.* **1996**, *105*, 6060–6067.

194. Koike, A.; Yoneya, M. Effects of molecular structure on frictional properties of Langmuir-Blodgett monolayers. *Langmuir* **1997**, *13*, 1718–1722.

195. Lewis, J. B.; Vilt, S. G.; Rivera, J. L.; Jennings, G. K.; McCabe, C. Frictional Properties of Mixed Fluorocarbon/Hydrocarbon Silane Monolayers: A Simulation Study. *Langmuir* **2012**, *28*, 14218–14226.

196. Lorenz, C. D.; Chandross, M.; Grest, G. S.; Stevens, M. J.; Webb, E. B. Tribological properties of alkylsilane self-assembled monolayers. *Langmuir* **2005**, *21*, 11744–11748.

197. Toton, D.; Lorenz, C. D.; Rompotis, N.; Lorenz, C. D.; Chandross, M.; Lane, J. M. D. Nanotribology of water confined between hydrophilic alkylsilane self-assembled monolayers. *Model. Simul. Mater. Sci. Eng.* **2010**, *18*, 34005.

198. Black, J. E.; Iacovella, C. R.; Cummings, P. T.; McCabe, C. Molecular Dynamics Study of Alkylsilane Monolayers on Realistic Amorphous Silica Surfaces. *Langmuir* **2015**, *31*, 3086–3093.

199. Summers, A. Z.; Iacovella, C. R.; Billingsley, M. R.; Arnold, S. T.; Cummings, P. T.; McCabe, C. Influence of Surface Morphology on the Shear-Induced Wear of Alkylsilane Monolayers: Molecular Dynamics Study. *Langmuir* **2016**, *32*, 2348–2359.

200. Tupper, K. J.; Brenner, D. W. Molecular dynamics simulations of friction in self-assembled monolayers. *Thin Solid Films* **1994**, *253*, 185–189.

201. Ramin, L.; Jabbarzadeh, A. Frictional properties of two alkanethiol self assembled monolayers in sliding contact: Odd-even effects. *J. Chem. Phys.* **2012**, *137*.

202. Ramin, L.; Jabbarzadeh, A. Effect of Water on Structural and Frictional Properties of Self Assembled Monolayers. *Langmuir* **2013**, *29*, 13367–13378.

203. Ewen, J. P.; Gattinoni, C.; Thakkar, F. M.; Morgan, N.; Spikes, H. A.; Dini, D. Nonequilibrium Molecular Dynamics Investigation of the Reduction in Friction and Wear by Carbon Nanoparticles Between Iron Surfaces. *Tribol. Lett.* **2016**, *63*, 38.

204. Liang, Q.; Tsui, O. K. C.; Xu, Y. B.; Li, H. N.; Xiao, X. D. Effect of C-60 molecular rotation on nanotribology. *Phys. Rev. Lett.* **2003**, *90*, 4.

205. Coffey, T.; Krim, J. C-60 molecular bearings and the phenomenon of nanomapping. *Phys. Rev. Lett.* **2006**, *96*, 4.

206. Lee, K.; Hwang, Y.; Cheong, S.; Choi, Y.; Kwon, L.; Lee, J.; Kim, S. H. Understanding the Role of Nanoparticles in Nano-oil Lubrication. *Tribol. Lett.* **2009**, *35*, 127–131.

207. Zhmud, B.; Pasalskiy, B. Nanomaterials in Lubricants: An Industrial Perspective on Current Research. *Lubricants* **2013**, *1*, 95–101.

208. Tevet, O.; Von-Huth, P.; Popovitz-Biro, R.; Rosentsveig, R.; Wagner, H. D.; Tenne, R. Friction mechanism of individual multilayered nanoparticles. *Proc. Natl. Acad. Sci.* **2011**, *108*, 19901–19906.

209. Lahouij, I.; Bucholz, E. W.; Vacher, B.; Sinnott, S. B.; Martin, J. M.; Dassenoy, F. Lubrication mechanisms of hollow-core inorganic fullerene-like nanoparticles: coupling experimental and computational works. *Nanotechnology* **2012**, *23*, 10.

210. Joly-Pottuz, L.; Bucholz, E. W.; Matsumoto, N.; Phillpot, S. R.; Sinnott, S. B.; Ohmae, N.; Martin, J. M. Friction Properties of Carbon Nano-Onions from Experiment and Computer Simulations. *Tribol. Lett.* **2010**, *37*, 75–81.

211. Bucholz, E. W.; Phillpot, S. R.; Sinnott, S. B. Molecular dynamics investigation of the lubrication mechanism of carbon nano-onions. *Comput. Mater. Sci.* **2012**, *54*, 91–96.

212. Bucholz, E. W.; Sinnott, S. B. Computational investigation of the mechanical and tribological responses of amorphous carbon nanoparticles. *J. Appl. Phys.* **2013**, *113*, 7.

213. Hu, C. Z.; Bai, M. L.; Lv, J. Z.; Liu, H.; Li, X. J. Molecular dynamics investigation of the effect of copper nanoparticle on the solid contact between friction surfaces. *Appl. Surf. Sci.* **2014**, *321*, 302–309.

214. Hu, C. Z.; Bai, M. L.; Lv, J. Z.; Kou, Z. H.; Li, X. J. Molecular dynamics simulation on the tribology properties of two hard nanoparticles (diamond and silicon dioxide) confined by two iron blocks. *Tribol. Int.* **2015**, *90*, 297–305.

215. Eder, S. J.; Feldbauer, G.; Bianchi, D.; Cihak-Bayr, U.; Betz, G.; Vernes, A. Applicability of Macroscopic Wear and Friction Laws on the Atomic Length Scale. *Phys. Rev. Lett.* **2015**, *115*.

216. Barwell, F. T. Wear of Materials. *Wear* **1958**, *1*, 317–332.

217. Bowden, F. P.; Tabor, D. *The Friction and Lubrication of Solids*; Oxford University Press, 1950.

218. Greenwood, J. A.; Williamson, B. P. Contact of Nominally Flat Surfaces. *Proc. R. Soc. A* **1966**, *295*, 300.

219. Maginn, E. J.; Elliott, J. R. Historical Perspective and Current Outlook for Molecular Dynamics As a Chemical Engineering Tool. *Ind. Eng. Chem. Res.* **2010**, *49*, 3059–3078.

220. Ewen, J. P.; Gattinoni, C.; Thakkar, F. M.; Morgan, N.; Spikes, H.; Dini, D. A Comparison of Classical Force-Fields for Molecular Dynamics Simulations of Lubricants. *Materials.* **2016**, *9*, 651.

221. Martin, M. G. Comparison of the AMBER, CHARMM, COMPASS, GROMOS, OPLS, TraPPE and UFF force fields for prediction of vapor-liquid coexistence curves and liquid densities. *Fluid Phase Equilib.* **2006**, *248*, 50–55.

222. Lorentz, H. A. Ueber die Anwendung des Satzes vom Virial in der kinetischen Theorie der Gase. *Ann. Phys. 248*, 127–136.

223. Berthelot, D. Sur le mélange des gaz. *Comptes rendus Hebd. des séances l'Académie des Sci. 126*, 1703–1855.

224. Al-Matar, A. K.; Rockstraw, D. A. Assessment of the Effect of Mixing Rules on Predicting the Second Virial Coefficient and a Further Evidence of the Inadequacy of the Lorentz-Berthelot Rules . *Dirasat Eng. Sci. 33*, 27–36.

225. Tobias, D. J.; Tu, K.; Klein, M. L. Assessment of all-atom potentials for modeling membranes: molecular dynamics simulations of solid and liquid alkanes and crystals of phospholipid fragments. *J. Chim. Phys. Phys.-Chim. Biol.* **1997**, *94*, 1482–1502.

226. Mie, G. Zur kinetischen Theorie der einatomigen Körper. *Ann. Phys. 316*, 657–697.

227. Potoff, J. J.; Kamath, G. Mie Potentials for Phase Equilibria: Application to Alkenes. *J. Chem. Eng. Data* **2014**, *59*, 3144–3150.

228. Ewald, P. Die Berechnung optischer und elektrostatischer Gitterpotentiale. *Ann. Phys. 369*, 253–287.

229. Hockney, R. W.; Eastmond, J. W. *Computer Simulation Using Particles*; CRC Press: NY, 1989.

230. Jorgensen, W. L.; Tirado-Rives, J. Potential energy functions for atomic-level simulations of water

and organic and biomolecular systems. *Proc. Natl. Acad. Sci. U. S. A.* **2005**, *102*, 6665–6670.

231. Xie, W. S.; Pu, J. Z.; MacKerell, A. D.; Gao, J. L. Development of a polarizable intermolecular potential function (PIPF) for liquid amides and alkanes. *J. Chem. Theory Comput.* **2007**, *3*, 1878–1889.

232. Cornell, W. D.; Cieplak, P.; Bayly, C. I.; Gould, I. R.; Merz, K. M.; Ferguson, D. M.; Spellmeyer, D. C.; Fox, T.; Caldwell, J. W.; Kollman, P. A. A second generation force-field for the simulation of proteins, nucleic-acids, and organic-molecules. *J. Am. Chem. Soc.* **1995**, *117*, 5179–5197.

233. Wang, J. M.; Wang, W.; Kollman, P. A.; Case, D. A. Automatic atom type and bond type perception in molecular mechanical calculations. *J. Mol. Graph. Model.* **2006**, *25*, 247–260.

234. Jorgensen, W. L.; Maxwell, D. S.; Tirado-Rives, J. Development and testing of the OPLS all-atom force field on conformational energetics and properties of organic liquids. *J. Am. Chem. Soc.* **1996**, *118*, 11225–11236.

235. MacKerell, A. D.; Bashford, D.; Bellott, M.; Dunbrack, R. L.; Evanseck, J. D.; Field, M. J.; Fischer, S.; Gao, J.; Guo, H.; Ha, S.; Joseph-McCarthy, D.; Kuchnir, L.; Kuczera, K.; Lau, F. T. K.; Mattos, C.; Michnick, S.; Ngo, T.; Nguyen, D. T.; Prodhom, B.; Reiher, W. E.; Roux, B.; Schlenkrich, M.; Smith, J. C.; Stote, R.; Straub, J.; Watanabe, M.; Wiorkiewicz-Kuczera, J.; Yin, D.; Karplus, M. All-atom empirical potential for molecular modeling and dynamics studies of proteins. *J. Phys. Chem. B* **1998**, *102*, 3586–3616.

236. van der Spoel, D.; Lindahl, E.; Hess, B.; van Buuren, A. R.; Apol, E.; Meulenhoff, P. J.; Tieleman, D. P.; Sijbers, A. L. T. M.; Feenstra, K. A.; van Drunen, R.; Berendsen, H. J. C. Gromacs User Manual version 4.5.6 2010.

237. Martin, M. G.; Siepmann, J. I. Transferable potentials for phase equilibria. 1. United-atom description of n-alkanes. *J. Phys. Chem. B* **1998**, *102*, 2569–2577.

238. Eggimann, B. L.; Sunnarborg, A. J.; Stern, H. D.; Bliss, A. P.; Siepmann, J. I. An online parameter and property database for the TraPPE force field. *Mol. Simul.* **2014**, *40*, 101–105.

239. Stubbs, J. M.; Potoff, J. J.; Siepmann, J. I. Transferable potentials for phase equilibria. 6. United-atom description for ethers, glycols, ketones, and aldehydes. *J. Phys. Chem. B* **2004**, *108*, 17596–17605.

240. Pettitt, B. M.; Karplus, M. Role of electrostatics in the structure, energy, and dynamics of biomolecules: A model study of methylalanylacetamide. *J. Am. Chem. Soc.* **1985**, *107*, 1166–1173.

241. Price, D. J.; Brooks, C. L. Modern protein force fields behave comparably in molecular dynamics simulations. *J. Comput. Chem.* **2002**, *23*, 1045–1057.

242. Ryckaert, J. P.; Bellemans, A. Molecular-dynamics of liquid normal-butane near its boiling point. *Chem. Phys. Lett.* **1975**, *30*, 123–125.

243. Jorgensen, W. L.; Tiradorives, J. The OPLS potential functions for proteins: Crystals of cyclic-peptides and Crambin. *J. Am. Chem. Soc.* **1988**, *110*, 1657–1666.

244. Maerzke, K. A.; Siepmann, J. I. Transferable Potentials for Phase Equilibria-Coarse-Grain Description for Linear Alkanes. *J. Phys. Chem. B* **2011**, *115*, 3452–3465.

245. Braga, C.; Travis, K. P. Computer simulation of the role of torsional flexibility on mass and momentum transport for a series of linear alkanes. *J. Chem. Phys.* **2012**, *137*, 11.

246. Allen, W.; Rowley, R. L. Predicting the viscosity of alkanes using nonequilibrium molecular dynamics: Evaluation of intermolecular potential models. *J. Chem. Phys.* **1997**, *106*, 10273–10281.

247. Dysthe, D. K.; Fuchs, A. H.; Rousseau, B. Fluid transport properties by equilibrium molecular

dynamics. III. Evaluation of united atom interaction potential models for pure alkanes. *J. Chem. Phys.* **2000**, *112*, 7581–7590.

248. Payal, R. S.; Balasubramanian, S.; Rudra, I.; Tandon, K.; Mahlke, I.; Doyle, D.; Cracknell, R. Shear viscosity of linear alkanes through molecular simulations: quantitative tests for n-decane and n-hexadecane. *Mol. Simulat.* **2012**, *38*, 1234–1241.

249. Murzyn, K.; Bratek, M.; Pasenkiewicz-Gierula, M. Refined OPLS All-Atom Force Field Parameters for n-Pentadecane, Methyl Acetate, and Dimethyl Phosphate. *J. Phys. Chem. B* **2013**, *117*, 16388–16396.

250. Gordon, P. A. Development of intermolecular potentials for predicting transport properties of hydrocarbons. *J. Chem. Phys.* **2006**, *125*, 9.

251. Bareman, J. P.; Klein, M. L. Collective tilt behavior in dense, substrate-supported monolayers of long-chain molecules - a molecular dynamics study. *J. Phys. Chem.* **1990**, *94*, 5202–5205.

252. Mar, W.; Klein, M. L. Molecular-dynamics study of the self-assembled monolayer composed of S(CH2)(14)CH3 molecules using an all-atoms model. *Langmuir* **1994**, *10*, 188–196.

253. Bolton, K.; Bosio, S. B. M.; Hase, W. L.; Schneider, W. F.; Hass, K. C. Comparison of explicit and united atom models for alkane chains physisorbed on alpha-Al2O3 (0001). *J. Phys. Chem. B* **1999**, *103*, 3885–3895.

254. Kong, L. T.; Denniston, C.; Muser, M. H. The crucial role of chemical detail for slip-boundary conditions: molecular dynamics simulations of linear oligomers between sliding aluminum surfaces. *Model. Simul. Mater. Sci. Eng.* **2010**, *18*, 17.

255. Plimpton, S. Fast parallel algorithms for short-range molecular-dynamics. *J. Comput. Phys.* **1995**, *117*, 1–19.

256. Ryckaert, J. P.; Ciccotti, G.; Berendsen, H. J. C. Numerical-integration of Cartesian equations of motion of a system with constraints: molecular-dynamics of n-alkanes. *J. Comput. Phys.* **1977**, *23*, 327–341.

257. Cui, S. T.; Cummings, P. T.; Cochran, H. D. The calculation of viscosity of liquid n-decane and n-hexadecane by the Green-Kubo method. *Mol. Phys.* **1998**, *93*, 117–121.

258. Chynoweth, S.; Michopoulos, Y. An improved potential model for n-hexadecane molecular-dynamics simulations under extreme conditions. *Mol. Phys.* **1994**, *81*, 133–141.

259. Nath, S. K.; Escobedo, F. A.; de Pablo, J. J. On the simulation of vapor-liquid equilibria for alkanes. *J. Chem. Phys.* **1998**, *108*, 9905–9911.

260. Schuler, L. D.; Daura, X.; Van Gunsteren, W. F. An improved GROMOS96 force field for aliphatic hydrocarbons in the condensed phase. *J. Comput. Chem.* **2001**, *22*, 1205–1218.

261. Mayo, S. L.; Olafson, B. D.; Goddard, W. A. Dreiding: A generic force-field for molecular simulations. *J. Phys. Chem.* **1990**, *94*, 8897–8909.

262. Sun, H. COMPASS: An ab initio force-field optimized for condensed-phase applications - Overview with details on alkane and benzene compounds. *J. Phys. Chem. B* **1998**, *102*, 7338–7364.

263. Hoover, W. G. Constant-pressure equations of motion. *Phys. Rev. A* **1986**, *34*, 2499–2500.

264. Humphrey, W.; Dalke, A.; Schulten, K. VMD: Visual molecular dynamics. *J. Mol. Graph. Model.* **1996**, *14*, 33–38.

265. Cui, S. T.; Gupta, S. A.; Cummings, P. T.; Cochran, H. D. Molecular dynamics simulations of the

rheology of normal decane, hexadecane, and tetracosane. *J. Chem. Phys.* **1996**, *105*, 1214–1220.

266. Savio, D.; Fillot, N.; Vergne, P. A Molecular Dynamics Study of the Transition from Ultra-Thin Film Lubrication Toward Local Film Breakdown. *Tribol. Lett.* **2013**, *50*, 207–220.

267. Ewen, J. P.; Gattinoni, C.; Morgan, N.; Spikes, H.; Dini, D. Nonequilibrium Molecular Dynamics Simulations of Organic Friction Modifiers Adsorbed on Iron Oxide Surfaces. *Langmuir* **2016**, *32*, 4450–4463.

268. Casford, M. T. L.; Davies, P. B. The Structure of Oleamide Films at the Aluminum/Oil Interface and Aluminum/Air Interface Studied by Sum Frequency Generation (SFG) Vibrational Spectroscopy and Reflection Absorption Infrared Spectroscopy (RAIRS). *ACS Appl. Mater. Interfaces* **2009**, *1*, 1672–1681.

269. Campen, S.; Green, J. H.; Lamb, G. D.; Spikes, H. A. In Situ Study of Model Organic Friction Modifiers Using Liquid Cell AFM: Self-Assembly of Octadecylamine. *Tribol. Lett.* **2015**, *58*, 39.

270. Maslen, E. N.; Streltsov, V. A.; Streltsova, N. R.; Ishizawa, N. Synchrotron X-ray study of the electron-density in alpha-Fe2O3. *Acta Crystallogr., Sect. B Struct. Sci.* **1994**, *50*, 435–441.

271. Kawaguchi, M.; Yamamoto, M.; Nakamura, T.; Yamashita, M.; Kato, T. Surface properties of mono-, di-, and triglycerol monostearate monolayers spread at the air-water interface. *Langmuir* **2001**, *17*, 4677–4680.

272. Kaminski, G. A.; Friesner, R. A.; Tirado-Rives, J.; Jorgensen, W. L. Evaluation and reparametrization of the OPLS-AA force field for proteins via comparison with accurate quantum chemical calculations on peptides. *J. Phys. Chem. B* **2001**, *105*, 6474–6487.

273. Yeh, I. C.; Berkowitz, M. L. Ewald summation for systems with slab geometry. *J. Chem. Phys.* **1999**, *111*, 3155–3162.

274. Sivebaek, I. M.; Samoilov, V. N.; Persson, B. N. J. Squeezing molecular thin alkane lubrication films between curved solid surfaces with long-range elasticity: Layering transitions and wear. *J. Chem. Phys.* **2003**, *119*, 2314–2321.

275. Persson, B. N. J.; Mugele, F. Squeeze-out and wear: fundamental principles and applications. *J. Phys. Condens. Matter* **2004**, *16*, R295–R355.

276. Gosvami, N. N.; Sinha, S. K.; Hofbauer, W.; O'Shea, S. J. Solvation and squeeze out of hexadecane on graphite. *J. Chem. Phys.* **2007**, *126*, 5.

277. Salacuse, J. J.; Denton, A. R.; Egelstaff, P. A. Finite-size effects in molecular dynamics simulations: Static structure factor and compressibility .1. Theoretical method. *Phys. Rev. E* **1996**, *53*, 2382–2389.

278. Toton, D.; Lorenz, C. D.; Rompotis, N.; Martsinovich, N.; Kantorovich, L. Temperature control in molecular dynamic simulations of non-equilibrium processes. *J. Phys. Condens. Matter* **2010**, *22*, 74205.

279. He, G.; Robbins, M. O. Simulations of the kinetic friction due to adsorbed surface layers. *Tribol. Lett.* **2001**, *10*, 7–14.

280. McDonald, I. K.; Thornton, J. M. Satisfying hydrogen-bonding potential in proteins. *J. Mol. Biol.* **1994**, *238*, 777–793.

281. Mikulski, P. T.; Gao, G.; Chateauneuf, G. M.; Harrison, J. A. Contact forces at the sliding interface: Mixed versus pure model alkane monolayers. *J. Chem. Phys.* **2005**, *122*, 9.

282. Chandross, M.; Webb, E. B.; Stevens, M. J.; Grest, G. S.; Garofalini, S. H. Systematic study of the effect of disorder on nanotribology of self-assembled monolayers. *Phys. Rev. Lett.* **2004**, *93*, 4.

283. Ruths, M.; Lundgren, S.; Danerlov, K.; Persson, K. Friction of fatty acids in nanometer-sized contacts of different adhesive strength. *Langmuir* **2008**, *24*, 1509–1516.

284. Lee, D. H.; Oh, T.; Cho, K. Combined effect of chain length and phase state on adhesion/friction behavior of self-assembled monolayers. *J. Phys. Chem. B* **2005**, *109*, 11301–11306.

285. Tang, Z. L.; Li, S. H. A review of recent developments of friction modifiers for liquid lubricants (2007-present). *Curr. Opin. Solid State Mater. Sci.* **2014**, *18*, 119–139.

286. Ingram, M.; Noles, J.; Watts, R.; Harris, S.; Spikes, H. A. Frictional Properties of Automatic Transmission Fluids: Part I-Measurement of Friction-Sliding Speed Behavior. *Tribol. Trans.* **2011**, *54*, 145–153.

287. Mazuyer, D.; Cayer-Barrioz, J.; Tonck, A.; Jarnias, F. Friction dynamics of confined weakly adhering boundary layers. *Langmuir* **2008**, *24*, 3857–3866.

288. Yoshizawa, H.; Chen, Y. L.; Israelachvili, J. Fundamental mechanisms of interfacial friction. 1. relation between adhesion and friction. *J. Phys. Chem.* **1993**, *97*, 4128–4140.

289. Jahanmir, S.; Beltzer, M. An adsorption model for friction in boundary lubrication. *ASLE Trans.* **1986**, *29*, 423–430.

290. Simic, R.; Kalin, M. Comparison of Alcohol and Fatty Acid Adsorption on Hydrogenated DLC Coatings Studied by AFM and Tribological Tests. *Stroj. Vestn.-J. Mech. E.* **2013**, *59*, 707–718.

291. Lundgren, S. M.; Persson, K.; Mueller, G.; Kronberg, B.; Clarke, J.; Chtaib, M.; Claesson, P. M. Unsaturated fatty acids in alkane solution: adsorption to steel surfaces. *Langmuir* **2007**, *23*, 10598–10602.

292. Loehle, S.; Matta, C.; Minfray, C.; Le Mogne, T.; Martin, J. M.; Iovine, R.; Obara, Y.; Miura, R.; Miyamoto, A. Mixed Lubrication with C18 Fatty Acids: Effect of Unsaturation. *Tribol. Lett.* **2014**, *53*, 319–328.

293. Loehle, S.; Matta, C.; Minfray, C.; Le Mogne, T.; Iovine, R.; Obara, Y.; Miyamoto, A.; Martin, J. M. Mixed lubrication of steel by C18 fatty acids revisited. Part II: Influence of some key parameters. *Tribol. Int.* **2016**, *94*, 207–216.

294. Kamath, G.; Cao, F.; Potoff, J. J. An improved force field for the prediction of the vapor-liquid equilibria for carboxylic acids. *J. Phys. Chem. B* **2004**, *108*, 14130–14136.

295. Ewen, J. P.; Echeverri Restrepo, S.; Morgan, N.; Dini, D. Nonequilibrium molecular dynamics simulations of stearic acid adsorbed on iron surfaces with nanoscale roughness. *Tribol. Int.* **2017**, *107*, 264–273.

296. Loehle, S.; Matta, C.; Minfray, C.; Le Mogne, T.; Iovine, R.; Obara, Y.; Miyamoto, A.; Martin, J. M. Mixed lubrication of steel by C18 fatty acids revisited. Part I: Toward the formation of carboxylate. *Tribol. Int.* **2015**, *82*, 218–227.

297. Vernes, A.; Eder, S.; Vorlaufer, G.; Betz, G. On the three-term kinetic friction law in nanotribological systems. *Faraday Discuss.* **2012**, *156*, 173–196.

298. Jacobs, T. D. B.; Ryan, K. E.; Keating, P. L.; Grierson, D. S.; Lefever, J. A.; Turner, K. T.; Harrison, J. A.; Carpick, R. W. The Effect of Atomic-Scale Roughness on the Adhesion of Nanoscale Asperities: A Combined Simulation and Experimental Investigation. *Tribol. Lett.* **2013**, *50*, 81–93.

299. Spijker, P.; Anciaux, G.; Molinari, J. F. Dry sliding contact between rough surfaces at the atomistic scale. *Tribol. Lett.* **2011**, *44*, 279–285.

300. Spijker, P.; Anciaux, G.; Molinari, J. F. The effect of loading on surface roughness at the atomistic level. *Comput. Mech.* **2012**, *50*, 273–283.

301. Spijker, P.; Anciaux, G.; Molinari, J. F. Relations between roughness, temperature and dry sliding friction at the atomic scale. *Tribol. Int.* **2013**, *59*, 222–229.

302. Zheng, X.; Zhu, H. T.; Tieu, A. K.; Kosasih, B. A molecular dynamics simulation of 3D rough lubricated contact. *Tribol. Int.* **2013**, *67*, 217–221.

303. Zheng, X.; Zhu, H. T.; Tieu, A. K.; Kosasih, B. Roughness and Lubricant Effect on 3D Atomic Asperity Contact. *Tribol. Lett.* **2014**, *53*, 215–223.

304. Zhu, H. T.; Zheng, X.; Kosasih, P. B.; Tieu, A. K. Tribo-surface charge and polar lubricant molecules on friction and lubrication under multiple 3D asperity contacts. *Wear* **2015**, *332*, 1248–1255.

305. Sivebaek, I. M.; Persson, B. N. J. The effect of surface nano-corrugation on the squeeze-out of molecular thin hydrocarbon films between curved surfaces with long range elasticity. *Nanotechnology* **2016**, *27*, 445401–445409.

306. Yamada, S.; Inomata, K. A.; Kobayashi, E.; Tanabe, T.; Kurihara, K. Effect of a Fatty Acid Additive on the Kinetic Friction and Stiction of Confined Liquid Lubricants. *Tribol. Lett.* **2016**, *64*, 23.

307. Nalam, P. C.; Clasohm, J. N.; Mashaghi, A.; Spencer, N. D. Macrotribological studies of poly(L-lysine)-graft-Poly(ethylene glycol) in aqueous glycerol mixtures. *Tribol. Lett.* **2010**, *37*, 541–552.

308. Graham, J.; Spikes, H.; Jensen, R. The Friction Reducing Properties of Molybdenum Dialkyldithiocarbamate Additives: Part I - Factors Influencing Friction Reduction. *Tribol. Trans.* **2001**, *44*, 626–636.

309. Chai, L.; Klein, J. Large area, molecularly smooth (0.2 nm rms) gold films for surface forces and other studies. *Langmuir* **2007**, *23*, 7777–7783.

310. Campen, S. Fundamentals of Organic Friction Modifier Behaviour, [PhD Thesis], 2012.

311. Mulakaluri, N.; Persson, B. N. J. Adhesion between elastic solids with randomly rough surfaces: Comparison of analytical theory with molecular-dynamics simulations. *Europhys. Lett.* **2011**, *96*, 66003.

312. Eder, S. J.; Bianchi, D.; Cihak-Bayr, U.; Vernes, A.; Betz, G. An analysis method for atomistic abrasion simulations featuring rough surfaces and multiple abrasive particles. *Comput. Phys. Commun.* **2014**, *185*, 2456–2466.

313. Mendelev, M. I.; Han, S.; Srolovitz, D. J.; Ackland, G. J.; Sun, D. Y.; Asta, M. Development of new interatomic potentials appropriate for crystalline and liquid iron. *Philos. Mag.* **2003**, *83*, 3977–3994.

314. Miura, K.; Kamiya, S.; Sasaki, N. C-60 molecular bearings. *Phys. Rev. Lett.* **2003**, *90*, 4.

315. Gupta, B. K.; Bhushan, B. Fullerene particles as an additive to liquid lubricants and greases for low-friction and wear. *Lubr. Eng.* **1994**, *50*, 524–528.

316. Ginzburg, B. M.; Kireenko, O. F.; Shepelevskii, A. A.; Shibaev, L. A.; Tochilnikov, D. G.; Leksovskii, A. M. Thermal and tribological properties of fullerene-containing composite systems. Part 2. Formation of tribo-polymer films during boundary sliding friction in the presence of fullerene C-60. *J. Macromol. Sci.* **2005**, *B44*, 93–115.

317. Ku, B. C.; Han, Y. C.; Lee, J. E.; Lee, J. K.; Park, S. H.; Hwang, Y. J. Tribological Effects of Fullerene (C-60) Nanoparticles Added in Mineral Lubricants According to its Viscosity. *Int. J. Precis. Eng. Manuf.* **2010**, *11*, 607–611.

318. Chou, C. C.; Lee, S. H. Tribological behavior of nanodiamond-dispersed lubricants on carbon steels and aluminum alloy. *Wear* **2010**, *269*, 757–762.

319. Ugarte, D. Curling and closure of graphitic networks under electron-beam irradtiation. *Nature* **1992**, *359*, 707–709.

320. Hawelek, L.; Brodka, A.; Tomita, S.; Dore, J. C.; Honkimaki, V.; Burian, A. Transformation of nano-diamonds to carbon nano-onions studied by X-ray diffraction and molecular dynamics. *Diam. Relat. Mater.* **2011**, *20*, 1333–1339.

321. Xu, T.; Zhao, J. Z.; Xu, K. The ball-bearing effect of diamond nanoparticles as an oil additive. *J. Phys. D-Applied Phys.* **1996**, *29*, 2932–2937.

322. Peng, D. X.; Kang, Y.; Hwang, R. M.; Shyr, S. S.; Chang, Y. P. Tribological properties of diamond and SiO(2) nanoparticles added in paraffin. *Tribol. Int.* **2009**, *42*, 911–917.

323. Ivanov, M. G.; Pavlyshko, S. V; Ivanov, D. M.; Petrov, I.; Shenderova, O. Synergistic Compositions of Colloidal Nanodiamond as Lubricant-additive. *J. Vac. Sci. Technol. B* **2010**, *28*, 869–877.

324. Hsin, Y. L.; Chu, H. Y.; Jeng, Y. R.; Huang, Y. H.; Wang, M. H.; Chang, C. K. In situ de-agglomeration and surface functionalization of detonation nanodiamond, with the polymer used as an additive in lubricant oil. *J. Mater. Chem.* **2011**, *21*, 13213–13222.

325. Mosleh, M.; Shirvani, K. A. In-situ nanopolishing by nanolubricants for enhanced elastohydrodynamic lubrication. *Wear* **2013**, *301*, 137–143.

326. Nunn, N.; Mahbooba, Z.; Ivanov, M. G.; Ivanov, D. M.; Brenner, D. W.; Shenderova, O. Tribological properties of polyalphaolefin oil modified with nanocarbon additives. *Diam. Relat. Mater.* **2015**, *54*, 97–102.

327. Matsumoto, N.; Joly-Pottuz, L.; Kinoshita, H.; Ohmae, N. Application of onion-like carbon to micro and nanotribology. *Diam. Relat. Mater.* **2007**, *16*, 1227–1230.

328. Joly-Pottuz, L.; Matsumoto, N.; Kinoshita, H.; Vacher, B.; Belin, M.; Montagnac, G.; Martin, J. M.; Ohmae, N. Diamond-derived carbon onions as lubricant additives. *Tribol. Int.* **2008**, *41*, 69–78.

329. Joly-Pottuz, L.; Vacher, B.; Ohmae, N.; Martin, J. M.; Epicier, T. Anti-wear and friction reducing mechanisms of carbon nano-onions as lubricant additives. *Tribol. Lett.* **2008**, *30*, 69–80.

330. Yao, Y. L.; Wang, X. M.; Guo, J. J.; Yang, X. W.; Xu, B. S. Tribological property of onion-like fullerenes as lubricant additive. *Mater. Lett.* **2008**, *62*, 2524–2527.

331. Hunter, C. N.; Check, M. H.; Hager, C. H.; Voevodin, A. A. Tribological properties of carbon nanopearls synthesized by nickel-catalyzed chemical vapor deposition. *Tribol. Lett.* **2008**, *30*, 169–176.

332. Matsumoto, N.; Mistry, K.; Kim, J.-H.; Eryilmaz, O.; Erdemir, A.; Kinoshita, H.; Ohmae, N. Friction reducing properties of onion-like carbon based lubricant under high contact pressure. *Tribol. - Mater. Surfaces Interfaces* **2012**, *6*, 116–120.

333. Jeng, Y. R.; Huang, Y. H.; Tsai, P. C.; Hwang, G. L. Tribological Properties of Carbon Nanocapsule Particles as Lubricant Additive. *J. Tribol. Asme* **2014**, *136*, 9.

334. Stuart, S. J.; Tutein, A. B.; Harrison, J. A. A reactive potential for hydrocarbons with intermolecular interactions. *J. Chem. Phys.* **2000**, *112*, 6472–6486.

335. O'Connor, T. C.; Andzelm, J.; Robbins, M. O. AIREBO-M: A reactive model for hydrocarbons at extreme pressures. *J. Chem. Phys.* **2015**, *142*, 9.

336. Brenner, D. W.; Shenderova, O. A.; Harrison, J. A.; Stuart, S. J.; Ni, B.; Sinnott, S. B. A second-

generation reactive empirical bond order (REBO) potential energy expression for hydrocarbons. *J. Physics-Condensed Matter* **2002**, *14*, 783–802.

337. Banerjee, S.; Naha, S.; Puri, I. K. Molecular simulation of the carbon nanotube growth mode during catalytic synthesis. *Appl. Phys. Lett.* **2008**, *92*, 3.

338. Gao, Y.; Ruestes, C. J.; Urbassek, H. M. Nanoindentation and nanoscratching of iron: Atomistic simulation of dislocation generation and reactions. *Comput. Mater. Sci.* **2014**, *90*, 232–240.

339. Gao, Y.; Brodyanski, A.; Kopnarski, M.; Urbassek, H. M. Nanoscratching of iron: A molecular dynamics study of the influence of surface orientation and scratching direction. *Comput. Mater. Sci.* **2015**, *103*, 77–89.

340. Abouei, V.; Saghafian, H.; Kheirandish, S. Effect of microstructure on the oxidative wear behavior of plain carbon steel. *Wear* **2007**, *262*, 1225–1231.

341. Lee, W. G.; Cho, K. H.; Jang, H. Molecular Dynamics Simulation of Rolling Friction Using Nanosize Spheres. *Tribol. Lett.* **2009**, *33*, 37–43.

342. Guo, J. J.; Liu, G. H.; Wang, X. M.; Fujita, T.; Xu, B. S.; Chen, M. W. High-pressure Raman spectroscopy of carbon onions and nanocapsules. *Appl. Phys. Lett.* **2009**, *95*, 3.

343. Zhang, W. W.; Yao, M. G.; Fan, X. H.; Zhao, S. J.; Chen, S. L.; Gong, C.; Yuan, Y.; Liu, R.; Liu, B. B. Pressure-induced transformations of onion-like carbon nanospheres up to 48 GPa. *J. Chem. Phys.* **2015**, *142*, 6.

344. Lu, C.; Gao, Y.; Michal, G.; Deng, G. Y.; Huynh, N. N.; Zhu, H. T.; Liu, X. H.; Tieu, A. K. Experiment and Molecular Dynamics Simulation of Nanoindentation of Body Centered Cubic Iron. *J. Nanosci. Nanotechnol.* **2009**, *9*, 7307–7313.

345. Bowden, F.; Tabor, D. Friction, lubrication and wear: a survey of work during the last decade. *Br. J. Appl. Phys.* **1966**, *17*, 1521–1544.

346. Zheng, B.; Huang, Z.; Xing, J.; Wang, Y.; Jian, Y.; Xiao, Y.; Fan, X. Three-Body Abrasive Behavior of Cementite–Iron Composite with Different Cementite Volume Fractions. *Tribol. Lett.* **2016**, *62*, 1–11.

347. Olomolehin, Y.; Kapadia, R.; Spikes, H. Antagonistic Interaction of Antiwear Additives and Carbon Black. *Tribol. Lett.* **2010**, *37*, 49–58.

348. Bhowmick, H.; Majumdar, S. K.; Biswas, S. K. Influence of physical structure and chemistry of diesel soot suspended in hexadecane on lubrication of steel-on-steel contact. *Wear* **2013**, *300*, 180–188.

349. Zhang, Z. C.; Cai, Z. B.; Peng, J. F.; Zhu, M. H. Comparison of the tribology performance of nano-diesel soot and graphite particles as lubricant additives. *J. Phys. D-Applied Phys.* **2016**, *49*, 45304.

350. Gupta, S. A.; Cochran, H. D.; Cummings, P. T. Shear behavior of squalane and tetracosane under extreme confinement .3. Effect of confinement on viscosity. *J. Chem. Phys.* **1997**, *107*, 10335–10343.

351. Jabbarzadeh, A.; Harrowell, P.; Tanner, R. I. Crystal bridges, tetratic order, and elusive equilibria: The role of structure in lubrication films. *J. Phys. Chem. B* **2007**, *111*, 11354–11365.

352. Ta, D. T.; Tieu, A. K.; Zhu, H. T.; Kosasih, B. Thin film lubrication of hexadecane confined by iron and iron oxide surfaces: A crucial role of surface structure. *J. Chem. Phys.* **2015**, *143*, 164702.

353. Cui, S. T.; Cummings, P. T.; Cochran, H. D. Molecular simulation of the transition from liquidlike to solidlike behavior in complex fluids confined to nanoscale gaps. *J. Chem. Phys.* **2001**, *114*, 7189–7195.

354. Butler, S.; Harrowell, P. Simulation of the coexistence of a shearing liquid and a strained crystal. *J. Chem. Phys.* **2003**, *118*, 4115–4126.

355. Butler, S.; Harrowell, P. Structure and stability of the interface between a strained crystal and a shearing liquid. *Phys. Rev. E* **2003**, *67*, 51503.

356. Zhang, J.; Spikes, H. On the Mechanism of ZDDP Antiwear Film Formation. *Tribol. Lett.* **2016**, *63*, 24.

357. Ovarlez, G.; Rodts, S.; Chateau, X.; Coussot, P. Phenomenology and physical origin of shear localization and shear banding in complex fluids. *Rheol. Acta* **2009**, *48*, 831–844.

358. Schall, P.; van Hecke, M. Shear Bands in Matter with Granularity. *Annu. Rev. Fluid Mech.* **2010**, *42*, 67–88.

359. Shi, Y.; Falk, M. L. Atomic-scale simulations of strain localization in three-dimensional model amorphous solids. *Phys. Rev. B* **2006**, *73*, 214201.

360. Varnik, F.; Bocquet, L.; Barrat, J.-L.; Berthier, L. Shear localization in a model glass. *Phys. Rev. Lett.* **2003**, *90*, 95702.

361. Yeo, K.; Maxey, M. R. Ordering transition of non-Brownian suspensions in confined steady shear flow. *Phys. Rev. E* **2010**, *81*, 51502.

362. Holmes, W. M.; Callaghan, P. T.; Vlassopoulos, D.; Roovers, J. Shear banding phenomena in ultrasoft colloidal glasses. *J. Rheol.* **2004**, *48*, 1085.

363. Cao, J.; Likhtman, A. E. Shear Banding in Molecular Dynamics of Polymer Melts. *Phys. Rev. Lett.* **2012**, *108*, 28302.

364. Mohagheghi, M.; Khomami, B. Molecular Processes Leading to Shear Banding in Well Entangled Polymeric Melts. *ACS Macro Lett.* **2015**, *4*, 684–688.

365. Yasuda, K.; Armstrong, R. C.; Cohen, R. E. Shear flow properties of concentrated solutions of linear and star branched polystyrenes. *Rheol. Acta* **1981**, *20*, 163–178.

366. He, Y.; Zolper, T. J.; Liu, P.; Zhao, Y.; He, X.; Shen, X.; Sun, H.; Duan, Q.; Wang, Q. Elastohydrodynamic lubrication properties and friction behaviors of several ester base stocks. *Friction* **2015**, *3*, 243–255.

367. Archard, J. F. The temperature of rubbing surfaces. *Wear* **1959**, *2*, 438–455.

368. Johnson, K. L.; Greenwood, J. A. Thermal analysis of an eyring fluid in elastohydrodynamic traction. *Wear* **1980**, *61*, 353–374.

369. Spikes, H.; Zhang, J. Reply to the Comment by Scott Bair, Philippe Vergne, Punit Kumar, Gerhard Poll, Ivan Krupka, Martin Hartl, Wassim Habchi, Roland Larson on “History, Origins and Prediction of Elastohydrodynamic Friction” by Spikes and Jie in Tribology Letters. *Tribol. Lett.* **2015**, *58*, 17.

370. Pluhackoya, K.; Morhenn, H.; Lautner, L.; Lohstroh, W.; Nemkovski, K. S.; Unruh, T.; Bockmann, R. A. Extension of the LOPLS-AA Force Field for Alcohols, Esters, and Monoolein Bilayers and its Validation by Neutron Scattering Experiments. *J. Phys. Chem. B* **2015**, *119*, 15287–15299.

371. Ta, T. D.; Tieu, A. K.; Zhu, H.; Kosasih, B.; Zhu, Q.; Phan, H. T. The structural, tribological, and rheological dependency of thin hexadecane film confined between iron and iron oxide surfaces under sliding conditions. *Tribol. Int.* **2017**, *113*, 22–35.

372. Ponjavic, A.; Dench, J.; Morgan, N.; Wong, J. S. S. In situ viscosity measurement of confined liquids. *RSC Adv.* **2015**, *5*, 99585–99593.

373. Dench, J.; Morgan, N.; Wong, J. S. S. Quantitative Viscosity Mapping Using Fluorescence Lifetime Measurements. *Tribol. Lett.* **2017**, *65*, 25.

374. Evans, C. R.; Johnson, K. L. The rheological properties of elastohydrodynamic lubricants. *Proc. Inst. Mech. Eng. C* **1986**, *200*, 303–312.

375. Yamano, H.; Shiota, K.; Miura, R.; Katagiri, M.; Kubo, M.; Stirling, A.; Broclawik, E.; Miyamoto, A.; Tsubouchi, T. Molecular dynamics simulation of traction fluid molecules under EHL condition. *Thin Solid Films* **1996**, *281*, 598–601.

376. Washizu, H.; Ohmori, T. Molecular dynamics simulations of elastohydrodynamic lubrication oil film. *Lubr. Sci.* **2010**, *22*, 323–340.

377. Kobayashi, H.; Fujita, Y. Mechanisms for three kinds of limiting shear stresses appearing in the traction modes of viscous, viscoelastic, and glassy states of lubricants. *J. Appl. Phys.* **2014**, *115*, 223509.

378. Mendonca, A. C. F.; Padua, A. A. H.; Malfreyt, P. Nonequilibrium Molecular Simulations of New Ionic Lubricants at Metallic Surfaces: Prediction of the Friction. *J. Chem. Theory Comput.* **2013**, *9*, 1600–1610.

379. Canova, F. F.; Matsubara, H.; Mizukami, M.; Kurihara, K.; Shluger, A. L. Shear dynamics of nanoconfined ionic liquids. *Phys. Chem. Chem. Phys.* **2014**, *16*, 8247–8256.

380. van Duin, A. C. T.; Dasgupta, S.; Lorant, F.; Goddard, W. A. ReaxFF: A reactive force field for hydrocarbons. *J. Phys. Chem. A* **2001**, *105*, 9396–9409.

381. Senftle, T. P.; Hong, S.; Islam, M. M.; Kylasa, S. B.; Zheng, Y.; Shin, Y. K.; Junkermeier, C.; Engel-Herbert, R.; Janik, M. J.; Aktulga, H. M.; Verstraelen, T.; Grama, A.; van Duin, A. C. T. The ReaxFF reactive force-field: development, applications and future directions. *npj Comput. Mater.* **2016**, *2*, 15011.

382. Bohm, O.; Pfadenhauer, S.; Leitsmann, R.; Planitz, P.; Schreiner, E.; Schreiber, M. ReaxFF+-A New Reactive Force Field Method for the Accurate Description of Ionic Systems and Its Application to the Hydrolyzation of Aluminosilicates. *J. Phys. Chem. C* **2016**, *120*, 10849–10856.

383. Chenoweth, K.; van Duin, A. C. T.; Goddard, W. A. ReaxFF reactive force field for molecular dynamics simulations of hydrocarbon oxidation. *J. Phys. Chem. A* **2008**, *112*, 1040–1053.

384. Yue, D. C.; Ma, T. B.; Hu, Y. Z.; Yeon, J.; van Duin, A. C. T.; Wang, H.; Luo, J. B. Tribochemistry of Phosphoric Acid Sheared between Quartz Surfaces: A Reactive Molecular Dynamics Study. *J. Phys. Chem. C* **2013**, *117*, 25604–25614.

385. Ostadhossein, A.; Rahnamoun, A.; Wang, Y.; Zhao, P.; Zhang, S.; Crespi, V. H.; Van Duin, A. C. T. ReaxFF Reactive Force-Field Study of Molybdenum Disulfide (MoS2). *J. Phys. Chem. Lett.* **2017**, *8*, 631–640.

386. Mosey, N. J.; Woo, T. K. Finite temperature structure and dynamics of zinc dialkyldithiophosphate wear inhibitors: A density functional theory and ab initio molecular dynamics study. *J. Phys. Chem. A* **2003**, *107*, 5058–5070.

387. Mosey, N. J.; Muser, M. H.; Woo, T. K. Molecular mechanisms for the functionality of lubricant additives. *Science.* **2005**, *307*, 1612–1615.

388. Mosey, N. J.; Woo, T. K. Insights into the chemical behavior of zinc dialkyldithiophosphate anti-wear additives in their isomeric and decomposed forms through molecular simulation. *Tribol. Int.* **2006**, *39*, 979–993.

389. Mosey, N. J.; Woo, T. K. An ab Initio Molecular Dynamics and Density Functional Theory Study of

the Formation of Phosphate Chains from Metathiophosphates. *Inorg. Chem.* **2006**, *45*, 389–395.

390. Levita, G.; Righi, M. C. Effects of Water Intercalation and Tribochemistry on MoS2 Lubricity: An Ab Initio Molecular Dynamics Investigation. *ChemPhysChem* **2017**, *18*, 1–7.

391. Minfray, C.; Le Mogne, T.; Martin, J. M.; Onodera, T.; Nara, S.; Takahashi, S.; Tsuboi, H.; Koyama, M.; Endou, A.; Takaba, H.; Kubo, M.; Del Carpio, C. A.; Miyamoto, A. Experimental and Molecular Dynamics Simulations of Tribochemical Reactions with ZDDP: Zinc Phosphate-Iron Oxide Reaction. *Tribol. Trans.* **2008**, *51*, 589–601.

392. Onodera, T.; Morlta, Y.; Suzuki, A.; Koyama, M.; Tsuboi, H.; Hatakeyama, N.; Endou, A.; Takaba, H.; Kubo, M.; Dassenoy, F.; Minfray, C.; Joly-Pottuz, L.; Martin, J. M.; Miyamoto, A. A computational chemistry study on friction of h-MoS2. Part I. Mechanism of single sheet lubrication. *J. Phys. Chem. B* **2009**, *113*, 16526–16536.

393. Onodera, T.; Morita, Y.; Suzuki, A.; Sahnoun, R.; Koyama, M.; Tsuboi, H.; Hatakeyama, N.; Endou, A.; Takaba, H.; Del Carpio, C. A.; Deka, R. C.; Kubo, M.; Miyamoto, A. Tribochemical Reaction Dynamics of Molybdenum Dithiocarbamate on Nascent Iron Surface: A Hybrid Quantum Chemical/Classical Molecular Dynamics Study. *J. Nanosci. Nanotechnol.* **2010**, *10*, 2495–2502.

394. Onodera, T.; Morita, Y.; Nagumo, R.; Miura, R.; Suzuki, A.; Tsuboi, H.; Hatakeyama, N.; Endou, A.; Takaba, H.; Dassenoy, F.; Minfray, C.; Joly-Pottuz, L.; Kubo, M.; Martin, J. M.; Miyamoto, A. A Computational Chemistry Study on Friction of h-MoS2 Part II Friction Anisotropy. *J. Phys. Chem. B* **2010**, *114*, 15832–15838.

395. Onodera, T.; Martin, J. M.; Minfray, C.; Dassenoy, F.; Miyamoto, A. Antiwear chemistry of ZDDP: Coupling classical MD and tight-binding quantum chemical MD methods (TB-QCMD). *Tribol. Lett.* **2013**, *50*, 31–39.

396. Singh, M. K.; Ilg, P.; Espinosa-Marzal, R. M.; Kroger, M.; Spencer, N. D. Polymer Brushes under Shear: Molecular Dynamics Simulations Compared to Experiments. *Langmuir* **2015**, *31*, 4798–4805.

397. Singh, M. K.; Ilg, P.; Espinosa-Marzal, R. M.; Spencer, N. D.; Kröger, M. Influence of chain stiffness, grafting density and normal load on the tribological and structural behavior of polymer brushes: A nonequilibrium-molecular-dynamics study. *Polymers (Basel).* **2016**, *8*.

398. Farrow, M. R.; Chremos, A.; Camp, P. J.; Harris, S. G.; Watts, R. F. Molecular Simulations of Kinetic-Friction Modification in Nanoscale Fluid Layers. *Tribol. Lett.* **2011**, *42*, 325–337.

399. Fajardo, O. Y.; Bresme, F.; Kornyshev, A. A.; Urbakh, M. Electrotunable Friction with Ionic Liquid Lubricants: How Important Is the Molecular Structure of the Ions? *J. Phys. Chem. Lett.* **2015**, *6*, 3998–4004.

400. Holland, D. M.; Lockerby, D. A.; Borg, M. K.; Nicholls, W. D.; Reese, J. M. Molecular dynamics pre-simulations for nanoscale computational fluid dynamics. *Microfluid. Nanofluidics* **2015**, *18*, 461–474.

401. Smith, E. R.; Heyes, D. M.; Dini, D.; Zaki, T. A. Control-volume representation of molecular dynamics. *Phys. Rev. E* **2012**, *85*, 19.

402. Smith, E. R.; Heyes, D. M.; Dini, D.; Zaki, T. A. A localized momentum constraint for non-equilibrium molecular dynamics simulations. *J. Chem. Phys.* **2015**, *142*.

403. O'Connell, S. T.; Thompson, P. A. Molecular dynamics-continuum hybrid computations: A tool for studying complex fluid flows. *Phys. Rev. E* **1995**, *52*, 5792–5795.

404. Flekkøy, E. G.; Wagner, G.; Feder, J. Hybrid model for combined particle and continuum dynamics. *Europhys. Lett.* **2000**, *52*, 271–276.

405. Nie, S. Y.; Chen, W. N. E.; Robbins, M. O. A continuum and molecular dynamics hybrid method for micro- and nano-fluid flow. *J. Fluid Mech.* **2004**, *500*, 55–64.

406. Ren, W. Analytical and numerical study of coupled atomistic-continuum methods for fluids. *J. Comput. Phys.* **2007**, *227*, 1353–1371.

407. Mohamed, K. M.; Mohamad, A. A. A review of the development of hybrid atomistic-continuum methods for dense fluids. *Microfluid. Nanofluidics* **2010**, *8*, 283–302.

408. Smith, E.; Trevelyan, D.; Ramos-Fernandez, E. cpl-library 2016.

Appendix A. Supporting Information for Chapter 4

The work described in this appendix has been published as Supporting Information in *Langmuir* (ref. [267]). Table 4 shows the force-field parameters used in these simulations. They are taken from; L-OPLS-AA for the alkyl and alkenyl chains [26], an updated OPLS-AA for ester groups , and the original OPLS-AA for carboxylic acid, amide and alcohol groups [234], which had not been updated since the original parameterization at the time of submission (have been since [370]). Parameters for the hematite surface are those developed by Berro *et al.* [169]. Non-bonded parameters are shown for all of the OFM functional groups with OPLS atom types. For full bonded parameters, see the references provided.

Table 4. Full non-bonded force-field parameters

Ref	Atom Type	Description	q (e)	σ (Å)	ε (kcal mol^{-1})
Ester (Glyceride)					
32	C	C=O	0.510	3.750	0.105
	O	O=C	-0.430	2.960	0.210
	OS	ROR	-0.330	3.000	0.170
	CT	RCH2OR	*0.110	3.500	0.066
Alcohol (Glyceride)					
[234]	OH	ROH	-0.683	3.120	0.170
	HO	ROH	0.418	**0.200	**0.030
	CT	RCH2OH	*0.125	3.500	0.066
	CT	R2CHOH	*0.175	3.500	0.066
Amide					
[234]	C	C=O	0.500	3.750	0.105
	O	O=C	-0.500	2.960	0.210
	N	RCONH2	-0.760	3.250	0.170
	H	RCONH2	0.380	**0.200	**0.030
Acid					
[234]	C	RCOOH	0.520	3.750	0.105
	O	RCOOH	-0.440	2.960	0.210
	OH	RCOOH	-0.530	3.000	0.170
	H	RCOOH	0.450	**0.200	**0.030
Alkyl/Alkenyl					
[26]	CTT	CH3 alkane	-0.222	3.500	0.066
	CT	CH2 alkane	-0.148	3.500	0.066
	CM	CH alkene	-0.160	3.550	0.076
	HCT	CH3 alkane	0.074	2.500	0.030
	HC	CH2 alkane	0.074	2.500	0.026
	HC	CH alkene	0.160	0.242	0.030
Surface					
[169]	FE	Surface Fe	0.771	2.320	0.340
	OX	Surface O	-0.514	2.960	0.170

*Partial charges slightly modified to allow neutral glyceride molecules with L-OPLS alkyl CT and HC charges.

**H atoms are assigned very small L-J parameters to prevent overlap with OX slab atoms (does not affect dynamics).

Fig. 56 shows results of squeeze-out simulations for representative OFM (SA, high coverage) for different system *x y* dimensions (Å); variation in number of hexadecane molecules within contact volume over 300 ps, Pz = 0.5 GPa. It shows that the two-molecular layer equilibrium thickness outlined in the manuscript is not significantly influenced by the system size (boundary effects).

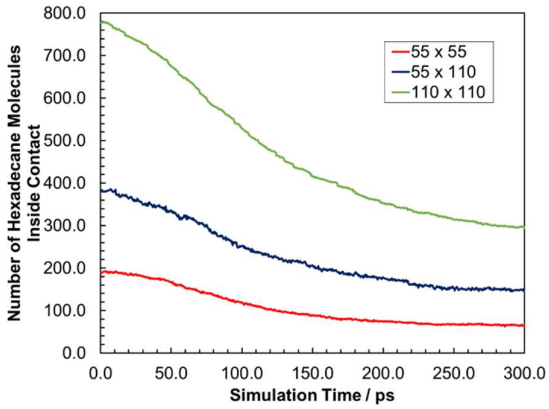

Figure 56. Variation in the number of hexadecane molecules inside the contact volume with simulation time for different slab sizes (Å)

Fig. 57 shows how the structure of the system changes under compression (dotted) and sliding (solid) at i) high, ii) medium and iii) low coverage for a representative OFM (SA). One can observe that the changes are minimal and thus the structure of the system is mainly governed by the response to the applied pressure.

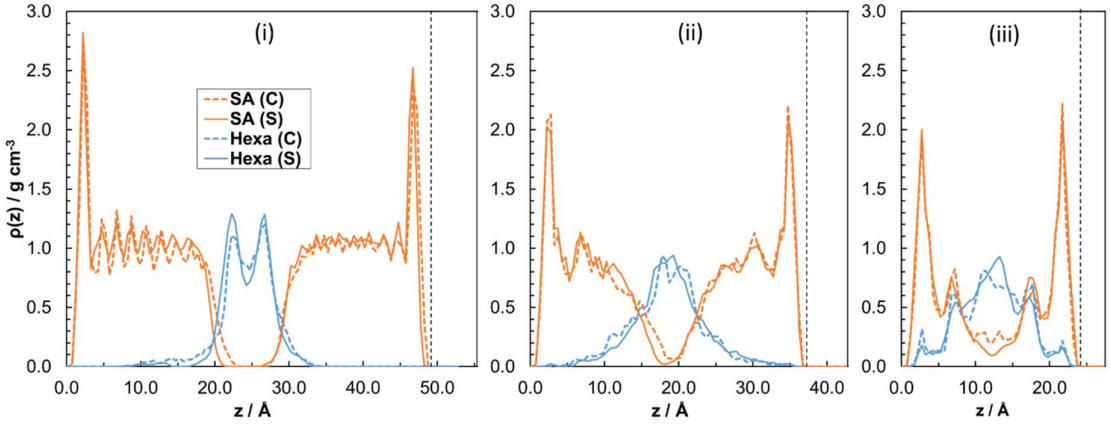

Figure 57. Mass density profile in z, ρ(z), of OFM (orange) and hexadecane (blue) for representative OFM (SA) under compression (dotted) and sliding (solid)

Fig. 58 and Fig. 59 show mass density profiles and number density profiles for SAm (solid) and OAm (dotted) at i) high, ii) medium and iii) low coverage. These profiles represent an intermediate case between OFMs with acid and glyceride headgroups in terms of the interdigitation between the lubricant and hexadecane layers. This is reflect in the fact that amides show intermediate friction between OFMs with acid and glyceride headgroups.

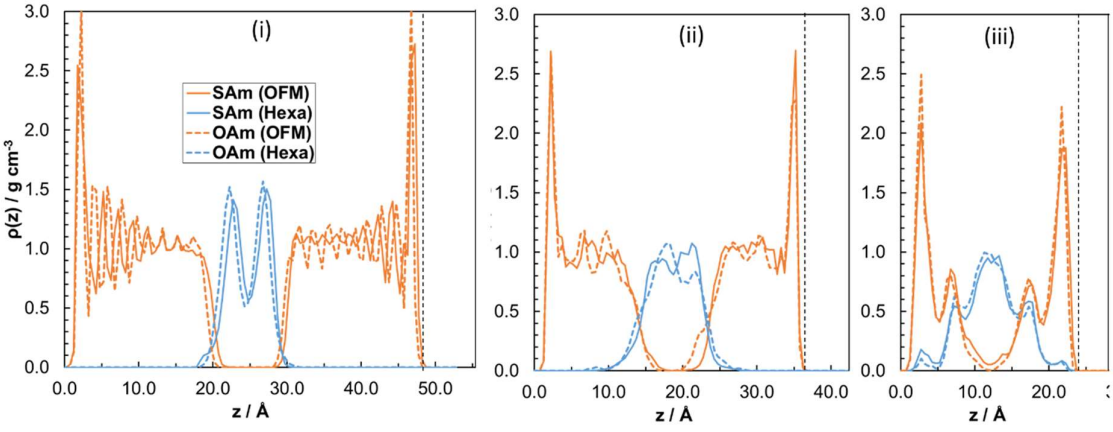

Figure 58. Atomic mass density profile in z, ρ(z), for SAm (solid) and OAm (dotted) under shear

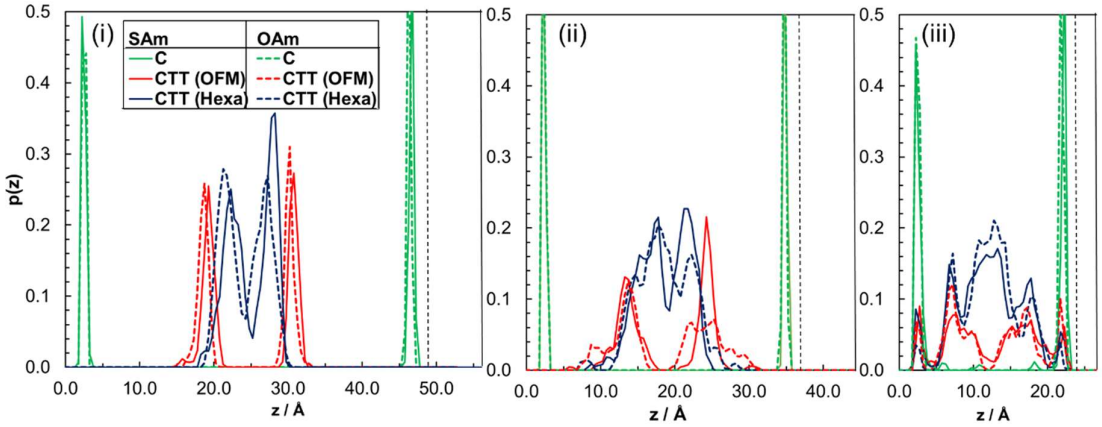

Figure 59. Atomic position probability profile for SAm (solid) and OAm (dotted) under shear

Fig. 60 shows the variation in the block averaged friction coefficient with simulation time for representative OFM (GMS, high coverage), P_z = 0.5 GPa, v_s = 10 m s^{-1}. Block averages are calculated every 100 ps and the first 100 ps average is not included in the overall average because steady state sliding has not been achieved. Green circles show data for first 1 ns (as used for all 10 m s^{-1} results described in main publication), green crosses show data for extended simulation. Note that the friction is coefficient is consistent and that virtually the same average friction coefficient can be obtained after 1 ns as after 10 ns.

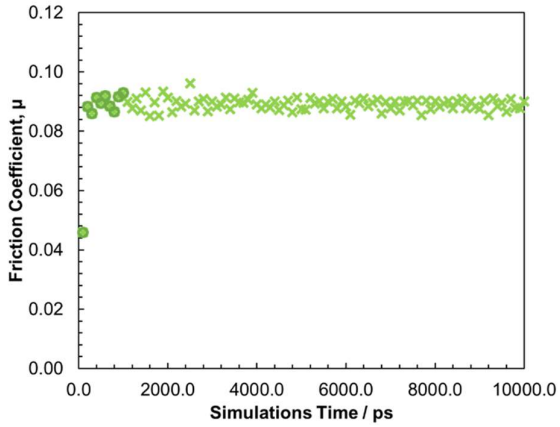

Figure 60. Variation in the block-averaged friction coefficient with simulation time for extended 10 ns, 10 m s^{-1} sliding simulation for GMS at high coverage

Appendix B. Supporting Information for Chapter 8

The work described in this appendix has been published as Electronic Supplementary Information in *Physical Chemistry Chemical Physics* (ref. [42]).

Thermal Correction Procedure

The equations governing temperature rise under EHL conditions were first described by Archard [367]. There are two components, the 'flash temperature rise', $\Delta\bar{T}_{surf}$, of the solid surfaces in response to transient heat input as they traverse the contact, and an additional rise of oil film temperature above that of the bounding solid surfaces, $\Delta\bar{T}_{oil}$, due to the relatively low thermal conductivity of the oil.

The total mean temperature rise of the oil film above the inlet temperature is then given, for a point contact, by:

$$\Delta\bar{T}_{tot} = \Delta\bar{T}_{surf} + \Delta\bar{T}_{oil}$$

$$\Delta\bar{T}_{tot} = \left(\frac{1}{(2\pi K_s \rho c)^{0.5}} {t_i}^{0.5} h + \frac{1}{8K_{oil}} h^2\right) \bar{\tau}\,\dot{\gamma} \qquad \text{(Equation 5)}$$

where the first term describes the mean flash temperature rise and the second the additional mean oil film temperature rise. In Equation 5, K_s, ρ and c the thermal conductivity, density and specific heat of the solid bodies, respectively, t_i is the time of transit of the surfaces across the contact, h the film thickness and K_{oil} the thermal conductivity of the oil at the mean pressure of the contact, $\bar{\tau}$ is the mean shear stress and $\dot{\gamma}$ is the strain rate. The flash temperature term in Equation 5 assumes that both solids are of the same material and travel at approximately the same speed with respect to the contact, but it can quite easily be adjusted to accommodate different materials and speeds. In the second term, the value in the denominator (8) is debated and depends on where heat is generated in the oil film. Archard derived the value of 8 assuming that heat is generated evenly through the oil film thickness (i.e. Couette flow), while a value of 4 was obtained if all the heat is generated at the midplane (i.e. central localisation) [8,367].

Equation 5 shows that at high values of shear stress and strain rate, the mean oil film temperature can rise very significantly, particularly when the film thickness, h, is large. This complicates the interpretation of traction curves since it must be accounted for before any model of rheology can be inferred [8]. To achieve this, we assume a mean temperature rise across the contact, Johnson and Greenwood have demonstrated the validity of the mean temperature approach [368]. We start with a set of mean shear stress versus strain rate curves made at a series of different bulk temperatures between 30 and 120 °C (*e.g.* Fig. 61). Note that in Fig. 61, the 110 and 120 °C data are not shown since we do not determine a thermal correction at these temperatures as this would involve extrapolation [369]. Our correction of the experimental shear stress measurements involves two stages [8,369].

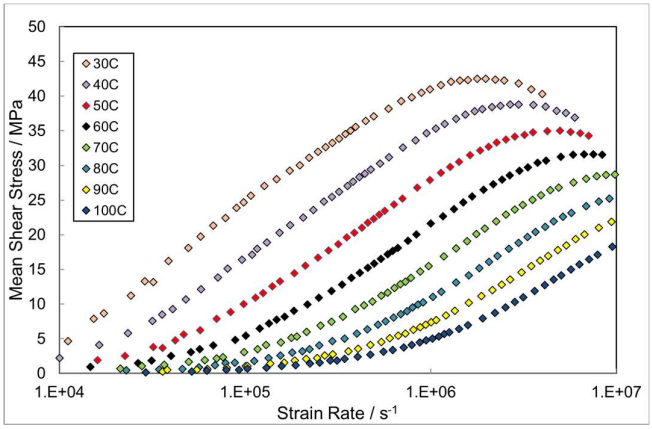

Figure 61. Mean shear stress *versus* strain rate for squalane at 0.75 GPa (50 N, steel/steel) with different bulk oil temperatures

In the first stage, we use Equation 5 to estimate the mean temperature rise for every single measurement, based on the mean shear stress and strain rate of this measurement; thus, for each measured data point, we now have a corrected mean film temperature which is equal to or higher than the bulk test temperature [369].

In the second stage, for all shear stress data points, we identify its strain rate and extract, from the data measured at other temperatures, measurements made at this identical strain rate (with interpolation when necessary). We thus obtain a plot of mean shear stress versus corrected mean temperature at this fixed strain rate (see for example Figure 1 in reference [369]). We fit a smooth

curve to this and use interpolation to determine, for each data point, how much the mean shear stress will have been reduced by the calculated rise in temperature. We then add this value to the measured mean shear stress. When carried out on all points in a shear stress *versus* log(strain rate) curve, this gives us an isothermal mean shear stress *versus* log(strain rate) curve at the bulk test temperature. We only do this for mean temperature rises of <10°C, since we recognise that the procedure becomes less exact as temperature rise increases [369].

It is important to note that this procedure makes no assumptions about the rheology of the film nor how mean shear stress varies with temperature. Instead, the latter is extracted directly from our measurements made at a series of different temperatures. The thermally-corrected mean shear stresses calculated using this interpolation method are very similar to those calculated using a 3-D fitting procedure [15].

Fluid Force-Field Parameters

Interactions between the liquid molecules are represented with an updated form of the all-atom 'optimized potential for liquid simulations' (OPLS) force-field [234], L-OPLS-AA [26]. In this force-field, both bonded and non-bonded parameters have been updated for several atom types to provide a more realistic description of long-chain alkanes [26] and, more recently, alcohols and esters [370]. Specifically, parameters for all primary and secondary carbon atoms and aliphatic hydrogen atoms in squalane, DEHS, DCMP and DM2H were taken from ref. [26]. Tertiary and quaternary carbon atoms have the same Lennard-Jones parameters as primary and secondary carbon atoms [26], with their partial charges adjusted to ensure that the molecules have no overall charge. Parameters for the ester group in DEHS are taken from ref. [370].

In order to be confident that the force-field was suitable for the molecules chosen in this study, it was ensured that their experimental liquid density, ρ, was accurately reproduced in bulk simulations of 100 molecules in the isothermal-isobaric (NPT) ensemble (see reference[69] for full methodology). Table 5 shows that the experimental and simulated densities are in good agreement, confirming the suitability of chosen force-field for the studied fluids.

Table 5. Experimental and simulated densities of the studied fluids, high pressure data is from references [48,49], ambient data was measured using an Anton Paar Density Meter

Fluid	T / °C	P / GPa	Experimental ρ / g cm^{-3}	Simulated ρ / g cm^{-3}	Simulation Error / %
Squalane	20	0.796	0.976	0.960	-1.7
	20	0.875	0.984	0.967	-1.8
	20	0.955	0.991	0.974	-1.7
	8	0.955	0.995	0.978	-1.7
	25	0.000101	0.810	0.812	0.2
DM2H	25	0.000101	0.961	0.972	1.1
DCMP	25	0.000101	0.890	0.901	1.2
DEHS	25	0.000101	0.914	0.926	1.3

Boundary Slip

Boundary slip occurs when the fluid cohesion is relatively stronger than its adhesion to the solid slabs [90], meaning that the slabs do not transfer sufficient momentum to shear the fluid [142]. The phenomenon is commonly observed in NEMD simulations of very thin films (<10 nm) between atomically smooth slabs [142–146]. The slip length has been shown to increase with increasing; fluid viscosity, wall stiffness, sliding velocity, and pressure [142–146]. Conversely, the slip length has been shown to decrease with increasing surface-fluid interaction strength and film thickness [143–145] and to be virtually eliminated in the presence of atomic-scale surface roughness [135].

Boundary slip has been observed experimentally for viscous polybutadiene between oleophobic surfaces;[150] however, this phenomenon is not expected to occur for the fluids, surfaces, and experimental conditions used in the current study (Table 1) [152,156]. Large-scale NEMD simulations of a >100 nm *n*-hexane film between iron surfaces under realistic EHL conditions (F_N = 1 GPa, $\dot{\gamma} = 10^5$ s^{-1}) confirmed the suitability of a macroscopic no-slip boundary condition for this system [144]. However, these simulations were extremely computationally expensive, making them unsuitable for the wide parameter study required here. Therefore, in order to increase computational efficiency, most of the NEMD simulations were performed on the thinnest systems (h ≈ 15 nm) for which boundary slip did not occur under the conditions of interest on the wetting [352] α-Fe_2O_3 slabs.

The parameters used for the α-Fe_2O_3 slabs were similar to those developed by Savio et al. [142] and Berro et al. [169]; ε_O = 0.21 kcal mol^{-1}, σ_O = 2.96 Å, q_O = -0.514 e; ε_{Fe} = 20.0 kcal mol^{-1}, σ_{Fe} = 2.32 Å, q_{Fe} = +0.771 e. The value of ε_{Fe} was increased relative to these previous studies to increase the strength of short-ranged surface-fluid interactions and discourage boundary slip, allowing a computationally-feasible film thickness to be simulated for this extensive parameter study. It is important to note that previous NEMD studies have shown that, once slip is prevented, an increase in the strength of surface-fluid interactions does not significantly affect the shear stress in the confined fluid [142,169].

Film Thickness

Apart from in very strongly confined systems [353], and in the absence of boundary slip, the shear stress in bulk and confined simulations is virtually indistinguishable [90,142,350]. In order to ensure that the choice of film thickness in the NEMD simulations did not significantly influence the mean shear stress results, some systems were also tested in systems with half and double the film thickness. Fig. 62 shows the variation in the block-averaged shear stress and pressure with sliding distance for three different film thicknesses for a representative case (squalane at 0.5 GPa, 80 °C, 3.1 x 10^8 s^{-1}). These systems all gave the same shear stress result at equal strain rate within the statistical uncertainty. This confirms that the shear stress measurements from the NEMD simulations (h ≈ 15 nm) are directly comparable to results from the thicker experimental films (h ≈ 150 nm).

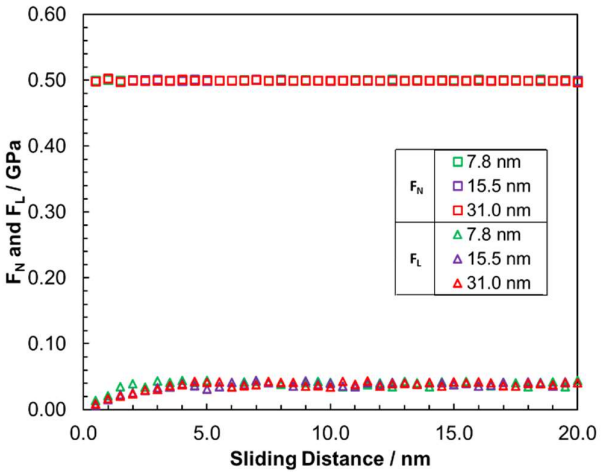

Figure 62. Example of the variation in the block-averaged shear stress (F_L) and pressure (F_N) with sliding distance for squalane systems with film thicknesses of 7.75 nm (2.5 m s^{-1}), 15.5 nm (5 m s^{-1}) and 31.0 nm (10 m s^{-1}) at 3.1 x 10^8 s^{-1}, 0.5 GPa, 80 °C

Additional Velocity Profiles

Fig. 63 shows how the *x*-velocity profile in the *z*-dimension, $v_x(z)$, and the atomic mass density profile in the *z*-dimension, changes with the applied pressure for DEHS. The profiles show similar flow behaviour as observed for the other lubricant (squalane).

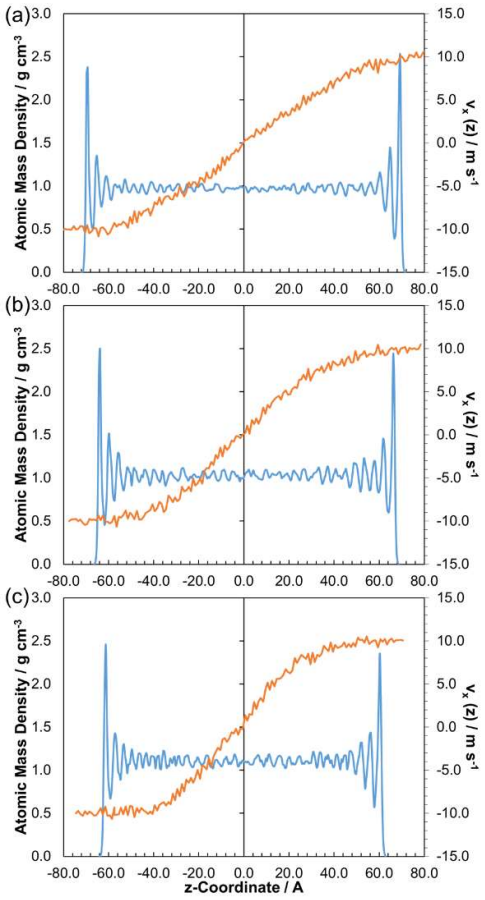

Figure 63. Atomic mass density (blue) and velocity (orange) profiles for DEHS at: 80 °C, 20 m s^{-1} ($\dot{\gamma} \approx 10^9$ s^{-1}), and; 0.50 GPa (a), 1.00 GPa (b), 2.00 GPa (c). Time-averaged for the final 5 nm of sliding.

Fig. 64 shows how the *x*-velocity profile in the *z*-dimension, $v_x(z)$, and the atomic mass density profile in the *z*-dimension, changes with the applied pressure for DCMP. The profiles show similar flow behaviour as observed for the other traction fluid (DM2H). However, at the lowest pressure considered (0.5 GPa), the flow is more Couette-like for DCMP than DM2H.

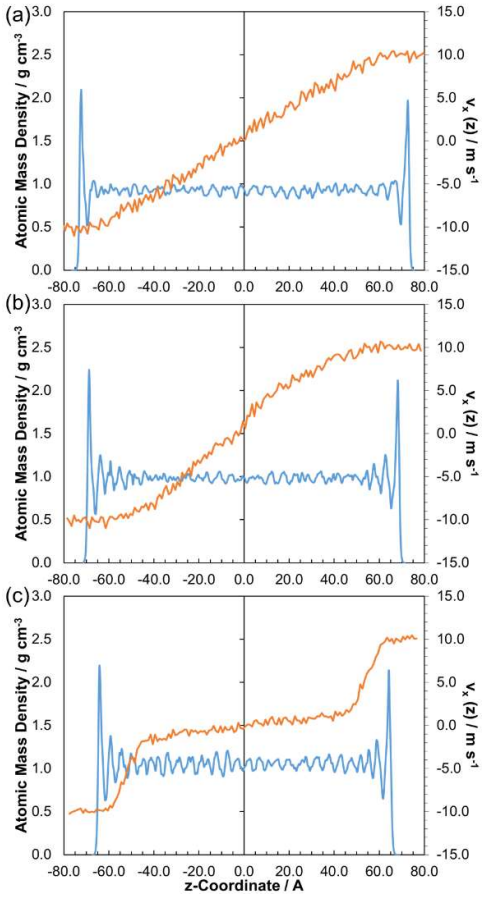

Figure 64. Atomic mass density (blue) and velocity (orange) profiles for DCMP at: 80 °C, 20 m s^{-1} ($\dot{\gamma} \approx 10^9$ s^{-1}), and; 0.50 GPa (a), 1.00 GPa (b), 2.00 GPa (c). Time-averaged for the final 5 nm of sliding.